GEORGIA INSTITUTE OF TECHNOLOGY LIBRARY

Regulations for the Use of Theses

Unpublished theses submitted for the Master's and Doctor's degrees and deposited in the Georgia Institute of Technology Library are open for inspection and consultation, but must be used with due regard for the rights of the authors. Passages may be copied only with permission of the authors, and proper credit must be given in subsequent written or published work. Extensive copying or publication of the thesis in whole or in part requires the consent of the Dean of the Graduate Division of the Georgia Institute of Technology.

This thesis by Roger Paul Woodward has been used by the following persons, whose signatures attest their acceptance of the above restrictions.

A library which borrows this thesis for use by its patrons is expected to secure the signature of each user.

NAME AND ADDRESS OF USER	BORROWING LIBRARY	DATE

AUGER ELECTRON SPECTROSCOPY FOR THE STUDY OF SURFACE CONTAMINATION IN SEMICONDUCTOR DEVICES

A THESIS

Presented to

The Faculty of the Division of Graduate

Studies and Research

By

Roger Paul Woodward

In Partial Fulfillment

of the Requirements for the Degree

Doctor of Philosophy

in the School of Electrical Engineering

Georgia Institute of Technology

May, 1973

AUGER ELECTRON SPECTROSCOPY FOR THE STUDY OF SURFACE CONTAMINATION IN SEMICONDUCTOR DEVICES

Approved:

Dale C. Ray, Chairman

E. J. Scheibner

G. P. Rodrigue

Date approved by Chairman: 5/24/73

ACKNOWLEDGMENTS

I wish to thank Dr. Dale C. Ray for his patient guidance during the research leading to this dissertation and for his critique of the manuscript. I would also like to thank Drs. E. J. Scheibner and G. P. Rodrique for their critical review of the dissertation. Dr. Scheibner in particular motivated my early interest in the work.

Dr. Scheibner and Dr. G. R. Harrison both contributed to the support of the research as heads of the Physical Sciences Division of the Engineering Experiment Station at Georgia Tech. Dr. L. N. Tharp assisted the early portion of the work with technical guidance. Mr. L. H. Glassman performed the electron microscopy.

I would also like to thank Ms. P. B. Woodward for drafting the figures and Mrs. Claudine Taylor for typing the thesis.

This thesis is dedicated to pfp.

TABLE OF CONTENTS

TABLE OF CONTENTS (Continued)

LIST OF TABLES

LIST OF ILLUSTRATIONS

LIST OF ILLUSTRATIONS (Continued)

LIST OF ILLUSTRATIONS (Continued)

LIST OF ILLUSTRATIONS (Continued)

LIST OF ILLUSTRATIONS (Continued)

LIST OF ILLUSTRATIONS (Continued)

LIST OF ILLUSTRATIONS (Continued)

SUMMARY

The objectives of this research were twofold: (1) to improve Auger electron spectroscopy as an analytical tool for detecting surface contamination in semiconductor devices, and (2) to apply Auger electron spectroscopy in the study of surface contamination on typical semiconductor devices.

The primary motivation for the improvement of Auger spectroscopy as an analytical tool is that it is still more qualitative than quantitative, which is not surprising since use of Auger spectroscopy for material identification is less than ten years old. Auger spectroscopy, being surface sensitive, is an ideal tool for the semiconductor industry, where surface treatments are critical to device performance, but still largely empirical in nature.

The improvement of the spectroscopy focused on two problems. The first was to improve the quantitative calibration of the spectroscopy. A new model, containing both isotropic and oriented source functions, was formulated to explain the behavior of Auger spectra as parameters of the spectrometer and specimen are varied. Each of the four quantities contributing to Auger peak height--the source functions, Auger electron yield, Auger electron escape probability, and detector efficiency--are discussed in detail. The calculations necessary both to predict Auger peak height a priori and to interpret peak heights using calibration spectra are demonstrated. The second problem was to develop the techniques to successfully perform the spectroscopy on oxide surfaces. These techniques are for the detection

and prevention of charging artifices. This compilation enables the Auger spectroscopist to take and interpret reliable data from commercial semiconductor surfaces.

The application of Auger spectroscopy to typical semiconductor surfaces concentrated on wafers removed from commercial manufacturing lines. Representative spectra from oxide surfaces are presented and quantitatively interpreted. Effects of the primary electron beam are described and electron stimulated desorption is shown to be a complementary technique to Auger spectroscopy. One particular aspect of the contamination found on commercial wafers, the sources and forms of carbon, is discussed in detail. The results of the Auger spectroscopy study into the nature of carbon contamination are correlated with electron microscopy of the same surfaces. Finally, some effects of the various forms of carbon are postulated.

CHAPTER I

INTRODUCTION

Auger electron spectroscopy is a method of determining the chemical nature of the surface of a solid by studying the energy distribution of secondary electrons emitted when the surface is bombarded by electrons or X rays. This research studied the application of Auger spectroscopy to partially completed semiconductor wafers taken from a commercial semiconductor device manufacturing process.

Chapter I of this dissertation contains a statement of the problem and a brief introduction to Auger spectroscopy. Specifically, the next section is a statement of the objectives of the research. The following section is a brief explanation of why the research was undertaken. The basic theory of the Auger effect is then discussed and a prototype Auger spectrometer is introduced. Following that is a discussion of some of the more practical aspects of Auger spectroscopy. Chapter I concludes with a statement of the nature of the contributions of this work.

Chapter II is concerned with prior attempts to apply Auger spectroscopy to semiconductor manufacturing problems. The general areas of accomplishment are stated and some of the problems of data interpretation are discussed. Detection of the artifices pointed out in this chapter constitutes an important part of this research.

Chapter III describes the instrumentation and equipment used in the work.

Chapter IV discusses the calibration of Auger spectroscopy, both from a theoretical and an experimental viewpoint. While the effects of various parameters can be qualitatively explained, a complete quantitative theory is not yet available, so calibration curves are given for the materials of interest in this work.

Auger spectroscopy results of various commercial oxide surfaces are given in Chapter V. Carbon, a common surface contaminant, was found to exist both in the form of graphite and silicon carbide. A variety of artifices were found to be caused by surface charging. Chapter VI is a description of these artifices found in the spectroscopy of silicon dioxide surfaces. Chapter VII is a more complete description of the nature of carbon on silicon dioxide surfaces. Electron microscopy was used to show that the silicon carbide exists in the form of particles on both silicon and silicon dioxide surfaces. Chapter VIII is a summary chapter with conclusions and recommendations for further work.

Objectives of the Research

The objectives of this research were twofold: (1) to improve Auger electron spectroscopy as an analytical tool for detecting surface contamination in semiconductor devices, and (2) to apply Auger electron spectroscopy in the study of surface contamination on typical semiconductor devices.

Improvement of Auger spectroscopy as an analytical tool focused on five technical problems. These were the charging problem on electrical insulator specimens, the nature of surface damage caused by the incident electron beam, quantitative calibration of common contaminants on semiconductor device surfaces, determination of the effect of the source electron beam parameters, and removal

of background slopes from the spectrum.

The application of Auger spectroscopy to semiconductor manufacturing problems involved several steps. The first was to achieve the capability of performing meaningful spectroscopy on non-uniform insulator surfaces. The surface of a partially completed semiconductor wafer contains oxide regions of differing thicknesses arranged in a complex pattern. These complex surfaces make the charging problems even more difficult to handle than those associated with smooth, uniform insulator surfaces. The second step was to determine typical contaminants on commercial wafer surfaces. The third step was to compare these contaminants with those found on "clean" surfaces prepared in the ultra high vacuum system. Finally, the potential effects of the contaminants seen on commercial wafers were postulated.

Motivation for the Work

The primary motivation for the improvement of Auger spectroscopy was that the spectroscopy is still more qualitative than quantitative, which is not surprising since use of Auger spectroscopy for material identification is less than ten years old. As an example, the ordinate of almost all published work is not calibrated. The abscissa (energy) axis of most work is poorly resolved and there are deviations between workers as to the exact location of peaks. Additionally there appear to be artifices in published curves for insulator surfaces. On the other hand, Auger spectroscopy has proven useful when results could be interpreted unambiguously or when "before and after" comparisons could be made.

The motivation for surface studies of semiconductors is that surface

conditions often determine the electrical performance of a device. For example, semiconductor devices are manufactured by controlled diffusion of impurity atoms through the surface and into the device. Imperfections in the surface thus can directly affect the manufacturing process.[1] As another example, the oxidation of silicon surfaces stabilizes the band structure and also prevents undesirable impurities from entering the device.[2] Surface contamination will affect this passivation. Contaminants can also introduce surface states, energy levels in the forbidden gap, which are correlated with transistor noise behavior and MOS threshold voltages.[3] Surface treatments used in semiconductor device manufacture are still largely empirical in nature. Low product yield and lack of understanding of what various surface treatments actually accomplish suggest that the study of semiconductor surfaces is a worthwhile undertaking.

The Auger Effect

The Auger effect was postulated by Pierre Auger[4] in 1925. While observed experimentally by Lander[14] in 1953, only through the efforts of Tharp and Scheibner,[15] Harris,[16] and others in the late 1960's did Auger spectroscopy become a useful surface analysis tool.

The Auger effect involves a radiationless transition between two energy states in an atom, and the emission of an electron with energy characteristic of the atom. As commonly utilized in Auger spectroscopy, the following model describes the three electron process by which an electron, the Auger electron, is emitted. This process is illustrated in Figure 1. The atom is first ionized by some excitation source, normally a primary beam of energetic electrons. The electron ejected in

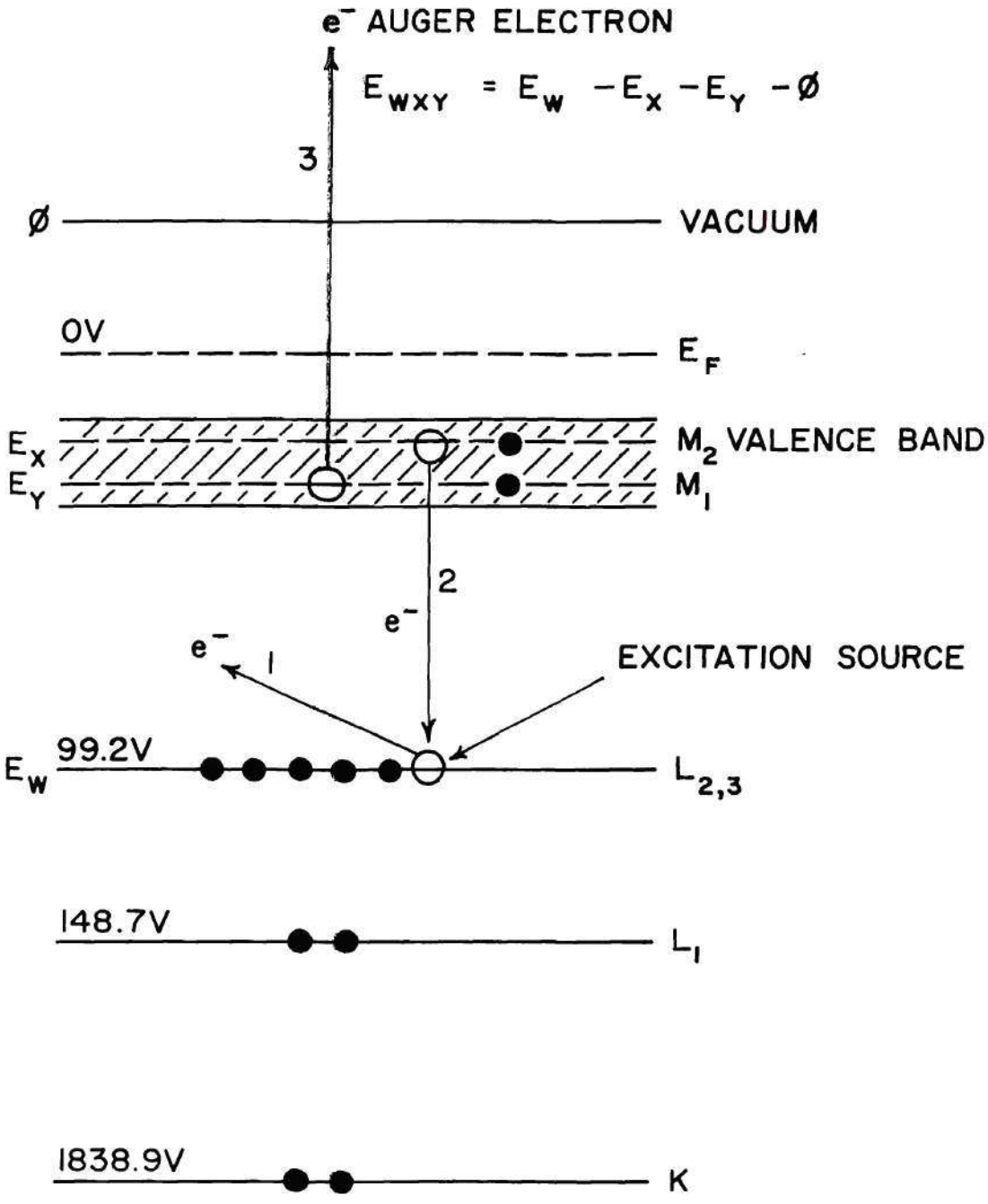

Figure 1. Energy Level Diagram of the $L_{2,3}M_2M_1$ Auger Transition in Si.

the initial ionization, number 1 in the figure, is not considered further. The vacancy is neutralized by an electron, number 2 in the figure, from a higher energy level in the same atom. The energy given up by the second electron is transferred entirely to a third electron, number 3 in the figure. If the third electron escapes the atom, or the solid containing the atom, with its characteristic energy intact it is called an Auger electron. The process of creating and detecting such electrons is Auger spectroscopy. A recently published review[9] provides a more detailed introduction to the Auger effect.

Figure 1 illustrates one of the possible transitions for silicon. Many transitions are possible for each element but only a few will be observed in practice. Thus each element has a "fingerprint" of probable transitions. Auger electrons which lose small, characteristic amounts of energy while escaping are still considered Auger electrons by the spectroscopy but electrons which suffer random losses become part of the background current and do not show as discrete peaks in the spectrum.

The utility of the Auger effect is that one can determine the chemical constituency of a surface by studying the emitted electrons. Furthermore, the spectroscopy is sensitive to only the first few layers of atoms because only from this region can Auger electrons escape, without losing energy in collisions and thereby becoming background current. Auger spectroscopy may be thought of as sampling the first 15 angstroms of a solid. This surface sensitivity may be compared with the electron microprobe which samples the first micron, or so, by electron beam induced X ray emission or with nuclear activation which samples bulk properties.

Only a small percentage of the electrons entering the energy analyzer of an Auger spectrometer are Auger electrons. Figure 2 shows a typical distribution of electrons with respect to energy for a specimen bombarded by an electron beam. Region I of the figure consists of those primary electrons scattered elastically from the sample. Perhaps ten per cent of the total current to the analyzer will be in this energy region. Region III, containing most of the current in this example, is the "slow secondary" region. The slow secondary peak reaches a maximum at a few electron volts and extends out to 50-100 eV. Auger electrons may be emitted with energies falling in region I, but they will be difficult to detect because of the large background current. Only those emitted with energies falling in region II are easily detected. An order of magnitude estimate would find .01% of the electrons into the analyzer to be Auger electrons.[5] Thus an Auger peak would barely show in a complete energy spectrum, such as Figure 2. The basic energy distribution curve is differentiated with respect to energy and amplified to yield the Auger spectrum. The Auger process gives rise to a peak a few electron volts wide in the energy distribution. The differentiated spectrum, the Auger spectrum, has peaks which first rise above and then fall below the background level.

Figure 3 illustrates the basic components of the Auger spectrometer used in this work. The specimen, housed in a high vacuum chamber, is bombarded by an energetic primary beam of electrons which excites the Auger electron emission. The electron energy analyzer determines the energy distribution of the emitted electrons and can also perform the differentiation necessary to produce the Auger spectrum. The synchronous detector is necessary to achieve a satisfactory signal

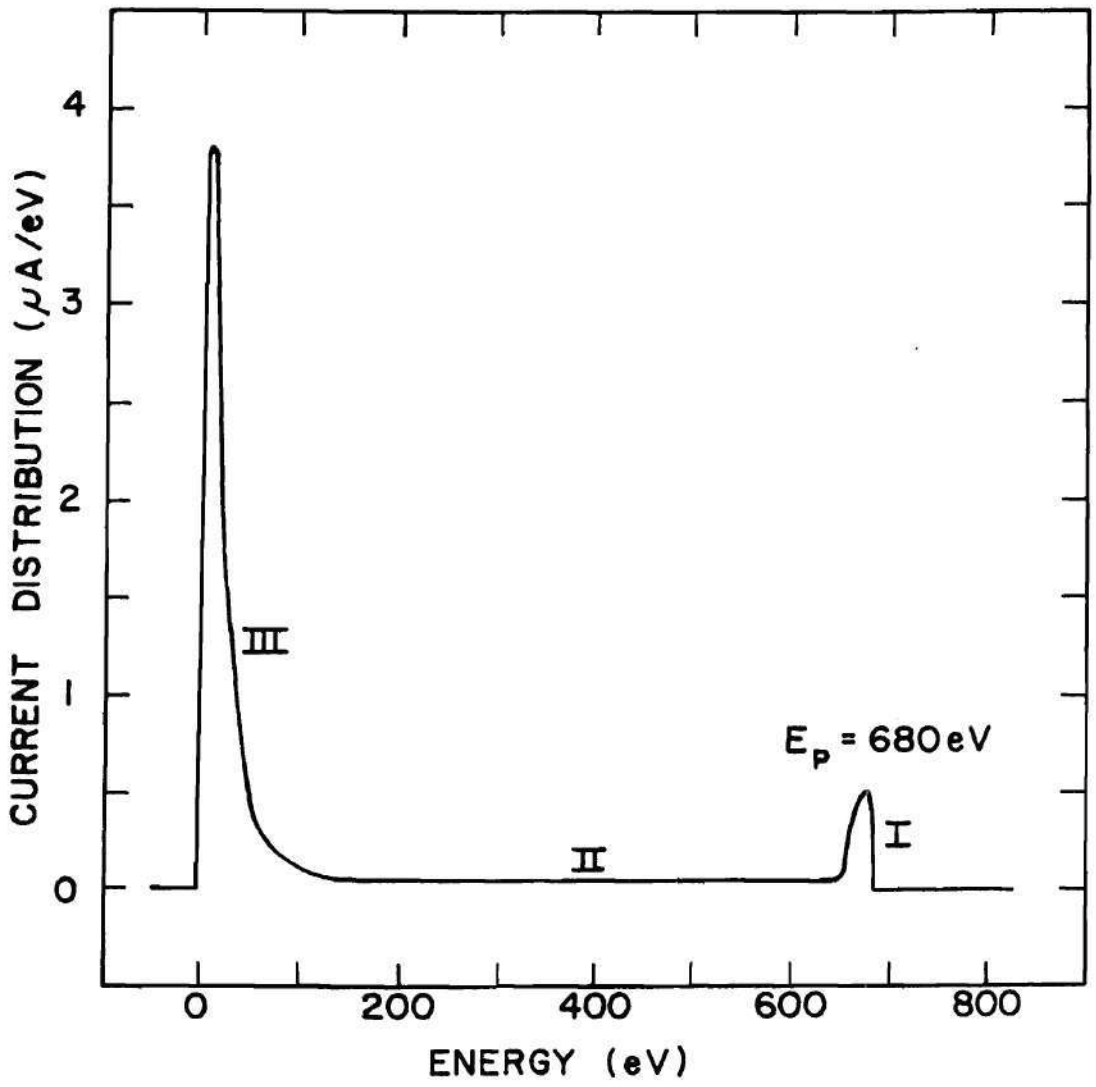

Figure 2. Idealized Electron Energy Distribution. The Primary Beam Energy is 680 eV.

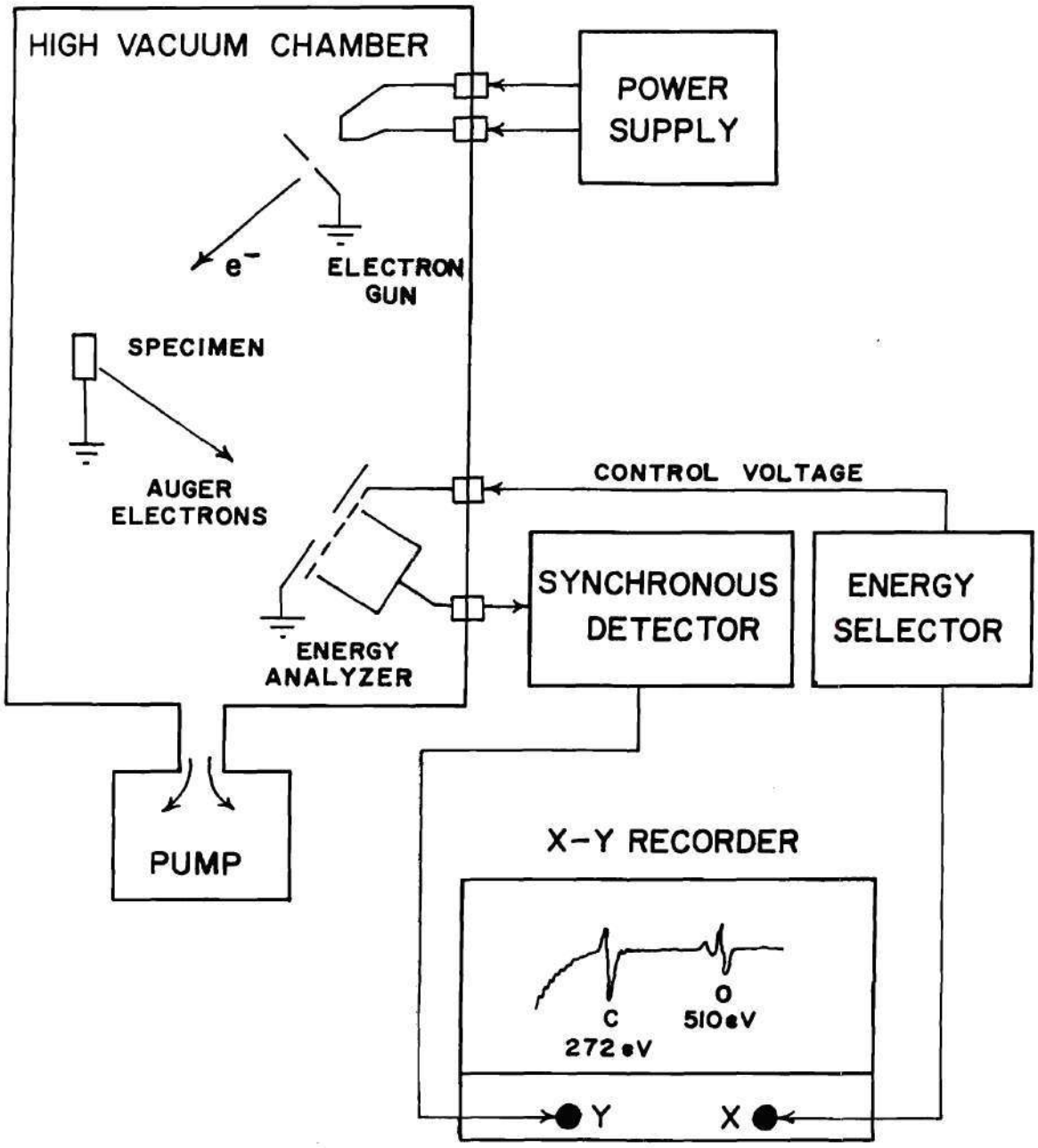

Figure 3. Block Diagram of the Auger Spectrometer.

to noise ratio.

It should be noted that various non-Auger processes can give rise to peaks in the Auger spectrum. The primary beam electrons can lose discrete amounts of energy by ionizing one atom and then being elastically reflected back out of the solid. Such ionization loss peaks may fall anywhere in the spectrum. Primary beam electrons can also lose discrete amounts of energy by exciting resonances in the valence electrons of the solid. Such peaks normally fall within a hundred electron volts of the primary beam energy. Of course, a great variety of instrument artifices can also cause peaks in a spectrum. Various tests have been devised which identify the "true" Auger peaks.

Prediction, a priori, of the energies of Auger peaks on a theoretical basis has received much effort and is the subject of recent research.[6] Even when the energy level can be predicted, there is no rule for predicting the amplitude (transition probability) of the peak. On the other hand, available models allow one to justify the location of observed Auger peaks within a few electron volts. The following model for estimating the energy of an Auger electron from a particular transition is due to Burhop,[7] Haas,[8] Chang,[9] and Simmons.[10]

Energies for Auger transitions are computed from ground state binding energies.[11] Since the Auger electron is emitted from an ionized atom, some correction must be made in the ground state binding energies when computing the energy level from which the Auger electron originates. The formula, as illustrated in Figure 1, for the characteristic energy is

$$E_{WXY} = E_W(Z) - E_X(Z) - E_Y(Z + \Delta) - \phi \qquad (1)$$

where E_{WXY} is the kinetic energy of the emitted Auger electron, $E_W(Z)$ is the binding energy of the electron removed in creating the initial vacancy in the material of atomic number Z, $E_X(Z)$ is the energy level from which this vacancy is filled, and $E_Y(Z + \Delta)$ is the energy level from which the Auger electron originates, with Δ expressing the correction necessary for the extra positive charge in the ionized atom. Normally $\Delta = 1$ is used, although $\Delta = 1/2$ or $3/4$ are sometimes used to achieve agreement between theory and experiment. Using the Fermi level as the reference, the Auger electron will be detected by the analyzer at

$$E_A = E_W(Z) - E_X(Z) - E_Y(Z + \Delta) - \phi_A \qquad (2)$$

where ϕ_A is the work function of the analyzer. Given the uncertainty in the value of the correction factor Δ, the following rules are employed when relating an Auger peak to a particular transition: (1) the experimental and calculated values should agree within ten electron volts, (2) transition assignments should predict observed trends in energies within a given period of the periodic table, (3) the primary beam energy limits the initial ionization level, and (4) transitions involving the valence band will be sensitive to the chemical state of the atom.

Computation of transition probabilities is made difficult by the lack of selection rules to relate the initial and final states for the electrons. It is noted experimentally that transitions involving the valence band result in larger Auger peaks; apparently the necessary coupling is more easily achieved between valence electrons than between electrons lying at lower energy levels. Valence bands give rise to a variety of complex peak shapes with peak widths of ten electron

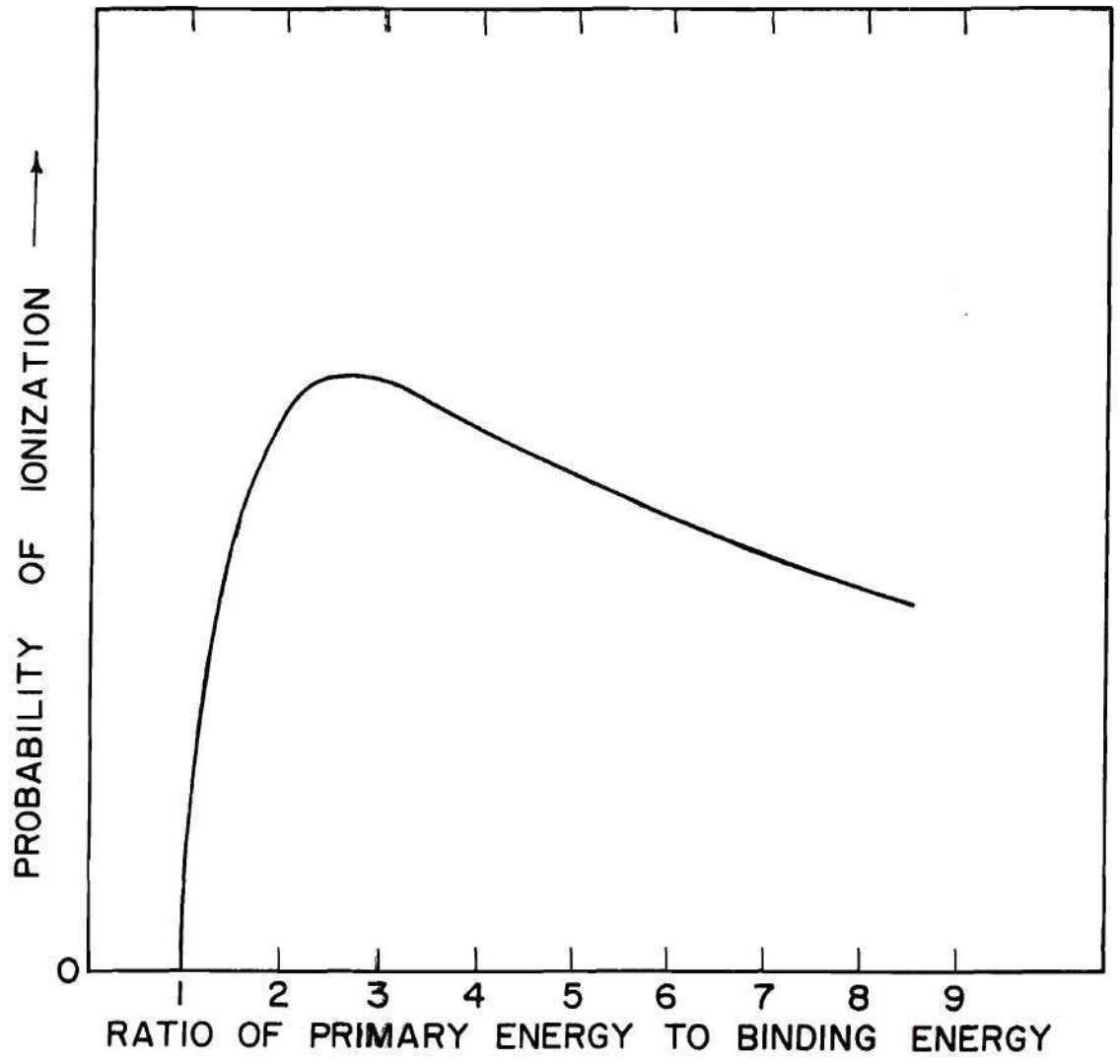

Figure 4. Probability of Ionization of K and L Shell Electrons, after Bishop and Rivière.[5] The Ordinate Scale is Linear but not Specified Since it Varies with Binding Energy.

volts or more. Thus the Auger peak becomes an indicator of the density of states within the energy band.[11]

The primary rate limiting factor for Auger emission is the ionization of the initial vacancy, since the competing mode of neutralization, X ray emission, is inefficient for the energy levels normally considered. Bishop and Rivière[5] have considered the basic efficiencies in producing and detecting Auger electrons. Their estimate of the behavior of the ionization cross section for K and L shell electrons is repeated in Figure 4. It is seen that the probability of ionization, shown with a linear scale, is zero for primary electrons of energy less than the binding energy of the initial vacancy, rises to a maximum for energies between two and three times the critical ionization level, and then slowly tapers off for higher energy primary electrons. Assuming that the initial ionization is neutralized by the Auger process, the probability of detecting an Auger electron depends on the probability of the Auger electron escaping. When the atom is part of a solid, this means the Auger electron must diffuse to the surface and escape without suffering an inelastic collision. On a practical basis, only those Auger electrons emitted within the first few atomic layers have a possibility of escaping. An upper bound for the escape depth is the first 50 angstroms for Auger electrons of energy less than 500 electron volts.

In summary, both the location of peaks and their relative amplitudes, as used in Auger spectroscopy, are based on experience rather than theory. Two compilations exist for the elements. Varian Associates[12] present theoretical and experimentally observed peak locations in chart form with atomic number the

abscissa and energy level the ordinate. Relative peak height is quantized into three levels and the probable source transition is shown. Physical Electronics Industries[13] present a typical Auger spectrum for each of the elements in book form. In general, neither source considers the location or shape of peaks when the elements are chemically bound as compounds.

Auger Electron Spectroscopy

Auger electron spectroscopy was suggested by Lander[14] in 1953 as a potentially useful technique for surface analysis. Tharp and Scheibner[15] demonstrated the ability of the retarding grid analyzer, already in use in low energy electron diffraction systems, to detect Auger electrons in the energy distribution plot. Harris[16] then used differentiation of the energy distribution plot to achieve sufficient sensitivity to be of practical use as a surface analysis tool. Palmberg[23] showed the utility of a grazing angle gun and a later paper by Palmberg[24] demonstrated the advantages of the cylindrical mirror velocity analyzer. A bibliography[25] published by Varian Associates contains the important material in the literature of Auger spectroscopy published through the middle of 1971. The review paper by Chang[9] is an excellent beginning point for the uninitiated.

Several types of excitation sources and detection means are possible in Auger spectroscopy. While this work is concerned with excitation of Auger processes by electron bombardment, ultra-violet radiation and soft X rays have also been used.[17] Use of X rays as the initial ionization mechanism is associated with the term ESCA, for Electron Spectroscopy for Chemical Analysis. While this

technique has definite technical advantages, it is much more expensive and complicated than electron excited Auger spectroscopy. Electron bombardment was chosen for this work because of its flexibility and economy.

Two classes of electron energy analyzers exist. The retarding grid analyzer utilizes a spherical grid to repel all electrons with energies less than the barrier created by the potential applied to the grid. Differentiation of the collector signal as the retarding potential is increased yields an energy distribution plot for the incident electrons. The second derivative of the collector signal is then the Auger spectrum. A velocity analyzer, by comparison, causes the incident electrons to travel in a curved path under the influence of electrostatic or magnetic fields. The path radius followed by the electron will be dependent on its energy. Only those electrons of the proper energy will pass through an exit aperture and be collected. Here the collector signal forms the energy distribution plot directly as the velocity for passage is swept by changing the applied fields. The first derivative of the collector signal is the Auger spectrum. The cylindrical mirror[18] velocity analyzer has the highest signal to noise ratio of all analyzers considered so far, but the sensitivity is not uniform with energy when utilized with an electron multiplier, and it requires precise placement of the specimen. While for most purposes the cylindrical mirror is technically superior to the retarding grid, similar results can be obtained with the retarding grid unit by running the sweep more slowly and using longer filter time constants to bring the signal to noise ratio up to an acceptable level.

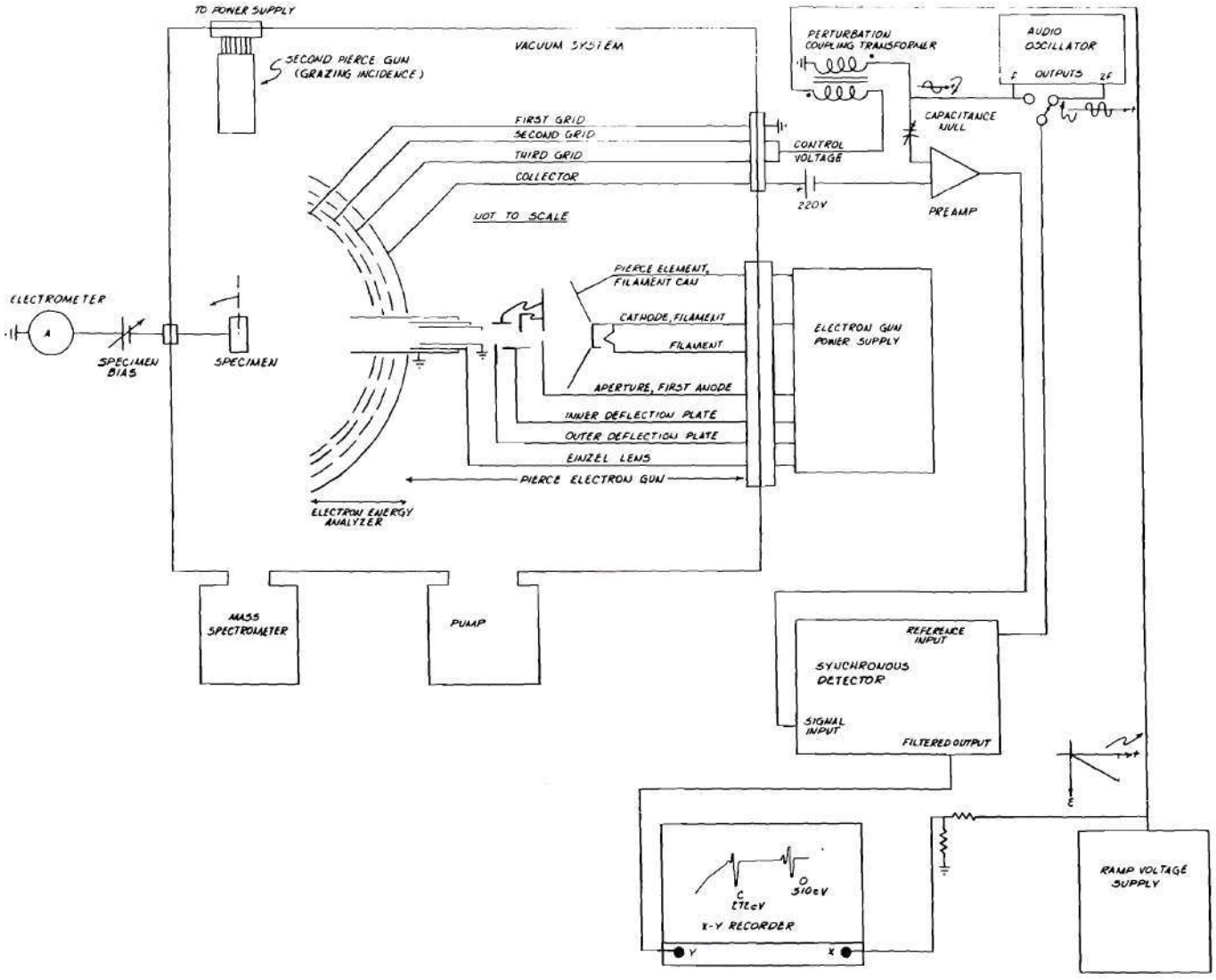

Figure 5. Schematic Diagram of the Auger Spectrometer.

The complete Auger spectrometer used in this work is shown schematically in Figure 5. Two Pierce type electron guns were used, one mounted at a grazing angle and one mounted normal to the specimen surface, with the specimen in the standard position. The specimen could be rotated also so as to obtain any other desired angle of incidence. A three grid retarding analyzer was used. The energy axis, the retarding potential, was obtained from a programmable power supply connected as an integrator to supply a ramp voltage. Superimposed on the dc ramp was a small ac perturbation voltage. As explained in Chapter III, tuning the synchronous detector to the first harmonic yields an energy distribution plot and tuning to the second harmonic gives the Auger spectrum.

Contributions of the Research

The contributions of this research may be grouped in two categories: those pertaining to the technical improvement of the spectroscopy and those pertaining to the improved understanding of the contaminants found on semiconductor wafer surfaces.

The most important technical contribution was the understanding of charging of oxide surfaces. Charging of surfaces causes a number of artifices in an Auger spectrum. Probable examples of such artifices in the literature are pointed out in Chapter II. The origins of several classes of artifices are explained in Chapter VI. Methods of detecting all of the artifices found in this research are also given in Chapter VI. Most of these can be prevented by specific techniques. Thus Chapter VI becomes a recipe for studying complex insulator surfaces.

A second technical contribution was that of improved understanding of the effects the primary electron beam has on the silicon dioxide surface. The electron beam was found to slowly convert carbon in the form of graphite to silicon carbide and also reduce SiO_2 to SiO. These effects prevent the application of electron excited Auger spectroscopy to non-destructive testing of semiconductor devices.

Calibration curves for the bulk form of the constituents of typical semiconductor wafer surfaces were obtained. These complement recently published work for fractional monolayer coverages of materials on silicon. The resolution of the curves obtained in this work allows significant information to be obtained about the chemical bonding of common constituents.

The influence of electron beam source parameters was studied in great detail. These results are discussed in Chapter IV. These results suggest that the basis for most quantitative models of the Auger process, the theory of Bishop and Rivière, needs some modification. A possible alternative model is discussed in Chapter IV which does explain the observed effects.

The final technical objective was the removal of background slopes from the Auger spectrum. Several methods were proposed and are illustrated in Chapter III. None were of sufficient utility, however, to warrant their use throughout the research. It is pointed out that careful choice of spectrometer operating parameters will circumvent most problems with background slopes.

The first important result from the application of Auger spectroscopy to

typical semiconductor wafers was a negative observation: many of the suspected trace contaminants seen in earlier work are likely to have been the result of artifices. Wafers taken from satisfactorily operating manufacturing processes were found to be extremely clean, with one important exception. Carbon was found on all surfaces examined. The contribution of the vacuum system to this carbon peak was found to be minimal. These results are discussed in Chapter V.

The second important observation was that carbon could exist both as graphite films and silicon carbide particles. Silicon carbide had been detected by previous workers as a contaminant on pure silicon surfaces after heating in the ultra high vacuum system. However silicon carbide particles were found in this work to be formed also on SiO_2 by heating in the high vacuum system. Additionally, they were detected on certain of the commercial wafers. Electron microscopy showed that the morphology was similar in all cases. Furthermore, the presence of silicon carbide was found to be localized to certain regions of the transistors in the one wafer which was studied in detail. Electron microscopy correlated the presence of particles with the Auger indication of silicon carbide. These results and the nature of carbon on semiconductor wafer surfaces are discussed in Chapter VII.

CHAPTER II

PREVIOUS APPLICATIONS OF AUGER SPECTROSCOPY TO SEMICONDUCTOR MANUFACTURING PROBLEMS

The first chapter of this dissertation was an introduction to the Auger effect and to Auger spectroscopy. Previous efforts at applying Auger spectroscopy to semiconductor manufacturing problems are the subject of this chapter. Some of the successful applications are described in the first section. Auger spectroscopy has been successful in identifying gross contamination on a wafer surface. It has been less successful in detecting trace contamination on commercial wafer surfaces because of difficulties in interpreting data from oxidized surfaces. The second section is a listing of some of the trace contaminants that workers believe they have found. The final section is a critique of some of the interpretations in the literature.

Utility for Identifying Gross Contamination

The initial applications of Auger spectroscopy were in characterizing specimens in surface science experiments. A typical surface science experiment might involve reacting a pure, single crystal specimen with a single adsorbate. In other words, the situation is well defined and interpretation is likely to be unambiguous. Interpretation of results from a semiconductor wafer removed from a commercial manufacturing process is a far greater challenge since one

cannot say a priori what surface contamination is likely.

L. A. Harris[19] performed the earliest work on wafers taken from an operational manufacturing facility. Some examples from his work are listed below. Harris was primarily concerned with identifying the source of problems when a nominally satisfactory manufacturing line developed difficulties. This might be contrasted with trying to raise the yield of an operating line with no outstanding problems. The former can be handled with some success; the latter is far more difficult.

One problem Harris studied was soldering failures involving a plated gold-copper alloy. He found that reject devices contained tin at the surface and an enhanced oxygen peak, suggesting the formation of tin oxide. In another case titanium was evaporated onto wafers before the main aluminum evaporation in the formation of bonding pads. Discoloration on wafers was correlated with the presence of Ti in areas supposedly protected by photoresist. In another case of visible residue, the presence of phosphorus, sulfur, and copper was traced to a faulty HF-NH_4F solution used as an etchant.

Harris also did a significant amount of work comparing the effectiveness of various photoresist removal techniques and comparing the effectiveness of different chemical cleaning techniques for removing carbon from the surface of wafers. Most of his specific results were applicable only to the particular manufacturing process he was studying, but nevertheless his work did establish the utility of the Auger spectrometer for studying semiconductor manufacturing processes.

Shortly after Harris published his reports, a program under the direction of L. N. Tharp[20] was begun at the Georgia Institute of Technology Engineering Experiment Station to study the application of the Auger spectrometer to the problems of manufacturing reliable power transistors for NASA. The primary result of this work was the identification of zirconium particles imbedded in the surface of the wafer after the final polishing before first oxidation. Several techniques for the removal of these particles were evaluated.

Harris and Tharp demonstrated that gross contamination on the surface of wafers could be identified and methods for removing such contaminants could be evaluated. They also noted, at one time or another, a variety of minor, or trace, contaminants. Among these were sulfur, chlorine, silver, ruthenium, boron, potassium, calcium, tin, and phosphorous, in addition to carbon and oxygen which were almost always present. The possibility of trace contaminants being present and influencing the electrical parameters of semiconductor devices was one of the motivating forces behind this work.

Trace Contaminants

Harris[19] obtained a number of spectra which he felt showed the presence of trace contaminants. In a study of the effectiveness of an asher, an oxygen plasma cleaner, as a photoresist remover he identified a tin peak in the Auger spectrum of an oxidized silicon wafer. When tin was found in the gold-copper alloy the tin spectrum consisted of a complex of three peaks with the largest at 430 eV. On the SiO_2 surface there indeed was a peak at 430 eV but the other two peaks of the complex were missing. This same sequence of spectra also showed

a broad peak at 350 eV which Harris doubted was an Auger peak because of its slightly variable shape from run to run, but he did believe it to be evidence of some real property of the surface.

Chang[21] studied contaminants on chemically etched silicon surfaces. He found the two major surface contaminants to be carbon and oxygen. In addition he showed a spectrum with a peak at 250 eV which he interpreted as either potassium, even though the normal peak location for K is 243 eV, or a hydrocarbon gas. He noted that there was, in either case, a large unexplained shift in energy. The spectrum also contained many irregular small unidentified peaks.

Tharp[20] obtained a number of spectra from oxidized silicon wafers which he interpreted as showing trace contaminants. Figure 6, reproduced from his report, shows a spectrum for a wafer after base diffusion. Silicon in the form of SiO_2 and oxygen are the predominant peaks, with a moderate amount of carbon present. Two interesting trace contaminants are identified. These are argon and silver. Argon could be adsorbed on the surface as a result of an argon bombardment cleaning operation in the high vacuum system. There is no ready explanation for the presence of silver. Figure 7, taken from the same report, is even more interesting in that it indicates ruthenium to be present on a particular wafer after first oxidation. Again there is no ready explanation for the source of such contamination. Figure 8, also from the same report, is the spectrum of a wafer after the aluminum metalization step. In this case the aluminum was evaporated onto the wafer and then completely etched off. Aluminum, potassium, carbon, and chromium are identified as remaining on the SiO_2 surface.

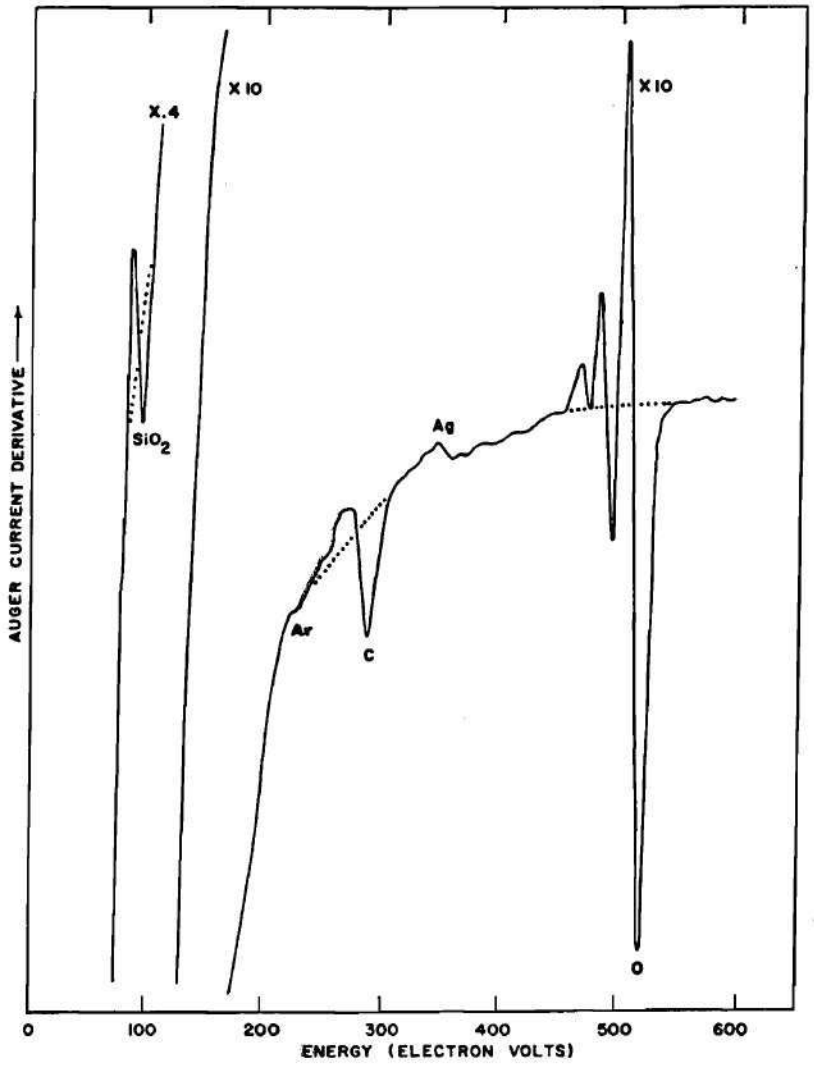

Figure 6. Auger Spectrum of Wafer after Base Diffusion, from Tharp.[20]

Dotted Line was Added to Show Background Function.

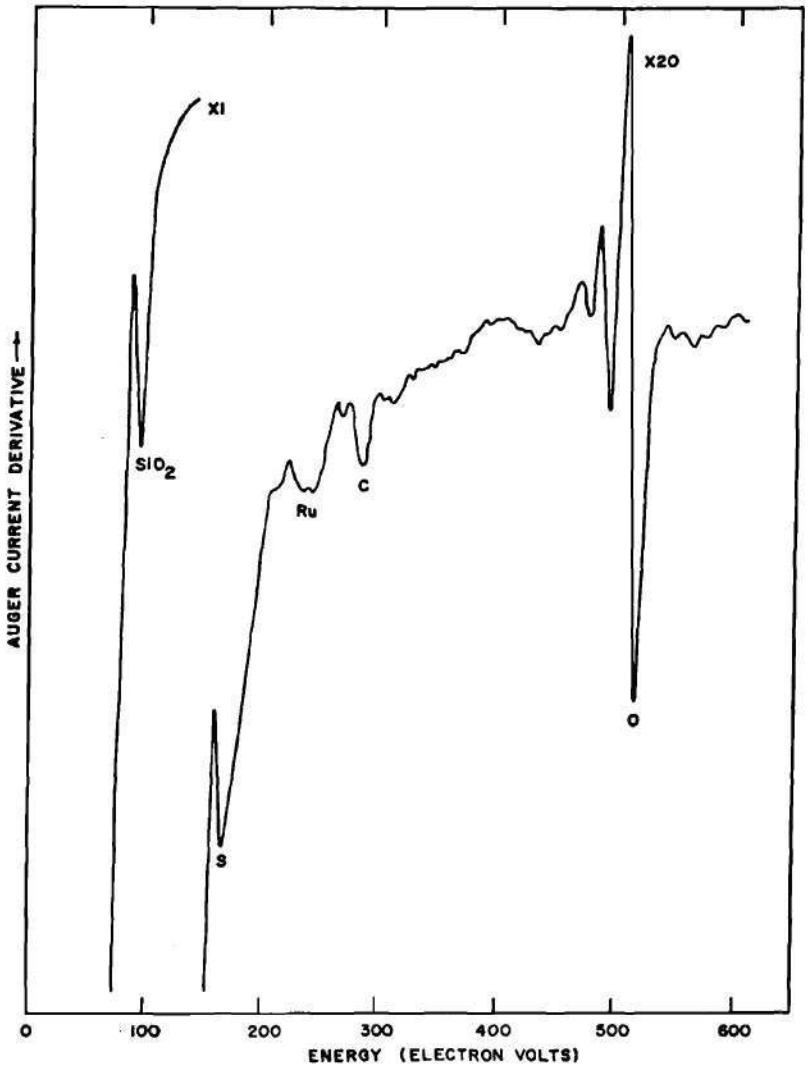

Figure 7. Auger Spectrum of Wafer After First Oxidation, from Tharp.[20]

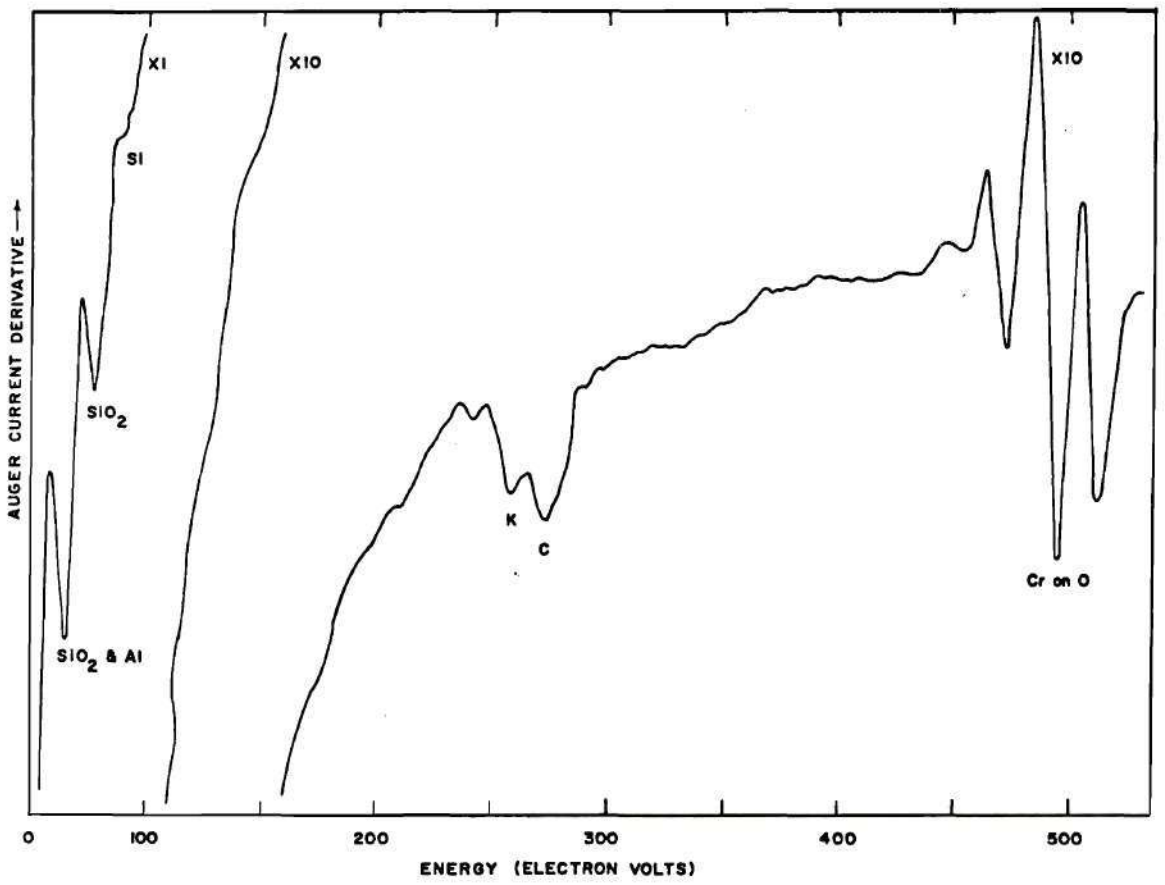

Figure 8. Auger Spectrum of Wafer after Metalization, from Tharp.[20]

One feature that all of the cited spectra have in common is that they were, at least partially, oxidized surfaces. Thus there exists the possibility that some surface charging mechanism was giving rise to artifices in the spectra.

Critique of Interpretations

The motivation for investigating trace contamination on wafer surfaces is simply stated: very small amounts of contamination can have profound effects on the electrical performance of devices. Given the strong motivation for finding trace contamination, the spectroscopist must not overlook the possibility that charging artifices might be present in his spectrum. Although they may appear almost trivial, substantial experience with Auger spectroscopy of SiO_2 indicates that the following tests should be applied to any Auger spectrum.

All spectra must be reproducible. There should be no noticeable shift in peak location from run to run. Peak locations are reproducible within 1.0 eV on true spectra. The ordinate of the spectrum is naturally subject to fluctuations because of random noise in the system. The amount of this noise present is easily determined by stopping the sweep of the energy axis and observing the fluctuations of the recorder. Peak heights will be reproducible within the noise level of the system unless the electron beam is causing adsorption or desorption on the surface. While some artifices caused by surface charging detected in this work were absolutely stable in energy and amplitude over time periods of several hours or more, most were found to vary by a few electron volts in energy and a detectable amount in amplitude from run to run. Thus one might interpret the 350 eV peak noted by Harris as a charging artifice because of its variability.

If there is any possibility of artifices causing improper interpretations, the entire spectrum should be shown. The low energy secondary peak tells much about the quality of the spectrum. Surfaces which are electrical insulators tend to charge irregularly so that some regions are at one potential and others at another potential. Irregular charging will cause dispersion of the low energy secondary peak. The complete spectrum will also show whether or not the regions supposedly without Auger peaks have the appearance of white noise, as they should. Irregular peaks, some going negatively before going positively with increasing energy, are often symptomatic of charging problems. On this basis one might question Chang's interpretation of his data.

Each element has its characteristic energy. The only known causes for a shift in the location of a true Auger peak are the work function of the analyzer and chemical bonding of the element. The work function of most analyzers is that of gold, which is stable, so one is left with chemical bonding as the only likely cause. With the exception of the low energy silicon peak, the commonly observed chemical shifts[22] are less than four electron volts and all are negative. On this basis one might question Chang's interpretation of his 250 eV peak.

Each element has its characteristic fingerprint. Of all the possible transitions, certain ones are most likely and therefore observed. When the spectrum contains some of the peaks but lacks others of the fingerprint, it should be suspected. The one reasonable cause for a change in fingerprint is chemical bonding. Such cases must be investigated individually, but most bonding does not cause a significant change in the fingerprint of an element. Two exceptions to this rule,

carbon and silicon, are explored in this work. Application of this rule might cause one to question the interpretation by Harris of tin in certain of his spectra.

The three figures reproduced from Tharp's work illustrate the problems of studying SiO_2 surfaces. Figure 6 showed a peak identified as silver. The author's application of the above tests to verify the silver peak was not conclusive, one way or the other. Inspection of the original data did show some minor variations in the peak location, but these could be attributed to noise fluctuations. The one significant characteristic of the peak is its shape. Recall that the Auger spectrum is the derivative of the electron energy distribution function. Auger peaks are narrow, positive, peaks added to a smooth, slowly varying background in the energy distribution plot. The derivative of this distribution function should have a slowly varying background, shown by the dotted line added to the figure, and, added to this, the contribution from the Auger peak. The O and SiO_2 peaks are obviously local perturbations added to the background slope. The C peak can likewise be interpreted, although with more difficulty. The silver peak appears more as a change in background slope, rather than the addition of a symmetrical silver peak to the slowly changing background. Just such changes in background slope were detected in this work and are discussed in Chapter VI, which is concerned with artifices on oxide surfaces.

Figure 7 showed a peak identified as ruthenium. This spectrum is not as "clean" as the one shown in Figure 6. The irregular peaks of this spectrum are symptomatic of charging problems. Finally, Figure 8 is striking in that it can also be interpreted as the summation of two shifted spectra, each containing simply

SiO_2, C and O. The peaks identified as SiO_2 and Al, K, and Cr on O are all about 30 eV lower in energy than the corresponding SiO_2, C and O peaks. The ability of a surface to divide into domains and charge one of these to one potential and another to another potential is discussed in Chapter VI. One might then interpret this spectrum as consisting of the spectra of one domain charged 30 eV more negatively than the other.

A significant portion of this work was devoted to the problem of identifying and eliminating artifices which can obviously cloud the interpretation of data from electrically insulating surfaces.

CHAPTER III

INSTRUMENTATION AND EQUIPMENT

This chapter describes briefly the Auger spectrometer used in this research and the basic specimen surface treatment techniques utilized. The Auger spectrometer consists of an ultra high vacuum system and an electronic system for electron energy analysis. The ultra high vacuum system maintains the environment necessary for the specimen surface to be prepared and studied. The basic capabilities of the high vacuum system are described in the first section. The Auger spectrometer electronics are described in the following section, with emphasis on the method of obtaining the second derivative of the collector current necessary to form the Auger spectrum. The resolution of the energy analyzer is defined and two methods for subtracting the background slope in the low energy portion of the spectrum are illustrated. The next section compares the triode and Pierce type electron guns as electron beam sources. A simple power supply for the electron gun is also shown. The final section of this chapter is a very brief introduction to surface treatment techniques which can be carried out within the vacuum system without exposure to air.

High Vacuum System

The experiments reported in this work were performed in a Varian Associates custom ultra high vacuum system. The system has a 15 liter working volume, two gas manifolds, and a roughing manifold. The entire system is constructed of

non-magnetic stainless steel, bakeable at 250°C. The vacuum system was leak free during all experiments. A mechanical pump with zeolite trap roughed the system from atmosphere to 50 microns of mercury. No pump oils were ever detected in the high vacuum portion of the system. A cryogenic sorption pump then reduced the pressure to 0.1 micron (10^{-4} torr). A 110 liter per second noble ion pump and a titanium sublimation pump provided the ultra high vacuum. Base pressure for the system was 4×10^{-10} torr when baked and 2×10^{-9} torr when not baked.

Two specimen holders allow a pair of samples to be studied during a pump-down. Each holder has four degrees of freedom and four electrical feedthroughs. One holder has an electron bombardment heater mounted on the back side of the specimen and the other holder has a pair of electrically isolated clamps for mounting specimens which are to be heated resistively. In each case the specimen is electrically isolated from ground so that any desired bias potential can be applied. Specimens can be manipulated to allow ion bombardment cleaning, RF sputtering, mass spectrometry of desorbed ions, or Auger analysis using either of two electron beam sources.

Two precautions were taken to minimize pumping problems: exposure of the vacuum system interior to the atmosphere was minimized by changing specimens quickly and all metal parts were vapor degreased or washed in acetone before introduction into the vacuum. A specimen would typically be loaded in the afternoon, the system rough pumped and ion pumped to the 10^{-6} torr range in an hour, be given a 10 hour 200°C bake overnight, and be on the 10^{-9} torr scale the

next morning. Residual gas analysis by a quadrupole mass spectrometer would show primarily water vapor when not baked and equal amounts of water vapor, CO and CO_2 when baked. The water vapor content would gradually decrease after a number of days. Operation of the electron guns and the titanium sublimation pump would increase the H_2 partial pressure. At these times H_2 and CO would be the primary residual gases. Figure 9 shows a typical mass spectrum after baking. The vertical scale is linear in ion current. The most probable identifications and the atomic mass to electronic charge ratio are indicated for principal peaks. The dominance of the water vapor peak is a result of the low baking temperature used.

Auger Spectrometer Electronics

The Auger spectrometer uses a Varian three grid retarding potential electron energy analyzer. The concentric spherical grids and collector subtend a solid angle of $2\pi/3$ stereradians. The first grid, the innermost grid, is operated at ground potential to maintain a field-free region between the specimen and analyzer. A retarding potential, negative for electrons, is placed on the second and third grids. These two grids are tied together so there is a uniform potential region between them; this maximizes the resolution of the analyzer. The collector, the outermost electrode, is a fluorescent screen operated at +220 volts to suppress secondary emission. The dc current to the collector is the sum of all incident electrons with energies greater than the retarding potential, multiplied by the transmission factor (0.5) for the grid system.

Placing a small perturbation voltage on the retarding grids allows the

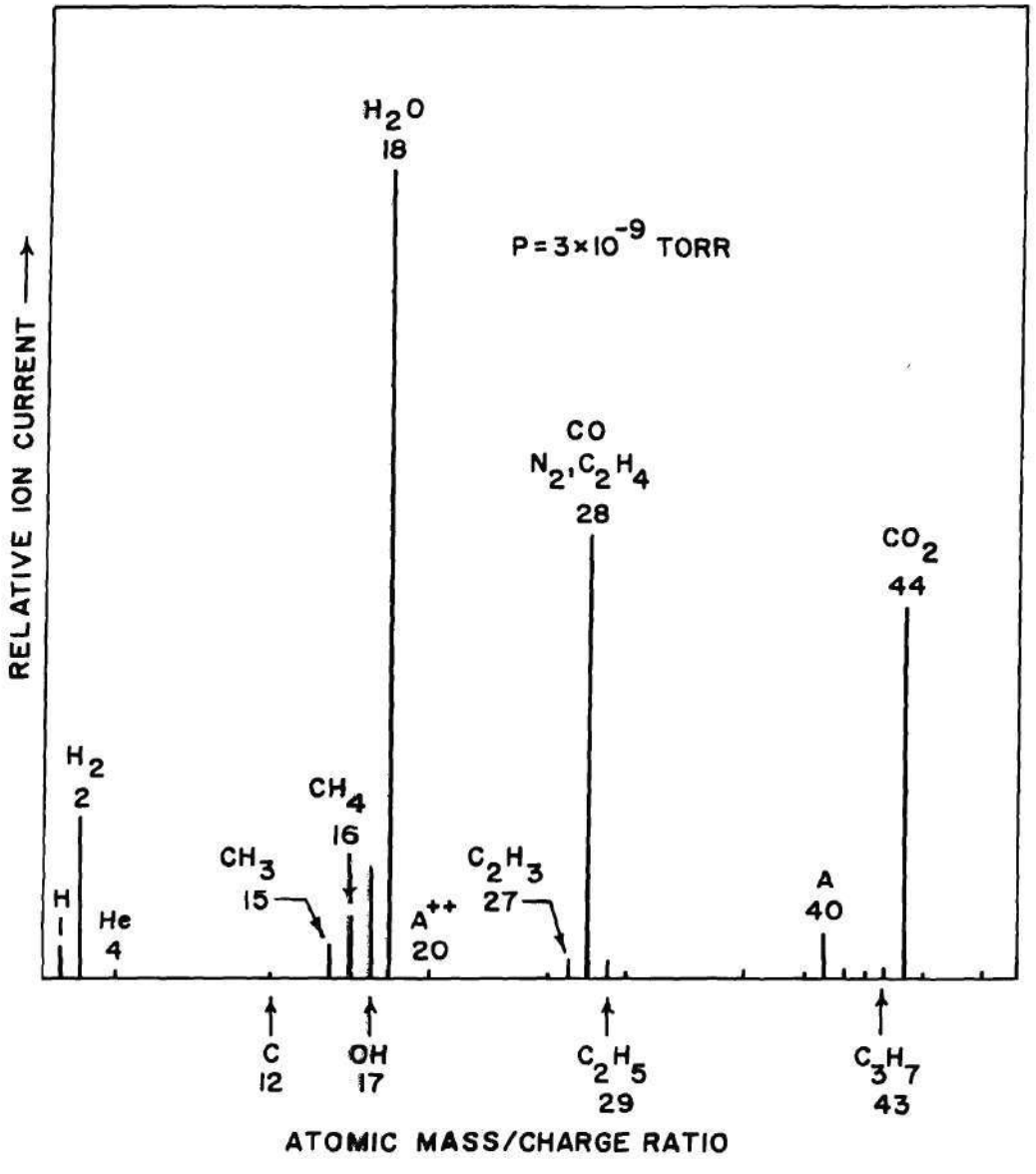

Figure 9. Typical Residual Gas Spectrum of High Vacuum System.

distribution of electrons with respect to energy to be determined by measuring the resultant perturbation in collector current. The collector current may be written in a Taylor series as a function of the retarding potential

$$i(V) = i(V_o) + \frac{di(V_o)}{dV}(V-V_o) + \frac{1}{2}\frac{d^2i(V_o)}{dV^2}(V-V_o)^2 + \ldots \qquad (3)$$

where V is the instantaneous retarding potential, V_o is the dc value (a slow ramp in practice), and i(V) is the total instantaneous current to the collector. The perturbation potential is a sine wave of amplitude A and radian frequency ω.

$$V = V_o + A \sin \omega t \qquad (4)$$

If the third and higher order terms may be neglected, substitution yields

$$i(V) = i(V_o) + \frac{di(V_o)}{dV} A \sin \omega t + \frac{1}{2}\frac{d^2i(V_o)}{dV^2} A^2 \sin^2 \omega t$$

$$= i(V_o) + \frac{di(V_o)}{dV} A \sin \omega t + \frac{1}{2}\frac{d^2i(V_o)}{dV^2} A^2 \frac{1-\cos 2\omega t}{2} . \qquad (5)$$

The first derivative of $i(V_o)$ is the distribution of electrons with respect to energy and the second derivative of $i(V_o)$ is the derivative of this distribution. Thus the energy distribution may be identified with ω in the frequency domain and the derivative of the energy distribution with 2ω. Auger spectra are normally the energy distribution derivative because small peaks on strong background slopes are more easily seen in the derivative plot. Taylor[26] describes the basic resolution

and sensitivity considerations for an Auger spectrometer based on a spherical grid analyzer. Equation (5), valid for small perturbations, shows that the cos $2\omega t$ term is proportional to the square of the perturbation amplitude. Taylor shows this relationship holds within 6% for Gaussian peaks if the peak-to-peak perturbation is equal to the full width at half-height. This relationship was verified and all spectra in this work meet this criterion.

Electrostatic resolution for the grid system is 0.5% of the retarding potential, measured as the full width at half height of the elastic peak (region I of Figure 2). Thus the resolution of the analyzer is 0.5 eV at 100 volts retarding potential and 2.5 eV at 500 volts retarding potential. Biasing the specimen off ground potential or incorrect placement of the specimen will degrade this resolution. The resolution of an Auger spectrum shows the combined effects of the electrostatic resolution of the analyzer and of the perturbation signal placed on the retarding grids. While the resolution of the peaks may be degraded by using perturbation amplitudes in excess of the electrostatic resolution, the optimum perturbation amplitude from a signal to noise ratio viewpoint is the largest possible without preventing a square law behavior of Equation 3.

As mentioned above, the second and third grids were tied together to improve analyzer resolution. A disadvantage of tying the second and third grids together is the high capacitive coupling, typically 30 pF, between the retarding grids and the collector. This coupling introduces a strong sin ωt current into the synchronous detector and can overload it. A bridge circuit is normally used to null this capacitively coupled current. A schematic of the bridge circuit and

preamplifier is given in Figure 10. The preamplifier is a source follower JFET amplifier. The main requirements are low noise at a high input impedance level and low second harmonic distortion. Second harmonic distortion contributes a $\sin 2\omega t$ term which would compete with the true Auger current. The noise figure for the entire system is less than three decibels, which means that the observed noise power at the synchronous detector output for a given bandwidth is within a factor of two of the shot noise associated with the dc current arriving at the collector. Thus the system becomes "shot noise limited" and increasing the primary beam current to the specimen improves the Auger signal to noise ratio as the square root of primary beam current.

A Princeton Applied Research model JB-4 lock-in amplifier is used as the synchronous detector. A transconductance type multiplier was fabricated to act as a frequency doubler to derive a reference sine wave of frequency 2ω. Figure 11 shows a schematic of the frequency doubler. The R and 10R resistors on the schematic are chosen to give the desired amplitude gain between the ω input and the 2ω output. A separate low distortion oscillator provides the perturbation signal and the frequency doubler input. Figure 5 shows the complete electronic system in block diagram form.

Inspection of typical Auger spectra shows there is a strong background slope from the slow secondary tail in the less than 200 eV energy region. This background tends to obscure small peaks. Since the background slope is similar to an exponential function of energy, an analog computer may be used to generate a sum of exponentials which is empirically matched to the average background.

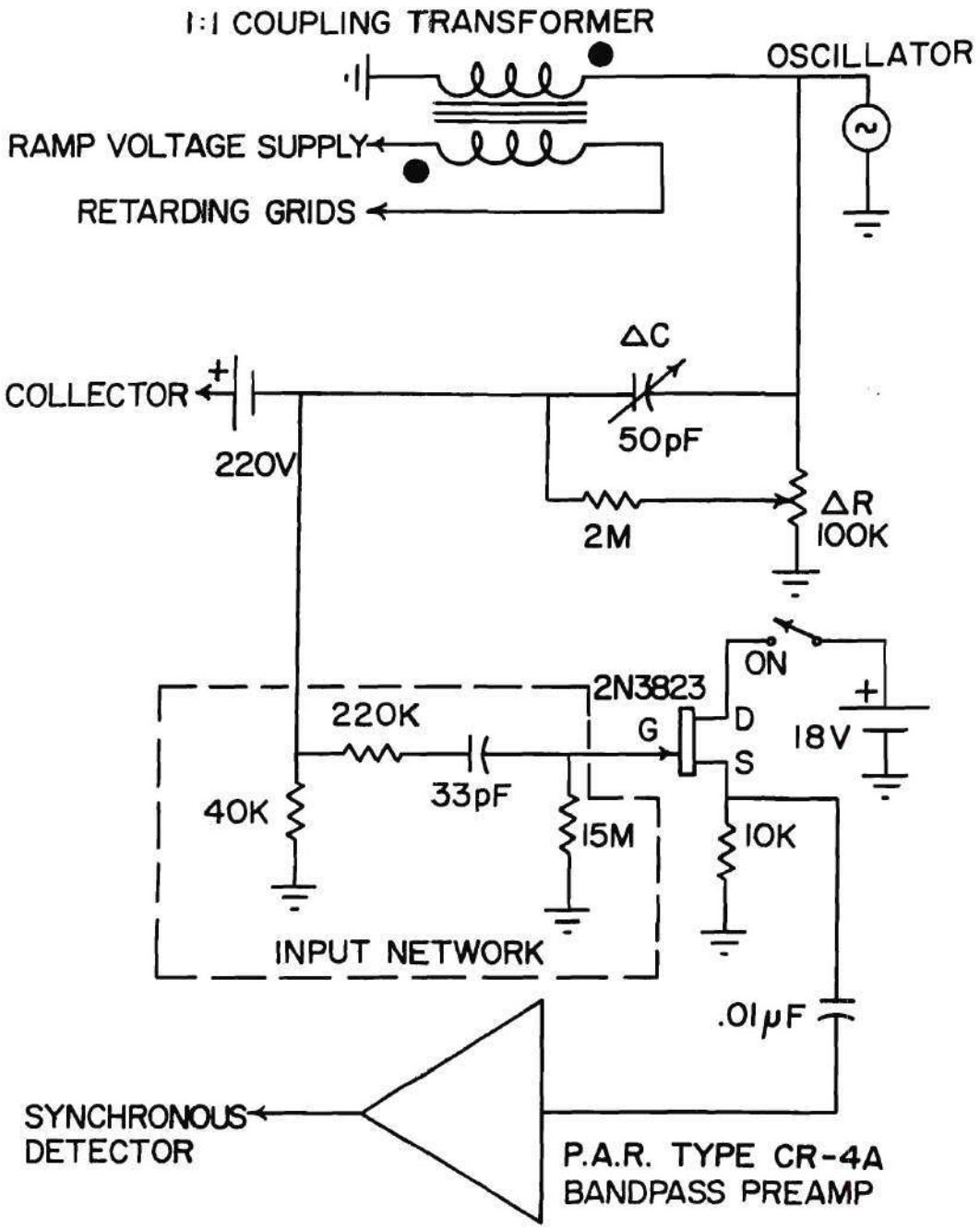

Figure 10. The Capacitive Coupling Null and Input Preamplifier Circuit.

ΔC and ΔR Adjust the Magnitude and Phase of the Null Current.

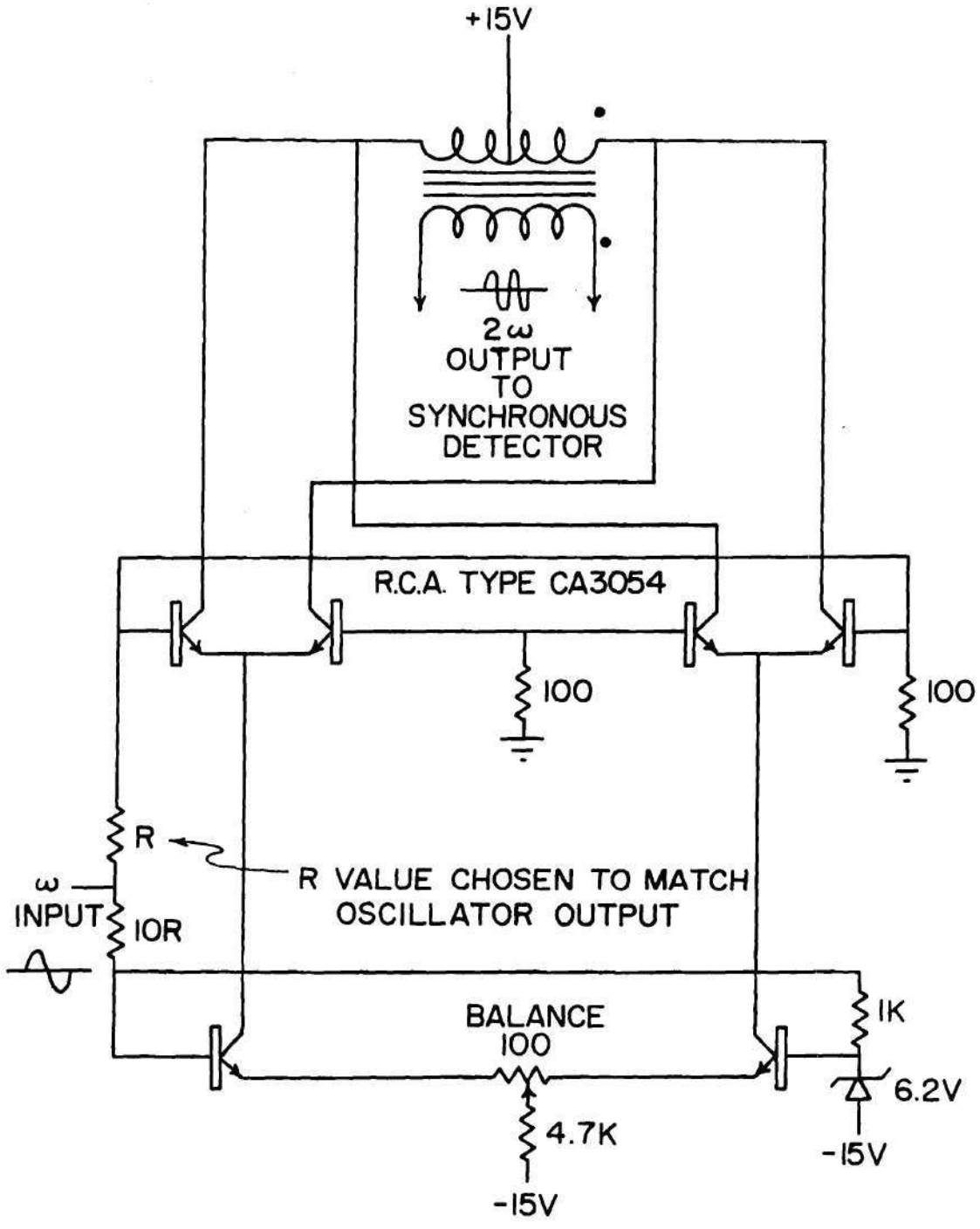

Figure 11. The Frequency Doubler Formed from a Transconductance Multiplier.

This sum is then subtracted from the spectrum and the result plotted on the recorder. An example of such a subtraction is shown in the two curves of Figure 12. Molybdenum peaks at 95 eV and 83 eV are seen more clearly and the inflection corresponding to a molybdenum peak at 40 eV can be seen in the improved spectrum. A pair of exponentials was used in this example to simulate the background. Adjusting the exponentials for a good fit becomes very tedious when a large background must be subtracted.

A second method considered was to regard the Auger spectrum as a video signal and remove the low frequency components which correspond to background. The analog computer formed the transfer function $s/(s + a)$ and the Auger spectrum was passed through the filter. An example is shown in Figure 13. While small perturbations are more noticeable, for example the 90 eV silicon peak, the distortion introduced in the spectrum is objectionable because peak shape is an important part of the fingerprint of an element.

These two methods have disadvantages which prevent their use in routine Auger spectroscopy. Satisfactory results normally were obtained by using a small perturbation amplitude so that sufficient resolution was available from the analyzer. This criterion implies amplitudes of one volt rms or less in the low energy region. Three volts rms was used in the region above, say, 150 eV. Larger perturbation amplitudes would cause the loss of deviation from background by Auger peaks while the full background slope would be preserved.

Electron Beam Sources

Electron guns used in Auger spectroscopy are normally similar to the type

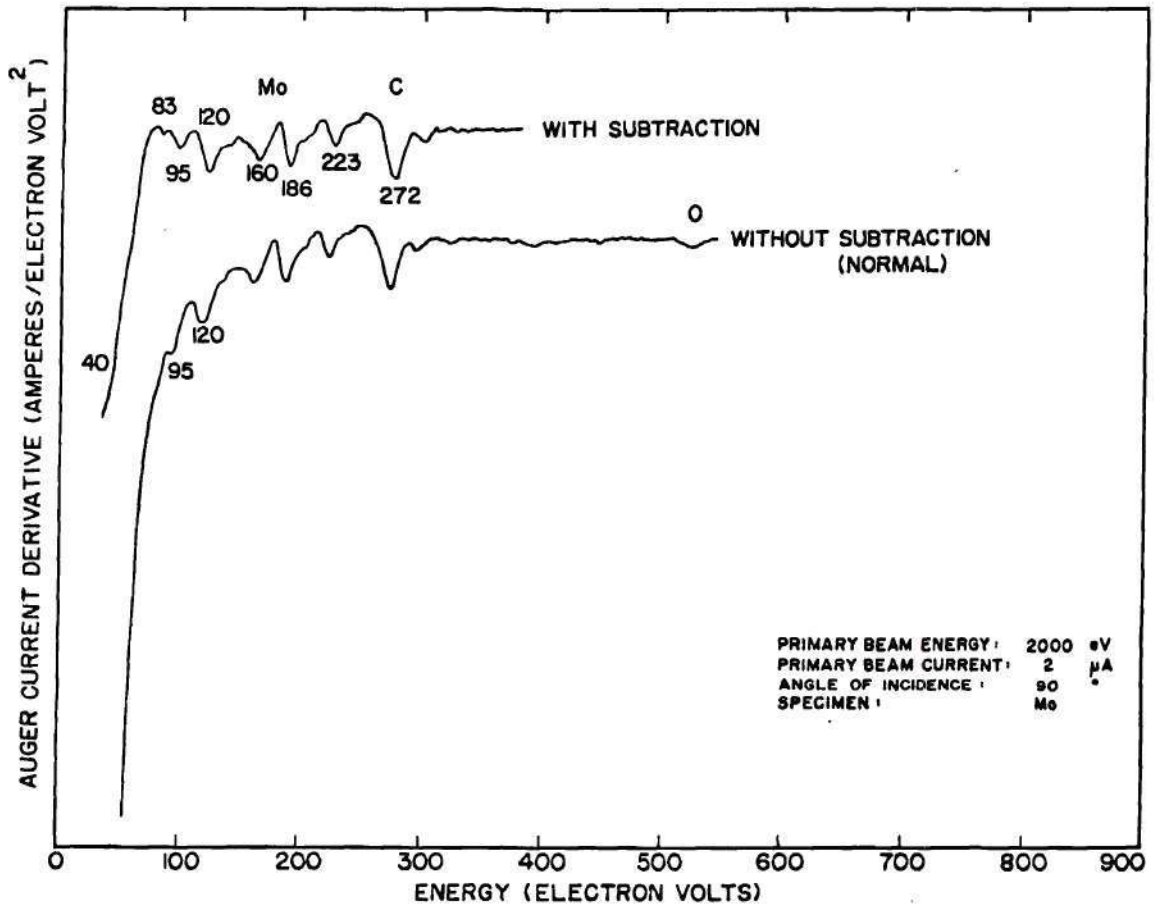

Figure 12. Molybdenum Auger Spectra with and without Subtraction of Background in the Low Energy Region.

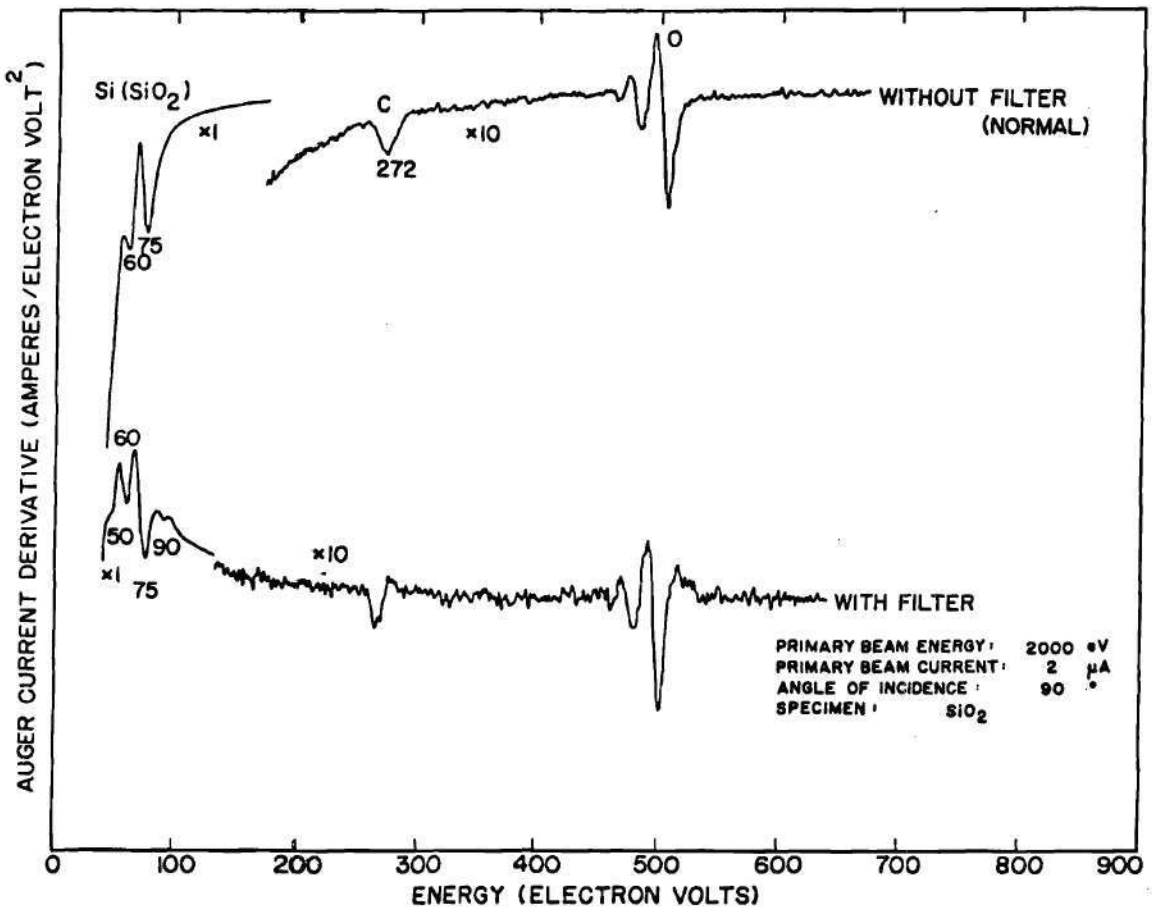

Figure 13. Silicon Dioxide Auger Spectra with and without High Pass Filtering to Remove Background Signal.

used in cathode ray tubes; in fact, the popular Superior Electronics type SE3K/5U was designed for cathode ray tube use. These guns are of the triode type. Figure 14 shows a schematic of the triode gun. The first electrode is either a filament, a bent tungsten wire shaped like a hairpin, or a cathode, oxide coated and heated indirectly by a filament. The second electrode is the filament can, which surrounds the cathode and has an exit aperture for the electron beam. The filament can is held at a negative potential with respect to the cathode so as to allow electrons to escape from only the center of the aperture. An image of the small escape region is focused on the specimen by an electrostatic lens structure. The first element of the lens structure is an accelerating electrode which forms the third element of the triode gun. While these electron guns can, and do, offer satisfactory service in many applications, they suffer two defects: the range of output current is limited and the beams have a current density cross section which varies as a Gaussian. The highest output current obtained with SE3K/5U type guns in this work was about 50 microamperes in a few millimeter diameter spot.

A second class of electron guns is those which use rectilinear electron flow, popularly called Pierce guns.[27] Figure 14 shows a schematic of this type gun. A cathode, operated in a space charge limited mode, forms a collimated beam with low divergence which exits through an aperture in the accelerating electrode. A second electrode, analogous to the filament can of the triode gun, is shaped so that the internal electric fields form the collimated beam. This shaped element approaches the surface of the cathode at an angle of 67.5^{o} with respect to the beam axis and is held at cathode potential or slightly negative with respect to

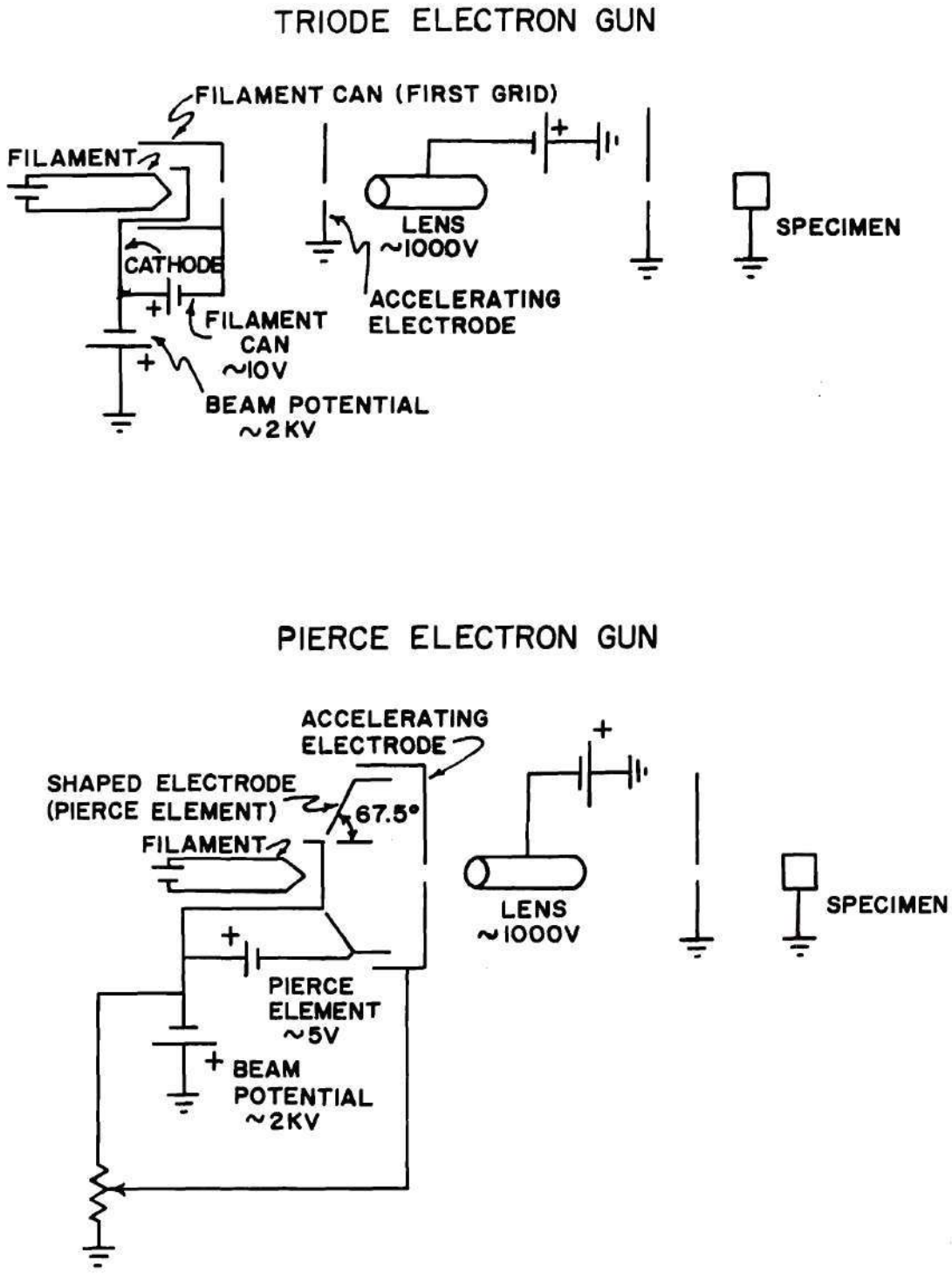

Figure 14. Schematics of the Triode and Pierce Type Electron Guns.

the cathode. The accelerating electrode may be operated at ground (specimen) potential or placed at a potential between ground and cathode potential. By the combined action of the shaped electrode and the accelerating electrode it is possible to form collimated beams of uniform current density with a variety of diameters and total currents. The Pierce guns used in this work were capable of 500 microamperes at 1200 volts accelerating potential into a 4 millimeter diameter spot and 1200 microamperes into the same spot at 2000 volts. Any desired smaller spot size was available with corresponding reduction in total current. Figure 15 shows typical beam current density profiles for the two gun types. The uniformity of the Pierce profile is of great advantage in studying insulator surfaces where the tendency of the surface is to charge to different potentials with different irradiation levels.

A Philips Metalonics Type B impregnated cathode was utilized in the Pierce gun. This cathode offers superior performance in applications requiring exposure to the atmosphere. Whereas oxide cathodes can not always be reactivated after atmospheric exposure, one Philips cathode performed throughout the experiments of this work, approximately fifty pump-downs. Furthermore the cathode did not require reactivation, i.e., heating above the normal operating temperature to restore emission, when operated in a 10^{-9} torr vacuum. The recommended filament current for this cathode was one ampere, but only six tenths of an ampere was required for emission in the high vacuum. Thus filament life was of no concern and outgassing held to a minimum. The final benefit of the Philips cathode-Pierce gun combination was an exceptionally stable emission current. Gun current

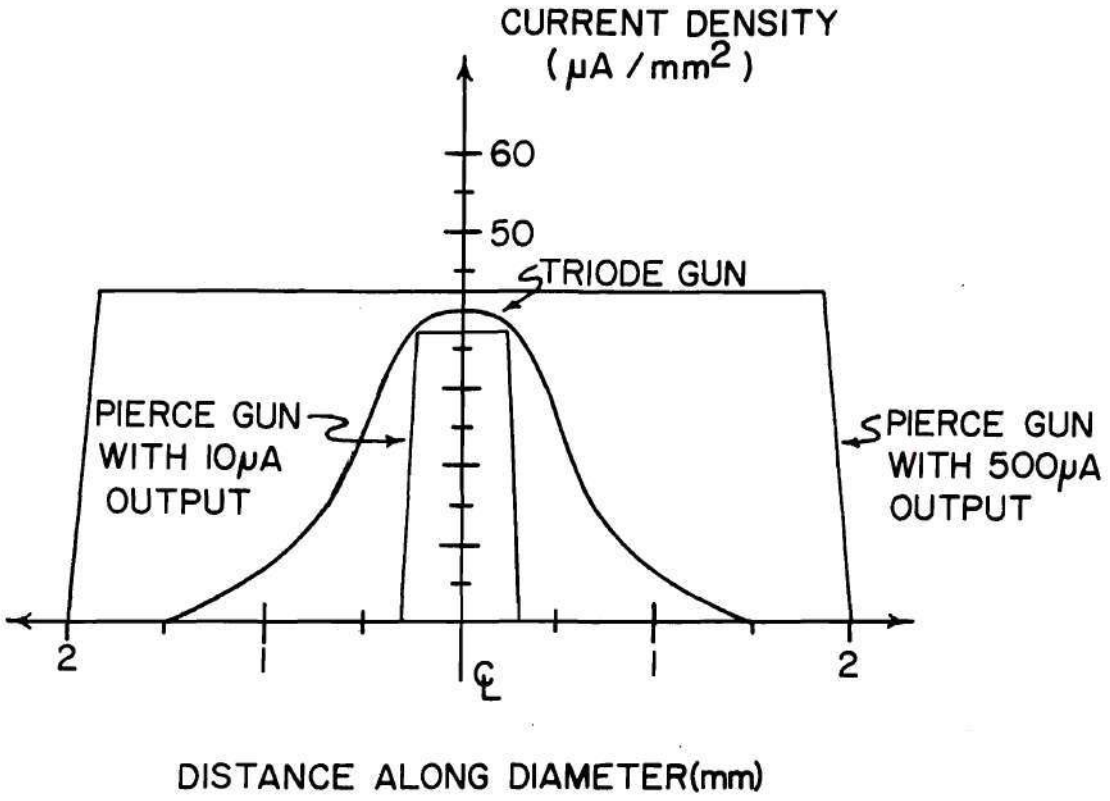

Figure 15. Typical Current Density Profiles for Triode and Pierce Type Electron Guns.

would vary less than one per cent over a day's operation or from one day to the next.

A simple power supply drove both the triode and Pierce guns in this work. A schematic is given in Figure 16. The primary requirements for such a supply are low ac ripple on the voltages, moderate long term stability, rejection of line voltage variations, and the ability to withstand a variety of fault conditions on the outputs. The ferroresonant transformer, T1, was chosen with just enough output capacity for normal operation; thus any overload from a fault condition would cause a drop in voltage to the various isolation transformers T2-T6. The ferroresonant transformer also provides a constant voltage in the face of line voltage variations and has an output waveform which resembles a square wave. The square waveform means that simple filters may be utilized and still maintain a low ripple output. The other feature of note is the ten second time delay incorporated in the filament supply. Approximately seventy per cent of line voltage is applied during the ten second warm-up period. This allows the supply to be turned on without excessive thermal shock to the filament and without adjusting the filament voltage control.

Surface Treatment Techniques

The high vacuum system in which this work was performed is capable of a number of surface treatment techniques. Specimens can be heated directly by passing current through them or indirectly by electron bombardment, reverse sputtered by argon ion bombardment, and reacted with gases.

Heating a specimen is the most basic surface treatment in high vacuum

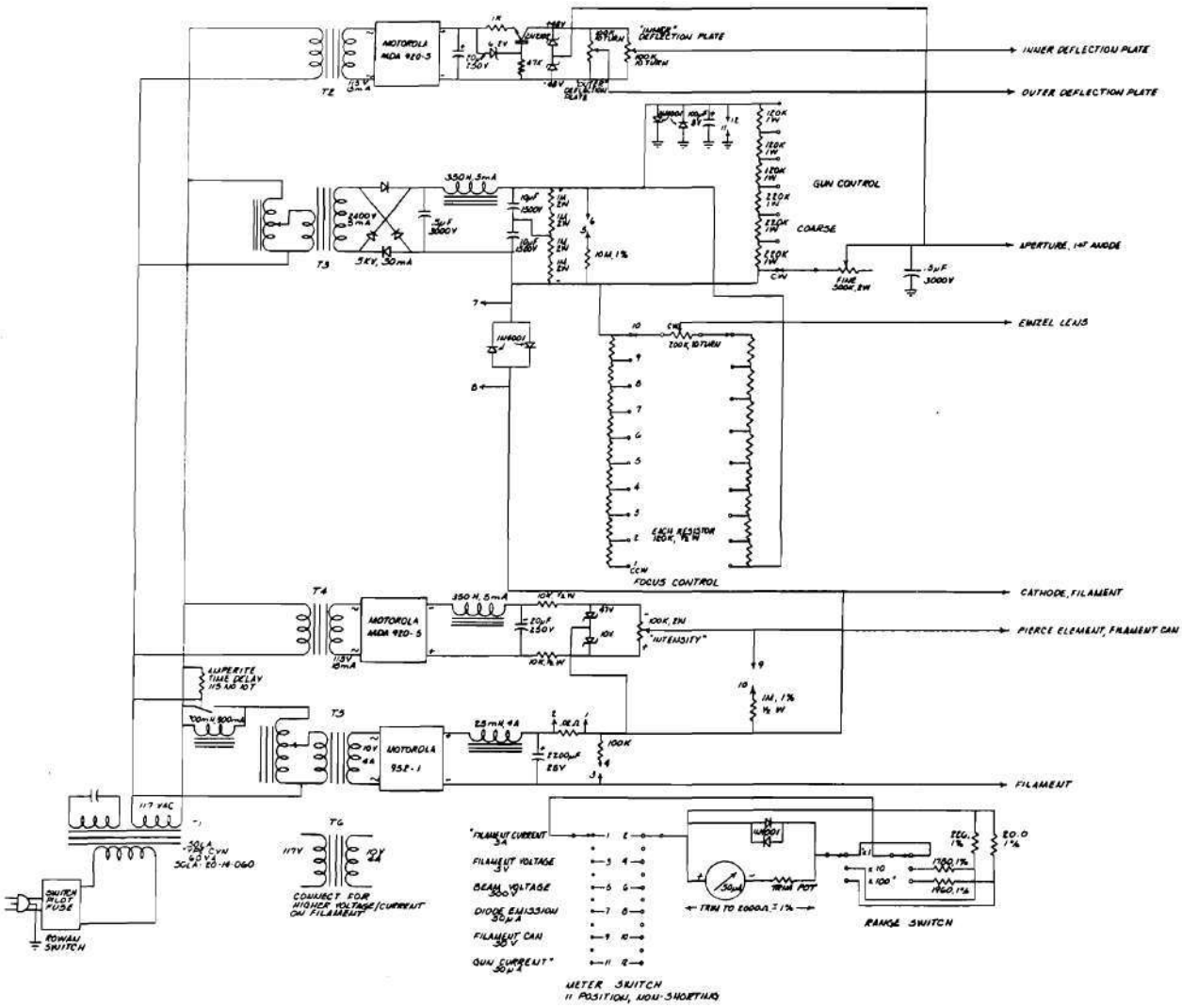

Figure 16. Schematic Diagram of Electron Gun Power Supply.

system. Conductors and semiconductors may be heated directly by passing current through the sample. Resistance of semiconductors varies inversely with temperature, so one is forced to use a current limited power supply to prevent a thermal runaway condition from destroying the sample. The constant voltage/constant current type of supply with automatic mode switching works very well. The output voltage-current product may be set so as to limit the maximum power to the specimen or, when contact resistance to the specimen is intermittant, the output voltage may be set high to break down insulating contact films and the output current set to deliver the desired current under normal conditions. Specimens taken from typical semiconductor wafers were heated to 950^{o}C with about 15 watts input power (3 amperes, 5 volts) in high vacuum and about 50% more input power in an atmosphere of oxygen.

While it is well known that achievement of a satisfactory contact to a specimen is easy in the high vacuum environment, a satisfactory high temperature contact for oxidizing atmospheres is more difficult. To make a satisfactory contact a slot was ground in alumina thermocouple tubing and a platinum contact wire passed through the center. A pair of such tubes would clamp the specimen, with the slots exposing the contact wire to the specimen. The alumina tubes are strong and completely inert at the temperatures utilized in this work. No evidence of migration of impurities from the support tubes was found, and furthermore contamination was not easily reverse sputtered from the tubes to the specimen (a problem with molybdenum holders). Platinum thermocouple wire made an excellent contact for moderate temperature applications. Platinum and silicon form an eutetic at 830^{o}C,

yet specimen temperatures of 950°C could routinely be held for several hours before contact failure. Either the region immediately around the contact was at a lower temperature because of thermal conduction down the platinum wire, or the silicon-platinum alloy is formed slowly. No difficulty was encountered in oxidizing a silicon specimen at 950°C for thirty minutes in one atmosphere of pure oxygen. The platinum wire is held in intimate contact with the silicon specimen by adjusting the support holder for the alumina tubes so as to squeeze them together slightly. The natural oxide on a specimen breaks down with the application of a few tens of volts. From that time on the contact normally behaves in an ohmic fashion.

Specimens which can not be heated resistively, such as complete wafers, are heated indirectly by electron bombardment. A small electron source was constructed on the rear of the ring holder used for complete commercial wafers. A three centimeter length of eight mil tungsten wire was coiled and placed in a small can so all emitted electrons are directed at the rear of the wafer. The filament and can are electrically isolated from the specimen ring. The filament is heated with about ten amperes to yield a temperature limited emission of 100 milliamperes. The filament and can are connected to a 1000 volt rms transformer secondary. Since the specimen is held at ground or biased positively, the heater functions as a half-wave rectifier. A 500 volt positive bias on the specimen is sufficient to heat a 1.25 inch diameter wafer to 900°C.

Ion bombardment is another basic surface cleaning technique, useful for removing monolayer coverages of contaminants. A Varian ionization gauge was modified by removing the center collector wire. In operation the filament is

heated sufficiently to emit about 40 milliamperes. These electrons are accelerated to an anode wire shaped in the form of a helix. Their spiral path increases the probability of ionizing a gas atom in the volume. The entire structure is floated at a positive potential of several hundred volts with respect to the grounded outside shield, thus forcing the positive ions out the exit aperture. A small magnet placed next to the ionizing volume on the outside of the vacuum system causes the electrons to travel a longer path before collection and increases ionization efficiency by a factor of three or more. The ions are focused on the specimen, and given the major portion of their energy, by biasing the specimen at -1500 volts. Twenty microamperes is delivered with an argon pressure of 2×10^{-4} torr under this arrangement.

Ion bombardment is a useful technique but can not be applied to insulating specimens because of charge build-up. Radio frequency sputtering can, however, be applied to insulators.[28] Here a plasma is created with about equal concentrations of electrons and positive ions. The RF is applied to the specimen in an argon pressure of typically ten microns. Electrons are accelerated into the specimen during the positive portion of the cycle and positive ions during the negative portion, with a charge balance being maintained. A commercial 90 watt "ham" transmitter served as a RF source. It was matched to the high impedance load by a 10:1 step-up autotransformer mounted next to the vacuum feedthrough. About 600 volts rms was available at the feedthrough. Typical sputter cleaning requires 300 volts rms, the lower pressures requiring higher voltages. The primary limitation of RF sputter cleaning seems to be the different sputtering rates for different

materials. For example, carbon was easily removed from aluminum but was not removed from silicon. Oxygen was easily removed from silicon but not from aluminum. Thus perhaps 40 angstroms of oxide was removed from a silicon sample while a monolayer or so of carbon remained in place. RF sputtering is useful for cleaning when the results can be verified independently, for example by using Auger spectroscopy. It is less useful for removing a known amount of material from the surface so as to expose an underlying layer. The plasma can be controlled by the placement of grounded electrodes where no plasma is desired. These are the "anode shields" well known in sputtering technology. An example of a well controlled RF plasma is shown in Figure 17. Such control insures that the surface is not contaminated by materials sputtered off surrounding surfaces.

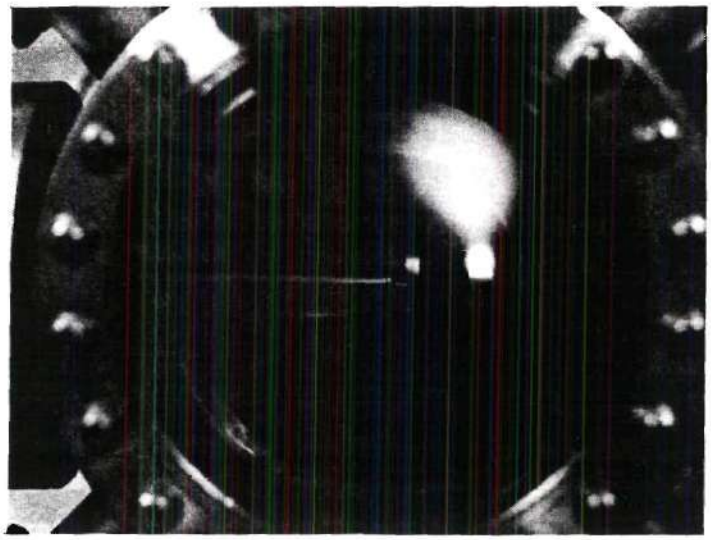

Figure 17. RF Etching of a Specimen.

CHAPTER IV

CALIBRATION AND INTERPRETATION OF AUGER SPECTROSCOPY

This chapter will describe the theory available for calibration of Auger spectroscopy, make some contribution to this theory, and describe the present state of the art for interpretation of Auger spectroscopy. The basic conclusion drawn in this chapter is that, while absolute quantitative calibration is not yet possible, much information is available from the size of peaks in Auger spectra. Maximizing the information obtainable from spectra of commercial wafer surfaces was the goal of the work described here.

The first section discusses the factors which allow identification of an Auger peak; these factors constitute the fingerprint of the peak. The second section introduces calibration spectra of substances of particular interest in this work. The third section lists the basic quantitative factors in Auger spectroscopy. These factors are then described in greater detail in the following sections. The chapter concludes with calculation techniques for interpreting spectra.

The Fingerprint of an Element

Each element has its own characteristic Auger spectrum, but when combined chemically with other elements it may exhibit an altered Auger spectrum. The details of the spectrum, the shape and location of the peaks, aid in identifying

each contributor to a complex spectrum and also convey considerable information about the chemical bonding of the elements. The first factor considered will be the energy of the peaks, their location in the Auger spectrum.

Equation 2 gave the retarding potential for an Auger transition as

$$E_A = E_W - E_X - E_Y - \phi_A \tag{6}$$

where E_A is the potential applied to the analyzer; E_W, E_X, and E_Y are the energy levels of the transitions involved, expressed in electron volts; and ϕ_A is the work function of the analyzer material (gold) exposed to the incident electrons. Consider the case for carbon.[29]

$$E_W = E_K(6) = 283.8 \text{ eV} \qquad E_X = E_{L_2}(6) = 6.4 \text{ eV}$$

$$E_Y = E_{L_2}(7) = 9.2 \text{ eV} \qquad \phi = 4.5 \text{ eV}$$

$$E_A = 263.7 \text{ eV} \tag{7}$$

A typical carbon spectrum is shown in Figure 24. What discrete energy should be associated with this complex curve, extending over a 20 eV range? The convention is to choose the energy of the most negative deflection of the Auger peak, since this will be the best defined point, particularly when the signal to noise ratio is poor. This energy is 272 eV for carbon. The width and structure of the carbon peak results from the expansion of discrete energy levels into bands in the solid state and from small energy losses suffered by Auger electrons while escaping the solid.

E_A expresses a most likely value of energy, or where one would expect the

maximum of the energy distribution peak for carbon to occur. This maximum corresponds to the internal zero in the Auger spectrum peak, shown at 262 eV in this example. The minimum of the Auger spectrum peak will normally occur at an energy slightly higher than the calculated value, E_A, but within a few electron volts so that the difference is not disturbing. Given the convention for choosing an energy value to represent a peak, emphasis will be placed on changes in this value as a result of chemical state.

Identification of peaks is normally accomplished with the aid of spectra from known standards because of the uncertainty in computed energy values. Thus the KL_2L_2 transition is assigned to the carbon peak on the basis of the above computation, but the Auger peak was first assigned to carbon on the basis of comparison with standards.

The above computation was based on the assumption that the difference in the Fermi level of the specimen and that of the analyzer was just the retarding potential. This assumption is valid for specimens which are electrical conductors, but is not valid for insulators. Some mechanism must insure that the surface potential of the insulator is a constant, stable value. Obtaining a constant surface charge state is part of the art of the spectrometry. The surface potential may be ascertained by noting the energy shift of some well known peak, e.g., carbon, in the Auger spectrum. Other peaks are then measured with respect to the reference peak. A second method is to note the location of the slow secondary peak and consider the initial rise as indicating the surface potential.

A second factor in identifying a peak, or set of peaks, is the pattern of

relative peak heights. Again reference is made to standards. In general, all peaks noted in the standard should be found in the unknown before identification is complete. The following exceptions apply. Weak peaks may be overshadowed by competing peaks of other elements. Peaks in the low energy region may be lost in the steep background slope, particularly when excessive perturbation voltage is used so that resolution is lost. Peaks in the low energy region tend to be narrow and require resolution of a few percent or better. Another cause of lost peaks in the low energy region is spatially uneven surface potential, so that the spectrum is a sum of slightly shifted spectra. Peaks in the high energy region may be lost because of inadequate analyzer resolution. Insufficient primary beam energy to cause the initial ionization will also reduce or eliminate high energy peaks. Thus a reference spectrum consisting of low energy peaks from an M level vacancy and high energy peaks from an L level vacancy might not be duplicated if the primary beam could not ionize the L level.

Two more criteria apply when identifying an Auger peak. Careful consideration should be given to the possibility of artifices before a peak is assigned to an element which is not plausible for the specimen. The relative height of the peak helps determine whether the assignment is plausible or not. A second test is to vary the primary beam potential by a few percent and see if the spectrum remains stable. Many artifices are sensitive to the beam energy and will "follow" the beam potential, whereas the energy level of a true Auger transition is independent of the primary beam energy.

Given that the energy levels of a spectrum and the relative peak heights are

correct, the next question of interest is the shape of the Auger peak. Again, does the peak in question agree with published standards? Several factors may influence the observed peak shape. The type of analyzer is important because varying resolution will obviously change details of the peak shape. A strong positive background slope will cause the initial rise in a peak to be larger and the following dip smaller. Non-instrumental effects include the superposition of two peaks at approximately the same energy and the shifts in peak shape caused by chemical bonding.[30] This latter effect, "chemical shifts," is useful in that it allows one to estimate how surface constituents are chemically bound. For example, the principal silicon peak changes from 92 eV to 75 eV when silicon is oxidized to form SiO_2. The shape of the carbon peak in graphite is significantly different from the carbide peak, e.g., SiC. Methods for estimating the magnitudes of chemical shifts caused by the change in binding energies with bonding have been given by Siegbahn.[17] Transitions reflect the density of states in the affected bands, as mentioned previously. Normally, the density of states is such that the Auger spectrum is symmetrical with respect to the background line, e.g., see Figure 18 for oxygen. Carbon and the low energy silicon peaks, on the other hand, involve valence band transitions which result in non-symmetrical peaks, as in Figure 24 and Figure 19. These transitions are particularly sensitive to bonding state.

The following is a summary of the features commonly seen in Auger spectra. The two dominant features are the elastically scattered primary peak and the slow secondary peak. The elastic peak has a number of subsidiary peaks, called characteristic loss peaks, in the 100 eV energy range below the primary beam

energy. These result from excitation of electron plasma resonances in the solid by the primary beam. Study of these losses is often coupled with low energy electron diffraction characterization of a surface. Another form of loss peak comes from the ionizations which lead to Auger emission. These ionization loss peaks are small compared to the dominant Auger peaks in a spectrum, whereas loss peaks associated with resonance excitation are much larger than Auger peaks. Ionization loss peaks are discussed in Chapters V and VI. In addition to the true Auger peaks, there often appear peaks caused by charging problems. These are called "artifices" because they are trickeries of the experiment. These peaks might also be called anomalies or spurious peaks, and are sometimes called artifacts. Chapter VI is devoted to the difficulties caused by specimen charging.

Calibration Spectra

Auger spectra from a sequence of calibration experiments will now be introduced. These spectra are for cleaned, bulk specimens. They aid in interpretation of Auger spectra of specimens containing many constituents and also motivate the following discussion of the theory of Auger spectroscopy.

The first substance considered is silicon. The specimen was a commercial wafer which had been polished. An Auger spectrum of the wafer, as inserted in the vacuum system, is shown in Figure 18. The dominant characteristic is the graphite contamination, although the silicon and oxygen peaks characteristic of SiO_2 are clearly seen. The specimen was then cleaned by argon ion bombardment for 18 hours with a current density of 20 microamperes/cm^2 and an accelerating potential of 1700 volts. The spectrum of the resulting surface is shown in Figure 19.

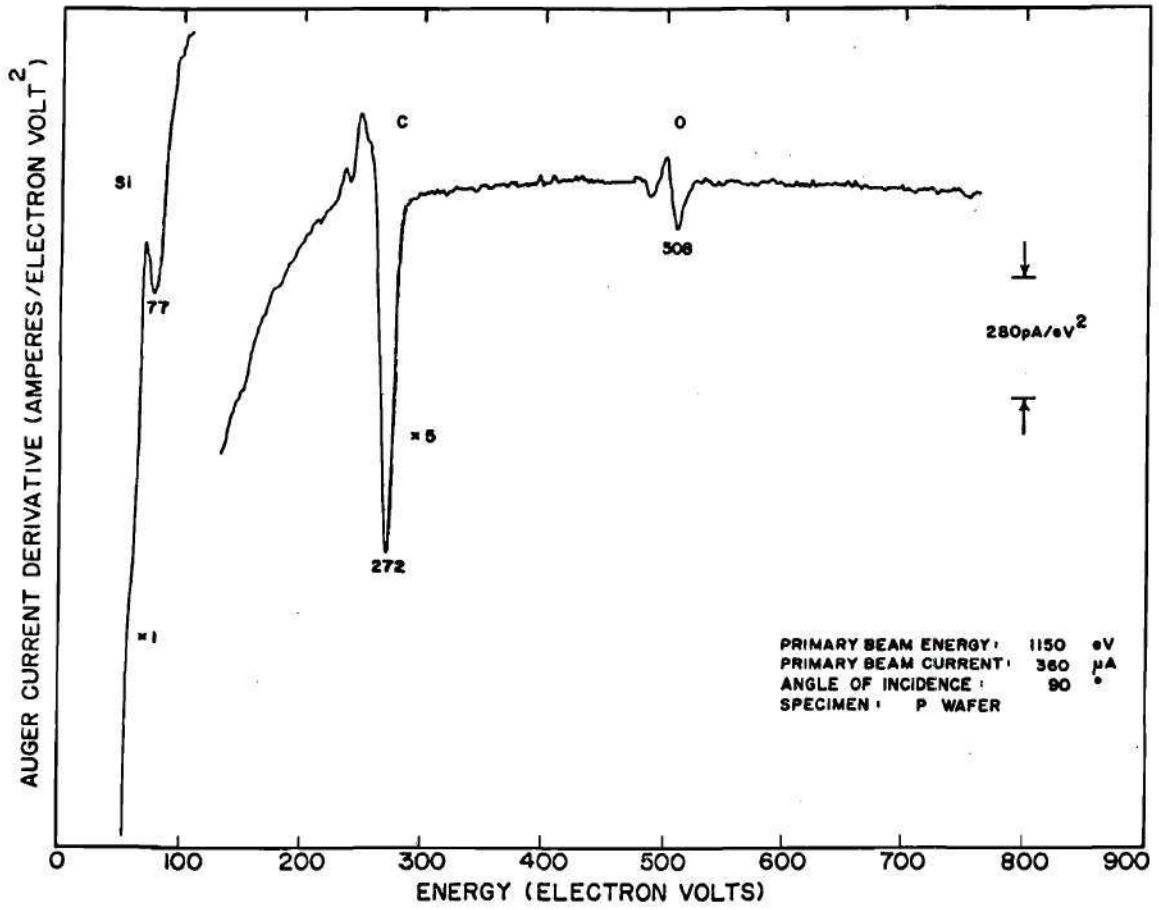

Figure 18. Auger Spectrum of Contaminated Silicon Wafer Before Cleaning.

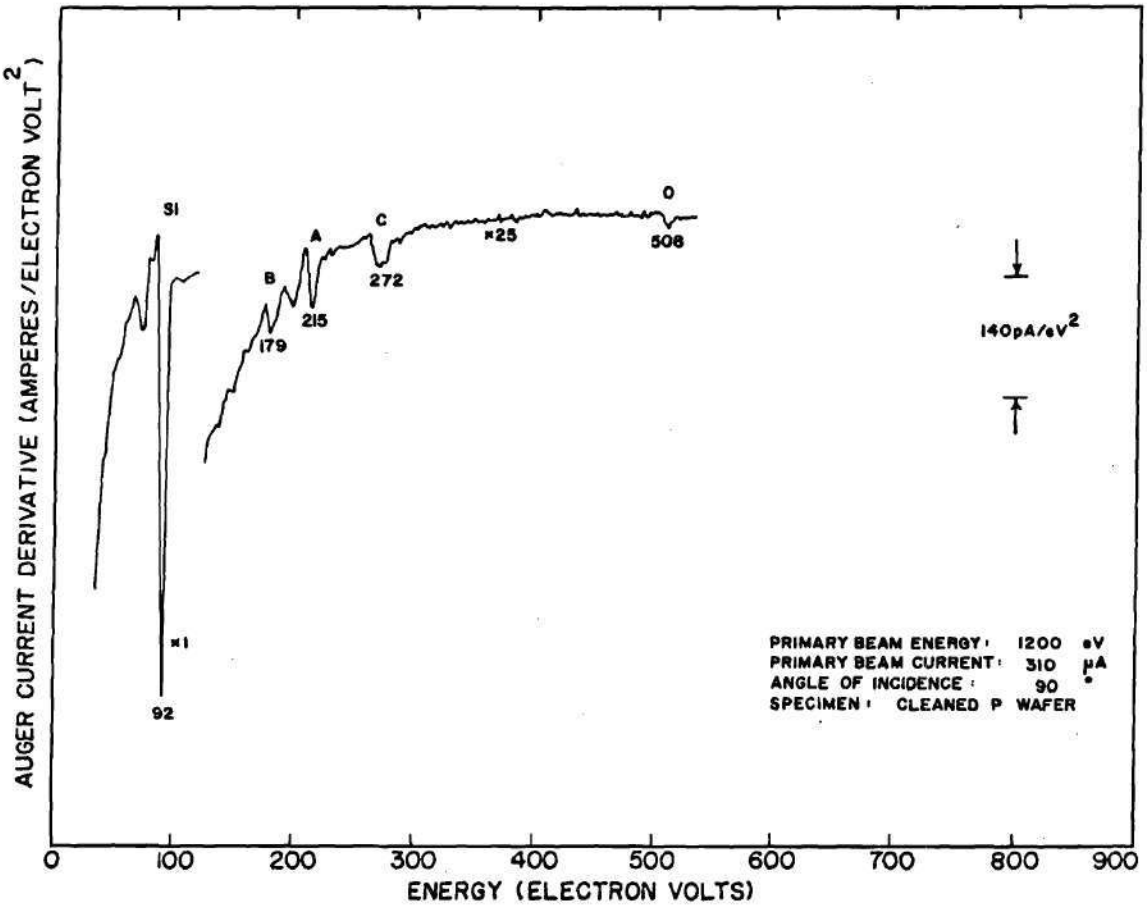

Figure 19. Auger Spectrum of Silicon Wafer after Cleaning.

The 92 eV peak, characteristic of elemental silicon, is now dominant with only a small residual of oxygen and carbon. The dopant, boron, is clearly seen. It should be noted that this wafer was heavily doped, $\rho = 5 \times 10^{-3}$ ohm-centimeters, so the strength of the boron peak is not surprising. The complex at 200 and 215 eV is from argon adsorbed on the surface during the bombardment. Heating the surface to about 750° C for 20 minutes in the high vacuum removed this argon.

A scale factor for the ordinate is shown on the spectra. The strength of an Auger peak is measured by the difference between the maximum and minimum deflections in the peak. The units for this measure are amperes/eV^2. The scale factor is shown as the distance between the arrowheads on the right hand side of the plot. A multiplication factor is often shown beside portions of the spectrum. This factor expresses the increase in sensitivity over the basic sensitivity implied by the scale factor. For example, if the scale factor is 10 picoamperes/eV^2, and the multiplication factor is X 25, a unit deflection in this portion of the spectrum corresponds to 0.40 picoamperes/eV^2.

An energy, expressed in electron volts, is often shown associated with important peaks in the spectrum. This energy is measured at the most negative deflection of the Auger peak. A pair of fast digital voltmeters were utilized to determine these values. Therefore, the accuracy of the measurement is higher than would be expected from a measurement based on the graphical data. The resolution of any energy is implied by the number of digits given; thus 272 means 272 ± 1 eV, and 91.5 means 91.5 ± 0.1 eV. The accuracy of the energy level measurement is limited by the uncertainty in the analyzer work function, the

accuracy of the voltmeter, noise in the ordinate channel, and any uncertainty in the specimen surface potential. The analyzer grids were gold-plated; comparison with analyzers employing a different material will require correction for the work function difference. The voltmeter was a calibrated $5\frac{1}{2}$ digit instrument. Noise in the spectrum was reduced to insignificant levels by adequate filtering. Surface potential uncertainties were accounted for by the techniques described in Chapter VI.

An expanded view of the silicon peak is shown in Figure 20. The scale of the energy axis is now 10 eV per unit. The silicon peak is characterized by a maximum negative deflection at 91.5 eV. This value will be used as a "tag" for elemental silicon in future work. There is a sequence of lower energy peaks associated with the 92 eV peak. These peaks are attributed to various phenomena[31,32] in the literature; the prevalent opinion is that they result from excitation of resonances in the valence electron cloud of the specimen. Thus some of the Auger electrons lose discrete amounts of energy before escaping the solid. These subsidiary peaks help fingerprint the element.

The silicon surface of Figure 19 was then oxidized thermally in an atmosphere of dry oxygen by heating to 875° C for 100 minutes. Standard tables[33] show this gives a 300-400 angstrom SiO_2 film. The Auger spectrum for the oxidized surface, shown in Figure 21, has only a trace of argon as contamination. The principal silicon peak shifted in energy to 75 eV because of the oxidation. There is also a significant peak at 60 eV for the oxidized state.

Figure 22 gives an expanded view of the oxidized silicon peak. Notice that a peak at 89.8 eV is seen in the expanded view, but not in the whole spectrum of

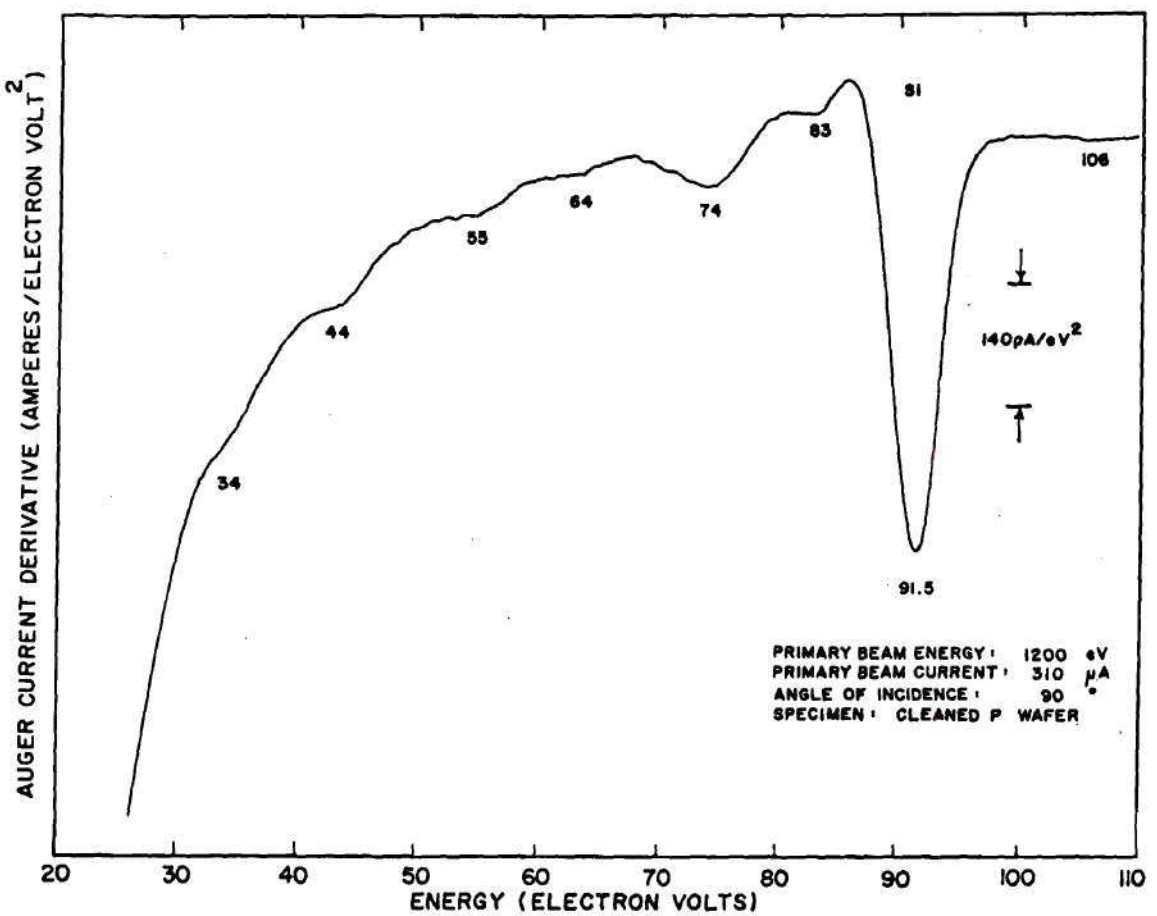

Figure 20. Expanded View of the Silicon Auger Peak.

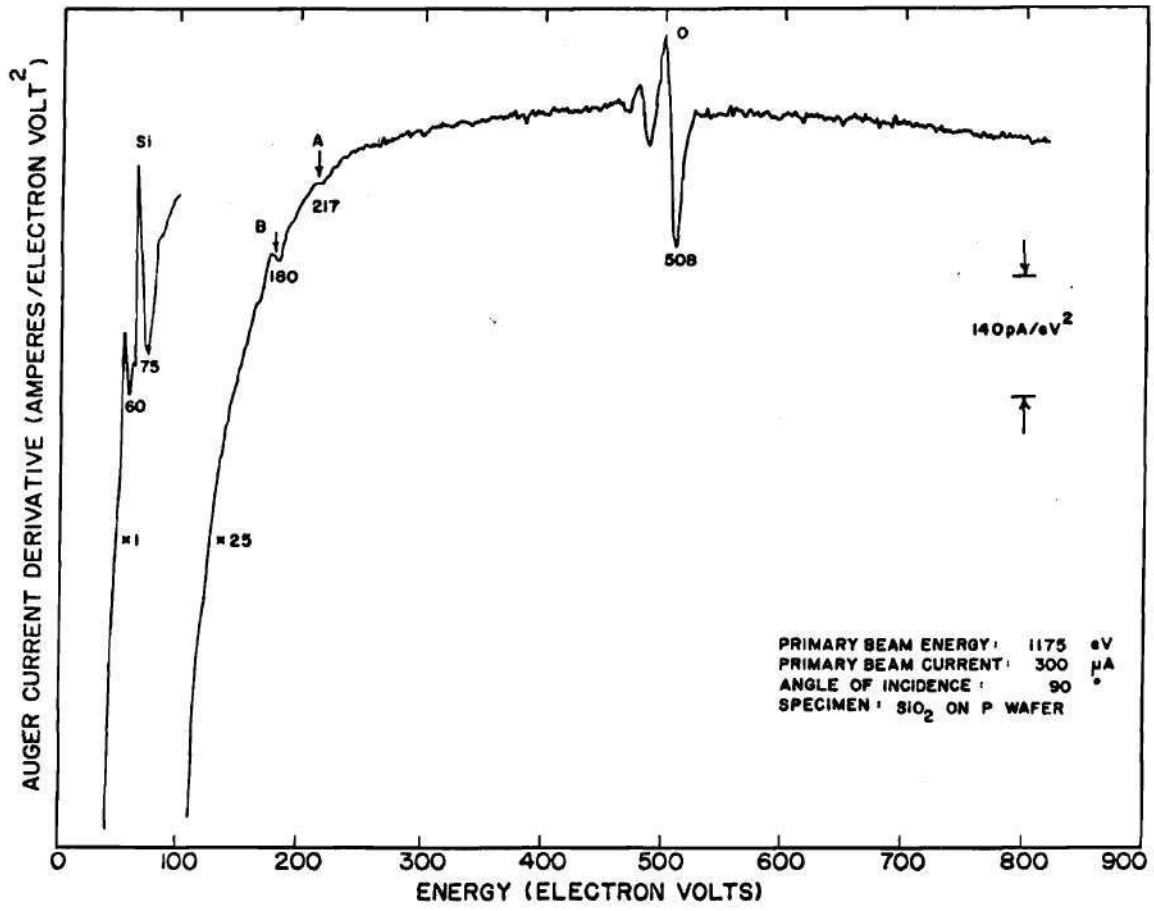

Figure 21. Auger Spectrum of Silicon Dioxide.

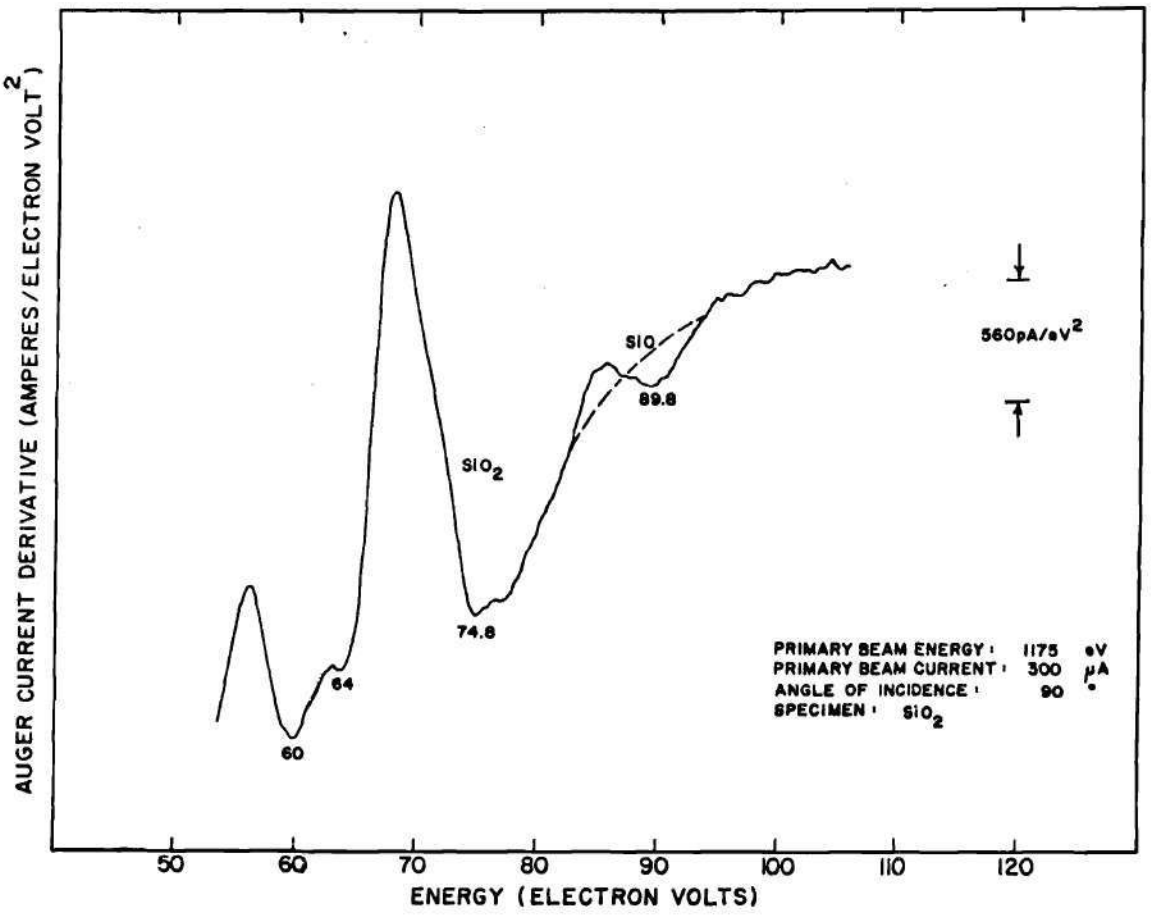

Figure 22. Expanded View of the Silicon, as SiO_2, Auger Peak.

Figure 21. The expanded view was taken after significant electron bombardment by the Auger spectrometer. The electron beam will reduce the oxide surface to form SiO and, if carbon as graphite is present, will also form SiC. These effects are discussed further in Chapter VII. The dashed line in the expanded view is an interpolation, based on Figure 21, for the case of only SiO_2 present.

A silicon monoxide specimen was the subject of the spectrum in Figure 23. The sample was a solid of the type used as an evaporation source. Obviously the surface was not cleaned. Several attempts were made using ion bombardment and reverse sputtering to clean the specimen. These were not successful because of specimen charging. Chemical treatment of the specimen before inserting it in the vacuum system was not utilized for fear of changing the oxidation state of the surface. Probably the only way to obtain a clean silicon monoxide surface is to evaporate SiO onto a substrate in the high vacuum. The difficulty of such a high temperature evaporation was not warranted in this work. Although Figure 23 can not be used to establish amplitude calibration for SiO, it does show the energy of the silicon peak, in the form of SiO, is 90 eV.

That the peak is truly for SiO is deduced by a process of elimination. The silicon is likely to be oxidized because of the significant oxygen peak. There is no 75 eV peak though, which would correspond to SiO_2. The 90 eV silicon peak is not from silicon carbide, for which the silicon peak occurs at 89 eV, because the carbon peak has the characteristic graphite shape, rather than the carbide shape. Therefore, since the specimen was bulk SiO, we conclude that the spectrum is characteristic of SiO.

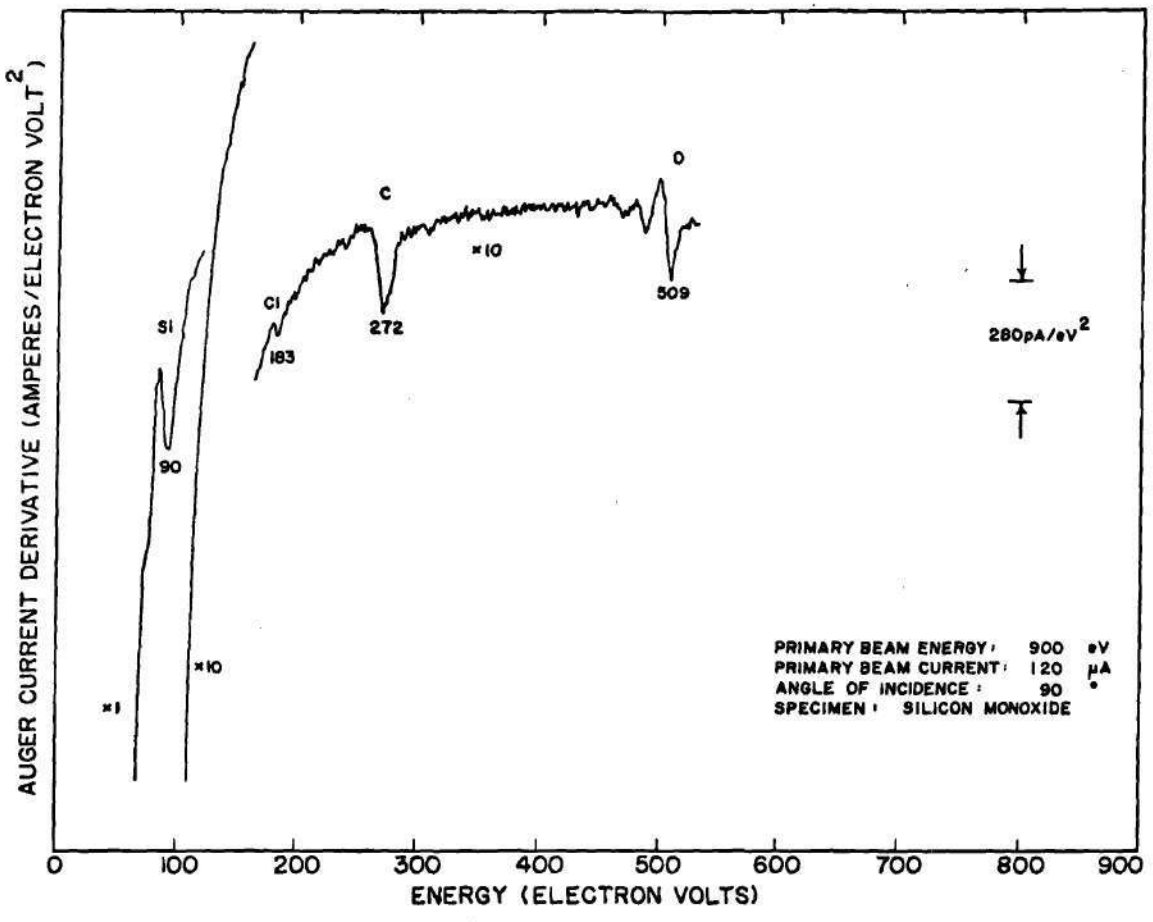

Figure 23. Auger Spectrum of Contaminated Silicon Monoxide.

The final specimens considered are graphite and silicon carbide. The graphite specimen was an amorphous solid cut from a graphite "brick" of the type used for nuclear shielding. No surface cleaning treatment was utilized. The spectrum is amazingly clean, with only traces of sulfur and chlorine. Figure 24 shows two views of the carbon, as graphite, peak. The minimum occurs at 272.5 eV. Notice there is a maximum at 250 eV and a minimum at 243 eV. Compare the graphite peak with the carbon peak of silicon carbide, shown in Figure 25. The SiC maximum deflection occurs at 274 eV and the peak is characterized by a maximum in the neighborhood of 243 eV and minima about 250 eV. In addition there is a prominent maximum at 263 eV, where the graphite peak shows a plateau.

The silicon peak of silicon carbide is shown in Figure 26. The maximum deflection is at 89.0 eV. There is a maximum at 75 eV, just where Si and SiO_2 have minima. These details assist in differentiating between the various forms of silicon and carbon on semiconductor wafers.

The energies and peak shapes presented in this section are in qualitative agreement with those in the literature. Grant and Hass,[34] and Taylor[31] made the basic contributions to the study of silicon with Auger spectroscopy. The data presented in this section are, however, significantly more detailed than that in the literature.

The calibration specimens were also studied as a function of primary beam energy and angle of incidence. The peak height was normalized by dividing by the primary beam current in the following figures. Thus the peak height is expressed in picoamperes/eV^2 for one microampere of beam current. The peak heights are

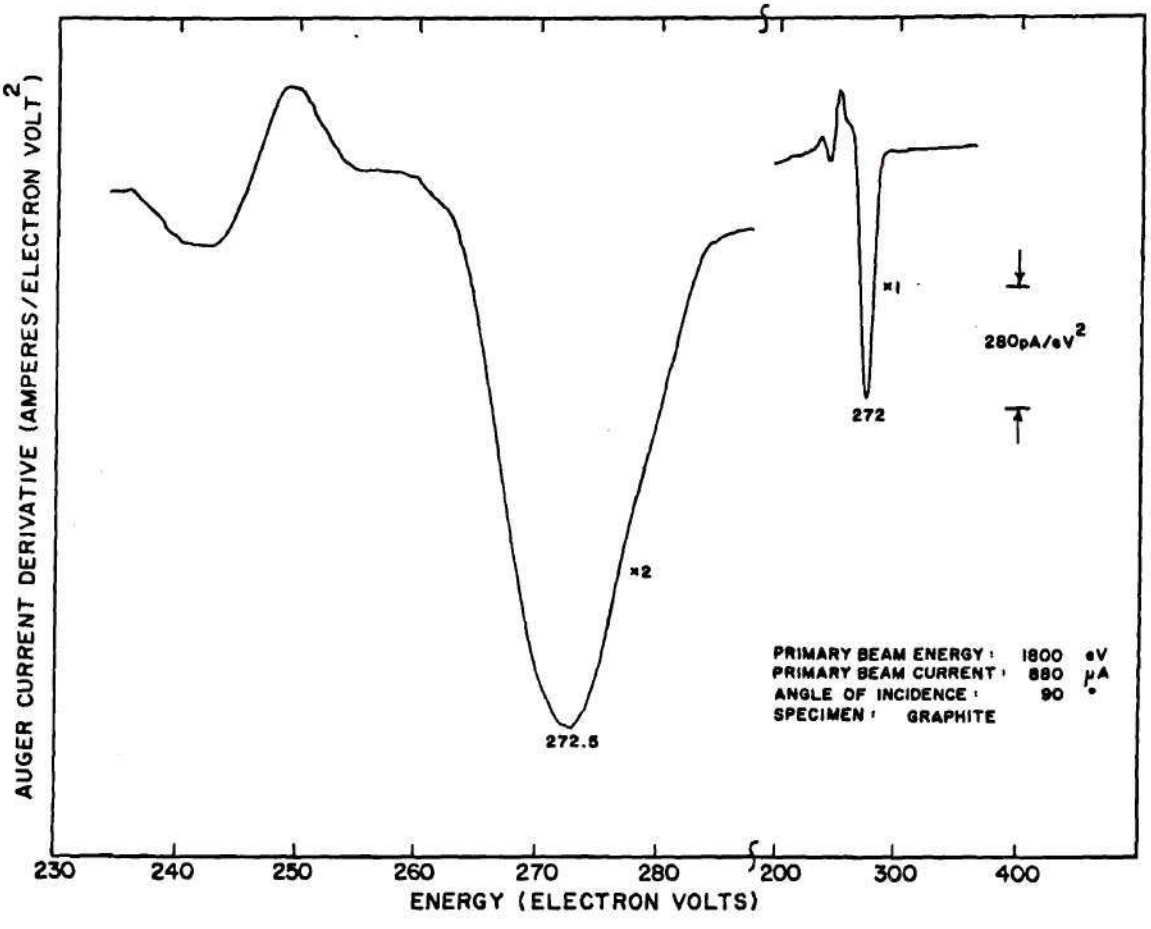

Figure 24. Auger Spectra of Carbon as Graphite.

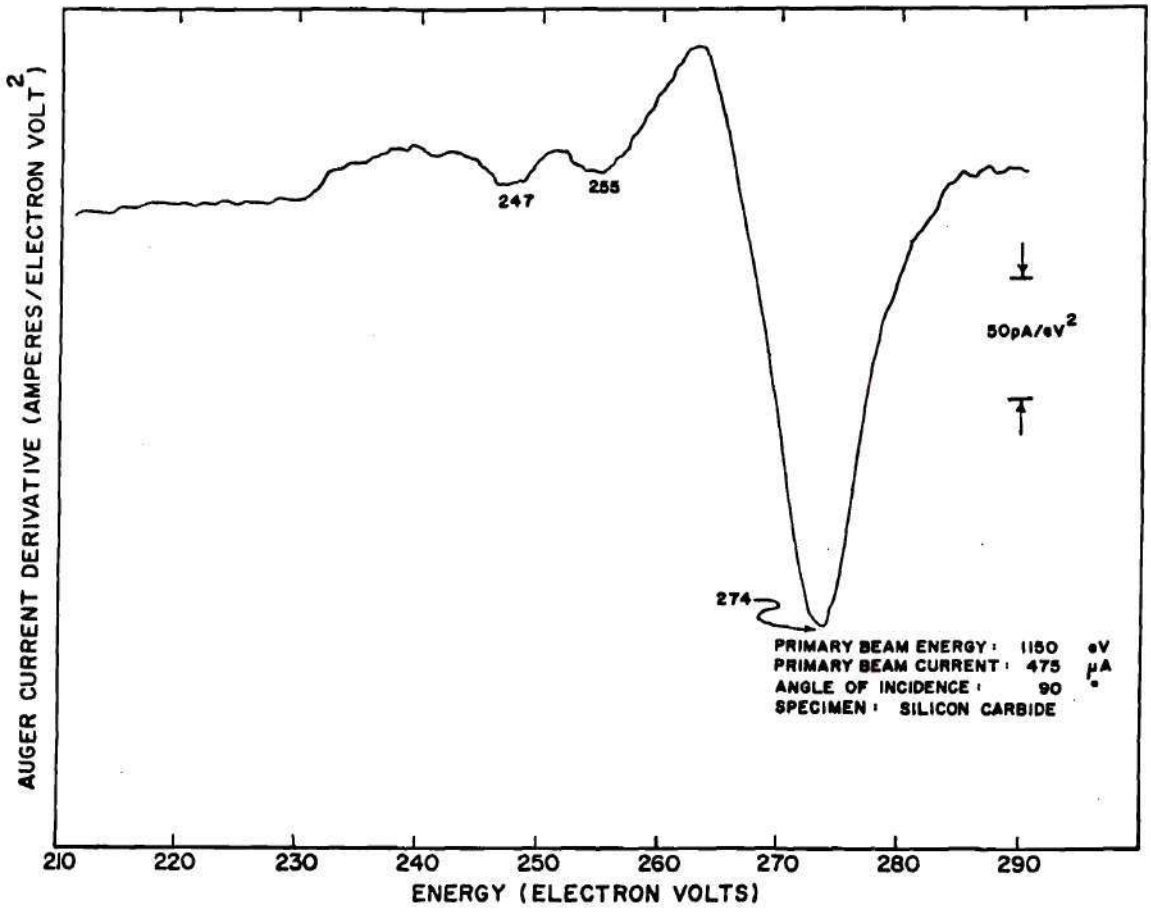

Figure 25. Expanded View of Carbon, as Silicon Carbide, Auger Peak.

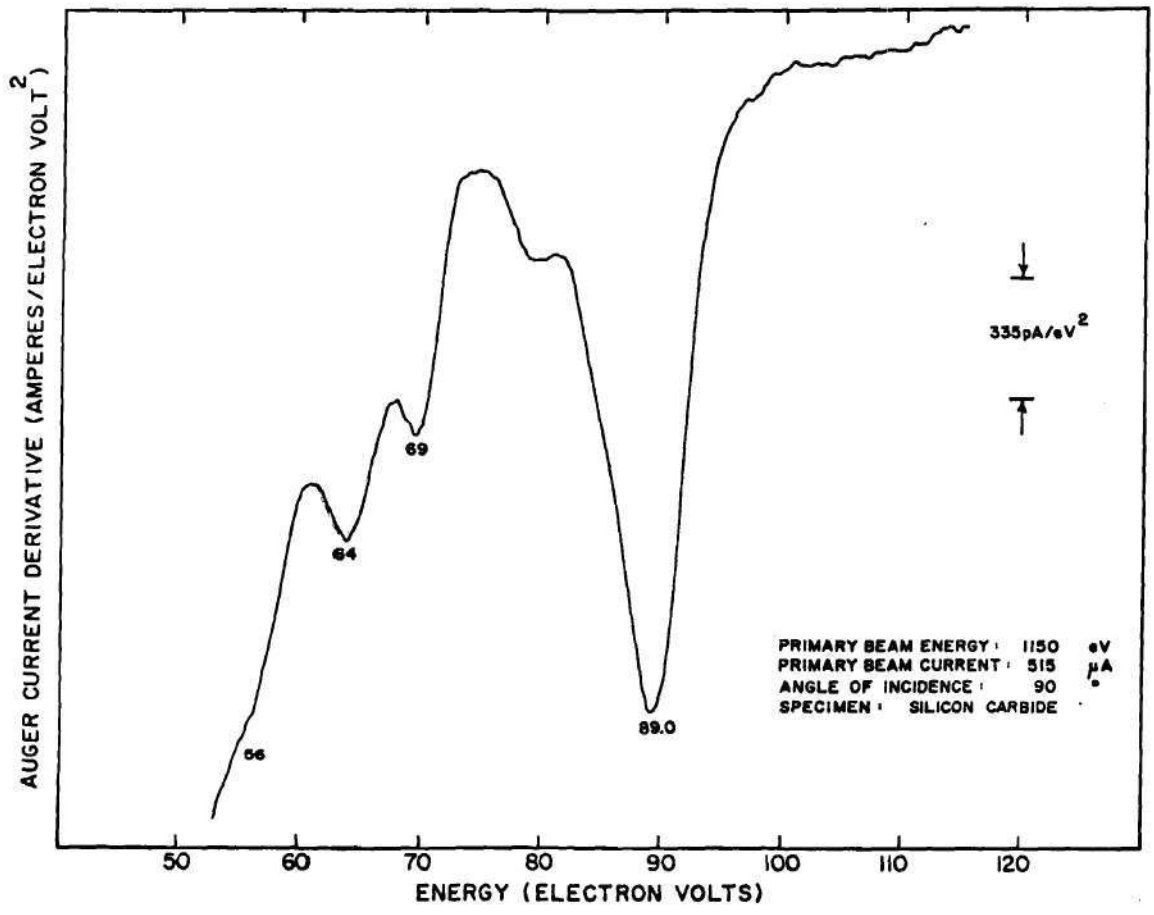

Figure 26. Expanded View of Silicon, as Silicon Carbide, Auger Peak.

linear in primary beam current, so comparison with data taken at different current levels is no problem.

The first figure, Figure 27, shows the variation in the silicon peak for elemental silicon and silicon dioxide as a function of incidence angle. The response of elemental silicon increases at grazing angles but the response of the oxidixed silicon does not. This variance in behavior as a function of incidence angle is typical. It is attributed to variations in the scattering of the primary beam as it passes through the surface region. A detailed theory predicting the behavior at grazing angle is not available at this time. Thus one is forced to use empirical calibration curves for each element when the angle of incidence is varied.

Figure 28 is the corresponding curve for silicon and carbon of silicon carbide. The behavior of silicon as SiC is seen to be essentially independent of incidence angle. The carbon peak, as SiC, is also essentially independent of angle. The response of carbon as graphite, shown in Figure 29, however, is different, showing a maximum at approximately 20 degrees. This maximum is stronger at higher beam energies. Notice that the graphite response falls to a low value at angles close to grazing.

The carbon peak was studied as a function of primary beam energy at normal incidence. This data is shown in Figure 30 as a function of the normalized energy variable U. The peak is seen to occur at about U = 5. Compare this with Figure 4, which showed the behavior of the K and L shell ionization probabilities as a function of U. The maximum of the ionization probability occurs at $U \sim 2.5$. The implication of this variance between the two curves is that the driving function

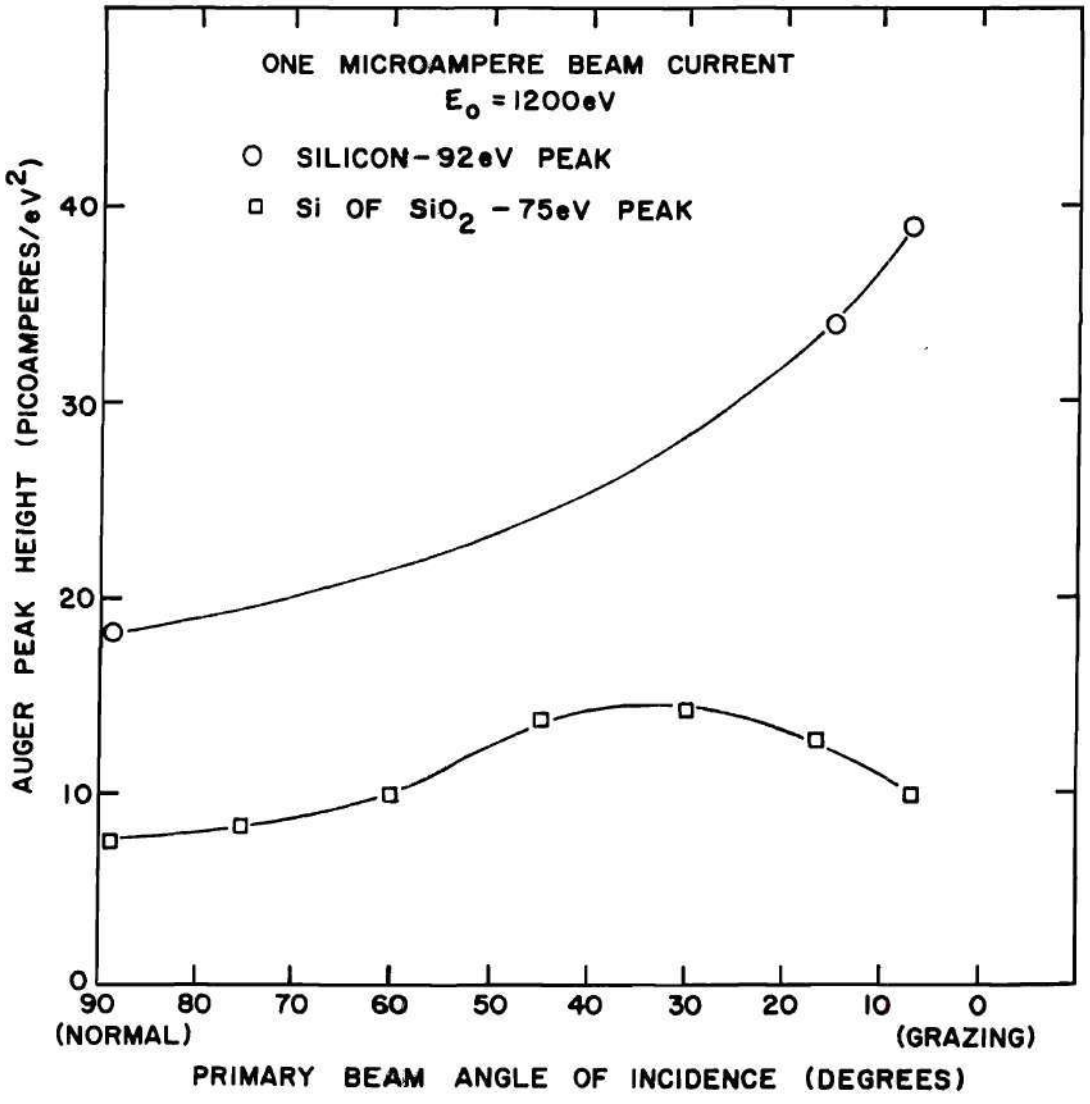

Figure 27. Auger Peak Height as a Function of Primary Beam Angle of Incidence for Silicon as Si and as SiO_2.

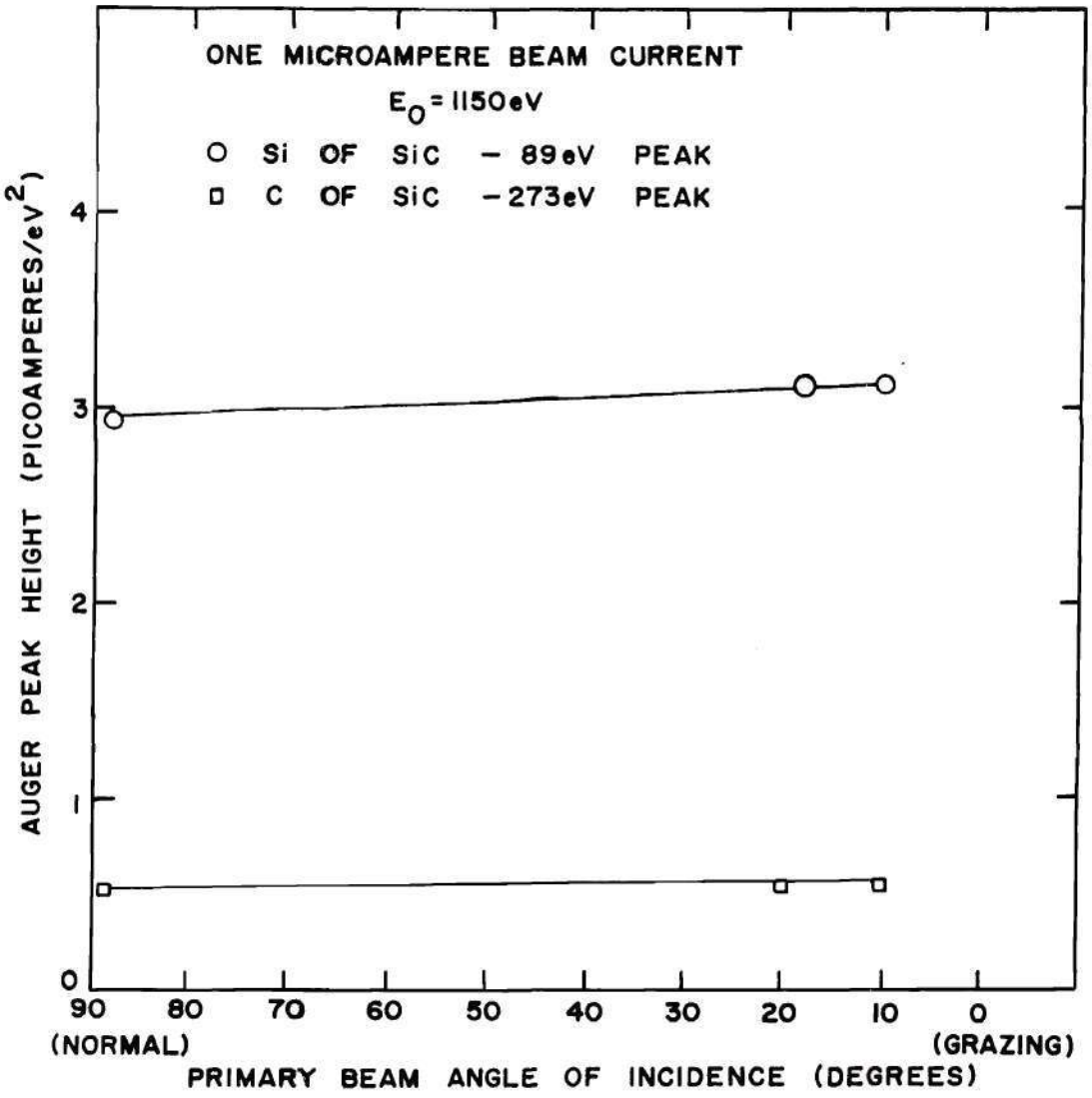

Figure 28. Auger Peak Height as a Function of Primary Beam Angle of Incidence for Silicon and Carbon of Silicon Carbide.

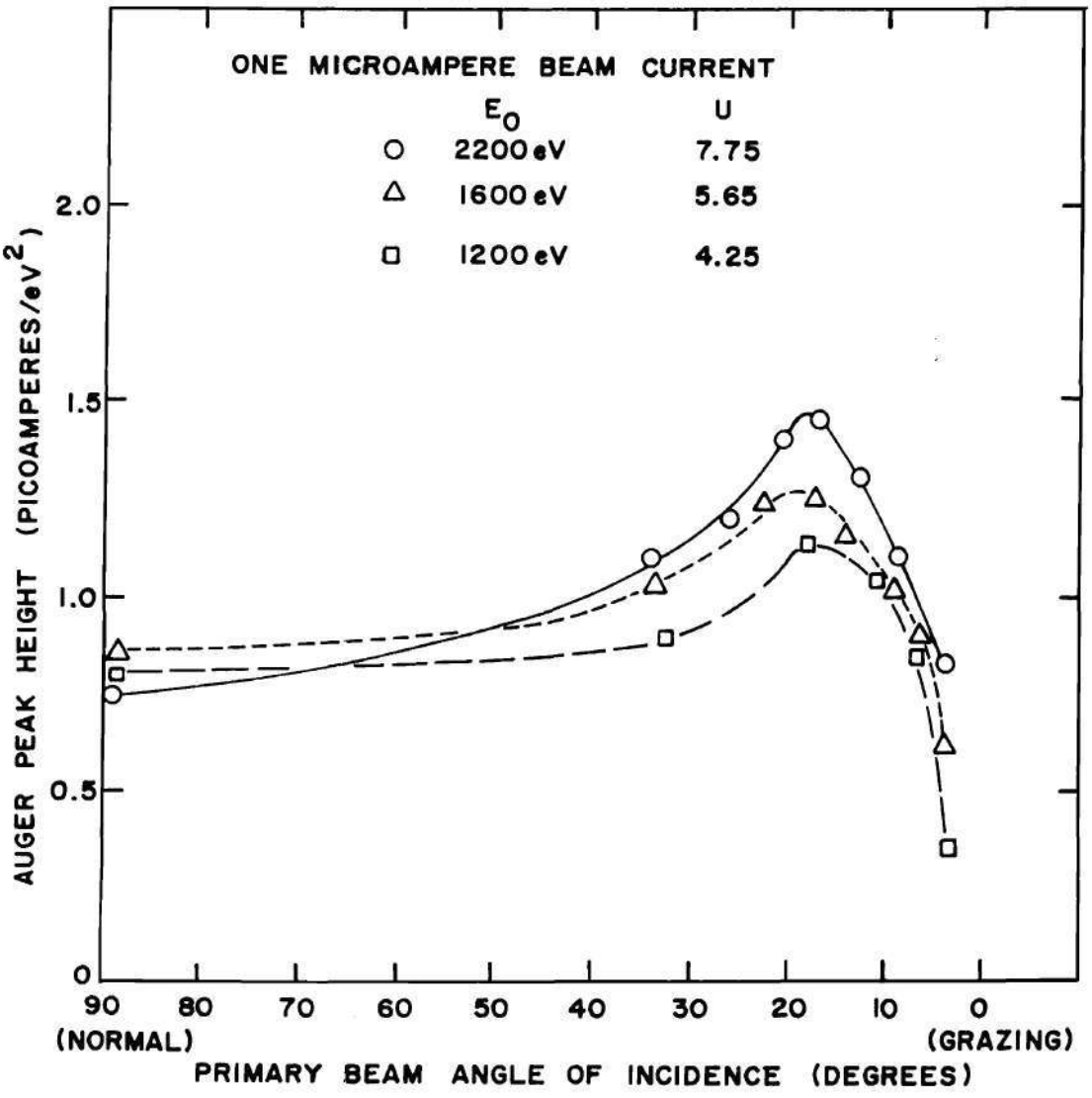

Figure 29. Auger Peak Height as a Function of Primary Beam Angle of Incidence and Energy for Carbon as Graphite.

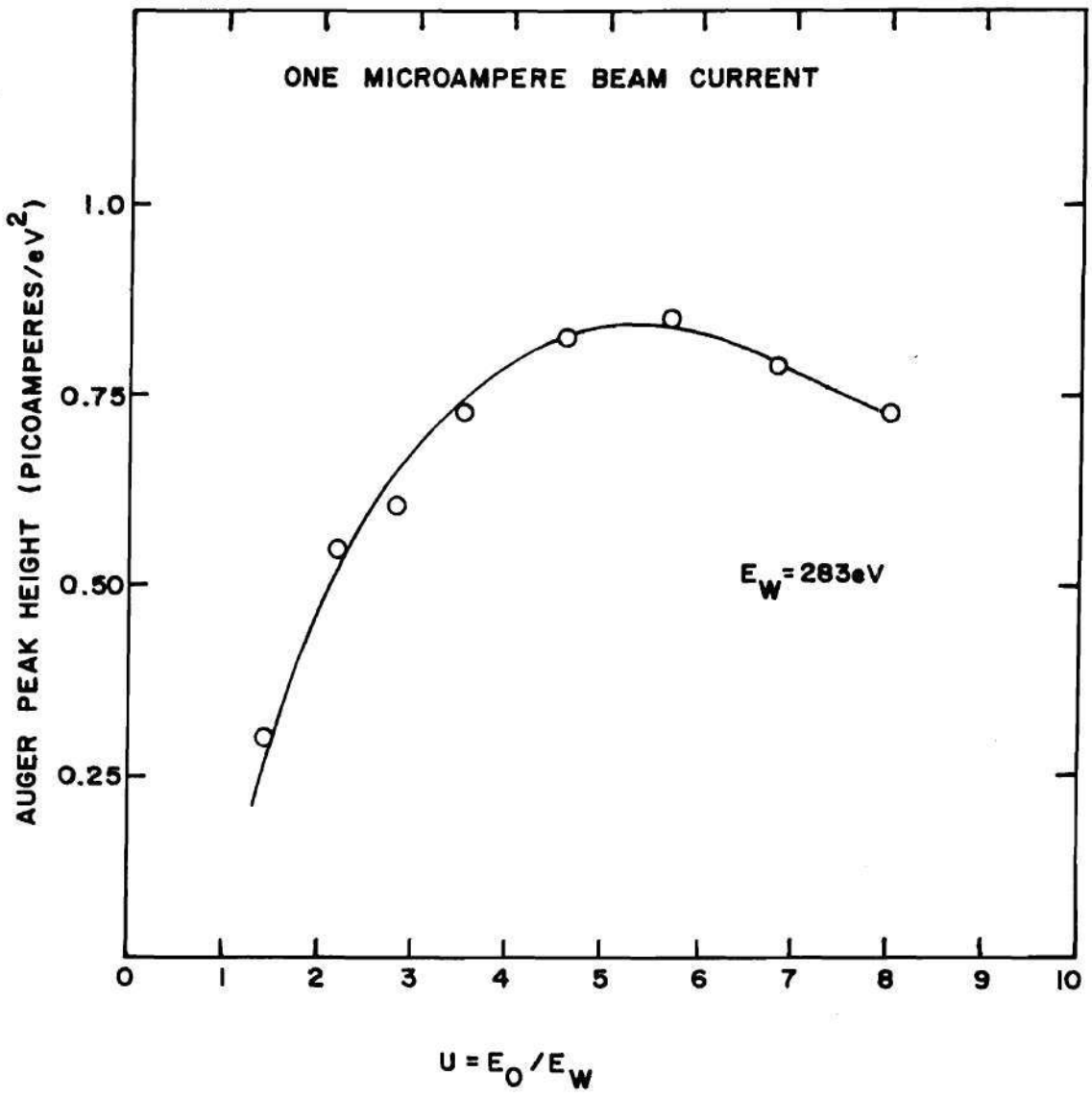

Figure 30. Auger Peak Height as a Function of Primary Beam Energy at Normal Incidence for Carbon as Graphite.

for Auger emission must contain terms in addition to the primary electrons at the beam energy. These additional sources cause the overall response to peak at a higher energy. This problem is discussed more later in this chapter.

Basic Quantitative Considerations

The interpretation problem facing the Auger spectroscopist may be stated thusly:

"Given the primary beam energy, current, and angle of incidence, and the energy analyzer characteristics, how does one calibrate the peak heights?"

The answer is that one cannot, without knowledge of the spatial distribution of the constituents in the specimen. This result follows from the fact that the observed Auger current is the summation of the Auger emissions from different points in the specimen, each point with its own peak amplitude weighting function. The problem can be solved exactly only in those simple cases when the constituent distribution is known a priori. An example of a known distribution would be a monolayer adsorption of a material onto a substrate. Even though the problem can not be generally solved at the present time, a thorough understanding of the available theory is useful to the spectroscopist in making qualitative interpretations. Additionally, certain quantitative interpretations can be made by utilizing the theory in conjunction with calibration spectra from standards.

The observed Auger spectrum may be written as a double summation:

$$\text{Auger Spectrum} = \sum_{\text{energy}} \sum_{\text{space}} (\text{Sources})(\text{Auger Electron Yield}) \times (\text{Escape Probability}) \quad (\text{Detector Efficiency}). \tag{8}$$

The sources are those electrons in the specimen which can cause the initial ionization of the Auger process. The sources have a spatial distribution in the specimen and also have an energy distribution. The Auger electron yield is determined by the numerical density of each constituent and the ionization and transition probabilities for each constituent atom. The numerical density obviously has a spatial variation and the ionization probability is a function of the energy of the source electron. The escape probability of the Auger electron depends on its location in the specimen and on its energy. Detector efficiency is often a function of Auger electron energy, and can also be a function of the location of the emitting atom in the solid.

Of all these factors, only the detector efficiency can be determined with precision. This is not to say that certain experiments can not be calibrated with precision. Again the common example is the adsorption of a monolayer onto a previously defined substrate. This type of experiment, unfortunately, does not allow a spectrum from an arbitrary specimen to be interpreted with like precision. For the case of commercial oxide surfaces, the calibration factors developed from adsorption type experiments might typically allow the peak heights to be calibrated to within $\pm$ 25%. This uncertainty is the result of the uncertainty introduced in each of the factors as one goes from the well defined monolayer adsorption experiment to the realistic case of several monolayers of varying composition contributing to the spectrum. The remainder of this section is a more complete description of each of the factors which contribute to the Auger response. The discussion of each of the primary factors is expanded in a later section.

The first factor considered in more detail will be the sources. At first glance, one might say there is only one source: the primary beam electron. However the primary electron may undergo both elastic and inelastic scattering before ionizing an atom and causing an Auger emission. Therefore the incident direction and energy of the ionizing electron is not known in the general case. For convenience the source electrons will be divided into three classes: (1) the primary electrons, (2) the electrons elastically scattered from deep within the solid back towards the surface, and (3) the energetic secondary electrons created by primary electron collisions. Obviously this division is somewhat arbitrary, but it is useful because these sources have characteristics which can be attributed to the specimen. The first class, the primaries, is that which is considered in simple theories. The second class, also called backscattered electrons, is the first refinement normally made to the theory, and the third class, the secondaries, has only recently been recognized as important.[35] The relative importance of each of the sources will be discussed fully in the following section.

The primary beam is characterized by four quantities: current content, current density, energy, and angle of incidence onto the specimen surface. The total source function is linear in primary beam current because each emission is independent of others. This linearity was verified over two orders of magnitude of primary beam current. If each emission is truly independent of other emissions, then the source function should be independent of the current density of the primary beam. This it was found to be. The Pierce gun made it possible to perform the experiment in two ways. In the first method the spot size of the beam was held

constant while the beam current was reduced by a factor of three. The Auger peak heights were similarly reduced by a factor of three. The second method was to hold the beam current constant while changing the spot area by a factor of ten. This time the peak heights remained constant. This experiment was performed on a clean graphite specimen in a well baked vacuum system. This surface was relatively free of adsorbed gases. A surface contaminated by adsorbed gases would likely not have an Auger response independent of current density because of electron beam induced adsorption or desorption. Harris[19] reported the adsorption of carbon onto his specimen surfaces by the electron beam and the present author noted the desorption of water vapor from graphite in an unbaked (10^{-8} torr H_2O partial pressure) vacuum system. Unless noted to the contrary, the results reported in this work were not affected by such phenomena. Maintenance of the residual gas pressure on the low 10^{-9}, or 10^{-10}, torr range is normally a sufficient precaution.

The third quantity of interest is the primary beam energy. The principal effect of primary beam energy is on the ionization cross section for each atom. The ionization cross section is an important factor in determining the Auger yield for each source electron. The cross section behavior with respect to source electron energy was shown in Figure 4, as the probability of ionization by a source electron. A more subtle influence of primary beam energy is on the scattering of the primary beam. It is this scattering which gives rise to the other two sources, the backscattered electrons and the secondaries. The fourth quantity of interest, the primary beam angle of incidence, is also important to scattering

phenomena; it is the scattering phenomena which prevent absolute calibration of the spectroscopy.

Summarizing, the primary beam is characterized by four quantities: total current, current density, energy, and angle of incidence. The first two quantities may be accounted for exactly, but the latter two contribute to scattering of the beam within the specimen and cannot be accounted for exactly.

The second factor contributing to the Auger peak amplitude is the yield per source electron. The ionization cross section gives the probability of an ionization, per incident source electron, when multiplied by the number of atoms per unit area in the bombarded film. Care must be exercised when computing the numerical density of the material, since the material may not be crystalline or, even if the specimen is a crystal, the density may depend on the incident direction of the source electron. Other factors influencing the yield are chemical bonding and competing neutralization processes, including electron stimulated desorption which is discussed in the next chapter. Thus the Auger yield factor can only be estimated for a general specimen.

The escape probability for the Auger electron is the third factor contributing to the peak amplitude. Inelastic scattering causes the Auger electron to become part of the background current. This scattering is energy dependent, so higher energy Auger electrons may, on the average, escape from greater depths than lower energy Auger electrons. Thus this energy dependence is on the energy of the Auger electron itself and not on the energy of the source electron. The escape probability obviously depends on the scattering characteristics of the

material between the point of origin and the vacuum interface. Therefore the escape probability of the Auger electron, a factor in determining the peak amplitude, is itself a function of the constituents of the specimen, the quantities to be determined by the Auger spectrum in the first place.

The fourth factor of the Auger spectrum is the efficiency of the detector. The efficiency of the energy analyzer and detector electronics can be measured in a straightforward fashion. A more subtle problem is that of the angular distribution of the emitted Auger electrons and any variation in this distribution with respect to the depth of the emitting atom in the solid. Fortunately the spherical retarding grid analyzer is relatively insensitive to the variations of those distributions encountered in practice.

The final consideration when interpreting Auger spectra is the influence of surface morphology. Consider a coordinate system in which the x-y plane is defined by the vacuum-specimen interface and the z direction is normal to the x-y plane. The above discussions have been based on a specimen homogeneous in the x and y directions, but with variations in depth, the z direction. Variations in the x and y directions lead to much more complicated problems. The most common example is that of a rough surface. A second common example is the localized adsorption of contaminants on the surface. Surface roughness will change the angle of incidence of the primary beam, and adsorption will often affect chemical bonding of the surface atoms which, in turn, changes the nature of the Auger peak.

Any theory which is to be used for calibrating Auger spectroscopy must account for the factors listed above. The theory prevailing in the literature at the

present time was originally proposed by Bishop and Rivière[5] in 1969. Several additions and modifications have recently been added.[36,37] The only significantly different theory that has been proposed was by Harris,[16] also in 1969. The principal point of difference is in the handling of the source factor. Bishop and Rivière model the primary electron as passing through the Auger escape volume on a straight line, oriented the same as it entered the specimen. Backscattered electrons are considered as an additional source, but the effect of energetic secondaries is not normally considered. The sources in the Bishop and Rivière model are characterized by well defined orientations. The source in the Harris model, on the other hand, is considered to be isotropic, because of the scattering of the primary beam as it passes through the solid. The model proposed in this work is, in a sense, midway between these two extremes. The primary beam is considered well oriented as it enters the first monolayer of the specimen. However it is quickly scattered, particularly when it approaches at grazing incidence. For the remainder of the Auger escape region the sources are essentially isotropic. This model is based on measurements of the Auger response as the primary beam angle of incidence was varied.

While the Bishop and Rivière model does make a prediction of the behavior of the Auger response as the beam angle is varied, there is no report in the literature of measurements, made over the complete range from grazing incidence to normal incidence, to support that theory. The only complete measurements reported were by Harris, and these were with an analyzer configuration which is

difficult to compare with the retarding grid or cylindrical mirror analyzers. Hopefully the measurements made in this work will stimulate additional investigations into the nature of the sources of ionization for Auger emission. These measurements are explained by the above model containing both oriented and isotropic characteristics. Unfortunately the model is not yet complete enough to predict a priori Auger response as a function of primary beam angle, based on primary beam energy, crystallographic data, etc. What the model does allow one to do is to explain, or justify, experimental data and to utilize the data in interpreting spectra from similar specimens. For example, data was presented in the previous section showing the variation in the Auger peak height with primary beam angle for an uncontaminated silicon specimen. This variation in peak height with beam angle is a result of the scattering characteristics of silicon. These same characteristics are present when, say, the surface is contaminated with a monolayer of graphite. Thus the practical case, the contaminated surface, is interpreted based on data from the calibration spectra of the previous section.

This section has attempted to give an overview of the factors which contribute to the height of an Auger peak. Each of these factors are discussed further in the following sections. It should be reiterated that while the theory of Auger spectroscopy is not yet complete, much is known about the interpretation problem and the spectroscopy has proven useful in applications. Perhaps the greatest contribution of this chapter is that all of the factors influencing calibration have been brought together so that at least the outline of a complete theory is now available.

Sources

This section describes the sources within the solid which cause the initial ionization necessary for Auger emission. With electron excited Auger spectroscopy these sources are energetic electrons in the solid. The simplest model for Auger spectroscopy would have only one source: primary electrons with energy and orientation equal to that of the incident beam. There is considerable evidence, however, that many of the ionizations leading to Auger emission are caused by scattered primary electrons and by energetic secondary electrons. Thus it is profitable to consider the response of the solid, that is, Auger electron emission, as the superposition of responses to elementary excitations: the sources. The analogy to linear circuit theory is obvious.

The remainder of this section will describe the nature of the excitation sources in general terms, specifically describe the model prevalent in the Auger literature, show the need for a more general description of the sources, and, finally, describe the characteristics of the elementary sources necessary for quantitative interpretation of Auger spectra.

The interaction of an electron beam with a solid is a complex process still not well understood. Figure 31 illustrates the general situation present in electron excited Auger spectroscopy. Consider the incident primary beam to be, for the moment, directed normal to the surface. The region from which an Auger electron can escape the solid, with little energy loss, is small compared to the region over which the primary beam is scattered and loses its energy. Most of the incident beam passes through the Auger escape region and is absorbed in the

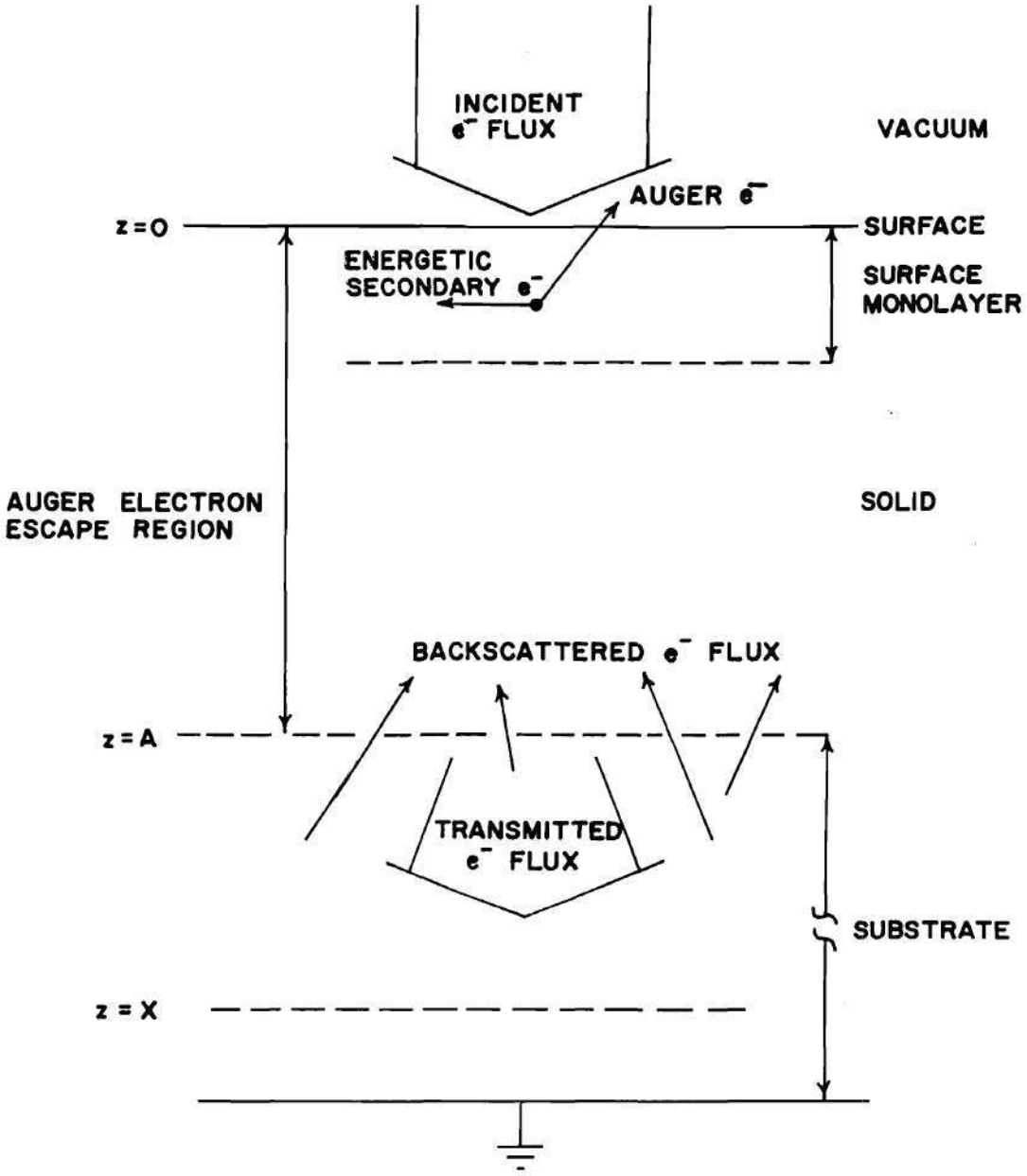

Figure 31. Schematic Representation of the Interaction of an Electron Beam with a Solid.

remainder of the solid. Therefore it is useful to think of the Auger escape region as a thin film, a few monolayers thick at most, on a substrate, the remainder of the solid. The thin film is almost transparent to the primary beam. Of course some of the primary electrons do cause ionizations in the film, and in so doing may create energetic secondary electrons also capable of causing ionizations. Additionally, there is a flux of backscattered electrons from the substrate into the film. These backscattered electrons may create additional secondaries. Each of these sources of energetic electrons must be considered by the model.

Two philosophically different approaches have been proposed in the Auger literature. One is microscopic in its level of detail; the other is macroscopic. The theory of Bishop and Rivière[5] is microscopic in detail. The interaction of the electron with the solid is described by separate representations for elastic and inelastic scattering, and the probability for ionization by the source electrons is described by the Worthington-Tomlin[5] approximation. The alternative approach, macroscopic in nature, was advanced by Harris[16] during the initial development of Auger spectroscopy but has not received the attention in the literature that the Bishop and Rivière theory has received. The present author believes that the macroscopic approach leads to a model of greater utility in interpreting Auger spectra, and much of the theoretical portion of this work is devoted to improving this macroscopic model. The trade-off is between the ultimate limitations of the model and its present utility. The microscopic model, when refined, will allow optimization of the spectroscopy and interpretation of spectra. On the other hand, within our available knowledge the microscopic model does not

permit interpretation of spectra from general specimens to the same degree of accuracy as the macroscopic model.

Rather than be concerned with separate elastic and inelastic scattering phenomena, the macroscopic approach is concerned with penetration of the electron beam into the solid and dissipation of the beam energy along its path. Harris described the dissipation of the energy as an exponential decay of energy with penetration depth. Makhov,[38] in work not concerned with the Auger effect per se, arrived at an empirical description of penetration depth and energy dissipation. The utility of Makhov's work is that the applicable energy range coincides with the primary beam energies used in Auger spectroscopy, whereas other models are based on significantly different energy ranges and must be extrapolated to the Auger spectroscopy range.

The Bishop and Rivière model considers two sources: primary electrons with energy and orientation equal to that of the incident beam, and backscattered electrons from the substrate. The backscattered electrons are characterized by their most probable orientation and their mean energy loss. The Auger electron yield factor of Equation 8 is accounted for by the Worthington-Tomlin approximation, discussed in the next section, and the escape probability is considered to be one for Auger electrons from the top monolayer if directed towards the surface and zero if otherwise directed. The escape probability factor was recently refined by Seah's work,[36] and now considers Auger electrons originating deeper within the solid.

The source function of the Bishop and Rivière theory is given for a primary

beam of N_o electrons by

$$N_s = N_o \, r \csc \phi \tag{9}$$

where N_s is the equivalent number of electrons passing through the Auger escape region at normal incidence, with the transmitted electrons absorbed by the substrate, r is then the correction factor for backscattering by the substrate, and ϕ is the angle of the primary beam, with 90^o for the normal to the surface. Values for r lie between 1.1 and 1.9 for the typical cases considered by Bishop and Rivière.

Some features of the Bishop and Rivière model have been verified experimentally. It estimates the Auger current for monolayer coverage on a substrate as 10^{-5} to 10^{-4} times the primary current for normal incidence. Meyer and Vrakking[39] have achieved good ($\pm$ 20%) agreement, after making adjustments to parameters in the model, for fractional monolayer coverages at normal incidence.

The Bishop and Rivière model might be called a "straight line" model since scattering of the incident beam is not assumed. Furthermore, the possibility of energetic internal secondary electrons contributing to the Auger yield is not considered. Houston and Park[35] have offered evidence that the internal secondaries are an important source of ionizations. This deficiency in the model would be most evident in homogeneous specimens where an appreciable contribution comes from the underlying layers. The Meyer and Vrakking work, on the other hand, was done on fractional monolayer coverages of an adsorbate on a foreign substrate.

There is no real question that the path length through the escape region has

an influence on the probability of ionization and Auger emission. The difficulty results from trying to relate the external parameters of the beam, the angle of incidence and energy, to the internal parameters, the energy and angular distributions as a function of depth into the material. Obviously it is the energetic electron inside the solid that gives rise to the Auger emission. It is worthwhile to compare the probability that an electron of energy E will be scattered through an angle θ by the time it has lost a fraction $\Delta E/E$ of its energy. Following Everhart and Hoff,[40] the rate of change of mean kinetic energy along a path s for nonrelativistic electrons is

$$-\frac{dE}{ds} = (2\pi N_A e^4)\ \frac{Z\rho}{A}\left[\frac{1}{E}\ \ell n\left(\frac{E}{I}\right)\right] \tag{10}$$

where e is the electronic charge, N_A is Avogadro's number, Z the atomic number, A the atomic weight, ρ the mass density, and I the mean excitation energy for electron energy loss in the solid. The large angle scattering is estimated by using the Rutherford cross section for an unshielded nucleus. The probability $p(\theta, E)$ of an electron of energy E being scattered through an angle θ in a distance Δs by a material characterized by Z, ρ, and A will be

$$p(\theta, E) = \frac{N_A e^4}{16}\left(\frac{Z\rho}{A}\right)\left(\frac{Z}{E^2}\right)\frac{\Delta s}{\sin^4(\theta/2)}\ d\Omega \tag{11}$$

where the electron is scattered into a differential solid angle $d\Omega$. To find the probability $P(\theta_1 < \theta < \theta_2)$, the above expression must be integrated through the angle θ using $d\Omega = 2\pi \sin\theta\, d\theta$. The probability for large angle scattering can be

written in terms of the fractional energy loss $\Delta E/E$ obtained from Equation 10.

$$\frac{\Delta E}{E} = \frac{2\pi N_A e^4}{A} \frac{Z\rho}{E^2} (\ln E/I)\, \Delta s \tag{12}$$

$$P(\theta_1 < \theta < \theta_2) = \frac{Z}{32\pi} \frac{\Delta E}{E} \frac{1}{\ln E/I} \int_{\theta_1}^{\theta_2} \frac{2\pi \sin\theta}{\sin^4(\theta/2)}\, d\theta \tag{13}$$

An approximate expression for the mean excitation energy[40] is $I = 13Z$. The integral obviously contains a singularity at zero deflection. This singularity is removed by restricting the minimum value of θ_1. The physical argument is that small deflections correspond to large impact parameters, that is, the electron passes by the atom at some distance and its path only mildly perturbed. But at this distance the nucleus is shielded by the outer electrons and so there is no real deflection for such paths.[41] In the present case we are not concerned with small deflections, so the formula may be used with confidence. The formula was evaluated numerically for the following case:

$Z = 6$ (carbon)

$I = 78$ eV

$E = 1500$ eV

$\Delta E = 300$ eV, corresponding to a K shell ionization

$\theta_1 = 30^\circ$

$\theta_2 = 90^\circ$

The resulting probability is 0.75. This is to be interpreted in the following way. The energy loss expression, Equation 12, is for loss of mean energy of an ensemble of electrons as a function of path length. Equation 12 is evaluated for 300 eV mean energy loss of a 1500 eV beam. The resulting path length Δs is substituted into Equation 11 to determine the probability of large angle scattering. Since the inelastic scattering model used here does not include any angular deflection (in this case, a conservative assumption), the high probability of elastic scattering says that direction of the primary electron is likely to be different from that of the incident beam by the time it has lost significant energy. Of course this still does not specify the angular distribution of primary electrons within the Auger escape region, since the mean energy loss for the beam takes place mostly outside the Auger escape region. One must have other evidence before this angular distribution may be hypothesized.

Further evidence of the diffuse scattering of energetic electrons in the solid is offered by the results of Jonker,[42] who experimentally studied the nature of secondary emission. In the low energy region, region III of Figure 2, the internal angular distribution of electrons is isotropic, with essentially no dependence on the angle of incidence of the primary beam. These are slow electrons, which are expected to have suffered many inelastic collisions before escaping the solid. In the intermediate energy range, region II of Figure 2, the angular distribution of the electrons is also isotropic internally. As the angle of incidence of the primary beam is changed towards a grazing angle, the distribution remains almost unchanged, with only a slight shift in the direction of the incident beam.

Thus those electrons which have lost a significant fraction of their energy also have suffered significant deflections. However, the electrons of region I, those which have not lost significant energy, show a distinct maximum in the direction of a specularly reflected beam. These electrons behave as if they have suffered one characteristic elastic, large angle, scattering; electrons which have lost significant energy behave as if they have suffered many random collisions.

A secondary electron cascade like that described by Wolff therefore seems an appropriate model.[43] The primary beam is likely to suffer large angle deflection by the time it has lost a significant fraction of its energy. When the primary electron does suffer an inelastic collision, it is likely to lose enough energy so that the secondary electron will have an energy falling in region II of Figure 2. The distribution of these energetic secondaries, as a function of energy E, is given by Wolff as proportional to $1/E^2$, for E larger than 100 eV.* Therefore, most of the energetic secondaries will have low or intermediate energies, but some will contain a significant fraction of the energy of the incident primary. Streitwolf[44] shows that most of these energetic secondaries produced by inelastic scattering of a primary electron to be initially contained within a 90° cone centered about the direction of the primary. These secondaries may be considered isotropically distributed because of the scattered nature of the primary

*The 100 eV lower energy limit was chosen by Wolff as the dividing line between the high energy region, where each collision results in small fractional energy loss, and the low energy region, where each collision results in significant ($\sim\frac{1}{2}$) fractional energy loss. Electrons of energy less than 100 eV may be neglected in practical Auger spectroscopy where the binding energies of interest in the initial ionization are greater than 50 eV. Thus the 100 eV lower limit does not impair the utility of the theory.

beam and the scattering the secondaries themselves will undergo.

The fundamental question, that of the nature of the source function inside the Auger escape region, has not yet been answered. Through some arbitrarily thin region one would heuristically expect the geometric argument to prevail. In the bulk material the diffuse, or scattered, model would seem logical. Behavior of the Auger yield as a function of incident beam angle suggests that a model midway between the above two extremes is appropriate. Auger yield does vary with the angle of incidence, but not as rapidly as predicted by Equation 9 and the response does not show the singularity at grazing incidence. Instead the Auger yield remains constant or actually drops off at incident angles very close to grazing. A model with isotropic sources is independent of incident angle; the Bishop and Rivière model with oriented sources is very dependent on the incident angle. Thus the experimental results suggest a model containing both types.

The behavior of the primary incident flux can also be studied using the model of Makhov and co-workers.[38] This macroscopic empirical model is based on electron transmission studies through thin films of Al, Si, Cu, Ge, and Al_2O_3. The behavior of these substances was found to be similar. Pb and Bi were found to obey the same laws but with significantly different parameter values. The basis of the model is a standardization, or normalization, process.

The fraction η of the normally directed N_o electrons of energy E_o which pass through a thin film of normalized thickness x was found to be, as a function of x,

$$\eta(x) = \exp(-x^p) \qquad (14)$$

where p is a parameter equal to 2 for the light elements and equal to 1 for Pb and Bi. Thus the transmission factor η is 1/e when the normalized thickness x = 1. The normalization equation is

$$x = z/X \tag{15}$$

where z is the measurement of depth and X is a function of the material and incident beam energy E_o given by the formula

$$X = CE_o^n \tag{16}$$

where C and n are constants for each material. Table 1 gives values for several substances according to Makhov. X is expressed in micrograms per cm^2 and E_o in keV. The above formula agrees with measured values for transmission within the experimental error in measuring film thickness, normally less than 15%. Furthermore, the formula checks against experimental data over the energy range of interest, 1 to 3 keV. When p = 2, X is interpreted as the mean square transverse path, where the transverse path of an electron is its penetration depth, or range. Figure 32 shows the dependence of X on E_o for several materials. The behavior of carbon is not shown but can be assumed to be similar to Al according to data by Bishop.[45]

As an example, consider a 1 keV beam of electrons incident on an aluminum crystal. X is found from the formula to be 140 angstroms for this case. A reasonable estimate of the escape region for Auger electrons would be the first four monolayers; that is, one would not expect an Auger electron to escape from

Table 1. Constants Utilized in Mahkov's Electron Penetration Expressions. From Mahkov.[38]

Substance	C	n	p	A	s
Al	3.8	1.68	2	0.9	0.9
Si	3.4	1.65	2	0.95	0.9
Cu	5.8	1.53	2	0.95	0.9
Ge	6.5	1.47	2	1.0	0.9
Bi	4.2	1.44	1	0.7	0.6
Al_2O_3	4.6	1.65	2	0.95	0.9

a greater depth without losing significant energy. Since the lattice constant for Al is 4.05 angstroms, the escape region is approximately the upper 14 angstroms. Thus x = 14/140 = 0.1, and Equation 14 yields n(0.1) = 0.99. That is, the exit flux is 99% of the incident flux, so most of the primaries must pass through the Auger electron escape region although they may suffer collisions and lose energy in the process. Since it is this energy loss which gives rise to ionizations and subsequent Auger emission, it will be discussed next.

Makhov determined the distribution function $g(N_o, E_o, x, \xi)$ which gives the absolute number of electrons passing through a film of normalized thickness x as a function of their normalized energy ξ,

$$\xi = E_x/E_o \tag{17}$$

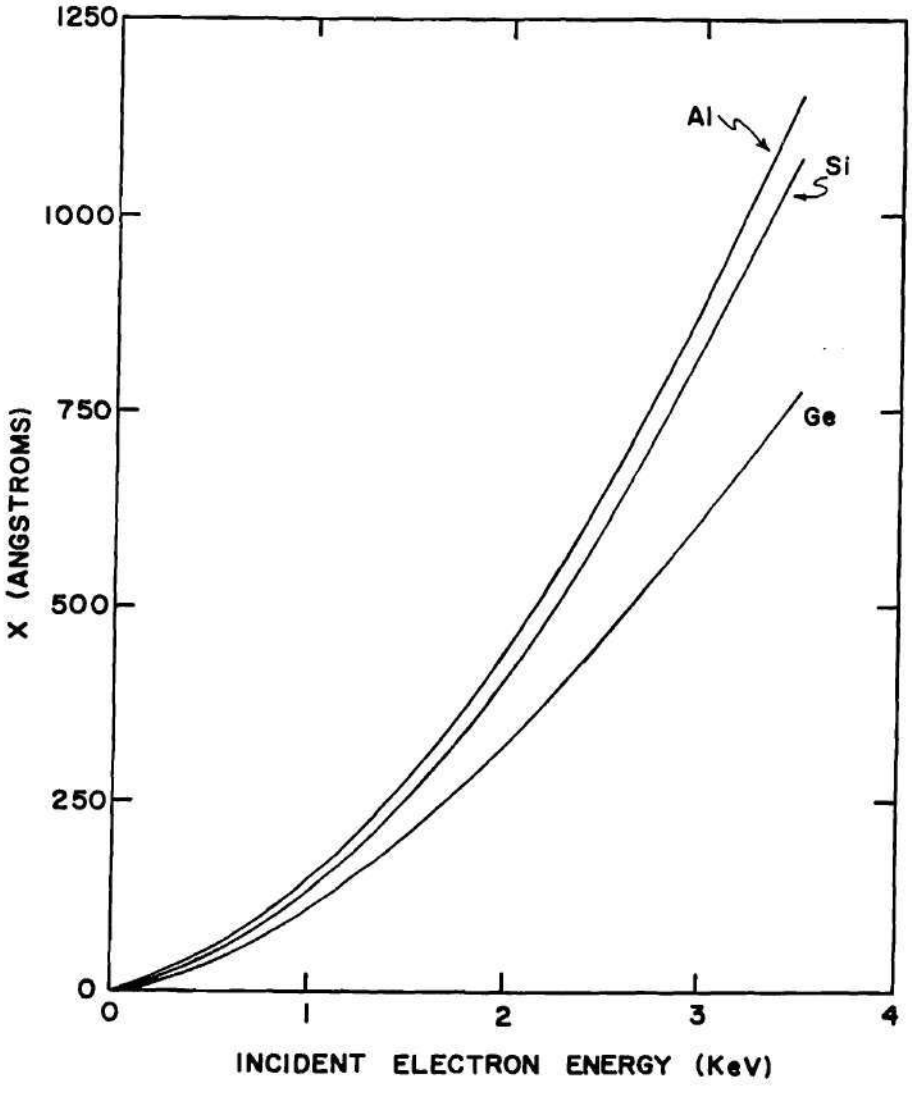

Figure 32. Characteristic Penetration Depth X as a Function of Primary Beam Energy for Several Materials.

where E_x is their energy at depth x, and E_o and N_o characterize the incident beam. The distribution function is

$$g(N_o, E_o, x, \xi) = N_o pnx^p \frac{\xi^{n-1}}{E_o(1-\xi^n)^{p+1}} \exp - \left(\frac{x}{1-\xi^n}\right)^p . * \tag{18}$$

Makhov plotted this function for a number of interesting cases. For x = 0.1, a typical case, the distribution function shows a sharp peak at $\xi = 0.9$ and is down to one-tenth of its peak value at $\xi = 0.70$ and 0.95. Therefore, almost all of the electrons have lost some energy and a few ($\sim$10%) have lost a great deal of energy, more than $0.25\ E_o$.

The energy loss suffered by the beam may be investigated by computing the mean energy $\bar{E}_x$ at depth x.

$$\bar{E}_x = W/N_o\eta \tag{19}$$

where W represents the total energy of the electrons at depth x (that is, after passing through a film of thickness x). W must be given by

$$W = E_o \int_0^1 \xi\, g(N_o, E_o, x, \xi)\, d\xi . \tag{20}$$

This integral may be reduced by integration by parts and then evaluated numerically. The result is conveniently expressed in terms of the normalized mean

* The English translation of Makhov's paper incorrectly omits the negative sign in the argument of the exponential function.

energy $\bar{\xi}$,

$$\bar{\xi} = \bar{E}_x / E_o . \tag{21}$$

Makhov evaluated this expression for a number of cases and determined that, for the substances shown in Table 1, the mean energy could be expressed by

$$\bar{\xi} = \exp(-Ax^s) \tag{22}$$

with a maximum error of two per cent over the range $0 < x < 2$. Here a and s are constants, also given in Table 1. Both are equal to or slightly less than one.

The absorption of energy from the beam is now easily computed. Continuing with normalized variables, the energy remaining in the beam at depth x is $\eta(x)\,\bar{\xi}(x)$, so the fractional energy absorbed w(x) is

$$\begin{aligned} w(x) &= 1 - \eta(x)\,\bar{\xi}(x) \\ &= 1 - \exp(-x^p)\exp(-Ax^s) \quad . \end{aligned} \tag{23}$$

The relative energy loss per unit depth $z = xX$ is

$$\frac{dw}{dz} = \frac{dw}{dx}\,\frac{dx}{dz} \tag{24}$$

using the chain rule.

$$\frac{dw}{dx} = [\exp(-x^p)]\,[\exp(-Ax^s)]\,[px^{p-1} + ASx^{s-1}] \tag{25}$$

Using typical values $A = 1$, $p = 2$, $S = 1$,

$$\frac{dw}{dx} = (\exp - x^2)(\exp - x)(2x + 1) \tag{26}$$

Since $x << 1$ in the region of interest, the Auger escape volume, the first two terms of the Maclaurin expansion for the exponential are sufficient. Recall that $X = CE_o^n$ and typically $n = 1.5$. With $z << X$,

$$\frac{dw}{dz} \approx \frac{1}{CE_o^n} \quad \frac{Z}{C^2 E_o^{2n}} \tag{27}$$

The absolute energy absorption per unit depth z is

$$N_o E_o \frac{dw}{dz} \approx \frac{N_o}{CE_o^{0.5}} + \frac{zN_o}{C^2 E_o^2} \tag{28}$$

and this expression is seen to be proportional to N_o, as expected, but the absolute energy less per unit depth decreases as the energy of the primary beam is increased. The beam is seen to "pass on through" the escape volume more easily as the primary energy is increased. The macroscopic model is therefore similar to the microscopic model in that both predict that the Auger yield will decrease with energy at sufficiently high beam energies. The exact behavior of Auger yield with primary beam energy depends on the individual ionization cross sections involved.

Since the above discussion has been quite extended, a summary is worthwhile.

1. Consideration of the scattering and energy loss equations of Everhart and

Hoff shows that angular deflection of the primary beam is important.

2. Jonker shows that electrons with energies in regions II and III of Figure 2 are isotropically distributed. The energetic secondary source function is thus isotropic.

3. The secondary electron cascade results in a distribution of secondaries in energy as $1/E^2$.

4. Makhov's work shows that while most primary electrons pass through the Auger escape region, most do lose a portion of their energy in the escape region. That essentially all of the electrons have suffered some energy loss, means that essentially all of the electrons are scattered within the escape volume. The energy loss within the escape region decreases at high beam energies which means that, when the behavior of Auger electron yield with energy is accounted for, the Auger response will decrease at sufficiently high beam energies.

5. The measured Auger response as a function of incidence angle does not follow the Bishop and Rivière theory, Equation 9, although some peaking at grazing angles is often noted. Thus a combination of oriented and isotropic sources is necessary to account for the observed behavior as a function of incidence angle.

The backscattered flux of electrons expresses the influence of the substrate on the generation of Auger electrons. The best available data are by Bishop, who performed Monte Carlo calculations on electron scattering in thick targets.[45] A screened Rutherford cross section was used to represent elastic scattering

and inelastic scattering was represented by a continuous loss Bethe equation, similar to Equation 10. The backscatter coefficient η_b and the energy distribution of these electrons are of interest. Table 2, taken from Bishop, shows the variation of the backscatter coefficient with atomic number for 10 keV and 30 keV electrons at normal incidence. For a given primary energy, η_b is seen to increase with atomic number. For a given atomic number, η_b decreases with primary energy at low atomic numbers but increases at higher atomic numbers. Bishop measured for carbon η_b = .06 at 30 keV and .07 at 10 keV. The present author obtained .08 at 1800 eV and 0.1 at 600 eV. Thus the general behavior of the backscatter coefficient holds over a wide energy range.

The mean energy loss for backscattered electrons varies smoothly with atomic number, decreasing with higher atomic number. Bishop calculated a mean energy loss of 45% of the primary energy for carbon and 25% for silver at 30 keV. He remarked that both calculated and experimental values are similar at 10 keV, so it may be assumed that the same behavior is present at lower primary energies. Summarizing, materials with higher atomic number backscatter more electrons, and these backscattered electrons have suffered less mean energy loss.

Backscattered electrons may be included in both models in a straightforward fashion. Bishop calculates that the most probable angle for the backscattered electrons from a normal beam is 135^{o} with respect to the incident beam. The Bishop and Rivière model applies the Worthington-Tomlin cross section across the energy distribution of the backscattered electrons and corrects

Table 2. Experimentally Determined Electron Backscatter Coefficients. From Bishop.[45]

Z	10 keV	30 keV
6	0.072	0.060
13	0.171	0.155
22	0.268	0.254
29	0.339	0.319
47	0.420	0.420
79	0.501	0.521

for the implied path length. This result varies from about 1.1 for a low atomic number (Z = 6) to 1.9 for a moderate atomic number (Z = 29), and increases little for higher atomic numbers. The macroscopic model utilizes the backscatter coefficient and mean energy from the calculations by Bishop to describe an isotropic source.

The above discussion has shown the need to consider the source function carefully when interpreting Auger spectra. A useful, and general, method of handling the source function description is to postulate a set of elementary source functions which can be summed, with appropriate weighting functions, to form an approximation to the source function of the experiment. The following postulated set is based on the theoretical models for the interaction of the electron beam with the solid, and on experimental results in the literature and obtained in this

work.

The source function is defined when the energy distribution of the electron flux incident on each elemental volume of the Auger escape region is known. The source function is written as the weighted sum of primary electrons, energetic secondaries, and backscattered electrons. Strictly speaking, these sources are sufficient (more than necessary), and therefore not independent; for example, there is strong correlation between the number of secondaries and the backscattered flux for any given material, since both quantities are the result of the scattering properties of the material. Thus there is no unique description of the source function. On the other hand, the variety of materials encountered in practical Auger spectroscopy is so great that having these source functions is useful and convenient, since each function is closely related to well known material characteristics.

The primary electron flux is characterized by an energy distribution equal to that of the incident beam, that is, N_o electrons per second with energy E_o. The angular distribution varies with path length in the solid. Through the first few monolayers the beam is oriented the same as the incident beam. The beam spreads out because of scattering until, at some characteristic distance, it may be considered isotropic. For convenience this characteristic distance may be taken equal to X, the characteristic penetration depth computed by Equation 16. Notice that this spreading of the beam may take place completely within the Auger escape region for grazing incidence beams. Essentially no spreading takes place within the Auger escape region when the beam is directed normal to the surface.

The energetic secondaries have an energy distribution proportional to $1/E^2$. While these secondaries are initially oriented in the same general direction as the primary creating them, scattering soon results in an isotropic distribution. For convenience the angular distribution is therefore taken as isotropic.

The number of electrons in this secondary cascade must be estimated. The behavior of Auger yield as a function of incident beam angle suggests that this source is of the same order of magnitude as the primary beam for a homogeneous specimen. Wolff sets the total energy between 100 eV and E_o equal to the primary beam energy.[43] Following his example, the energy distribution becomes

$$N_o E_o/[E^2 \ln(E_o/100 \text{ eV})] \text{ amperes/eV}$$

and the distribution extends from 100 eV to E_o. This is obviously only an educated guess which will be refined by later work. The nature of the distribution, increasing at lower energy, means that the source will be more important for ionizations requiring less energy. Also, this source will not be as important when glancing incident beams suffer significant reflection off of the top monolayer, because the origin of the secondary cascade is the inelastic scattering of the primary beam within the solid.

As an example, the number of secondaries N_s in the cascade for a 100 eV beam is

$$N_s = \int_{100}^{1000} 1000\, N_o/(E^2 \ell n\ 10)\, dE \tag{29}$$

$$N_s = 9\, N_o/\ln 10 = 3.9\, N_o. \tag{30}$$

The backscattered flux is characterized by mean energy, rather than actual energy distribution, because the former is available from Bishop[45] and the latter is not generally available. Meyer and Vrakking[39] have reported some results on backscattered energy distribution but the additional accuracy is probably not warranted by the additional complexity. This mean energy is shown in Figure 33, taken from Bishop. This source may be regarded as originating from an isotropic emitter in the substrate, with amplitude given by the backscattering coefficient times the primary beam amplitude.

A typical total source function is shown in Figure 34. The backscattering coefficient was assumed to be 0.2 and the mean energy of the backscattered electrons was taken as 70% of the primary beam energy. This source function must be multiplied by the Auger electron yield and integrated over the Auger escape region which is bombarded, taking into account the escape probability for each elemental volume. This calculation yields the number of emitted Auger electrons; multiplication by detector efficiency gives the measured Auger current.

Auger Electron Yield

This section describes the relationship between the source functions, the energetic electrons in the solid, and emission of Auger electrons by an atom. The probability that these Auger electrons will escape the solid with their energy intact is discussed in the following section. This treatment of Auger yield considers three factors: ionization cross section, numerical density, and the influence of chemical bonding.

Ionization cross section Φ and numerical density N of the scattering centers

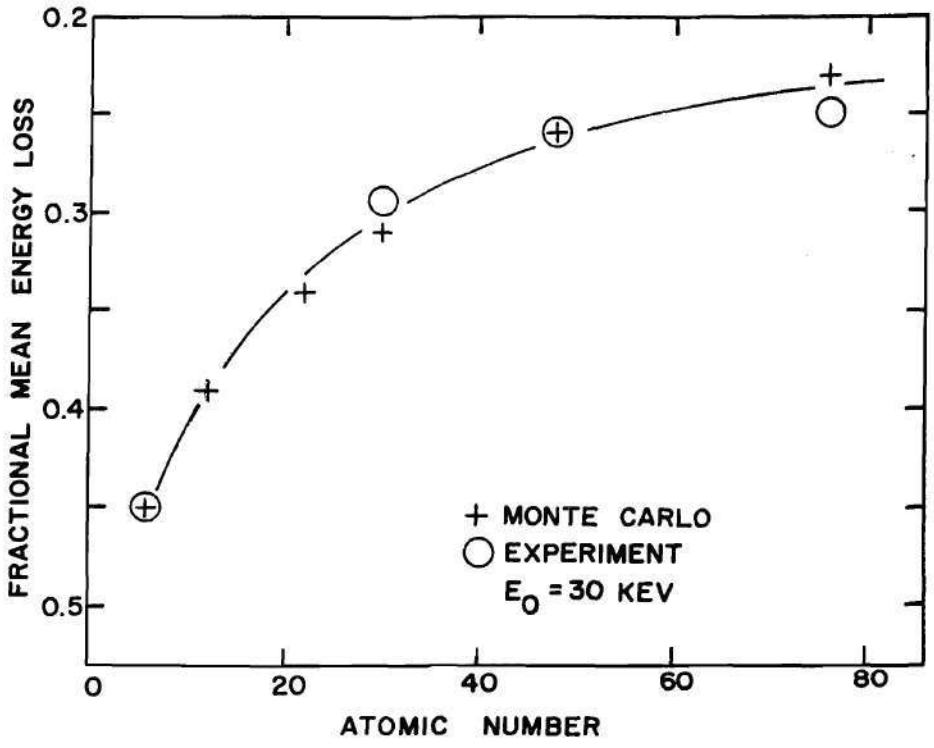

Figure 33. Fractional Mean Energy Loss for Backscattered Electrons, from Bishop.[45]

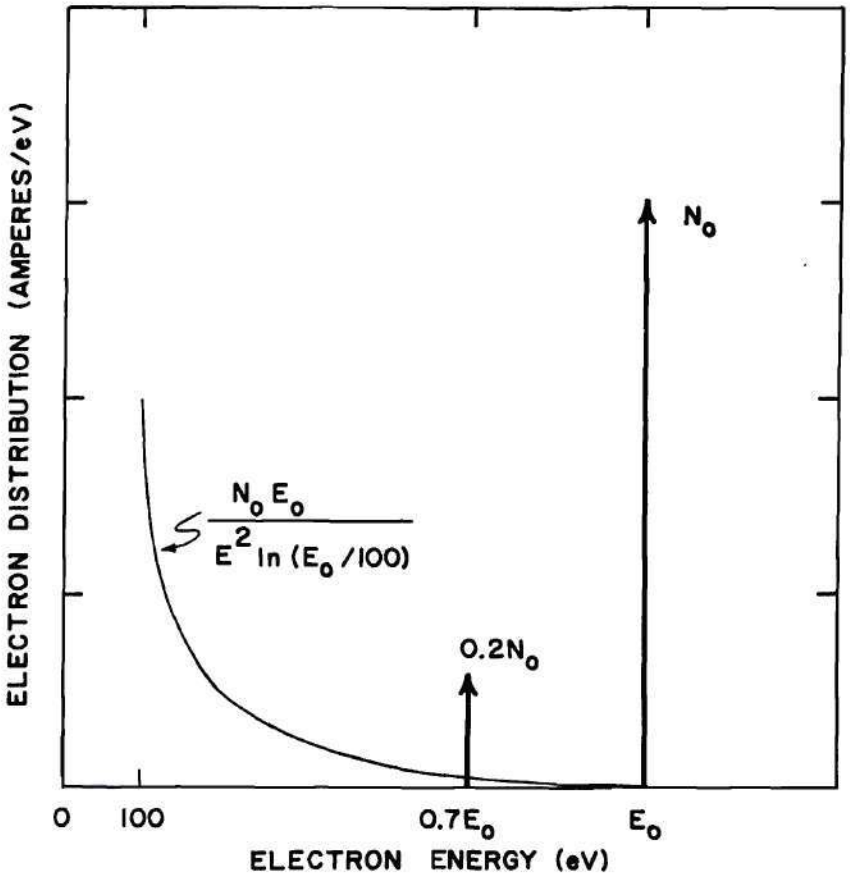

Figure 34. Example of Total Source Function for Ionizations.

(atoms) determine the probability P that an electron passing through a layer in the normal direction will cause an ionization. The cross section normally has units cm^2 and the numerical density of the scattering centers in the layer has units cm^{-2}. The probability is given by the product

$$P = \Phi N . \tag{31}$$

This relationship holds for layers sufficiently thin so that the atoms scatter incoherently and there is no multiple scattering of the primary electron. The cross section is determined for layers a monolayer or less thick. Since the numerical density of a monolayer is approximately 10^{15} atoms/cm^2, and the cross section is of the order of 10^{-19} cm^2, the probability of an ionization by a primary electron of typical energy passing through a monolayer is very small.

The cross section Φ is obviously a function of both the energy of the primary electron, the source electron, and the binding energy of the shell electron, the ejected electron. This functional dependence is simplified by introducing the normalized energy variable U,

$$U = E_o/E_W \tag{32}$$

where E_W is the binding energy of the shell electron and E_o is the kinetic energy of the source electron. The approximation used for computing Φ in the Auger literature is the Worthington-Tomlin approximation, as described by Bishop and Rivière.[5] Other available approximations have recently been discussed by Meyer and Vrakking.[39] The expression given by Bishop and Rivière is

$$\Phi = 1.3 \times 10^{-13} b(1/UE_W^2) \ln\{4U/[1.65 + 2.35 \exp(1-U)]\} \text{cm}^2 \qquad (33)$$

where E_W is expressed in electron volts, and b is a parameter assigned the value 0.35 for K shell electrons and 0.25 for L shell electrons. This formula was the basis of the probability of ionization curve shown, without a scale factor, in Figure 4.

The most relevant comment about this expression for ionization cross section is that reported Auger yields as a function of primary beam energy typically show a behavior similar to Figure 4 but the maximum occurs at a higher value of U. The implication is that other factors, besides the ionization cross section, enter into the Auger yield as a function of primary beam energy. The primary factor is the scattering of the primary electrons and the resultant secondary sources. Another factor is likely the approximate nature of the cross section expression.

The numerical density N is for one monolayer, as stated above. The extension of Equation 31 to a specimen made up of many monolayers requires that the scattering of the primary beam be taken into account. Consider the case of a monolayer adsorbate on a substrate, with the problem being to compute the probability of ionization as the primary electron passes through the adsorbate monolayer at other than normal incidence. As discussed in the previous section, Bishop and Rivière modify their probability equation, similar to Equation 31, by csc ϕ where ϕ is the angle of incidence of the primary beam. This results in a singularity at grazing incidence. This singularity is not observed in practice.

Grazing incidence corresponds to many monolayers when measured along the path of the incident electron. The angular scattering of the beam must be included in the model to achieve agreement with experiment.

Another ramification of Equation 31 is that single crystal specimens may show different yields for source electrons which see different densities along various crystallographic axes. This effect was not observed in this work, however. The specimens were amorphous, with the exception of the silicon used in the oxidation work; also one would expect the isotropic nature of the source functions to reduce any crystallographic influence in single crystal specimens.

To compute the total number of ionizations per second, one multiplies the source function, with units electrons per second, by the ionization probability P. P describes the probability that an electron passing through a layer in the normal direction will cause an ionization. Some method must be specified to handle the effect of an angular distribution in the source functions. Consider the secondary and backscattered source functions first. These are specified as isotropic. This means that these sources are independent of the incident direction of the primary beam, as long as there is not significant reflection of the beam at grazing angles. Therefore the effect of these sources is the same as a flux of electrons normal to the layer, with the appropriate amplitude weighting function. The weighting function is set equal to one in this work; on the other hand, Bishop and Rivière argue that $\sqrt{2}$ be used to account for the longer paths of electrons traveling in directions other than normal to the layer. The rationale behind the choice of one as the weighting function is that the source function

itself should relate the number of energetic electrons within the layer to the primary beam characteristics, with material characteristics as parameters.

The primary electron flux is not an isotropic source until it has passed through a considerable amount of material. This source is relatively more important at grazing angles; however, scattering of the beam prevents one from having a singularity at grazing incidence. Reference to the figures in the calibration spectra section shows that there is considerable variation in the Auger response as a function of incidence angle. Thus one must rely on calibration spectra taken at the desired angle of incidence. These calibration spectra determine the angular weighting function to be applied to the primary beam source in each case.

The final implication of Equation 31 is that the Auger response should be linear in coverage for sub-monolayer absorbate coverages. This result has been verified by a number of workers, most recently by Meyer and Vrakking.[39]

The expression for ionization cross section shows no dependence on atomic number or on the chemical state of the atom. The dependence on atomic number has been suppressed, or compensated for, by the introduction of the normalized energy variable U. The influence of chemical state has been largely unexplored. There is some evidence that the chemical state has a non-trivial influence on the probability of Auger emission.[39] This dependence arises when the remainder of the Auger process is considered. Given a vacancy at the E_W level, the probability that neutralization will be by the Auger process must be known. Bishop and Rivière consider photon production as the only alternative to Auger

neutralization. They compute the probability of photon production as approximately 0.03 for both K and L shell ionizations. Bishop and Rivière, Meyer and Vrakking, and others following the same theory therefore take the probability of Auger emission as essentially the same as K or L shell ionization.

On the other hand, work in the field of electron stimulated desorption, a subject discussed in the following chapter, has shown that the neutralization of a vacancy may result in a metastable state, rather than a direct return to the ground state via an Auger neutralization of the lower vacancy and some other relaxation process for the upper level vacancy. Electron stimulated desorption of the atom itself is an alternative to Auger neutralization. Both of these alternative neutralization processes are sensitive to chemical bonding. Experimental evidence of the influence of chemical state is scarce and difficult to obtain because one needs an independent method of determining the concentration of the species in question, besides the Auger technique. Meyer and Vrakking used ellipsometry to determine adsorbate coverages and correlated these results with the indicated Auger yield. They found that the response for oxygen, when in the form of adsorbed water vapor, is about one half as great as when in the form of SiO_2. One might explain this difference as resulting from scattering of emitted Auger electrons by the hydrogen atoms in the adsorbed water case. However, the scattering cross section of hydrogen should be very small because of its low atomic number and size. Furthermore, there was no variation in relative yield with emission angle reported by Meyer and Vrakking. Meyer and Vrakking chose to explain the variation in yield with a shielding argument, which states that the hydrogen atoms are arranged so

as to shield the oxygen atoms from the source electron beam. This argument is not valid for the same reason: hydrogen is not an effective scatterer of energetic primary electrons, and in no case is one monolayer going to attenuate the primary beam by a factor of two. A more plausible explanation is excitation of a metastable state or desorption of the water vapor as competing processes.

A similar phenomenon was noted in this work. Graphite was studied in an unbaked vacuum chamber. The partial pressure of water vapor was therefore in the low 10^{-8} torr range. One would expect, based on experience, a fractional monolayer of water vapor adsorbed on the graphite. The water vapor coverage can not be computed from available adsorption data because this was not a single crystal specimen; indeed, the specimen was graphite adsorbed on a graphite substrate. The oxygen Auger peak was barely visible in the spectrum. The Auger indicated coverage was less than 0.01 monolayers. On the other hand, mass spectroscopy showed that water vapor was being desorbed from the surface in substantial amounts. While these results are obviously qualitative, they do suggest that competing neutralization processes should be studied further. Electron stimulated desorption and this experiment are discussed further in the following chapter.

Two conclusions from this section deserve reiteration. First, Auger emission is linear with density for monolayer, or less, coverages, where the layer is measured in a plane normal to the direction of the source electron. Secondly, the ionization cross section is an important factor in determining the energy dependence of Auger yield, but it is not the only factor. The influence of scattering of

the source electrons must also be considered.

Escape Probability

The problem of computing the probability of escape for an Auger electron is one of the most important facing the Auger process theorist, and is also one of the most difficult. One would like to know the probability that an electron, excited to some energy level at a given point within the solid, will escape the solid without suffering a significant energy loss. The allowable energy loss is a function of the true shape of the Auger peak. The extent to which observed Auger peak shapes are influenced by random losses is not well established. It is true that many Auger peaks are broadened on the low energy side, for example, carbon and silicon. On the other hand, there was no experimental evidence obtained in this work that the observed peak shape is affected by random scattering, although the amplitude obviously is changed. For example, the silicon peak is merely attenuated when there is a graphite overlayer. Thus the problem is to explain the attenuation of Auger current by the host solid as a function of the energy of the Auger electron. The possible theoretical approaches will be described first, and then the empirical approach.

The most basic approach is to list each of the possible interactions, e.g., intraband transitions, interband transitions, Umklapp processes, etc., compute the transition probabilities, and sum the effects. Tharp[46] and Amelio[11] have studied the interactions of slow electrons with a solid on this basis. While these studies are instructive in the nature of the electron-solid interaction, they have

not yet yielded numerical data which can be used to deduce the composition of a specimen, given its Auger spectrum. Obviously, mathematical complexity forces the use of simplifying assumptions in the description of each process, and the relative weighting assigned to each process must be experimentally determined.

The nature of the slow electron-solid interaction may be summarized as follows. The range of electron energies under consideration is from 50 eV to, say, 500 eV. The penetration of the slow electron through the solid is very slight because of large cross sections for both elastic and inelastic scattering. These cross sections have a maximum near 100 eV, but vary slowly with energy. These cross sections are both qualitatively and quantitatively different from those of high energy electrons and X rays. Lander[47] has shown that the elastic cross section for electrons with energies similar to 100 eV is of the same magnitude as the area occupied by the atom in the lattice. Therefore a single monolayer is an efficient scatterer of Auger electrons. This is in agreement with measured escape depths for Auger electrons; these depths are a few monolayers, two to four being the typical range. Multiple scattering is likely, which implies that the angular distribution of Auger electrons which escape the solid is likely to be isotropic. Inelastic cross sections are also significant in this energy range. Lander reports energy losses as high as 50 per cent per atomic layer in this energy range. These heavy energy losses, coupled with the elastic scattering, lead to the small escape depths for Auger electrons.

Another approach would be to use the Bethe energy loss equation, Equation 10, which is a differential equation expressing the mean energy loss of an electron

passing through a solid. There are two objections to this method. The assumptions on which the equation is based are valid only if the energy E is large compared to the binding energies of the outer shell electrons of the atom. Everhart and Hoff[40] quote values above 1000 eV as being acceptable, which is outside the range of interest. A more basic objection is that one is trying to relate a change in mean energy, over the ensemble of electrons passing through the solid, to the probability that an electron will lose more than some specified amount of energy while transversing a particular path. Thus, one needs the distribution of energies after having the electrons transverse a path. The Bethe equation only gives the change in the mean of this distribution.

The work of Makov does give the energy distribution for electrons having passed through a solid. Unfortunately these results are based on measurements of electrons in the kilovolt energy range and do not scale to energies of concern. For example, for the 92 eV silicon Auger electron, the characteristic distance X is about two angstroms. The energy distribution for electrons passing through a solid of thickness X shows essentially no electrons which have lost less than 25 per cent of their energy. Thus the escape depth for silicon Auger electrons would be less than a monolayer by this theory, an unrealistically low number. For silicon the formula for X is based on measurements for electrons with energies greater than 1000 eV. The necessary measurements for lower energy electrons are very difficult and have not been performed. Since the formula is a fit to experimental results, there is indeed no reason to expect it to apply for an energy range an order of magnitude lower.

The most fruitful approach is to use available theory to formulate a qualitative model and then to quantify the model with experimental data. The three factors to be considered are the energy of the Auger electron, the scattering characteristics of the solid, and the angular distribution of the electrons which escape the solid without significant energy loss.

Five papers have made significant contributions in this area. Palmberg and Rhodin[24] made the first measurements of escape depth by correlating low energy electron diffraction and Auger yield measurements. Gallon[37] and Seah[36] have recently reported additional measurements of escape depth. Harris[16] reported both theoretical and experimental work on escape depth and the angular distribution of Auger electrons. Meyer and Vrakking[39] have also made measurements of the angular distribution of the Auger electrons.

The theory is based on the assumption that the loss of Auger electrons by inelastic scattering per unit path length s is independent of the path length, per se, but is dependent on the energy of the Auger electron and the constituents of the solid. If this loss per unit path length is called k, then k is a function of the material and the energy E_A of the Auger electron, but not of path length s. The transmission factor T is then given by

$$T = \exp(-ks). \tag{34}$$

The fraction 1/k is called the inelastic mean free path in the literature.

The relationship between path length s and depth z in the material must be must be known for the Auger electron. If elastic collisions are assumed

unimportant, then a geometric argument shows that

$$s = z \sec \theta \tag{35}$$

where θ is the angle of emission with respect to the surface normal. This assumption is used by Harris[16] and Seah.[36]

There are two objections to this assumption. First, the work of Lander[47] showed that elastic collisions are important in the energy range about 200 eV. The justification for ignoring elastic collisions in this energy range is based on extrapolation of formulas, such as presented by Everhart and Hoff,[40] which are valid only at keV energies. By comparison, the conclusions of Lander are based on low energy electron diffraction studies within the energy range of interest. Second, the experimental work of Meyer and Vrakking[39] did not show a strong variation with angle as the detector position was changed. A strong variation in T occurs for values of θ close to 90 degrees when Equation 35 is used. On the other hand, the inclusion of elastic scattering in the model results in a more isotropic like angular distribution.

The model utilized in this work is based on the above arguments. Consider the simplest possible relationship

$$s = \alpha z \tag{36}$$

$$\alpha > 1 \tag{37}$$

where α is, at most, a function of energy and material. This function is attractive for several reasons. It preserves the exponential relationship between the

depth of the emitting atom and the probability of transmission. This exponential relationship has been experimentally verified by Seah.[36] The inclusion of the parameter α offers a mechanism by which the mean free path $1/k$ may be longer than the mean escape depth $1/k\alpha$. Finally, it yields an isotropic distribution of Auger electrons, since the emission distribution is assumed to be isotropic. Therefore, the transmission factor is

$$T = \exp(-k\alpha z). \tag{38}$$

The fraction $1/k\alpha$ is the "film thickness" reported by Seah. Palmberg and Rhodin[24] and Seah[36] have performed experiments on a few materials to determine representative escape depth data. These experiments are based on sequentially covering the substrate by an evaporated adsorbate. These experiments are characterized by significant scatter in the data because of the difficulty in accurately measuring the deposited film thickness and the tendency of many evaporated materials to form uneven layers. Therefore, the realistic approach is to make a best estimate of $1/k\alpha$ based on the available theoretical and experimental information, recognizing this estimate will be improved in time. This estimate is shown as the interpolation line of Figure 35. The data points are from Seah's work on a variety of materials. Seah explains the experimental procedures and causes for the data spread in considerable detail; the interested reader is referred to his work for further discussion.

The film thickness $1/k\alpha$ is expressed in monolayers rather than angstroms. This is an attempt to account for material effects, since the Auger electron will

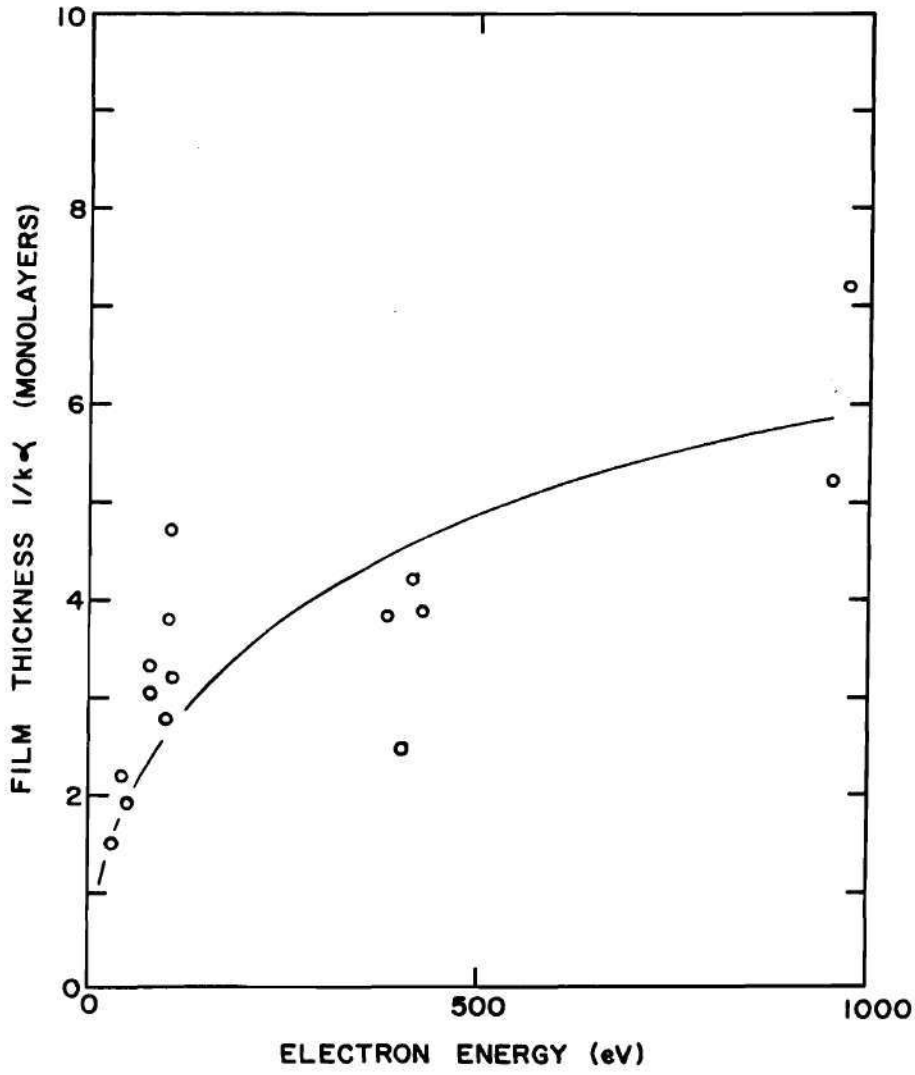

Figure 35. Film Thickness $1/k\alpha$, from Seah.[36] Interpolation Line has been Added to Seah's Data for Use in Calculations.

see roughly the same numerical density of scattering centers per monolayer with different materials. The limited amount of data available does not justify a more detailed accounting of material effects.

Detector Efficiency

The acceptance angle of the analyzer, transmission factor of the analyzer, misplacement of specimen, modulation voltage on the analyzer, and gain of the amplifiers determine the sensitivity of the retarding grid analyzer system. Knowledge of these factors enables one to quantitatively compare spectra from different spectrometers.

The acceptance angle of the analyzer used in this work is $2\pi/3$ steradians. The transmission factor for the grid system is 0.52. Comparison with other spectrometers will require correction for the relative acceptance angle and transmission factor.

Misplacement of the specimen will affect both the sensitivity and the resolution of the spectrometer. Specimen placement is particularly important when using a grazing incidence electron gun because the bombarded area tends to be rather large as the beam intersects the surface at grazing angles. The tolerance on specimen position is larger when using a normal incidence gun; a few millimeters or so from the optimum position is satisfactory. This inherent tolerance of the analyzer is used up by the spread of the grazing incidence beam. Sufficient care was exercised in this work to obtain spectra not limited by specimen misplacement.

A second form of specimen placement problem occurs when the specimen is rotated to obtain a desired primary beam incidence. The two electron guns utilized were mounted at right angles so that, when the specimen is in its standard position, the incident beam angles are $\phi = 90^{o}$ and $\phi = 0^{o}$. Other incidence angles are obtained by rotating the specimen. Rotating the specimen obviously changes the location of the analyzer relative to the emitting surface. Knowledge of the angular distribution should allow one to compute the effective acceptance angle, but in practice there are instrumental problems which complicate the issue. These include shadowing by the specimen holder and shadowing by the drift tube of the normal incidence electron gun. Therefore, the correction factor utilized in this work was determined by measuring the slow secondary peak amplitude as the specimen was rotated. A maximum of 45^{o} rotation is sufficient to realize all incidence angles with the orthogonal electron guns. Over this angular range it is known that the slow secondary peak if independent of the primary beam incidence angle. Figure 36 shows the resulting correction factor. Multiplication of the measured peak height by this correction factor yields the peak height which would have been obtained with an analyzer centered around the surface normal. The data on which this figure is based were taken on a graphite specimen with 2000 eV beam energy. Essentially the same results were also obtained on molybdenum and at lower beam voltages. All data reported in this work have been modified by this correction factor.

The amplitude of the perturbation voltage placed on the retarding grid also affects the calibration of spectra. The procedure adopted in this work was to

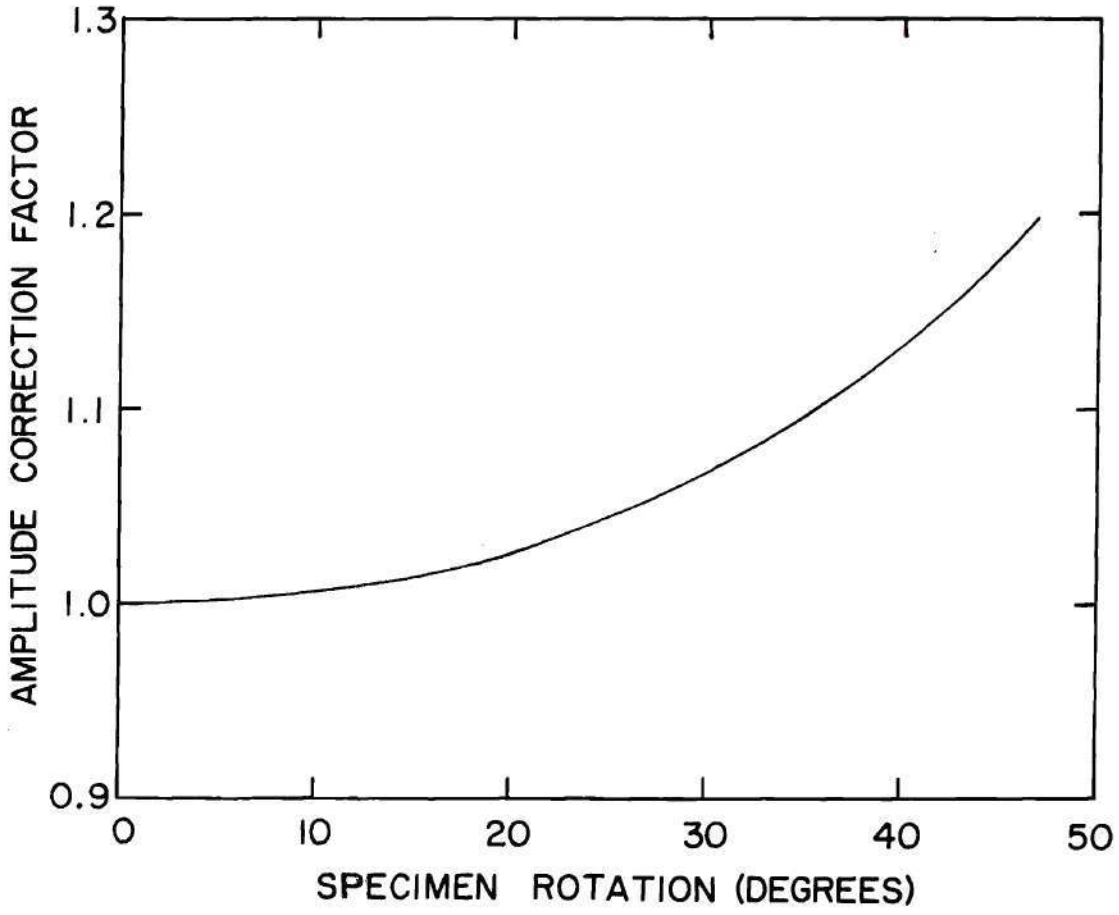

Figure 36. Correction Factor for Auger Peak Height to Account for Specimen Rotation.

limit the perturbation amplitude to that range where the amplitude of the Auger peak was proportional to the square of the perturbation amplitude. For peaks with energies less than 100 eV, the perturbations used were less than 1 volt RMS; for the 100-200 eV range, amplitudes less than 2 volts RMS were normally used; and, for energies greater than 200 eV, amplitudes were less than 3 volts RMS. Whenever accurate peak amplitude data were required, the effect of perturbation amplitude was checked by using a lower amplitude and noting whether the square law behavior was followed. The trade-off is always between resolution and sensitivity: the lower perturbation amplitudes give a more highly resolved peak and better adherence to the square law behavior, but at a sacrifice in signal to noise ratio.

The scale factor for Auger spectra taken in this work reflects the perturbation voltage and electronic amplification used. Other factors, such as the influence of primary beam current, beam energy, or angle of incidence must be accounted for separately. The scale factor is shown on the spectra as the distance between two arrowheads. Since these spectra are derivative plots, the scale factor applies to height of the peak, with the absolute position in the ordinate direction unimportant. The primary beam energy, beam current, angle of incidence, and the specimen type are listed on each spectra for reference purposes. A normalized peak height is obtained by dividing by the primary beam current.

There is a one to one correspondence between retarding potential, expressed in volts, and electron energy, expressed in electron volts, with the retarding grid analyzer. Therefore, the analyzer collector current may be written as a function

of energy E from Equation 5 as

$$i(E) = i(E_o) + \frac{di(E_o)}{dE} A \sin \omega t + \frac{d^2 i(E_o)}{dE^2} \frac{A^2}{4} (1 - \cos 2\omega t) \qquad (39)$$

where a sinusoidal perturbation is assumed. If G(E) represents the Auger spectrum, with units amperes per eV^2, then

$$G(E) = \frac{d^2 i(E_o)}{dE^2} . \qquad (40)$$

The coefficient associated with $\cos(2\omega t)$ is $A^2 G(E)/4$; this coefficient is the quantity measured by the synchronous detector (lock-in amplifier). Therefore, if $I(2\omega t)$ represents the second harmonic current, coherent with the reference signal, measured by the synchronous detector, the Auger spectrum is given by

$$G(E) = 4I(2\omega t)/A^2 \qquad (41)$$

where A is the amplitude of the perturbation, measured in volts. The gain of the preamplifier-synchronous detector used in this work is 1 volt dc output per 10^{-8} amperes RMS coherent input, with the total voltage gain of the pair set at x1. The maximum gain is limited only by noise considerations; it is approximately x1000. For a three second time constant on the output filter, the output noise is about 0.1 volt. This thermal noise is sufficiently low so that the system becomes shot noise limited when the primary beam is turned on. If the perturbation amplitude A is measured in volts RMS, then a one volt output from the synchronous

detector corresponds to $2\sqrt{2} \times 10^{-8}/A^2_{RMS}$ amperes per eV^2, when the voltage gain is set at x1.

Surface Morphology

This last section of the sequence describing basic factors is concerned with surface morphology, that is, the structure of the surface. The previous sections have assumed a specimen composed of idealized monolayers. It was assumed that the solid-vacuum interface was accurately described by a plane. This condition will be relaxed and the effect of having a rough surface will be examined.

The most obvious influence of a rough surface is on scattering of the primary beam, particularly at grazing incidence. Protuberances on the surface will shadow the remaining surface. This effect can be quantitatively important when the shadowed area becomes an appreciable portion, say 10%, of the total surface area. Electron microscopy must be used to estimate the shadowed area for any given angle of incidence. Once the average height, width, and density of the particles, or protuberances is known, it is only a geometry problem to estimate the portion of the surface shadowed.

Scanning electron microscopy was used to determine the morphology of the transistor wafer specimens examined by the Auger technique. These surfaces were smooth, that is, featureless, within the 150 angstrom resolution of the microscope except when silicon carbide particles were present. This case is discussed in Chapter VII. The effect of shadowing was important at grazing

incidence in this case because the protuberances, the silicon carbide particles, were of a different composition than the remainder of the surface, which was silicon or silicon dioxide. Thus, quantitative interpretation of spectra requires a knowledge of the spatial distribution of the constituents.

A second aspect of the scattering problem is that often at grazing angles enough of the primary beam is reflected back out of the specimen that the Auger source function is reduced. Specular reflection of the primary beam was noted on both graphite and silicon specimens at angles greater than 83 degrees from the surface normal. This behavior is analogous to the scattering of electromagnetic waves from rough surfaces,[48] where the Rayleigh criterion shows that a surface behaves as if it were smooth as either the ratio of protuberance height to wavelength becomes small, or the angle of incidence becomes grazing.

The quantitative effects of scattering the beam back out of the solid at grazing angle are difficult to estimate since the degree to which the beam interacts with the solid is not known. That is, the ionization effectiveness of these electrons scattered back out of the specimen is not known. When treating the scattering problem with normal incidence, it was reasonable to separate scattering phenomena into two classes: elastic and inelastic. The separate effects of these scattering events are summed over the path of the electron in the solid. The treatment of the grazing incidence case is more difficult since the reflected electron is likely to suffer only one collision with the solid; both the angular deflection and energy loss of this one collision must be modeled. This modeling problem was not solved

in this work. Rather than estimate the effects of grazing angle scattering analytically, measurements of the Auger response as a function of incidence angle were made close to grazing incidence. These results were shown in the section on calibration spectra. The result of these measurements is that the reflection of the primary beam is important only at angles greater than 80 degrees from the surface normal.

An attempt was made to correlate secondary emission and absorbed specimen current with Auger response at grazing incidence. Qualitative correlation was achieved, in that the specimen current decreased and the secondary emitted current increased as the incidence angle became grazing. Specimen current decreasing implies less interaction of the beam with the solid. Secondary current shows two opposing effects. The smaller interaction of the beam with the solid reduces secondary current. On the other hand, the secondaries are created in a region where their escape probability is much higher as the incidence angle becomes grazing.[51] Thus the secondary emission ratio is increased at grazing incidence. The net result is that the Auger response decreases more rapidly than secondary current but less rapidly than specimen current as the incidence angle is made grazing.

The final observation of the nature of primary beam scattering at grazing incidence is that the scattering of the beam is not due to the "potential" of the specimen, where "potential" refers to the bias voltage applied to a metallic specimen or the average potential of an insulator specimen as defined by the energy of emitted secondary electrons. Bias voltages to both conductor and insulator

specimens were varied over the range from -150 volts to +150 volts and there was no change in the Auger spectrum amplitude or shape. The implication is that the scattering is of the Rutherford type, that is, deflection of the electron because of the strong electrostatic field close to the nucleus.

Calculation Techniques

Two problems will be discussed in this section. The first is to compute the expected Auger peak amplitudes from the available theory, given a hypothetical specimen. The second is to interpret experimental results, given relevant calibration curves. In the latter case the majority of the factors influencing the Auger spectrum are determined experimentally, and it is only necessary to analytically account for a few of the factors.

Calculations of expected Auger current have been published by Bishop, et al.,[5] by Meyer, et al.,[39] and by Gallon,[37] among others. The calculation for the model proposed in this work will be outlined, because it serves as a useful summary to the previous sections. However, the utility of the model is not in computing a priori Auger spectra but rather in interpreting experimental results with the aid of calibration experiments.

1. Partition the surface volume according to the expected constituents; for example, one monolayer of graphite on a molybdenum substrate.
2. Compute the source functions. For example, let the primary beam be one microampere, 1000 eV, at normal incidence. The primary source function will be the beam passing through the Auger escape volume. This will be

$\sim 6.2 \times 10^{12}$ electrons per second at 1000 eV. The backscatter coefficient for molybdenum is, by interpolation of Table 2, about 0.4. The mean energy loss for these electrons is $0.275\ E_o$, by Figure 33. The backscatter source becomes 2.48×10^{12} electrons per second at 725 eV. The secondary source distribution, using the formula shown in Figure 34, is

$$\frac{2.7 \times 10^{12} \times 1000}{E^2} \quad \left(\frac{\text{electrons/second}}{\text{eV}}\right) .$$

These sources will be integrated with respect to energy in a later step. Let the total source function be S(E).

3. The probability of ionization is, from Equation 31,

$$P(E) = \Phi\ (E)\ N \tag{42}$$

where the numerical density of atoms N in each monolayer must be computed separately for each constituent.

4. The number of ionizations per second within each monolayer for the given source functions is

$$\int_o^{E_o} P(E)S(E)\ dE$$

5. Any correction for alternative neutralization processes is now applied. If all ionizations result in Auger emissions, the number of Auger electrons generated within each monolayer is known.

6. The escape probability is computed next. The transmission factor for Auger electrons generated at depth z is, by Equation 38, $\exp(-k\alpha z)$. This factor is used to compute an equivalent, isotropic, radiator of Auger electrons. Figure 35 gives $(1/k\alpha) = 4$ monolayers for the 272 eV carbon Auger electrons. Therefore,the top monolayer of graphite is equivalent to an isotropic radiator N_E, having no attenuation, with source strength

$$N_E = \int_0^1 \exp(-z/4)dz = 0.88 \text{ monolayers} \qquad (43)$$

For a 186 eV molybdenum Auger electron, the characteristic film thickness is 3.4 monolayers, from Figure 35. The molybdenum extends from the bottom of the first monolayer into the specimen. Therefore, the equivalent radiator is

$$N_E = \int_1^\infty \exp(-z/3.4)dz = 2.25 \text{ monolayers.} \qquad (44)$$

7. The integral of step 4 gives the number of Auger emissions per second for a monolayer, given the source function. The number of Auger electrons from carbon leaving the specimen surface per second is, therefore,

$$0.88 \int_0^{E_o} P(E)\, S(E)\, dE$$

and these are assumed to be isotropically oriented. Multiplication by the

acceptance factor of the analyzer and the transmission factor of the analyzer gives the number of Auger electrons collected per second. The acceptance angle of the retarding field analyzer used is $2\pi/3$ steradians. Since an isotropic source radiates into 4π steradians and the transmission factor for the grid system is 0.52, the collector current I_c should be

$$I_c = (2\pi/12\pi)(0.52)(0.88 \int_0^{E_o} P(E)S(E)dE) \qquad (45)$$

for the 272 eV carbon peak. A similar calculation must be made for the molybdenum peak.

8. The Auger spectrum is the derivative of the energy distribution, so the shape of the energy distribution peak determines the height of the Auger peak. I_c of step 7 gives the total current in the energy distribution peak. Once the peak shape is ascertained, either by assumption or by reference to standards, the Auger peak height is determined.

The more realistic problem is that of interpreting Auger spectra from complex specimens, specimens with many constituents. The accuracy of these interpretations is improved with the use of calibration spectra. The most useful calibration spectra are those of pure substances, that is, uncontaminated, taken under similar experimental conditions to those of the unknown specimen. Any ancillary data, such as electron micrographs or mass spectroscopy, that can be obtained should also be utilized. Since the specimen cannot be analyzed exactly using Auger spectroscopy, the goal is to minimize the uncertainty in interpretation by using as

much information as is available.

Given the reference spectra and the spectrum for the specimen, the interpretation technique is outlined below.

1. Partition the surface volume according to qualitative interpretation of the Auger spectrum and other knowledge of the specimen. For example, an Auger spectrum showing carbon and molybdenum would be modeled as a layer of graphite on the molybdenum, if the molybdenum was not expected to contain significant quantities of carbon as a bulk impurity. The interpretation problem is now reduced to estimating the thickness of the carbon layer.
2. Continuing with the carbon-molybdenum example, use the carbon reference spectrum to obtain the Auger peak height per unit of beam current for a bulk specimen. For the 272 eV carbon Auger electron, the equivalent radiator for a bulk specimen is

$$N_E = \int_0^\infty \exp(-z/4)\, dz = 4 \text{ monolayers}, \qquad (46)$$

from Figure 35. From Figure 30 the Auger peak height is 0.80 amperes/eV^2 for a 1200 eV, one microampere primary beam at normal incidence. Thus the carbon Auger peak height is 0.20 amperes/eV^2 for a one monolayer ($N_E = 1$) radiator and the given source function.
3. Correct for different source strengths utilized in the reference and specimen spectra. Peak heights are linear in primary beam current. If the angle of incidence and primary beam energy are the same for both the reference and

specimen spectra, correct only for the difference in the backscatter source using the mean energy loss, backscatter coefficient, and ionization cross section. If the primary beam energy is also different, then correction of the secondary source and ionization cross section is also necessary. Finally, if the angle of incidence is different, correction for the relative influence of the different sources is necessary. After correcting for the different source strengths, the peak height per equivalent monolayer radiator on the unknown specimen is known.

4. The number of equivalent monolayers of carbon is obtained from the Auger spectrum of the specimen, using the results from step 3. Let N_E (specimen) be the radiating strength of the unknown layer, expressed in monolayers. Then the coverage z_o is determined from

$$N_E \text{ (specimen)} = \int_0^{z_o} \exp(-z/4)\, dz \qquad (47)$$

5. A check is available by using the calibration spectrum for the substrate. Proceed through steps 2, 3, and 4 to obtain the radiating strength for the molybdenum, N_E (substrate). The following equality should hold for the 186 eV molybdenum peak.

$$N_E \text{ (substrate)} = \int_{z_o}^{\infty} \exp(-z/3.4)\, dz \qquad (48)$$

Any significant difference suggests that the assumed partition of the surface

volume in step 1 is in error.

Two examples of the problem of estimating source functions conclude this section and the chapter. Additional examples follow in later chapters. The first example is a contaminated molybdenum surface, a specimen holder, which was studied as a function of primary beam energy. Figure 37 shows the peak heights of the principal constituents of the spectrum. Carbon, as graphite, nitrogen, and oxygen are the main contaminants. Note that the nitrogen peak height was multiplied by ten in making Figure 37. Since the molybdenum was from high purity stock, one would conclude that the contaminants are localized on the surface. Therefore, the contaminants form a film on a molybdenum substrate. The scattering properties of the molybdenum determine the source functions for the Auger escape volume. Molybdenum is an efficient backscatterer of the primary beam. Thus, we expect the secondary electron and backscattered electron sources to be relatively important compared to the primary beam flux. The secondary and backscattered electrons should increase in importance with higher beam energy. This is observed in the figure, because the peak heights increase monotonically with energy up to 2250 eV, the highest primary energy studied. The decrease in response at high energy, evident in the graphite response shown in Figure 30, is not seen. Whereas molybdenum has a high backscatter coefficient, ~ 0.4, which remains constant with energy, graphite has a low backscatter coefficient, ~ 0.1, which decreases with energy. The primary beam penetrates deeply into the graphite and "never comes back." Thus the secondary and backscattered electrons are not relatively as important in the pure graphite sample.

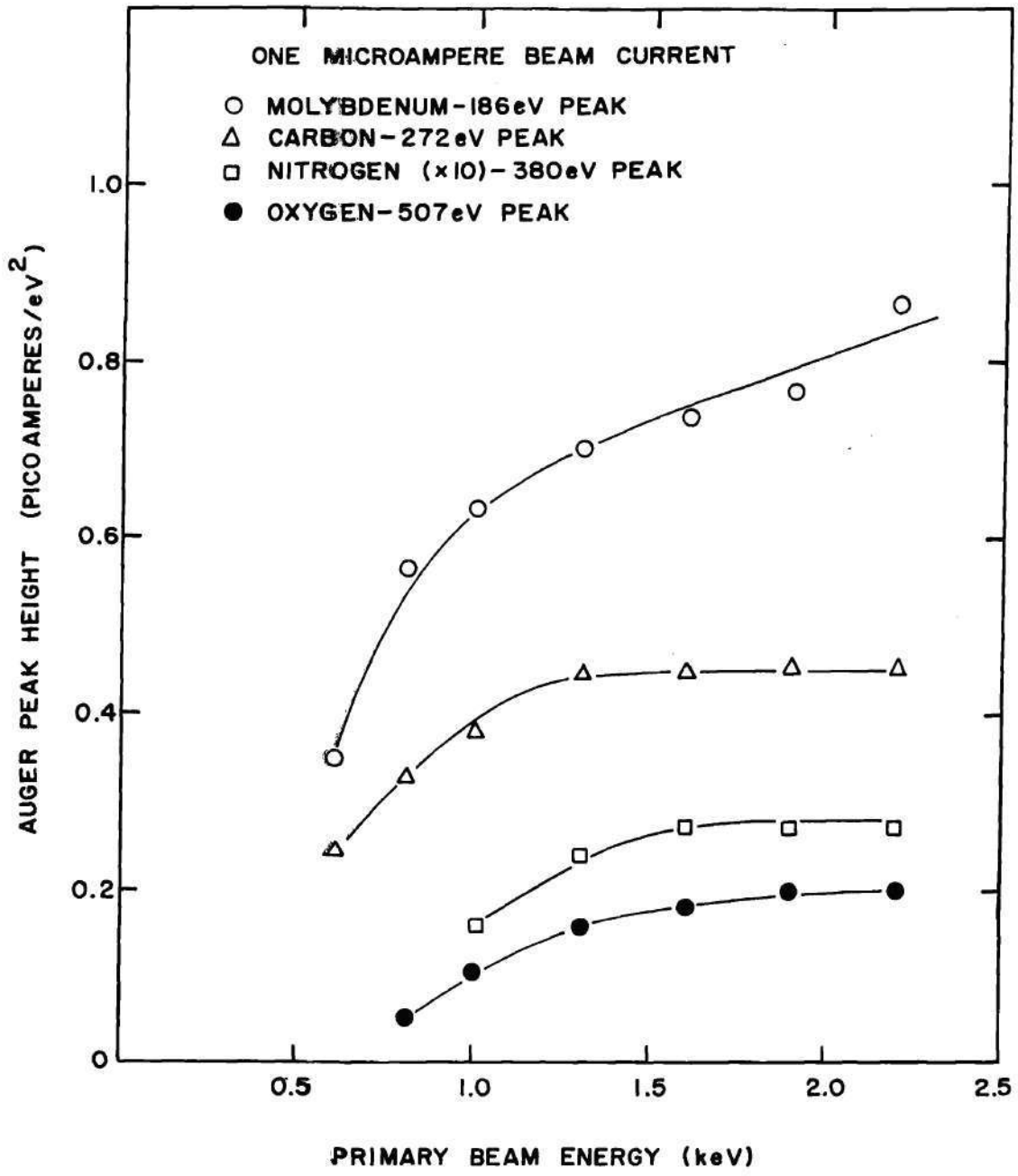

Figure 37. Auger Peak Heights of a Contaminated Molybdenum Sample as a Function of Primary Beam Energy.

The graphite layer thickness will now be estimated. This requires a calculation of the source functions. We must compare the strength of the source functions for the molybdenum substrate with a graphite substrate, and thereby compute the sensitivity for carbon on molybdenum. Notice that only a calculation of relative strengths is necessary. The simplest procedure is to refer the individual source strengths to the primary beam source: N_o electrons per second at E_o. This source is the same for both substrates.

The secondary electron source is also the same for both substrates. It is distributed in energy according to

$$\frac{N_o E_o}{E^2 \ln(E_o/100)}$$

and depends on the choice of E_o. Let the primary beam energy be specified as 1200 eV. The distribution in energy is removed by referring the source to primary beam energy; that is, by computing the number of electrons at E_o required to cause the same number of ionizations as the distribution. From Equation 31 the number of ionizations per second within a monolayer from the primary beam source is $N_o P(E_o)$.

The number of ionizations per second in a monolayer from the secondary source is

$$\int_{100}^{1200} P(E) \frac{1200\, N_o}{E^2 \ln(E_o/100)}\, dE = 0.7\, N_o\, P(E_o) \qquad (49)$$

where the integral was evaluated numerically.

The backscattered source must also be considered. The normalized energy variable U is given by

$$U = E_o/E_W = 1200/283 = 4.25 \tag{50}$$

for carbon and the primary beam energy utilized. The graphite substrate is characterized by a backscatter coefficient of 0.1, as previously discussed, and a mean energy loss of 0.45 E_o, from Figure 33. The molybdenum substrate is characterized by a backscatter coefficient of 0.4 and a mean energy loss of 0.275 E_o. Thus, the backscattered electrons from the graphite substrate will cause 0.1 $N_o P$ (0.55 E_o) ionizations per second within a monolayer and the backscattered electrons from the molybdenum substrate will cause 0.4 $N_o P(0.725\ E_o)$ ionizations per second. Evaluation of the expression for the ionization cross section, Equation 33, shows that

$$P(0.55\ E_o) \sim P(0.725\ E_o) = 1.1\ P(E_o) \tag{51}$$

for the case where U = 4.25. Therefore, the contribution from the backscattered electrons is 0.11 $N_o P(E_o)$ for the graphite substrate and 0.44 $N_o P(E_o)$ for the molybdenum substrate.

The comparison between the substrates may now be made. The number of ionizations per second in the monolayer on the molybdenum substrate is 2.14 $N_o P(E_o)$, and on the graphite substrate, 1.81 $N_o P(E_o)$. Therefore, the response of a carbon film on molybdenum should be 2.14/1.81 times as great as on graphite.

Figure 37 shows that the carbon peak height was approximately 0.45 picoamperes/eV^2 per microampere of beam current for this specimen at 1200 eV beam energy. Reference to Figure 30 shows that a one monolayer radiator yields 0.80/4 0.80/4 = 0.20 picoamperes/eV^2 per microampere beam current at 1200 eV. Therefore, a monolayer radiator on molybdenum should yield

$$(2.14/1.81)0.20 = 0.235 \text{ picoamperes/eV}^2. \tag{52}$$

Thus, the observed carbon peak height is equal to 0.45/0.235 monolayers radiating strength. The actual thickness z_o of the film is, from Equation 47, given by

$$N_E = 0.45/0.235 = \int_0^{z_o} \exp(-z/4)\, dz. \tag{53}$$

Evaluation of the integral yields

$$z_o = 2.60 \text{ monolayers}. \tag{54}$$

The second example is also a contaminated molybdenum spectrum. This specimen was studied as a function of angle of incidence of the primary beam. Only one beam energy, 1200 eV, was used. Figure 38 shows the molybdenum and carbon peak heights as a function of angle. The essentially identical behavior of the carbon and molybdenum peaks shows the influence the scattering properties of the substrate has on the Auger response of the surface film. Compare the angular behavior shown here of carbon on molybdenum with that shown in Figure 29, which is carbon on a graphite substrate. Carbon on graphite shows a maximum at about 20^o and then drops off at grazing angles. Carbon on molybdenum shows no drop even at 4^o, as it follows the response of molybdenum at grazing incidence.

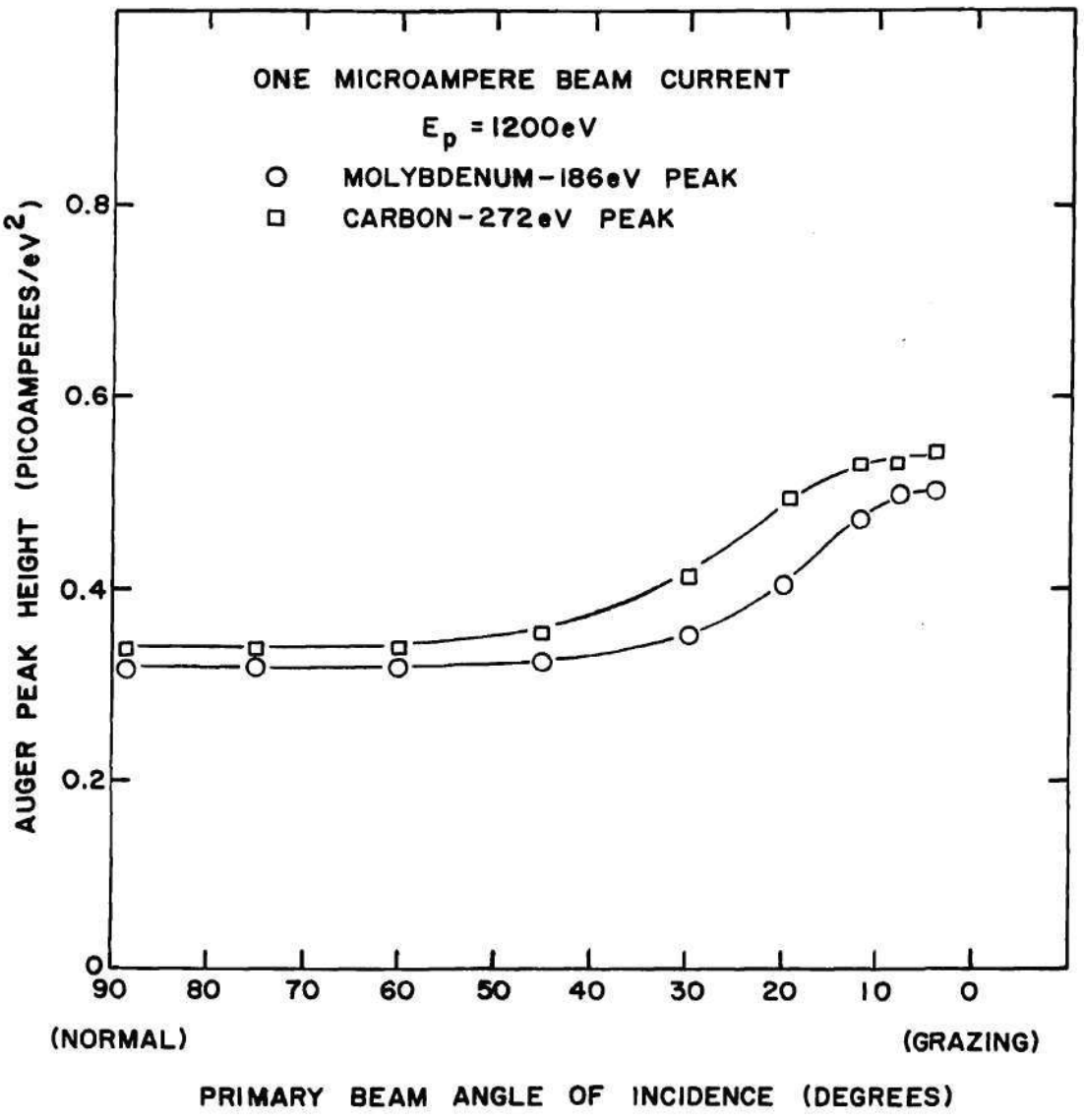

Figure 38. Auger Peak Heights of a Contaminated Molybdenum Sample as a Function of Primary Beam Angle of Incidence.

CHAPTER V

STUDY OF WAFER SURFACES WITH AUGER SPECTROSCOPY

This chapter is a survey of Auger spectroscopy findings from the study of transistor wafers taken from various stages of a commercial manufacturing process. Chapters VI and VII explore in detail the most interesting findings of this study.

The first section of this chapter explains the decision to concentrate on oxide surfaces in the study. The second section presents Auger spectra from typical oxide surfaces. The natural constituents, silicon, oxygen, and dopants, are discussed, as are the various contaminants. The effect of the primary beam on the oxide is also discussed. The third section explores an alternative technique for detection of materials easily desorbed by the electron beam and difficult to detect by Auger spectroscopy. The final section of this chapter introduces some of the charging artifices noted during the study and relates these to those noted in the critique of the literature presented in Chapter II. These charging artifices are discussed in detail in Chapter VI. The nature of the principal contaminant, carbon, is discussed in greater detail by Chapter VII.

Oxide Surfaces

The manufacture of a transistor or integrated circuit is a complex process. Even a simple breakdown of the process will involve thirty or forty steps. Any

decision to select a few of these steps for detailed study reflects the background and prejudices of the worker. The author visited three different commercial facilities during preliminary phases of the work and talked to a number of manufacturing personnel. The importance of oxide covered surfaces was a common thread through most of the process steps for silicon devices. In fact, the ease of formation and stability of silicon dioxide is the motivation for using silicon rather than germanium in the great majority of semiconductor devices.

Silicon dioxide is used as a mask for diffusions in the manufacturing process, as an electrical insulator in completed devices, and as a passivation and protective coating on completed devices. For example, a typical impurity diffusion operation begins by growing a thermal oxide over the entire wafer. Photolithography forms a pattern of "windows" which expose the underlying silicon surface. The diffusion of impurities takes place through these windows, with the remainder of the surface shielded by the oxide. As another example, silicon dioxide is used as an electrical insulator in integrated circuits and as the gate insulation in MOS transistors. Silicon dioxide, along with silicon nitride, is also used as an overcoating to electrically stabilize silicon p-n junctions and protect the device against the inward diffusion of unwanted impurities from the environment.

Given that silicon dioxide is an important constituent of contemporary semiconductor devices, the question remains as to the best method for its study. At least three methods have merit: (1) controlled experiments to study silicon dioxide per se, (2) analysis of completed semiconductor devices which are electrically defective, and (3) study of wafers taken from manufacturing steps in which silicon

dioxide is important. The third method was selected because it is the method which will lead to any on-line monitoring technique utilizing Auger spectroscopy and it is the method least explored in the literature. The desire for on-line monitoring techniques has been voiced by many manufacturing personnel and was the motivation for Tharp's work.[20]

Auger Spectra of Typical Wafer Oxides

This section is a summary of Auger spectroscopy findings from oxide covered wafers taken from a commercial manufacturing line. An effort by Dr. L. N. Tharp[20] preceded the work reported in this dissertation. Tharp studied wafers taken from a commercial line after final polishing, first oxidation, a photoresist removal, base diffusion, emitter diffusion, and metalization. Based on Tharp's results, the study was specialized for this dissertation to wafers taken after first oxidation, base diffusion, and emitter masking.

Three conclusions are presented in this section: (1) the oxide surface displays silicon and oxygen clearly, but dopants are seen only if the doping level is high or the surface very clean, (2) the surface displays certain contaminants, carbon being the principal one, and (3) electron beam induced charging artifices, desorption of adsorbates, and chemical reactions are important when interpreting spectra. Auger spectra from three typical wafers, one each after first oxidation, base diffusion, and emitter masking, will now be discussed. These wafers were NPN power transisters and were all selected from the same line.

The first spectrum is from a wafer taken after first oxidation. Figure 39

shows the spectrum for this N type oxide. Silicon is seen in the form of SiO_2 with the principal peak at 77 eV. Carbon is the main contaminant, with a trace of sulfur. Notice that there is no evidence of silicon carbide. The carbon peak has the form characteristic of graphite with the maximum at 250 eV, and there is no peak at 89 eV which would indicate silicon in the form of SiC. The graphite coverage will now be computed using the techniques introduced in Chapter IV.

This is the interpretation problem, the easier of the two calculations described in the last chapter. It is easier, and more accurate, because reference spectra are available for each of the bulk materials in the spectrum in question, Figure 39. The first step is to postulate the spatial distribution of the constituents. In this case the carbon will be assumed to be a uniform layer on top of the SiO_2. The second step is to compute source strengths since the scattering properties of SiO_2 determine the response of the graphite layer. Corrections must be made in the carbon sensitivity both for the backscattered source and the increased importance of the primary source at grazing incidence.

The first comparison is made between a graphite substrate and a SiO_2 substrate, both at normal incidence. This comparison will determine the correction for the backscattered source. The primary source contributes $N_o P(E_o)$ ionizations per second in a monolayer in both substrates. Since the primary beam energy E_o is the same (1200 eV) as in the contaminated molybdenum example of the last section of Chapter IV, the evaluation of the secondary source strength made there also applies here. The result was that the secondaries contribute 0.7 $N_o P(E_o)$ ionizations per second in both substrates. The backscattered source is evaluated using

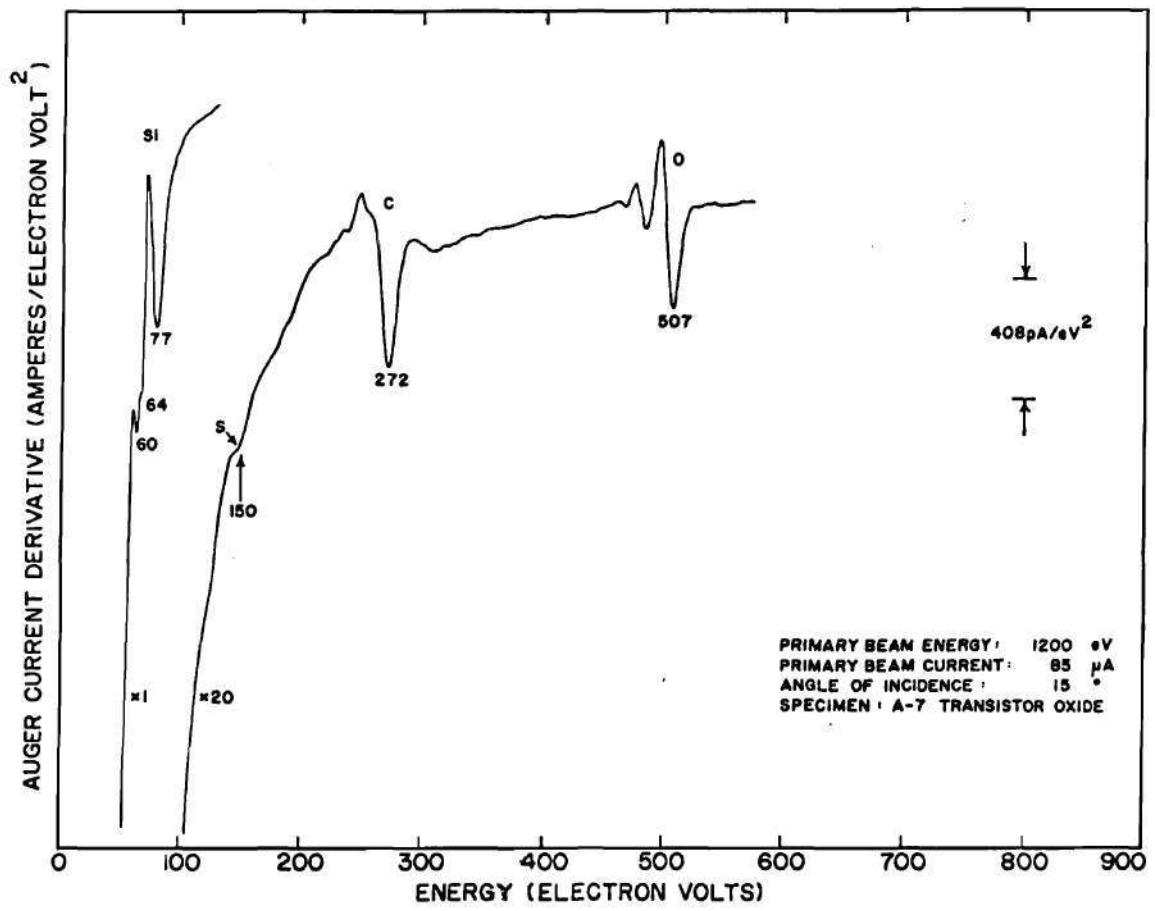

Figure 39. Auger Spectrum of Commercial Wafer After First Oxidation.

a backscatter coefficient of 0.1 for graphite at 1200 eV, with mean energy loss 0.45 E_o, and 0.2 for SiO_2, with mean energy loss 0.38 E_o. The mean energy loss figures are obtained from Figure 33 and the backscatter coefficients are extrapolated from Table 2. Evaluation of the ionization cross section at the appropriate values of normalized energy U gives 0.11 $N_o P(E_o)$ ionizations per second for graphite and 0.22 $N_o P(E_o)$ ionizations per second for SiO_2. The total number of ionizations per second per monolayer for graphite is thus 1.81 $N_o P(E_o)$ and for SiO_2 it is 1.92 $N_o P(E_o)$. Therefore, the increase in sensitivity for carbon on SiO_2 as compared with graphite is 1.92/1.81.

The influence of the primary source at grazing incidence will now be determined. The response of SiO_2 at normal incidence is 8 picoamperes/eV^2 per microampere beam current, from Figure 27, and 12 picoamperes/eV^2 at 15^o. Thus the total source strength at 15^o is 50% greater than at 90^o in SiO_2. The number of ionizations per second in a monolayer on SiO_2 at 15^o is therefore

$$1.5 \times 1.92\ N_o P(E_o) = 2.88\ N_o P(E_o). \qquad (55)$$

Notice that this requires the primary source to increase from $N_o P(E_o)$ to 1.96 $N_o P(E_o)$ ionizations per second as the angle is changed from 90^o to 15^o.

The radiating strength of graphite is 0.20 picoamperes/eV^2 per microampere beam current, per monolayer, at 1200 eV primary beam energy and normal incidence (Figures 29 and 35) on graphite. Therefore on SiO_2 the radiation strength is

$$(2.88/1.81)\ 0.20 = 0.32 \text{ picoamperes/eV}^2 \qquad (56)$$

per microampere beam current. This is the sensitivity for graphite to be used in interpreting Figure 39. As stated before, the sensitivity for SiO_2 is 12 picoamperes/eV^2 for Figure 39.

The third step is to measure the peak heights from the spectrum. The scale factor shown on Figure 39 is 408 picoamperes/eV^2 and the beam current shown is 85 microamperes. Therefore, a unit deflection corresponds to 408/85 picoamperes/eV^2 per microampere beam current. Since the silicon peak at 77 eV is 1.25 units high, the silicon peak height is

$$(408/85)\ 1.25 = 6.0 \text{ picoamperes/eV}^2 \tag{57}$$

per microampere current. Similarly, the carbon peak height is

$$(408/85)(1.5)(1/20) = 0.36 \text{ picoamperes/eV}^2 \tag{58}$$

where the 1/20 factor accounts for the increased amplification used in the latter portion of the spectrum.

The fourth, and final, step is to compute the coverage. Recall that for the 272 eV Auger electron (carbon) the equivalent radiator is

$$N_E = \int_0^\infty \exp(-z/4)dz = 4 \text{ monolayers} \tag{59}$$

for a bulk specimen. Each monolayer radiating strength is 0.32 picoamperes/eV^2 in this example. The observed peak height is 0.36 picoamperes/eV^2. Therefore, we write the following pair of equations relating peak height to monolayer coverage.

$$4 \times 0.32 \text{ picoamperes/eV}^2 = \int_0^{\infty} \exp(-z/4)dz \tag{60}$$

$$0.36 \text{ picoamperes/eV}^2 = \int_0^{z_o} \exp(-z/4)dz \tag{61}$$

Notice that the limits of integration are expressions of monolayer coverage. Since the integral in Equation 60 is simply 4, we divide Equation 61 by Equation 60. The result is particularly convenient to use.

$$0.36/(4 \times 0.32) = - \exp(-z/4) \Big|_0^{z_o} \tag{62}$$

Thus, the observed peak height is divided by the bulk response (the response per equivalent monolayer multiplied by the number of equivalent monolayers in the bulk specimen), and this result is equal to the antiderivative evaluated between the limits of integration. Equation 62 may be simplified to read

$$0.36/1.28 = 1 - 0.72 = 1 - \exp(-z_o/4). \tag{63}$$

Evaluation of the exponential yields

$$z_o = 1.3 \text{ monolayers.} \tag{64}$$

Since the only other significant constituent is the SiO_2 itself, the consistency of the calculation can be estimated by checking the SiO_2 response. The equation analogous to Equation 62 is

$$6.0/12.0 = - \exp(-z/2.4) \Big|_{z_o}^{\infty} \tag{65}$$

where z_o expresses the depth, in monolayers, at which the SiO_2 begins. Analogous to Equation 63 we have

$$0.5 = \exp(-z_o/2.4) \tag{66}$$

and the result is

$$z_o = 1.7 \text{ monolayers} \tag{67}$$

The discrepancy in the location of the graphite - SiO_2 interface can be either in the initial assumption that the graphite was in the form of a uniform layer, or it can in the details of the calculation. Notice that the result of Equation 67 could be "adjusted" by changing the mean escape depth used for the 77 eV silicon Auger electrons. The value used, 2.4 monolayers, was determined from Figure 35 and the comments made in describing the figure certainly apply here.

A number of base diffusion oxides were also studied. These were similar in nature to the above discussed oxide. The only significant difference was the indication of boron at 179 eV. Boron, of course, is used as a P type dopant. An example of a P type oxide showing the boron dopant was given in the section on calibration spectra in Chapter IV; see Figure 21 and the associated discussion.

The next example is a wafer taken after base diffusion which shows significant silicon carbide. Approximately one third of the wafers studied had a silicon carbide indication, although few were as contaminated by silicon carbide as this example. Figure 40 is the Auger spectrum of the wafer. The wafer was rinsed in methanol and distilled water before insertion in the vacuum system but received

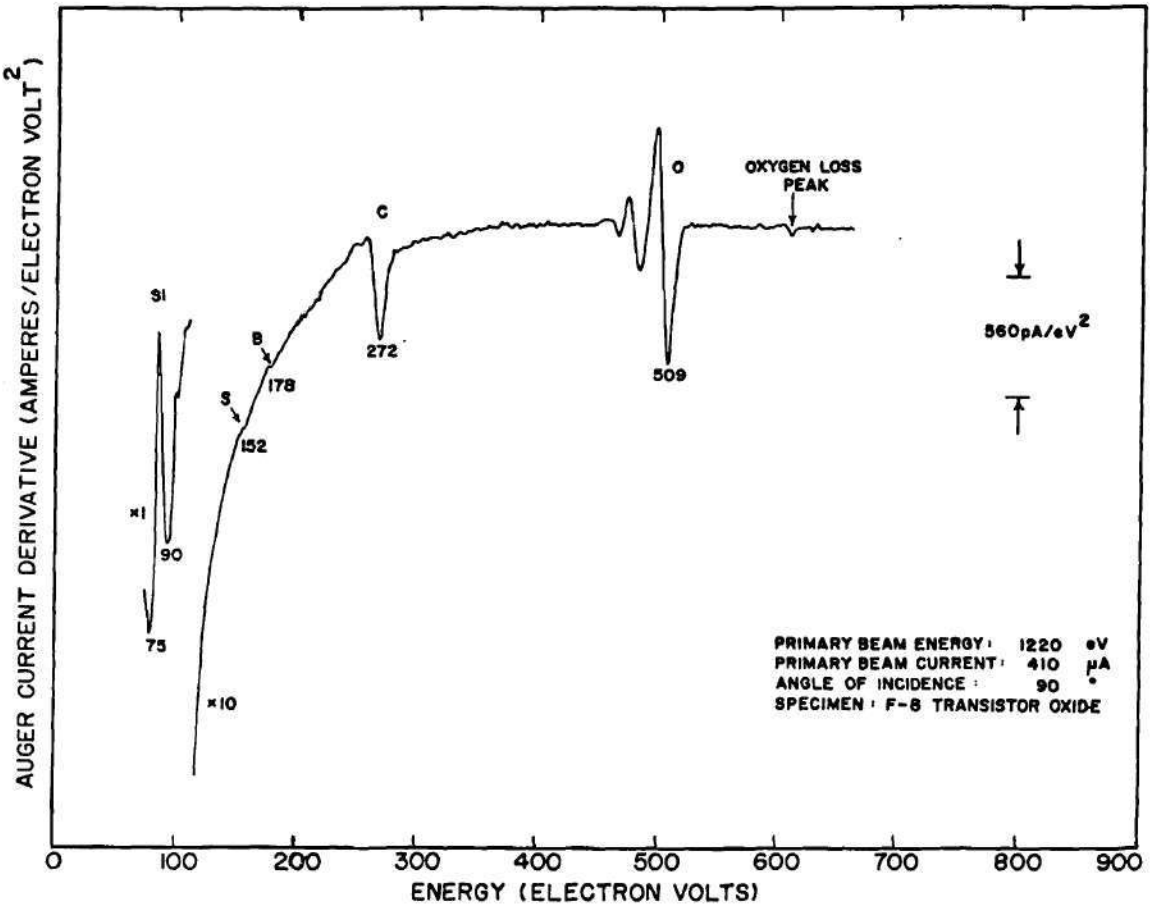

Figure 40. Auger Spectrum of Commercial Wafer after Base Diffusion, Showing Silicon Carbide Contamination.

no other treatment. In particular it was not subjected to heat treatment or electron bombardment before this spectrum was recorded. Thus, the SiC indication is representative of the wafer as removed from the process line, since it received no treatment known to form SiC after removal from the line.*

Identification of SiC is made in the following way. The broad peak at 90 eV could be the result of Si, SiO, SiC, or some combination of these. Only a higher resolution spectrum in the low energy range would say specifically. However, the large oxygen peak and the fact that the wafer was subjected to an oxidizing step as part of the diffusion process suggest that SiO is not the only contributor to the 90 eV peak. Similarly, the presence of oxygen suggests that Si is not the principal contributor. Thus a process of elimination and the characteristic carbide shape of the carbon peak lead to SiC. An equivalent coverage for the SiC can not be computed because it exists as particles,[49] rather than as a smooth layer in the fashion of graphite.[50] Experience though has shown that the peak height in the figure corresponds to fairly heavy coverage. An estimate of the magnitude of the SiC coverage can be made in the following way. The sensitivity of silicon in SiC, at normal incidence and 1150 eV, is 3.9 picoamperes/eV^2 per microampere beam current, from Figure 28. The 90 eV peak in Figure 40 is 2.35 picoamperes/eV^2 per microampere beam current. The corresponding numbers for the carbon peak are 0.5 picoamperes/eV^2 for bulk SiC and 0.12 picoamperes/eV^2 for Figure 40. The shape of the carbon peak, with the maximum at approximately 260 eV, is that

---

*Formation of SiC is discussed in Chapter VII.

of carbide, not graphite. Thus the entire carbon peak may be allocated to SiC. This peak height is about one fourth that of a bulk specimen. One fourth of the bulk silicon, as SiC, peak is 0.975 picoamperes/eV^2; the implication is that a little less than one half of the 90 eV peak is due to SiC. The remainder is likely SiO. If one assumes the scattering properties of SiC are similar to those of SiO and SiO_2, the constituents of the substrate, then of the order of one fourth of the surface is covered by SiC particles.

Two spectra, Figures 41 and 42, are from the final wafer considered in this sequence of examples. The emitter masking operation was completed before this wafer was removed from the line. The next process step would have been the emitter diffusion. Figure 41 is the Auger spectrum for a transistor which showed little SiC contamination but substantial graphite coverage. The silicon (as SiO_2), carbon (as graphite), and oxygen peaks dominate the spectrum, as expected. The minor peak at 107 eV belongs to the silicon complex. There is a minor inflection at 150 eV likely caused by sulfur, and there is another minor inflection at 179 eV, which is interpreted as boron. A distinct oxygen ionization loss peak is seen at 460 eV; such loss peaks are discussed in Chapter VI.

Figure 42 shows the Auger spectrum of a second transistor on the same wafer. The primary difference between the two transistors is that this unit shows a definite indication of SiC both with the 89 eV silicon peak and the shape of the carbon Auger peak. The remaining interpretations are identical.

The Auger spectroscopy findings from these wafers may be summarized for reference.

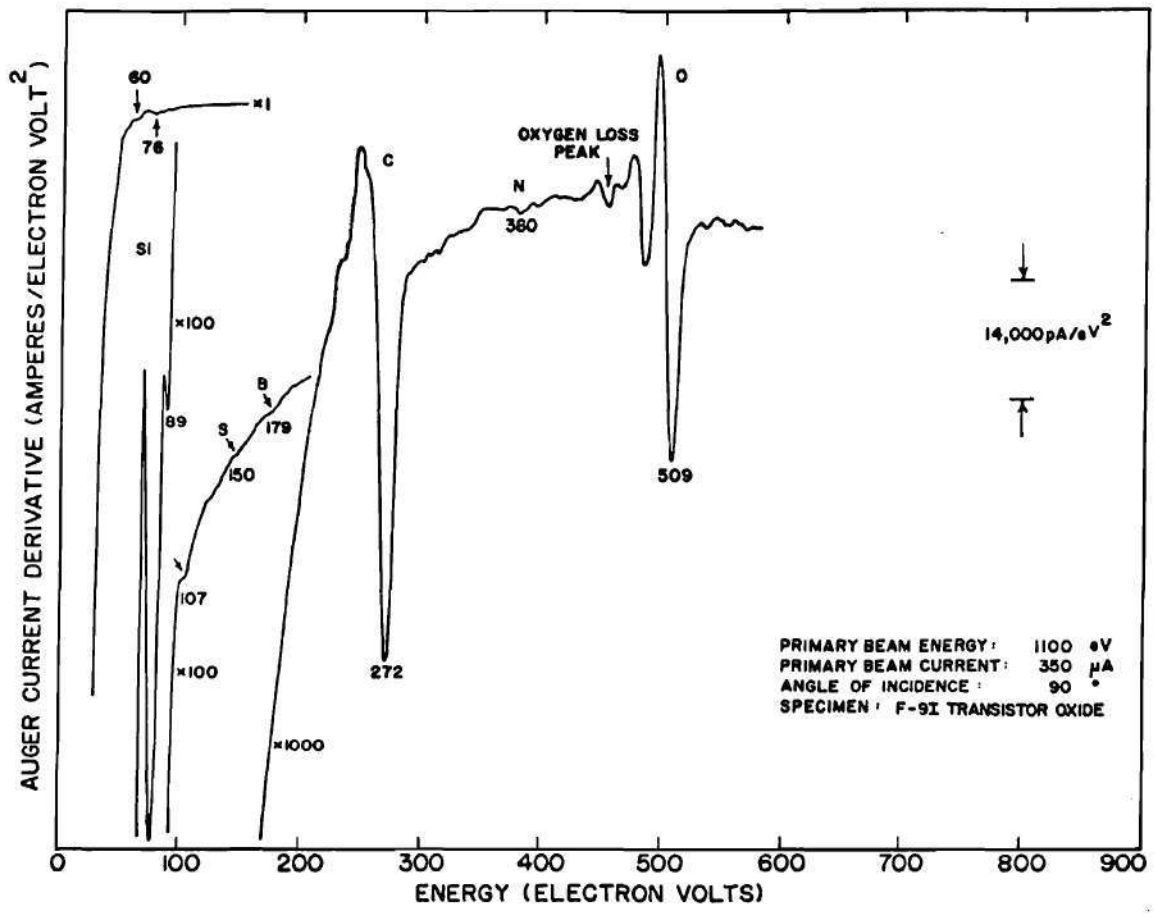

Figure 41. Auger Spectrum of Commercial Wafer after Emitter Masking, Showing Little Silicon Carbide Contamination.

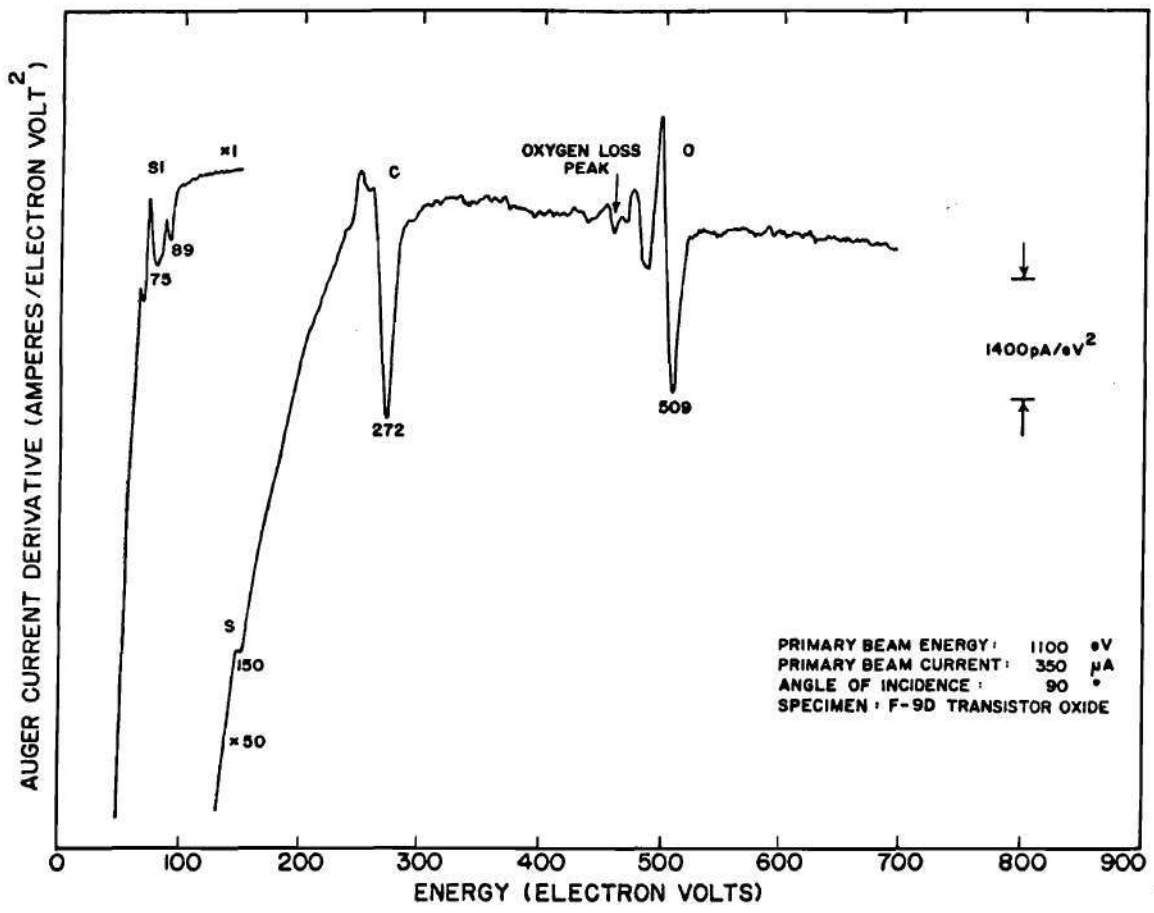

Figure 42. Auger Spectrum of Commercial Wafer after Emitter Masking, Showing Silicon Carbide Contamination.

1. Silicon, oxygen, and carbon are the three constituents always seen in the Auger spectrum. The following section on electron desorption techniques will show that hydrogen is also present.
2. Carbon exists both in the form of graphite and silicon carbide on commercial oxide surfaces. Some wafers showed no silicon carbide and others, supposedly identical, showed substantial SiC. Furthermore, there was a varying amount from transistor to transistor on several wafers studied in detail. Generally speaking, the amount of SiC found increased with the number of processing steps which had been completed. For example, almost all emitter masked wafers showed SiC contamination and almost none of the wafers taken after first oxidation showed it. Data presented in Chapter VII will show that the amount of SiC actually varies across a single transistor on a wafer.
3. The dopants, phosphorus and boron, may occasionally be seen but the indication is always small and unambiguous interpretation difficult.
4. Sulfur, and sometimes chlorine, are the two principal trace contaminants found.
5. Oxygen loss peaks are found and should not be confused with Auger peaks. Loss peaks are discussed in the following chapter.

Concluding this section is an introduction to electron beam induced phenomena associated with Auger spectroscopy. The first phenomenon is that of the primary beam causing atoms or molecules, adsorbed on the specimen surface, to leave the surface either by diffusing into the solid or, in the more likely case, escaping into the vacuum. The most common example is that of the electron beam

sputtering sodium off of silicon surfaces.[19] The only example noted in this work occurred when the vacuum system was not baked and therefore the water vapor pressure was in the 10^{-8} torr range. Presumably an appreciable amount of water vapor would then be adsorbed on specimen surfaces, particularly SiO_2. The tendency of the Auger spectra then was for all of the peaks, except oxygen, to increase with exposure to the electron beam. The implication is that the electron beam was causing desorption of H_2O, and hence reducing the oxygen indication, and thereby exposing the underlying surface to vacuum and increasing the Auger electron escape probability for the underlying surface region. Electron stimulated desorption can be a very useful analytical phenomenon when the desorbed species are identified with a mass spectrometer. This technique is the subject of the next section.

The second phenomenon of interest is the ability of the electron beam to promote chemical reactions on the surface. The principal reaction noted in this w ork was the reduction of silicon dioxide. While it is known that the electron beam will reduce silicon dioxide,[9] the actual reactions are not well understood. Careful measurements in this work indicate that two possibilities exist, depending on the presence of carbon as graphite. When carbon as graphite is present, the elect ron beam will reduce silicon dioxide and form silicon carbide. The fate of the excess oxygen, whether it desorbed into the vacuum or diffused into the remaining oxide, was not determined. When carbon is not present, the electron beam will reduce silicon dioxide to form what is believed to be silicon monoxide. Again the fate of the excess oxygen was not determined. These reactions are discussed in

more detail in Chapter VII.

The final phenomenon of interest is the ability of the electron beam to cause charging artifices. These artifices are discussed somewhat in the final section of this chapter and then the entirety of Chapter VI is devoted to them.

Electron Stimulated Desorption and Mass Spectroscopy

This section briefly describes a technique which is actually closely related to Auger spectroscopy, although at first glance it does not appear to be. The method consists of determining the mass of atoms removed from the surface by the action of an electron beam. The beam used for Auger spectroscopy was also used for this electron stimulated desorption work. A quadrupole mass spectrometer performed the mass analysis. The most important characteristic of electron stimulated desorption is that the technique is highly selective; that is, only certain adsorbates will be removed from certain substrates. Therefore, electron stimulated desorption is not a general analytical technique for surface studies. It is, however, complementary to Auger spectroscopy when the primary goal is detection of certain contaminants, and the lack of absolute calibration of coverage can be accepted.

The recent review paper by Madey and Yates[52] serves as a reference for the following description of electron stimulated desorption phenomena.

1. (Utility) Electron stimulated desorption of adsorbates and detection by a mass spectrometer is a useful surface analysis technique for elements of low or zero (H, He) Auger sensitivity. It is also useful when the primary beam

causes rapid desorption of the material (e.g., Na on SiO_2). It is particularly useful when both circumstances apply. Auger spectroscopy and electron stimulated desorption are complementary,* for they utilize competing physical processes: Auger neutralization of primary beam ionized atoms can prevent their escape from the surface. Therefore, materials with low cross sections for Auger neutralization will likely be desorbed.

2. (Technique) The surface to be analyzed is bombarded by a primary beam of electrons. While previous workers used beams with less than 500 eV energy, the author utilized the same primary beam as used for Auger spectroscopy. The primary beam energy ranged from 900 eV to 2300 eV. The principal effect of increased energy was higher efficiency. The primary beam ionizes atoms adsorbed on the surface of the solid and often the resulting field repels the ion from the surface. If the ion is not neutralized before it moves a characteristic distance from the solid, it will escape completely and thereby be desorbed. An ion neutralized before moving the characteristic distance away from the surface will return. A third possibility is that the ion will move sufficiently far away to escape but will then be neutralized. In this case it will escape as a neutral atom rather than as an ion. The mass spectrometer is placed with a line-of-sight view of the emitting surface. The mass spectrometer determines the mass of the ion or atom and thereby allows an identification of

*The two techniques are complementary because materials not detected by one are likely detected by the other. The two phenomena are competing because both require an initial ionization by the primary beam and if one form of neutralization takes place, the other form does not.

the species to be made.

3. (Mass Spectrometry) The mass spectrometer utilized herein is composed of three portions: (1) an ionizer to ionize neutrals, (2) a mass filter which passes only ions of a selectable mass-to-charge ratio, and (3) a collector system which forms a signal proportional to the number of ions passed by the filter. The ionizer can be turned off to allow analysis of incoming ions. The ionizer potentials prevent incoming ions from reaching the mass filter, so only neutrals in the ionizer volume are analyzed when the ionizer is on. However, residual gas atoms far outnumbered incoming neutrals from the bombarded surface with the experiment geometry necessary in this work. Thus, only residual gas analysis was possible with the ionizer activated. Only desorbed ions are analyzed with the ionizer turned off. The acceptance angle for desorbed ions cannot be computed exactly because of the presence of the ionizer structure in front of the mass filter; but 0.001 steradians is an order of magnitude estimate. Obviously, only a small fraction of the desorbed ions are analyzed. An electron multiplier provides suitable sensitivity when primary beams of 100 microamperes or more are used. The first dynode of the electron multiplier is biased negatively to collect positive ions and accelerate the resulting secondary electrons down the multiplier chain. Therefore, only positive ions are measured by the spectrometer.

4. (Sensitivity) Electron stimulated desorption techniques can not be absolutely calibrated at this time, because the ion transmission probability is not known for the mass filter; the angular distribution of emitted ions is not known, and

absolute ionic desorption cross sections are not known. Thus, the quadrupole mass spectrometer samples a small unknown fraction of the emitted ions. However, the ion current is proportional to the bombarding electron current and to the coverage of the particular species; coverage is the number of atoms or molecules of the species per unit area in the top monolayer of the substrate-adsorbate system. Unfortunately, as far as quantitative analysis of the chemical constituents of a surface is concerned, the desorption cross section varies by orders of magnitude even between different binding states of a particular adsorbate on a solid. The sensitivity variation between different elements is often many orders of magnitude.

5. (Applications) Only certain adsorbate-substrate combinations are sensitive to electron stimulated desorption. This selectivity to binding mechanism is a natural result of the desorption process. Neither thermal heating by the beam nor direct energy transfer from the electron to desorbed atom are important at the power and energy levels employed. The outer layer of atoms, the adsorbate, is attracted to the remainder of the solid, the substrate,by an electrostatic force. Nuclear forces give the net force function a repulsive nature at very small substrate-adsorbate spacing. The adsorbate will reside in the minimum of resulting potential energy-spacing function. Ionization of the adsorbate atom will cause many potential energy-spacing functions to become repulsive in nature. Thus, the ion will be accelerated away from the surface. The ion will escape if it acquires sufficient kinetic energy before neutralization. The nature of the binding of adsorbate to substrate determines

whether or not ionization will cause the atom to be accelerated away from the surface. Furthermore, the nature of binding determines the probability of neutralization by an electron from the substrate. This neutralization is often, but not always, by an Auger process. The one type of binding that has sufficiently efficient neutralization to prevent observation of electron stimulated desorption is the metal adsorbate on metal substrate system. On the opposite end of the spectrum is strong ionic bonding. The lack of available electrons for neutralization gives rise to appreciable sputtering by the electron beam and subsequent damage to the substrate. Most systems, though, shown an intermediate desorption cross section so that adsorbate atoms are removed but little damage is done to the substrate. In summary, electron stimulated desorption is applicable to certain binding states for adsorbate-substrate systems where neutralizat ion is not excessively probable.

The possibility of analyzing desorbed neutrals will be considered first. As mentioned above, the geometry of the experiment often prevents a conclusive experiment using residual gas analysis. Figure 43 shows the difficulty. The solid lines indicate the partial pressures of the constituent gases with the electron gun turned off. Excitation of the electron gun gives rise to the partial pressures indicated by the dashed lines. H_2, CO, and CO_2 are greatly increased by turning the gun on. The important point is that identical spectra were obtained when the beam was incident on the SiO_2 surface of a commercial wafer, the molybdenum specimen holder, the pyrex viewing window of the vacuum system, and the stainless steel drift tube of the electron gun assembly. Thus, the residual gas spectrum is not

Page missing from thesis

sensitive to the bombarded surface. Rather, it is sensitive to the residual gases of the system and the presence of a heated filament. Approximately one half of the increase in the H_2, CO, and CO_2 partial pressures occurs when the filament is heated and the remainder when the beam potential is applied. In contrast, mass spectrometry of desorbed ions is sensitive only to the bombarded specimen surface.

Graphite is an illustrative example and will be the first considered for the ion analysis technique. Then a "clean" oxide, fabricated in the vacuum system, and the "dirty" oxide of a commercial wafer will be compared.

Figure 44 shows a representative electron stimulated ion mass spectrum for a graphite specimen. The most significant feature of the spectrum is the large peak at mass 19, identified as H_3O^+. One might reasonably ask why this mass 19 peak is not associated with fluorine. The answer is there are a number of circumstances which point to H_3O^+. The source reaction for H_3O^+ is a classic ion-molecule reaction,

$$H^+ + H_2O \rightarrow H_3O^+ \quad . \tag{68}$$

The electron beam is an efficient ionizer of physically adsorbed gases, which is the situation for water vapor on graphite. Water vapor, of course, is one of the primary residual gases in the vacuum system and is known to adsorb on most surfaces in vacuum. The H_3O^+ peak is always correlated with the H_2O partial pressure of the residual gas. The H_3O^+ peak is also correlated with the mass 16, oxygen, mass 17, OH, and mass 1, hydrogen peaks. These are all products of the dissociation of the water molecule. The only obvious missing peak is that of the parent,

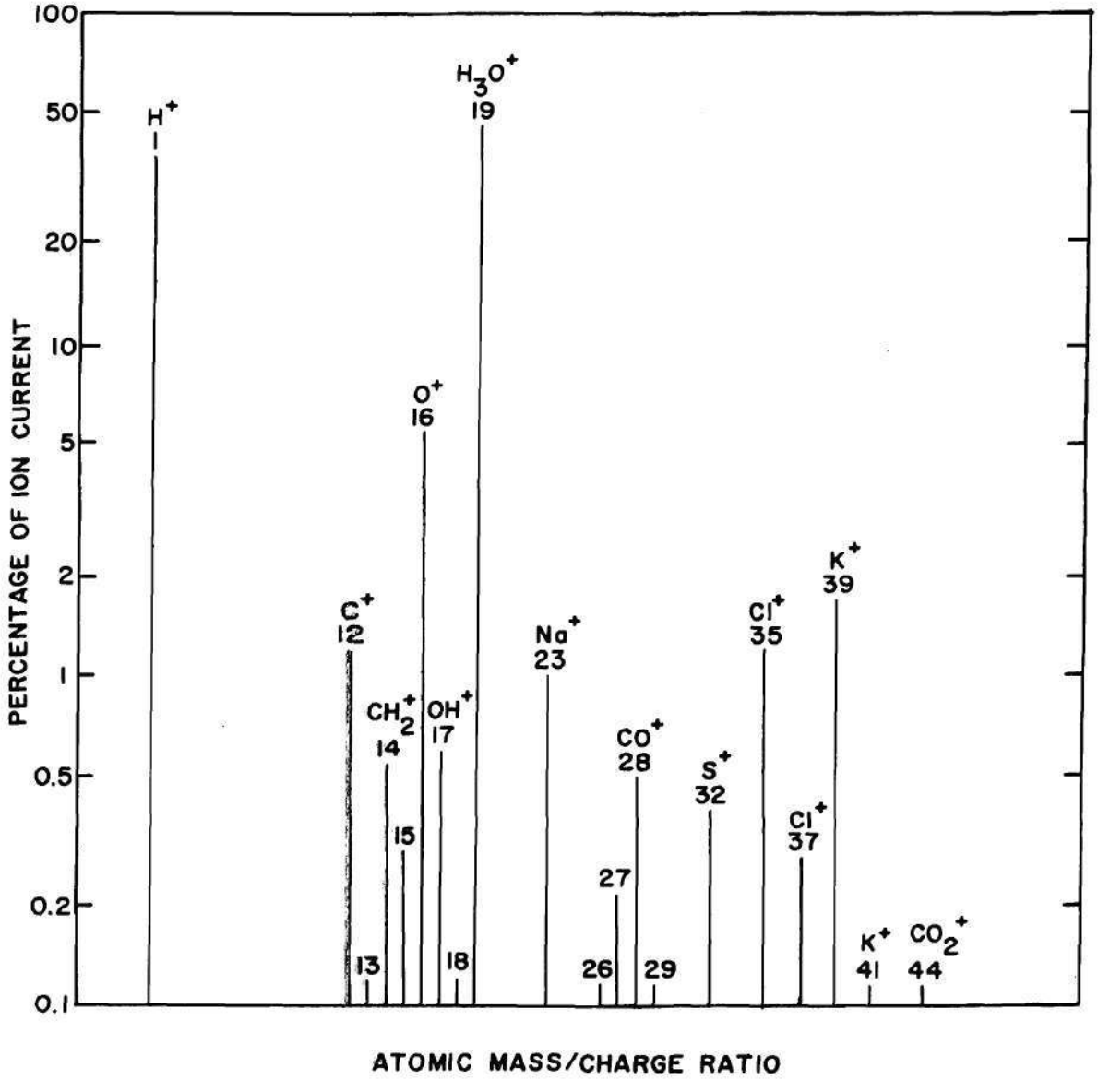

Figure 44. Ion Mass Spectrum for Graphite Specimen.

mass 18 for H_2O. Apparently dissociation of the H_2O molecule is much more likely on the surface than simple ionization of the molecule. The mass 18 peak grew when the graphite specimen was heated while bombarded, but it remained insignificant compared to masses 1, 16, 17, and 19. This family of masses dominated all surfaces studied, which included graphite (carbon), transistor oxides (SiO_2), and molybdenum. One would not expect to find fluorine as a dominant peak on all of these surfaces. Finally, fluorine was not found in the residual gas spectra or in the Auger spectra for the various surfaces. In summary, there is no supporting evidence for the mass 19 peak to be fluorine, whereas there is considerable evidence for it to be H_3O^+.

Interpreting the remaining peaks in Figure 44 is more straightforward. Sodium, mass 23, and potassium, masses 39 and 41, are two interesting contaminants from a semiconductor point of view. Chlorine, masses 35 and 37, is another common surface contaminant and may have been in the form of NaCl. Potassium and chlorine have two peaks each because of their isotopes. The ratio of peaks for chlorine (mass 35: 75%, 37: 25%) and for potassium (39: 93%, 41: 7%) is approximately correct. Sulfur, mass 32, is the other principal contaminant seen in the ion spectrum. The peaks at masses 13, 14, 15, 26, 27, and 29 are most likely C_xH_y type ions.

Comparison of the ion spectrum with the Auger spectrum for the same surface can be made with Figure 45, the Auger spectrum for the same specimen. Sulfur and chlorine are clearly shown in the Auger spectrum, along with the dominant carbon peak. Oxygen, a component of the adsorbed water vapor, is seen only with

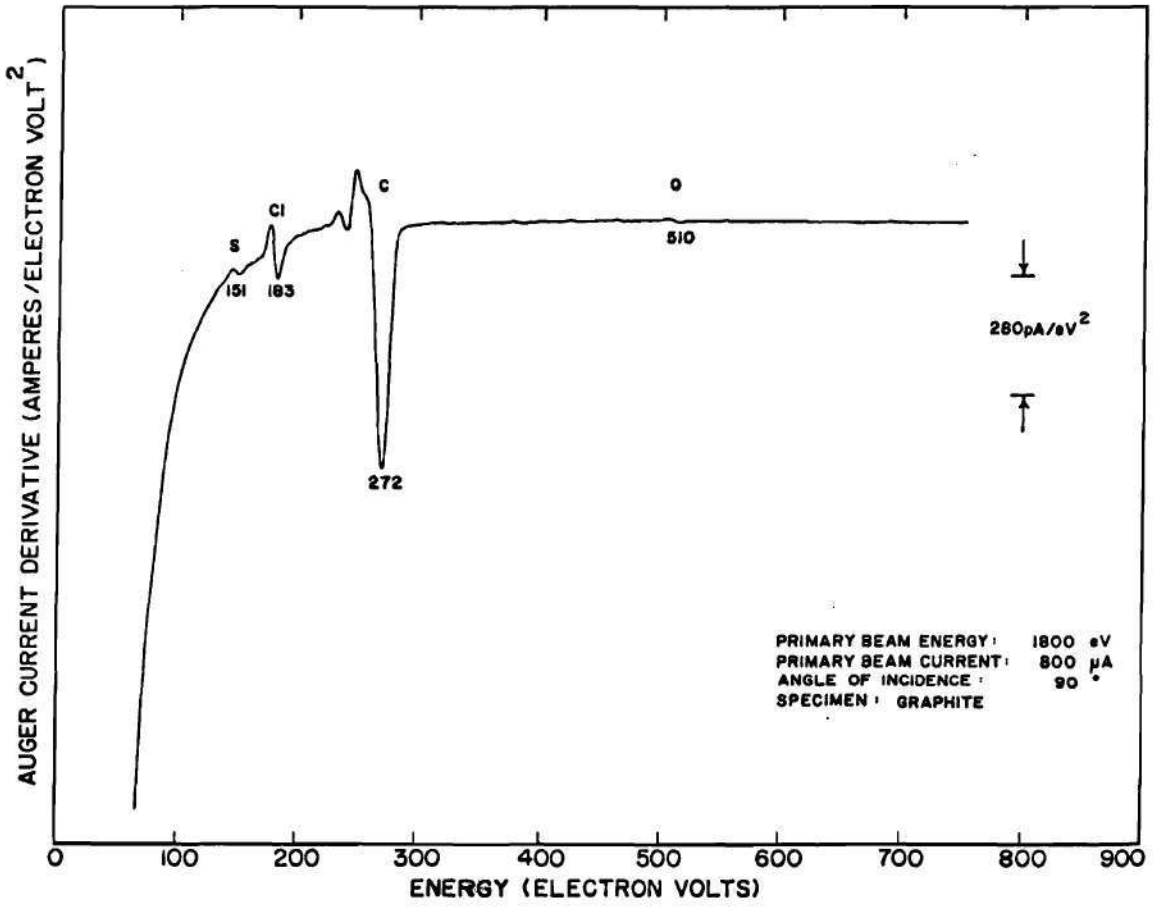

Figure 45. Auger Spectrum of Graphite Specimen Used for Ion Mass Spectrum of Figure 44.

some difficulty. Sodium is not seen. Potassium has its principal low voltage Auger peak at 252 eV, and so would be obscured by the carbon peak. Hydrogen, of course, has no Auger peak. In this particular case, all of the surface contaminants found in the Auger spectrum are also seen in the ion specimen, but not vice-versa.

Figure 46 shows an ion mass spectrum for a silicon dioxide surface which should be "clean." This surface was described in Chapter IV in reference to Figure 21. Silicon in the form of SiO_2, oxygen, a minor trace of imbedded argon, and the dopant boron are the only constituents of the Auger spectrum. The ion mass spectrum is dominated by the water peaks, masses 1, 16, 17, and 19 and by adsorbed residual gases CO and CO_2 which contribute the mass 12, 28, and 44 peaks. The only unexpected component is a trace of potassium, mass 39. This trace of potassium is attributed to the graphite specimen, discussed above, which was in the vacuum system with the SiO_2 specimen and studied before it. It is not unlikely that a small amount of potassium was removed from the graphite surface by the electron beam and was deposited on the SiO_2 surface a few centimeters away.

It is interesting to compare the ion mass spectrum of the clean oxide with that of a typical commercial wafer oxide, shown in Figure 47. The water and CO peaks still dominate but the trace contaminants are much more numerous. The potassium peak is an order of magnitude greater and there is a new, substantial, sodium peak, at mass 23. There are also hydrocarbon peaks at masses 27 and 29. Mass 31 may be either a hydrocarbon or the phosphorus which was used as a dopant. The comparison of this "dirty" oxide and the "clean" oxide will be completed by a

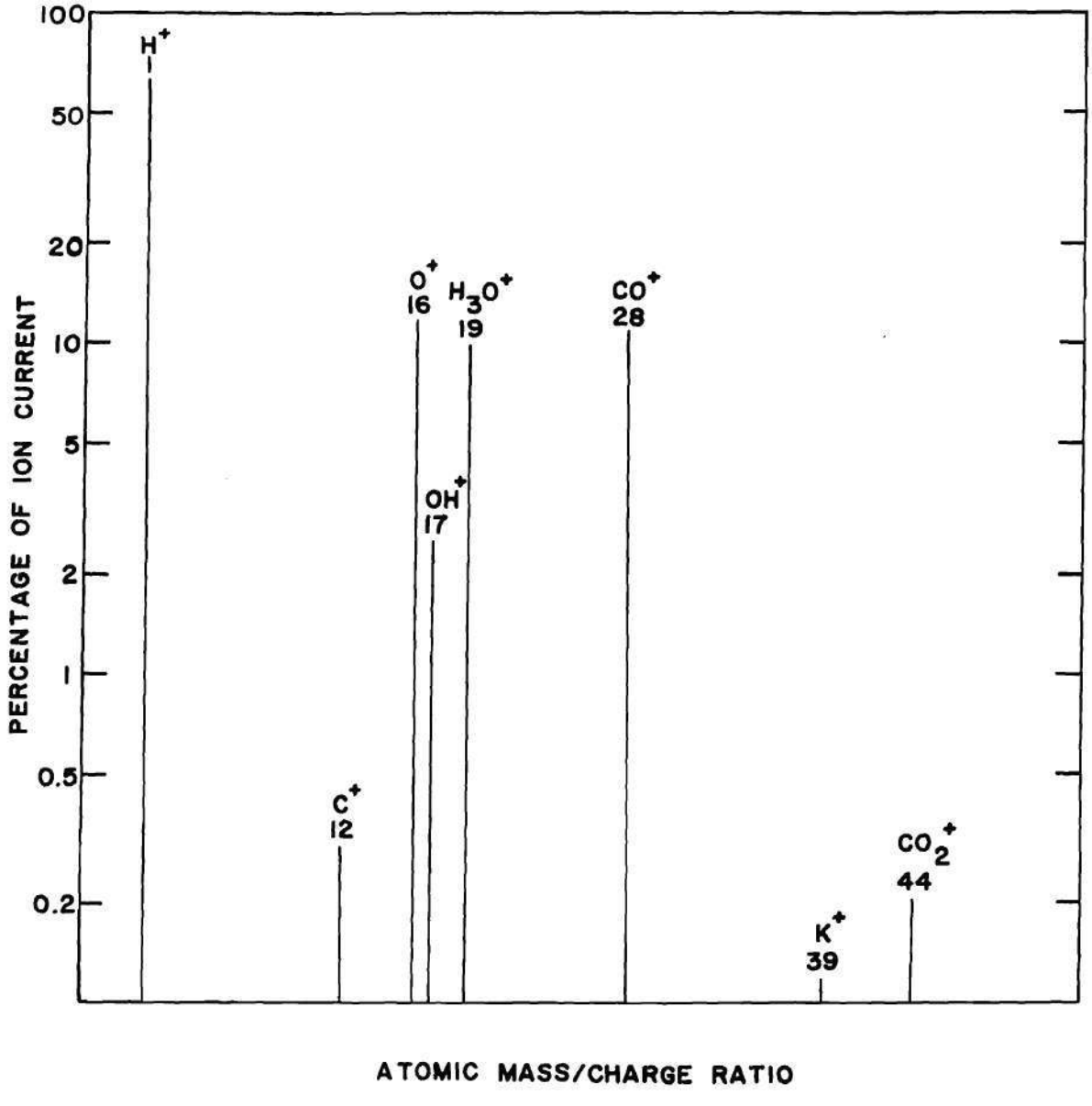

Figure 46. Ion Mass Spectrum of Silicon Dioxide.

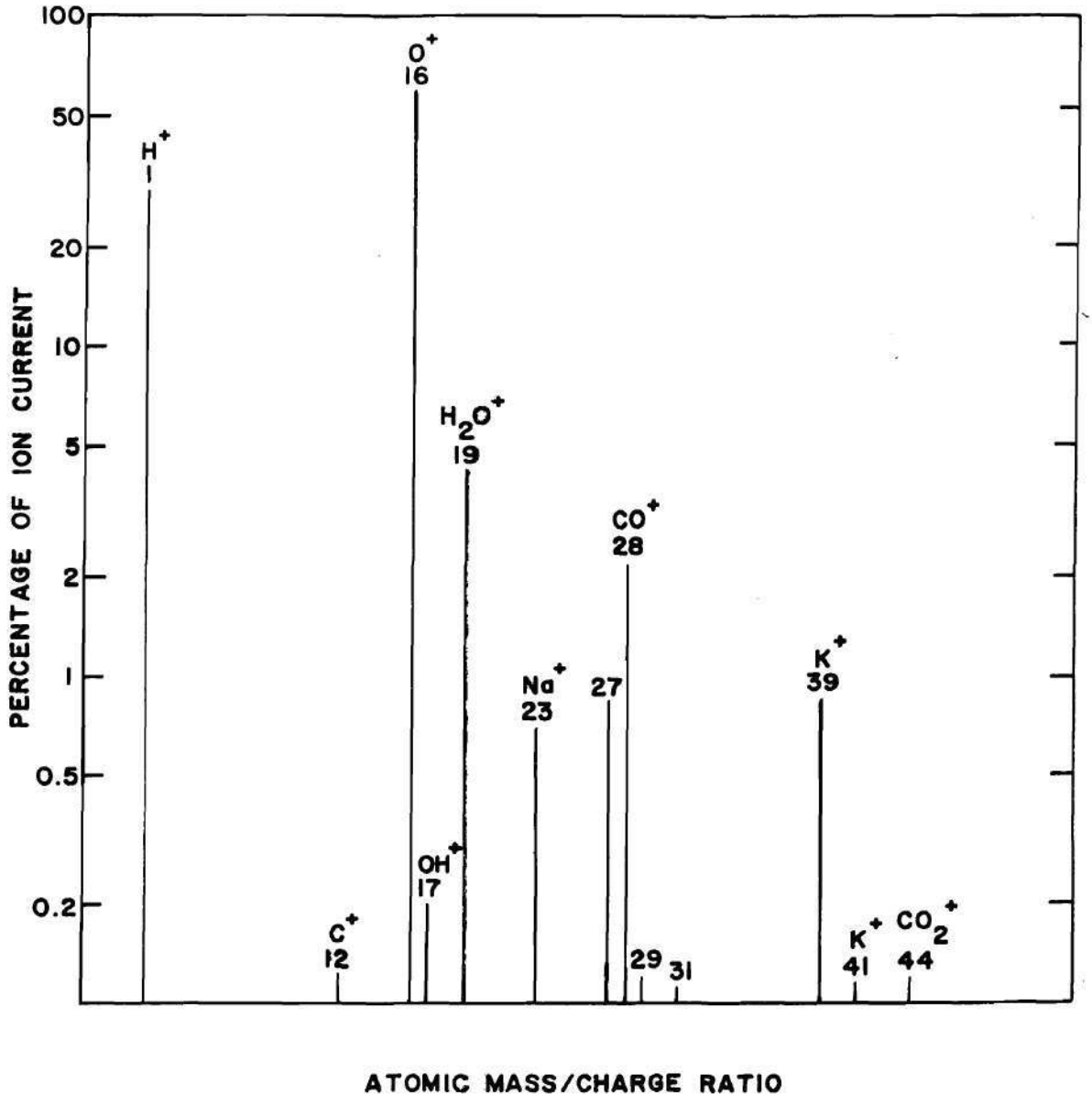

Figure 47. Ion Mass Spectrum of Commercial Oxide Surface.

worst case estimate of the sensitivity of electron stimulated desorption for sodium on SiO_2.

Sodium was not detected in any of the Auger spectroscopy studies of SiO_2. The signal to noise ratio, relative to a monolayer coverage of graphite, always exceeded 200:1 when a ten second time constant filter was used. Since the Auger sensitivity of sodium is about one half that of carbon, the sodium coverage was always less than 0.01 monolayers. Now the signal to noise ratio for sodium in the ion spectrum of Figure 47 exceeded 10:1 when using a one second time constant filter. Therefore, the minimum detectable sodium concentration, using electron stimulated desorption, is at least 10^{-3} monolayers and may be much better. A feasible way to increase the minimum detectable coverage by an order of magnitude would be to increase the filter time constant to 100 seconds for the mass 23 peak. This peak would then require about 15 minutes to scan.

The final portion of this section is a summary of the utility of ion mass spectroscopy to the Auger spectroscopist. The utilization of electron stimulated desorption techniques will certainly grow as they become better understood.

1. Electron stimulated desorption techniques are generally complementary to Auger spectroscopy, both in the nature of the physics and in implementation of the instrumentation. Auger neutralization is one of the primary competing processes to desorption. Thus, roughly speaking, adsorbate-substrate systems with high Auger cross sections will exhibit low desorption cross sections, and vice-versa. Only the presence of a mass spectrometer with a line of sight view of the bombarded surface is required. There is no reason why mass

spectrometry and Auger spectroscopy can not be performed simultaneously.

2. Electron stimulated desorption and mass spectroscopy exhibit useable sensitivity to sodium, a difficult contaminant to detect with Auger spectroscopy. While qualitative at this time, the sensitivity of ion mass spectroscopy to sodium could be calibrated for the important SiO_2-Na system.

3. Electron stimulated desorption techniques easily detect potassium, an element whose Auger peak is often masked by the carbon Auger peak. The minimum of the potassium peak occurs at 252 eV, just where carbon, in the form of graphite, exhibits a maximum. The combined spectra are difficult to separate, particularly when there is substantial carbon and a trace of potassium.

4. Electron stimulated desorption techniques detect hydrogen, an element not seen by Auger spectroscopy. Detection of hydrogen is useful because it allows other elements in an Auger spectrum to be associated with their likely parent compound. For example, oxygen seen in an Auger spectrum might be associated with water vapor, H_2O, when H is found in the ion mass spectrum. Similarly, Cl might be associated with HCl.

5. Electron stimulated desorption techniques often provide unambiguous interpretation of Auger spectra. For example, consider a small Auger peak at approximately 180 eV. Is it to be interpreted as boron, 179 eV, or chlorine, 183 eV? If the specimen were a boron doped transistor oxide, this would be a difficult decision (Figure 41 is such a case). If the ion mass spectrum shows no chlorine, then the best interpretation is boron.

6. Electron stimulated desorption techniques are sensitive to binding mechanisms

of adsorbates to substrates. The ion mass spectra of this section show distinct differences in the water complex, masses 1, 16, 17, 18, and 19, for three different substrates: graphite, a "dry" oxide grown in pure O_2, and a "wet" commercial oxide grown in a H_2O-O_2 mixture. Although these differences are difficult to explain in detail at this time, it is likely they will prove useful and be explained in the future.

Artifices Noted in the Oxide Studies

A number of anomalies appeared in the first spectra taken on commercial oxide covered wafers. These problems seemed to occur randomly, so the initial approach was to select those spectra which appeared free of anomalies. This was not a very satisfying solution, of course. Biasing the specimen a few tens of volts off of ground was soon discovered as an empirical cure. Varying the residual magnetic field by Helmholtz coils was another empirical cure. At the beginning of this work there was no explanation for the causes of these anomalies other than that they were connected with "charging" of the oxide (insulator) surface. Biasing the specimen was universally adopted as the cure for charging problems, since it removed the most obvious faults. Spectra with no peaks or a very noisy background were discarded. This was the state of the art when the initial wafers were studied in this work.

Problems still remained in studying oxide surfaces with Auger spectroscopy, but they were much more subtle than those described in the previous paragraph. Seemingly reproducible, stable, peaks were found on biased specimens which required unusual interpretations. Naturally, the critic of prior work can not say

absolutely that the published interpretations are in error, since the individual specimens can not be studied again with the improved methods presented in Chapter VI. However, for many of the interpretations there is no supporting evidence and many of the questionable peaks were duplicated, and shown to be artifices, on other insulator surfaces. Additionally, peaks were found where no known Auger peak is located. These peaks had to be ignored in the interpretations.

The critique in Chapter II of previous interpretations is obviously based on the experience gained throughout the experimental work for this dissertation, even though the justification for each of the criteria used in Chapter II lies in the basic theory of the Auger effect. In reality it was the difficulty of explaining results from biased specimens that forced a serious evaluation of the charging problem. The first quantity studied in this evaluation was specimen current. The unusual variations in speciment current, both synchronously and asynchronously with the retarding potential sweep, forced additional study of the secondary emission yield for the oxide surface. This in turn led to a study of the nature of the slow secondary peak for an oxide specimen. The nature of the slow secondary peak and the behavior of specimen current are two valuable indicators of the charge state on an oxide covered specimen. Chapter VI, the following chapter, is a very complete description of the charging problem on oxide covered specimens. Each of the phenomena found in this study is described, its effect on the Auger spectrum is shown, and a method of preventing or detecting it is given.

CHAPTER VI

ARTIFICES ON OXIDE SURFACES

The previous chapters have pointed out that many anomalies are possible when using Auger spectroscopy to study practical insulator surfaces. This chapter is an attempt to categorize these difficulties, present a qualitative model for their origin, and give a method of detecting or eliminating each. Silicon dioxide will be the insulator of interest, but the discussion should also apply to other electrical insulators.

Five specific problems associated with charging of oxide surfaces are discussed in the following sections. As an introduction to these discussions, a comment will be made based on experience in studying a variety of insulator samples. Specimens may be classed according to the distance an electron must travel to reach an electrical contact after entering the solid. Insulator specimens in the form of a thin film, a few hundred angstroms thick, on a conducting substrate behave well with few charging problems. They are similar to conductors or semiconductors. Insulator specimens in the form of a film of micron thickness will support a significant voltage drop between the contact and surface. The charging problems associated with these specimens are difficult but can be handled. Insulator specimens of millimeter thickness are extremely difficult to handle. The magnitude of the charging problem is thus correlated with the difficulty a charge distribution on the surface has in communicating with the electrical contact

to the specimen.

The first section discusses simple charging to a uniform potential by an oxide surface. This is a simple case to handle. The second section discusses the case when the surface does not charge to a uniform potential, but instead charges to different potentials in different regions. The third section discusses the situation when the charge state of an oxide is not constant in time, with emphasis on the correlation between charge state and retarding potential of the energy analyzer. The fourth section is concerned with loss peaks and charge states which behave in a fashion similar to loss peaks. The fifth section considers electrical breakdown of oxide films and the final section is a compilation of the tests and rules introduced in this chapter.

Simple Charging to an Uniform Potential

Two conditions are necessary for Auger spectroscopy to be successful on oxide surfaces. The charge distribution must reach a steady state, that is, it must be constant in time. The charge distribution must also be such that the potential in the Auger escape volume is uniform. If the charge distribution is constant throughout data accumulation, then it is possible to deduce the potential in the Auger escape volume if, and only if, the potential is uniform through this volume. It is convenient to consider the Auger escape volume as a thin planar film residing on a substrate, the remainder of the specimen. In this section we shall assume that the potential is uniform over the film and consider only the possible potential variation as one passes through the film and into the solid.

If the potential in the Auger volume is found and is uniform over the volume,

then the spectrum can be interpreted by merely considering the potential difference between the escape volume and the electrical contact to the specimen to be part of the retarding potential. If the potential is not uniform, then the measured spectrum is the summation of spectra from each little volume characterized by some potential. Such data is of little use. On the other hand, if the potential changes during the run, then a variety of artifices are introduced.

A model for the electronic band structure and the nature of the interaction between the primary beam electron and the oxide will now be introduced. The mechanism by which a steady state charge distribution is achieved will be described and compensation for the resulting surface potential is illustrated. Finally, the nature of the slow secondary peak of a charged insulator surface is explained.

The oxide formed during device fabrication is typically a glassy, amorphous solid with only short range order. Nevertheless, a simple energy band structure will be postulated, with the many defects of the solid giving rise to states, or traps, in the energy gap. The energy gap is taken as 8 eV and the barrier between the valence band in the silicon substrate and the conduction band in the oxide is taken as 4.25 eV. Excess silicon in the oxide will act as a donor when ionized by electron bombardment. Sodium and other ionic impurities will act as donors activated by thermal energy. Traps from other defects presumably can be ionized either way and can act as recombination centers.[53] Given this model, the process by which the incident primary electron disturbs the charge distribution in the oxide may be traced.

The energetic primary electron creates a cascade of fast secondaries as

it suffers inelastic collisions. These fast secondaries in turn lose energy in collisions until the majority of those which escape the region possess energies of the order of ten electron volts above the top of the valence band. The incident primary electron loses its energy, more or less uniformly along its path, while traveling a distance similar to the transverse path length discussed in Chapter IV. This distance is a few hundred angstroms for 1 keV primaries and a few thousand angstroms for 5 keV primaries. Most of the secondaries in the cascade have energies which place them in the conduction band of the oxide. It should be recognized that the primary beam really creates hole-electron pairs. However, the mobility-lifetime product of the electrons is greater than that of the holes, so the dominant free charge carriers are electrons.[53]

The mechanisms by which conduction band electrons can be scattered, lose energy, and eventually return to the valence band are of interest. Conduction band electrons are primarily scattered by lattice vibrations and ionized impurities. Electron-phonon interactions are the primary cause of inelastic scattering at room temperature in a clean oxide. Finally, recombination takes place primarily at the traps caused by imperfections in the solid.[54]

Secondary yield, or emission ratio, is the number of electrons emitted from the surface per incident primary electron. A hypothetical secondary yield as a function of primary beam energy curve is shown in Figure 48. The two energies where the yield is one are noted as E_1 and E_2. Most materials, particularly oxides, will have a maximum yield greater than one so that E_1 and E_2 exist. If the electrical contact to the specimen is removed, the specimen will charge to

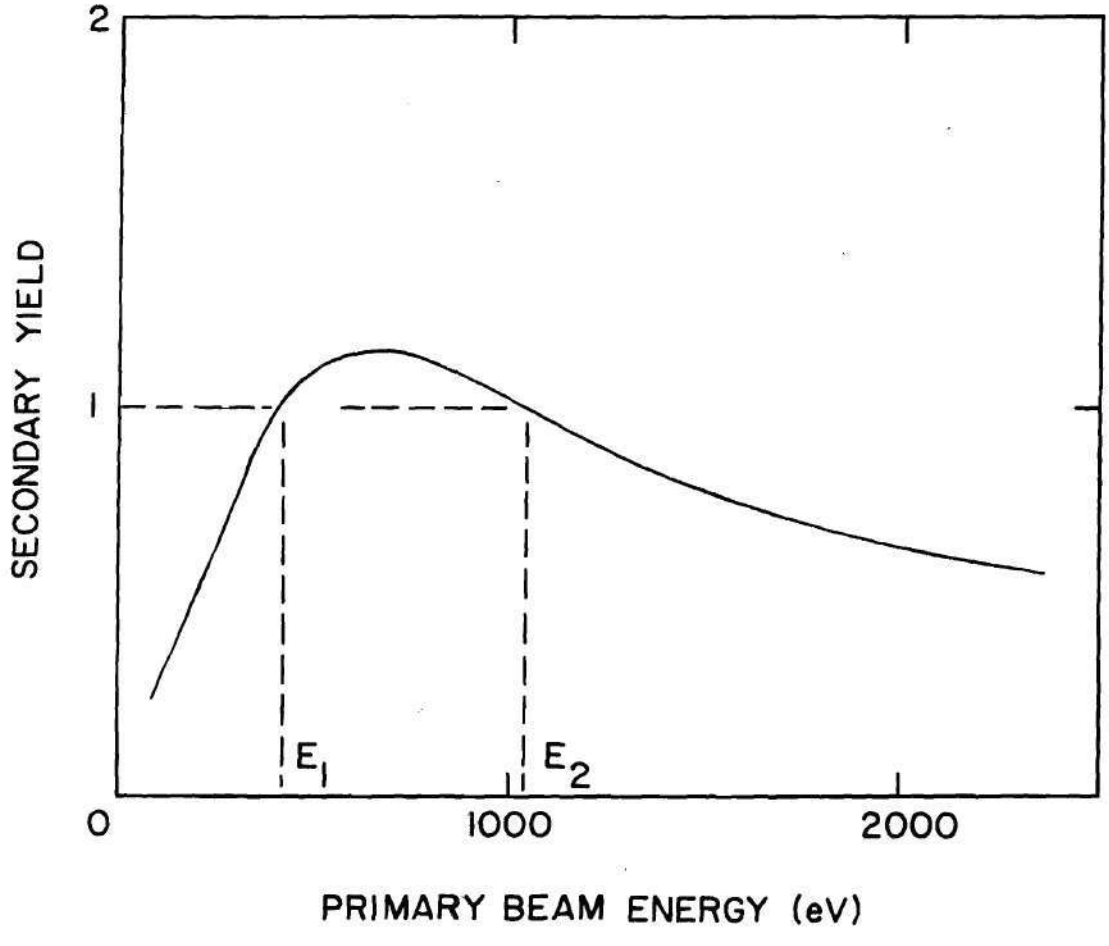

Figure 48. Secondary Electron Yield as a Function of Primary Beam Energy for a Typical Specimen.

some steady state potential. The abscissa of the plot is then equal to the product of the electron charge and the difference in potential between the electron gun cathode and the surface of the specimen. As is well known, there are two stable states. If the initial primary beam energy is less than E_1, the specimen collects negative charge, as the yield is less than one; the surface charges to the cathode potential and beam current to the specimen goes to zero. If the initial beam energy is greater than E_1, the specimen charges so that the effective beam energy is E_2; the net current to the specimen goes to zero although both the primary beam and emitted secondary currents continue to flow. The above situation is realized if the distance through the oxide from the bombarded surface to the electrical contact is infinite. The situation is modified by the extent to which charge can flow from the bombarded region to the contact and the potential drop caused by this charge flow.

The physical origin of the secondary yield curve is straightforward. The secondary cascade grows in number as the primary energy is increased from zero. However, the observed secondary emission is the product of the secondary electron generation function and the transport function which carries the secondary from its point of creation to the emission surface. As the beam energy is further increased, the secondaries are created more deeply in the solid and the transport function decreases, reducing the net yield.

Figure 49 illustrates the types of charge flow in and out of an imaginary Gaussian surface. The net charge flow must be zero in the steady state. One manner of satisfying this requirement is to have the secondary emission ratio one;

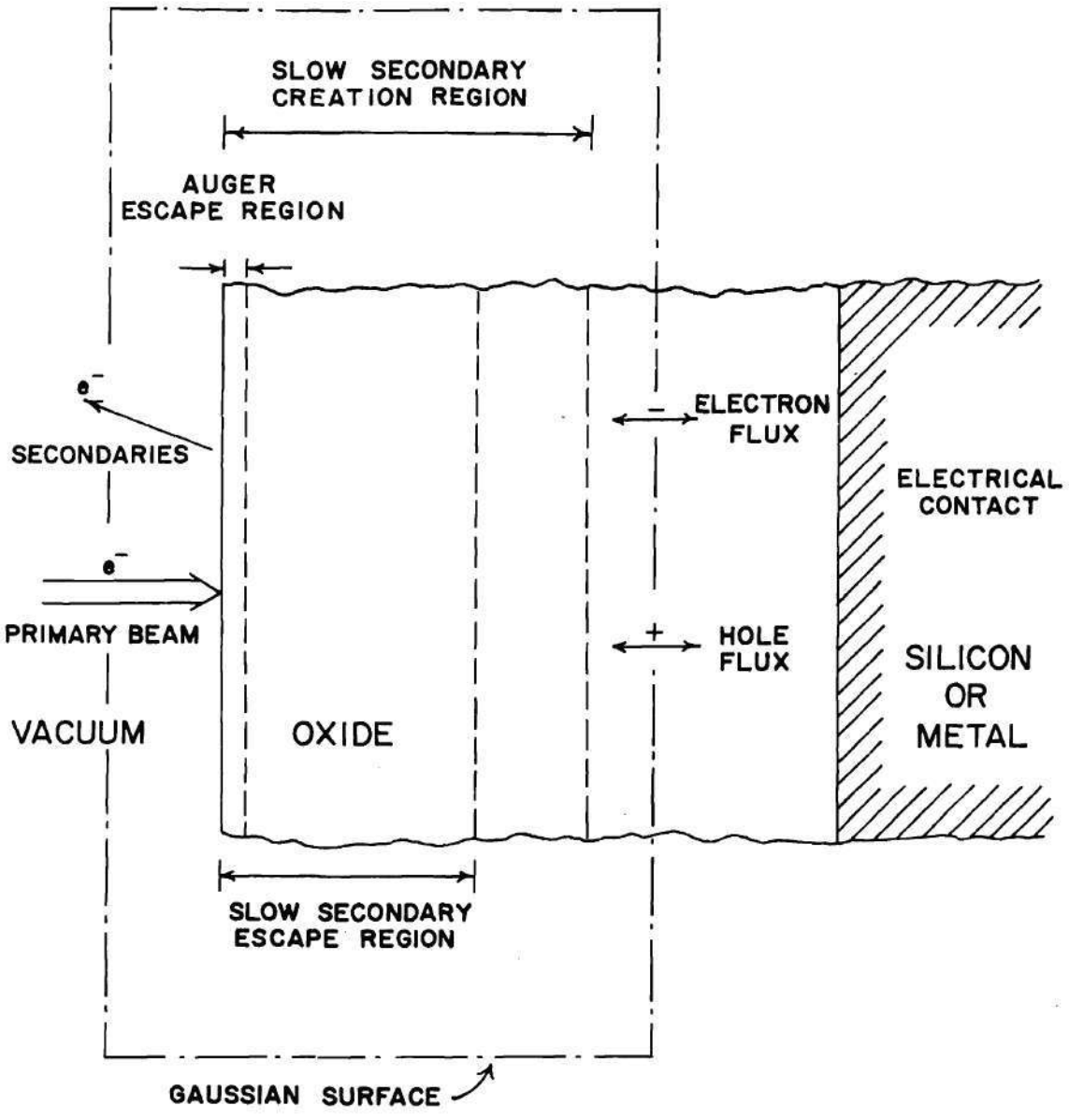

Figure 49. Schematic Representation of Charge Flow Through a Gaussian Surface.

the electron and hole flux to the contact may then be zero. In general, the secondary emission ratio will be different from one and some charge flow between the oxide and contact will exist.

The ideal charge flow condition for Auger spectroscopy is the situation which balances the potential in the Auger escape volume with that of the contact. Following MOS terminology, this is the "flat band" condition. It is illustrated in Figure 50 for SiO_2 with a silicon contact.

Consider a net flow of charge into the oxide from the left, given by the primary beam current minus the emitted secondary current. The steady state criterion requires some charge flow through the right side of the slow secondary creation region to the contact. The case of a small net electron flow to the contact will be considered first.

A small net electron flow from the oxide to the contact implies that the secondary yield is slightly less than one. There is a high concentration of electrons in the conduction band in the slow secondary creation region compared to the remainder of the oxide; these conduction band electrons result from primary beam ionizations. The consequence is a diffusion of electrons to the right towards the contact. Some of these however will be trapped in the oxide and give rise to a fixed negative charge distribution. Thus, a potential barrier will be created opposing the diffusion flux. If the oxide is thin, the amount of trapping is small and the band bending is minimal.* This is the case when the oxide is barely

*The term "minimal" is obviously qualitative. A "minimal" potential drop across the oxide would be one sufficiently small to neglect, e.g., the order of a volt.

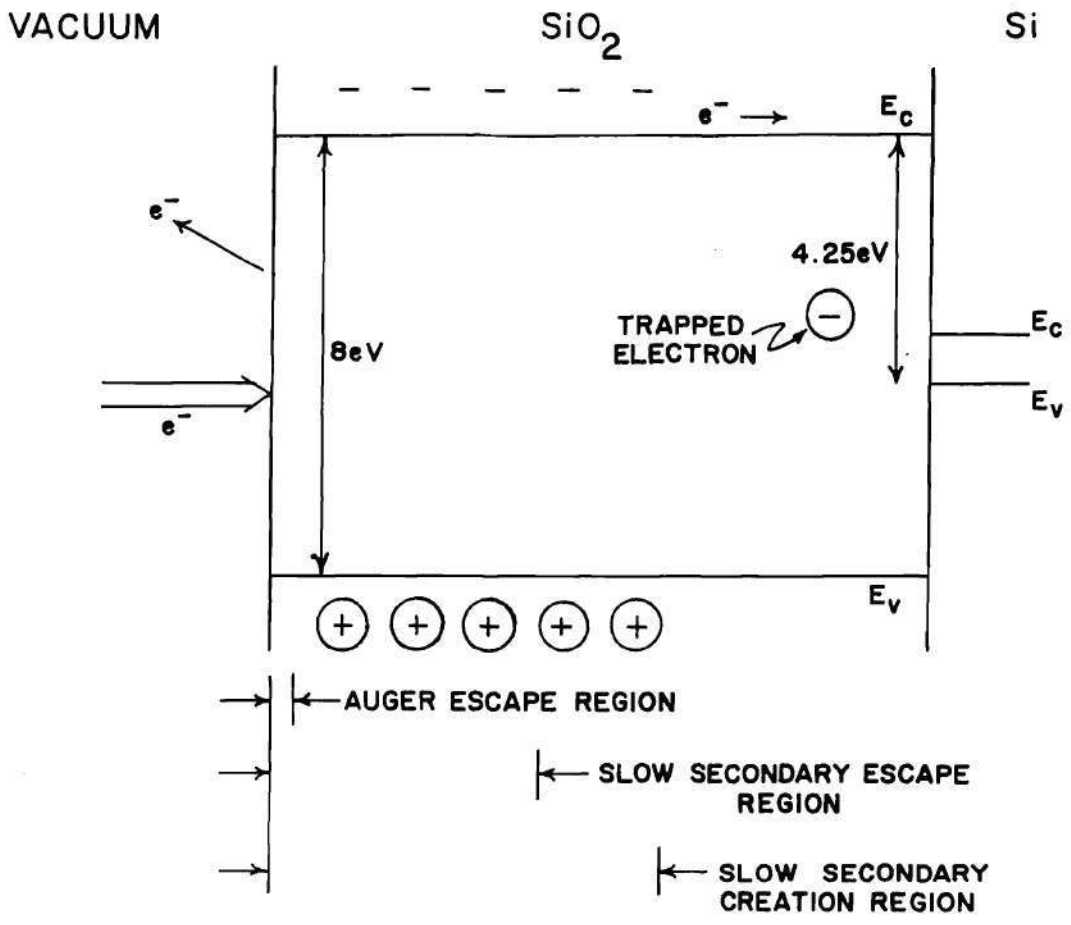

Figure 50. The Electronic Band Structure in SiO_2 When There is No Charging Problem.

thicker than the secondary creation region. As a consequence, thin oxides behave well with no charging problems.

Consider now the case when a small negative flow from the contact to the slow secondary creation region is required. This is the case when the yield is slightly greater than one. The barrier, 4.25 eV for valence band electrons, obviously precludes much injection from the silicon into the oxide. The alternative is to have a net flow of holes to the right, from the secondary creation region to the contact. The mobility of holes is low in the oxide and their lifetime short. To affect a hole current requires an electrostatic driving field. Since the secondary yield was postulated as greater than one, the surface region charges positively until equilibrium is established by hole current to the contact. Only a small hole current is allowable if the potential drop is to be minimal.

The surface will charge negatively with respect to the contact whenever a significant electron flow from the surface to the contact is required, or when the distance for electron flow through the oxide is great. In either case the traps become negatively charged to a significant degree and the barrier prevents any diffusion current from flowing. A driving field is obtained when the secondary yield is significantly less than one. The surface volume charges negatively until a sufficient electrostatic field is established to drive the electrons to the contact and restore equilibrium. The surface potential is negative of the order of tens of volts compared to the contact.

The requirement for a significant electrostatic driving field to move charge across the oxide to the contact prevents space charge neutrality in the slow

secondary creation region. Space charge neutrality will only exist, even approximately, in the slow secondary region when the required voltage drop across the oxide is of the order of a volt or less.

The case when the secondary yield is significantly greater than one, and the oxide thick, requires a significant hole flux to the contact, implying a positive potential in the slow secondary creation region with respect to the contact. This is illustrated in Figure 51. The surface region is of the order of tens of volts positive with respect to the contact. There is a net positive charge in the secondary creation region which gives rise to the electric field and potential gradient shown. Notice that the potential variation through the Auger escape region is very slight, a fortuitous circumstance indeed.

The electrostatic field required across the oxide depends on the amount of charge transported through the oxide and the distance it must travel. These arguments suggest two rules for Auger spectroscopy of oxide surfaces. These will help prevent charging problems; rules introduced later in this chapter will be also concerned with detection of charging problems.

1. (Prevention) Minimize oxide thickness, if allowable by other requirements of the experiment. A smaller driving field will be required to establish an equilibrium condition.

2. (Prevention) Chose a primary beam energy close to E_2, as defined in Figure 48. Having the secondary yield approximately one minimizes the net current to be transported through the oxide.

These rules were initially deduced empirically. It was found experimentally

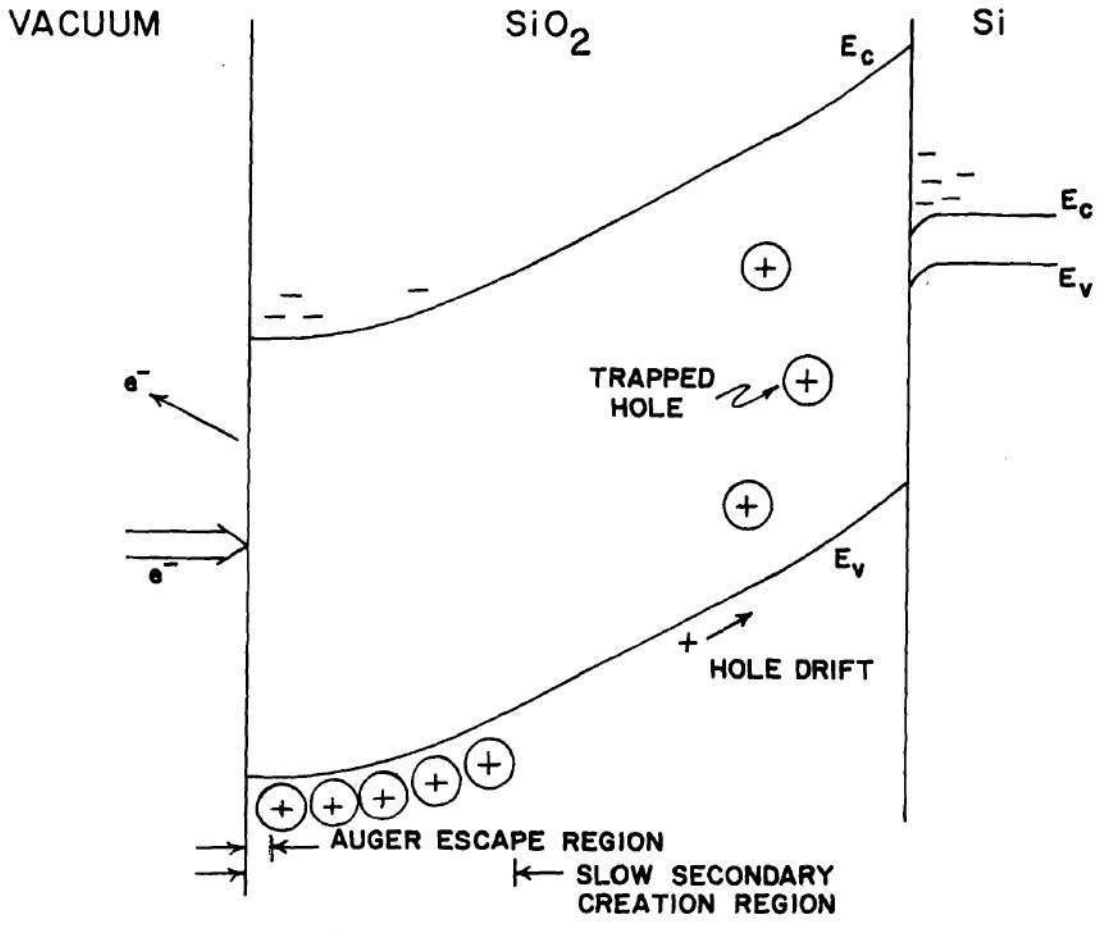

Figure 51. The Electronic Band Structure in SiO_2 When the Surface is Charged Positively with Respect to the Contact.

that the most stable charge state is that of the surface very slightly positive* with respect to the contact. It was also found that in general small contact currents are associated with stable charge states. These empirical rules are justified by the above model.

The statement was made at the beginning of this section that if the potential over the Auger escape region were uniform and stable, it could be measured and the spectrum compensated for the shift in the energy axis. This process will now be described.

Figure 52 is a spectrum, as recorded, for the oxide on a transistor wafer after the emitter masking step. The slow secondary peak is seen to begin at 52 eV. These slowest secondaries to escape the solid are characteristic of the potential in the Auger escape region. These secondaries entered the analyzer with 52 eV of energy. If they left the solid with essentially no kinetic energy, the 52 eV represents a potential drop of 52 volts between the analyzer and specimen surface. Now the carbon peak is located at 324 eV; since there was a 52 volt drop between the analyzer and specimen surface, the kinetic energy of the Auger electron as it left the solid was

$$324 - 52 = 272 \text{ eV}. \tag{69}$$

The work function effect of the analyzer is the same on both the slow secondaries

---

*The advantage of having the emitting surface slightly positive with respect to the contact and the remainder of the specimen is described in a following section on time varying charge states.

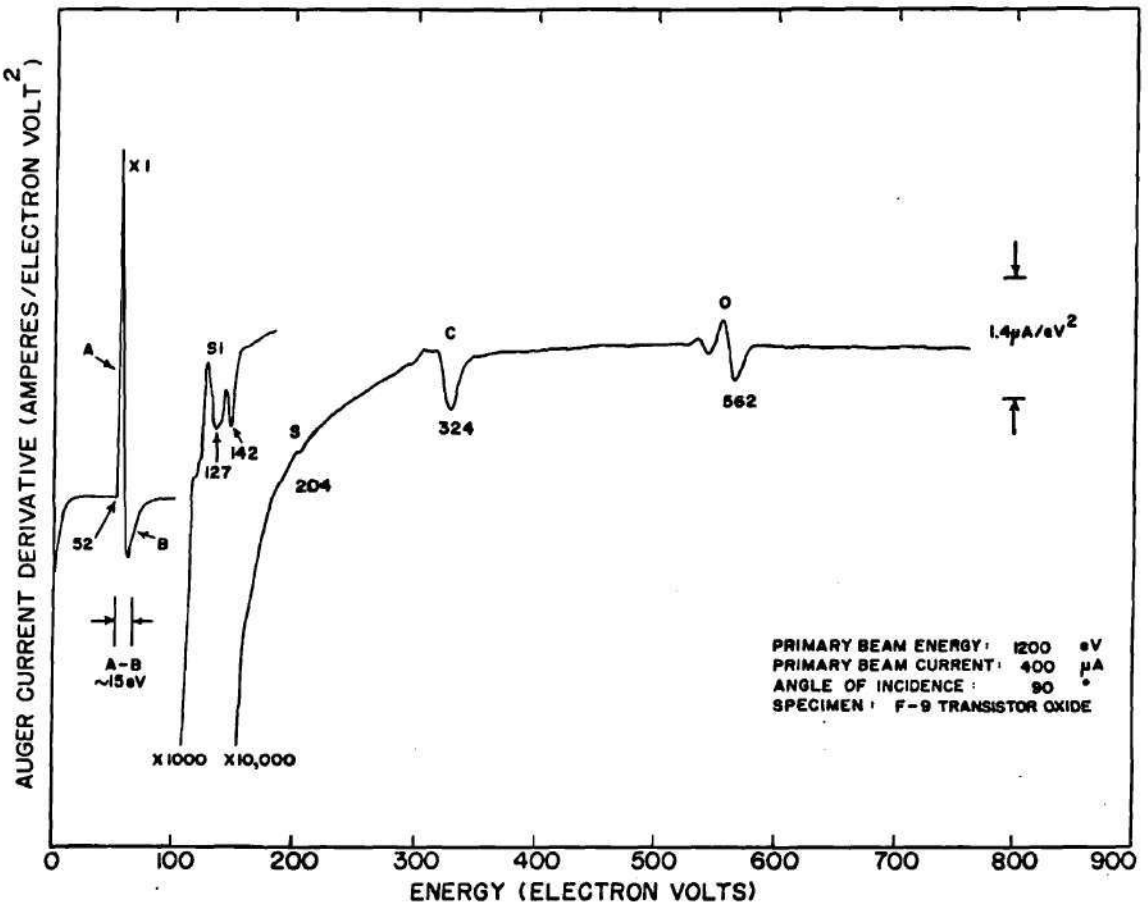

Figure 52. Example of Determination of Surface Potential from the Auger Spectrum.

and the Auger electrons, so it is ignored. As another example, the corrected energy of the sulfur peak is 152 eV, and the corrected energy of the other peaks may be obtained similarly. If the slow secondary peak is not shown, it is necessary to use an unambiguous peak, such as carbon, as a reference. Unless noted otherwise, the energy axis correction was made on all spectra in this work before reproduction.

Two comments may be made about the spectrum of Figure 52. The specimen contact was biased at -50 volts during the run. This biasing often improves the stability of the charge state, as explained in a later section of this chapter. The net difference in potential between the Auger escape region and the contact was -2 volts. The primary beam energy was 1200 eV; the effective energy, determined by the potential drop between the cathode and specimen surface, was therefore 1148 eV. This energy is very close to E_2, so the secondary yield was close to one. This is a desirable operating state.

The second comment concerns the width of the slow secondary peak for this thick oxide specimen. If one defines a full width at half height, indicated in the figure as the energy difference between points A and B, it is found to be about 15 eV in this spectrum. Similar measurements on a graphite specimen and a molybdenum specimen gave 5 eV and 7 eV, respectively. If the measurement is made on a thin oxide on a conducting substrate, a width of 5 to 7 eV is found. This width of the secondary peak for a thick oxide indicates a change in potential through the secondary escape region. Since the Auger escape region is only a fraction of the slow secondary escape region, it is possible to have negligible

potential variation (less than one volt) through the Auger region, but significant (ten or more volts) variation through the secondary region.

Obviously the observed secondary peak is a summation of electrons of different energies excited from different depths. Any barrier at the surface, an accelerating one from a positively charged surface or a decelerating one from a negatively charged surface, will drastically alter the observed energy distribution of the escaping secondaries. Correlating the slow secondary peak shape with a quantitative description of the potential variation through the escape region would be very difficult and was not attempted.

Another example of the degree to which the slow secondary energy distribution may be altered by potential variations inside the secondary escape region, and yet the potential within the Auger escape region remain well defined, is given in Figure 53. This specimen was a wafer taken after base diffusion. The specimen bias was -150 volts; the energy axis is not corrected. The initial rise of the slow secondary peak is at 120 eV, implying that the Auger escape region is 30 volts more positive than the contact. The full width at half height, the energy difference between points A and B in the figure, is approximately 30 eV. The Auger peaks show normal resolution, so one would conclude that the potential variation through the Auger escape region must be less than a volt or so. If the Auger peak locations are measured with respect to the initial rise at 120 eV, they are found at the correct energies. An example of distinct domain formation is shown in Figure 54. The specimen was a bulk polycrystalline silicon carbide sample. Silicon carbide is a semiconductor, but the long path length to the contact,

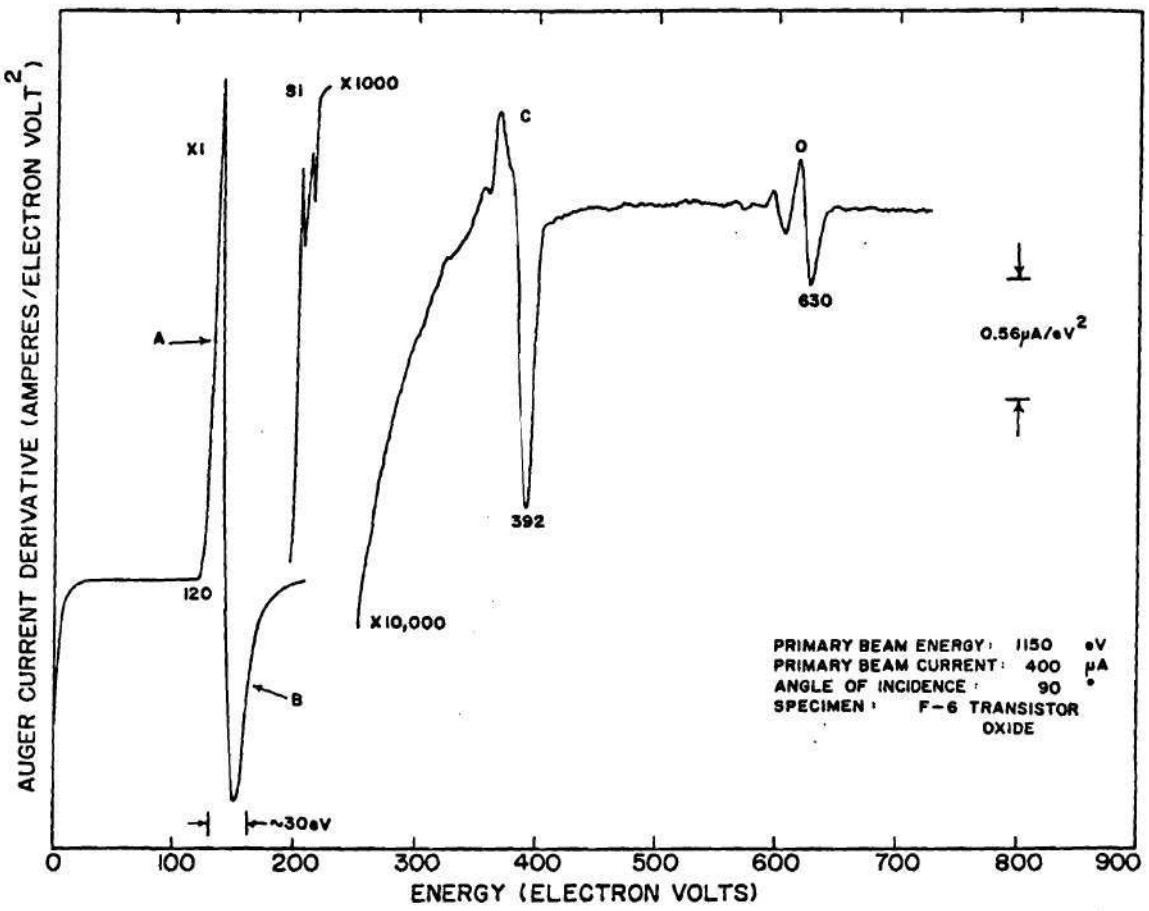

Figure 53. Auger Spectrum and Secondary Peak from an Oxide Surface.

about 1 centimeter, caused a surface charging problem. The slow secondary peak is shown for three runs. Run No. 1 was made with a 4 millimeter spot diameter. Three peaks, labeled A, B, and C, are seen. The primary beam was then reduced to a 2 millimeter spot diameter, with correspondingly less total current. Only peak C remains in curve No. 2. The curve was stable in time, being reproduced several times. The primary beam was then returned to its original 4 millimeter diameter for run No. 3. Peaks A and B returned essentially as they were originally. The implication is that peaks A and B are associated with the region irradiated in runs 1 and 3 but not irradiated in run 2.

The specimen contact bias in Figure 54 was -150 volts. The initial rise in runs 1 and 3 is at 142 eV, showing a positively charged surface with respect to the contact, and the initial rise during run 2 is at 153 eV, showing a negatively charged region. Such a variance is not at all unusual with semiconductor or insulator specimens.

A comment about the effect of carbon deposits and particles on the charging problem is worthwhile to interject at this point. It is well known that the electron beam will decompose carbon bearing gases on a surface in a vacuum system.[9] This problem is particularly apparent in the scanning electron microscope. The vacuum in the typical scanning microscope is only of the order of 10^{-5} torr during operation. One particular specimen in this research was scanned for ten minutes and then returned to the Auger spectrometer. Enough carbon was deposited on the specimen so that no Auger peaks from the substrate were visible. Thus, it is obvious that many monolayers of carbon may be deposited quickly in the scanning

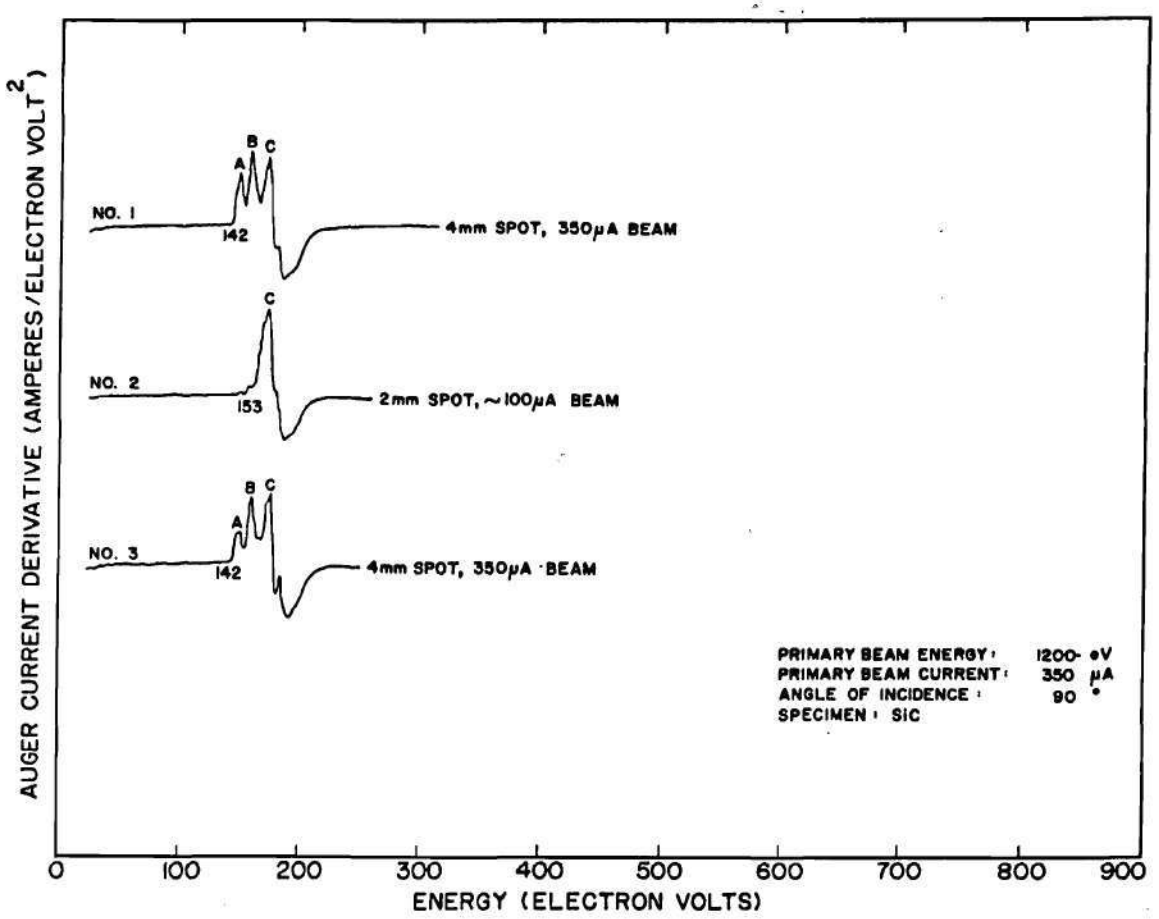

Figure 54. Example of Charge Domain Formation on an Oxide Surface.

microscope. These deposits are a function of electron beam exposure and are not uniform across the surface. Since carbon is characterized by a much lower secondary yield than most insulators, it is not surprising that carbon deposits charge to a different potential than the remaining insulator surface. Images formed in the scanning microscope by collecting the slow secondaries, the typical method, will be affected by the irregularly charged carbon deposits. This is a well known rule of thumb in scanning microscopy. However, this rule of thumb does not apply to most situations in Auger spectroscopy. Pressures are a factor of 10^4 lower in Auger spectrometer vacuum systems, and carbon build-up is not normally observed in such clean systems. The residual carbon found on typical specimens is a monolayer or so thick, not tens of monolayers. Such monolayer coverages on Auger specimens will not cause charging problems by supporting a significant potential difference. On the other hand, the presence of distinct particles, with thicknesses of the order of a hundred angstroms or more, can cause charging problems. Thus, one must be careful when attributing charging problems to "carbon."

Splitting of Auger Peaks

The two conditions necessary for successful Auger spectroscopy of insulator films are that the charge state be constant in time and that it be uniform across the irradiated surface of the film. Conditions which violate the spatial uniformity criterion will now be considered.

The previous section showed that the surface potential is determined by the magnitude and polarity of the charge to be transported across the oxide in the steady

state, and by the distance the charge travels through the oxide. The surface potential in the Auger region is primarily determined by the conditions prevailing in the immediate interior of the solid. Thus, one would expect a variation in surface potential if the oxide varies in thickness across the irradiated region. A significant change in the density of traps across the irradiated region will also affect the surface potential. Neither of these conditions can be changed by the spectroscopist; he can only decrease the primary beam diameter so that the remaining Auger escape region has a more uniform potential.

The remaining factor influencing the surface potential is the current density of the primary beam. A constant current density across the beam, like that given by the Pierce gun, will give rise to a uniform potential in the Auger escape region if the oxide thickness and trap density are constant across the irradiated portion. Two more rules for successful study of oxide surfaces, therefore, follow.

3. (Prevention) Use a primary electron beam with as small a diameter as possible, so as to minimize the effects of oxide variations.

4. (Prevention) Use a primary beam with a constant current density. This insures that all portions of the oxide under the irradiated region have the same current flow through them.

The formation of distinct domains, each with its characteristic potential, is an interesting phenomena. Each domain will contribute a distinct spectrum, shifted in energy with respect to each other, to the composite spectrum for the specimen. The overlapping of the peaks in the composite spectrum causes the

"split" appearance. The potential can also vary continuously across a surface which charges nonuniformly. If the potential variation is only a few volts, the composite spectrum appears to have lost resolution. If the variation in potential is greater, no distinct peaks appear in the composite spectrum.

Time Varying Charge States

Conditions which violate the criterion of a steady state charge distribution will now be discussed. Artifices caused by a time varying charge state may conveniently be divided into those which are synchronized to the retarding potential sweep and those which are asynchronous. The retarding potential analyzer has a distinct disadvantage in that the electrons with insufficient energy to climb the barrier are reflected back to the specimen surface. Obviously, the number returned varies during the sweep of the energy axis in recording a spectrum. The resulting change in charge state of the surface is synchronized to the sweep. This problem will be studied first.

Recall that the retarding grid analyzer uses a negative potential applied to a grid to prevent electrons of insufficient energy from reaching the collector. The grids are spherical and the specimen is positioned so that electrons emitted from the specimen travel on radial paths with respect to the grids. If there are no residual electrostatic or magnetic fields in the analyzer other than the radial retarding field, and there should be no other such fields, then the electrons repelled by the retarding grid are returned towards the specimen surface from which they originated. The action of the ideal retarding grid is that of an 180^{o} elastic

collision. Since most secondary electrons have initial kinetic energies of an electron volt or more, one would expect the returned electrons to re-enter the solid. This behavior may be contrasted with thermionic emission, where the average energy of the emitted electron is a fraction of an electron volt and the tendency is to form a space charge and a "virtual cathode." Space charge formation was not noted under normal operating conditions in this work.

The majority of the electrons emitted from the surface have energies less than 100 eV, as was illustrated in Figure 2. The secondary yield for such slow secondaries returned to the specimen is a small fraction of one. Therefore, there are really two electron fluxes impinging on the specimen: the primary beam and the reflected secondaries. The problem is to compute the potential of an insulator as the retarding grid potential is swept from zero to a high negative value. This is accomplished by constructing a secondary yield plot for the sum of the two incident fluxes, with retarding potential as a parameter.

Consider the situation shown in Figure 55. Assume for the moment that the secondary yield curve, curve A, is for a conductor. A primary beam of electrons with energy E_p is directed at the surface. The secondary yield is δ_p. For each primary electron bombarding the surface, δ_p electrons leave the surface. According to Figure 2 the great majority of these are slow secondaries. Define an energy E_s characteristic of the secondary electrons. It will be a low energy, in the neighborhood of 50 eV. Some $K\delta_p$ of these electrons will be returned to the surface by the retarding grid. The function K is the product of two factors

$$K = k_v \, k_f \tag{70}$$

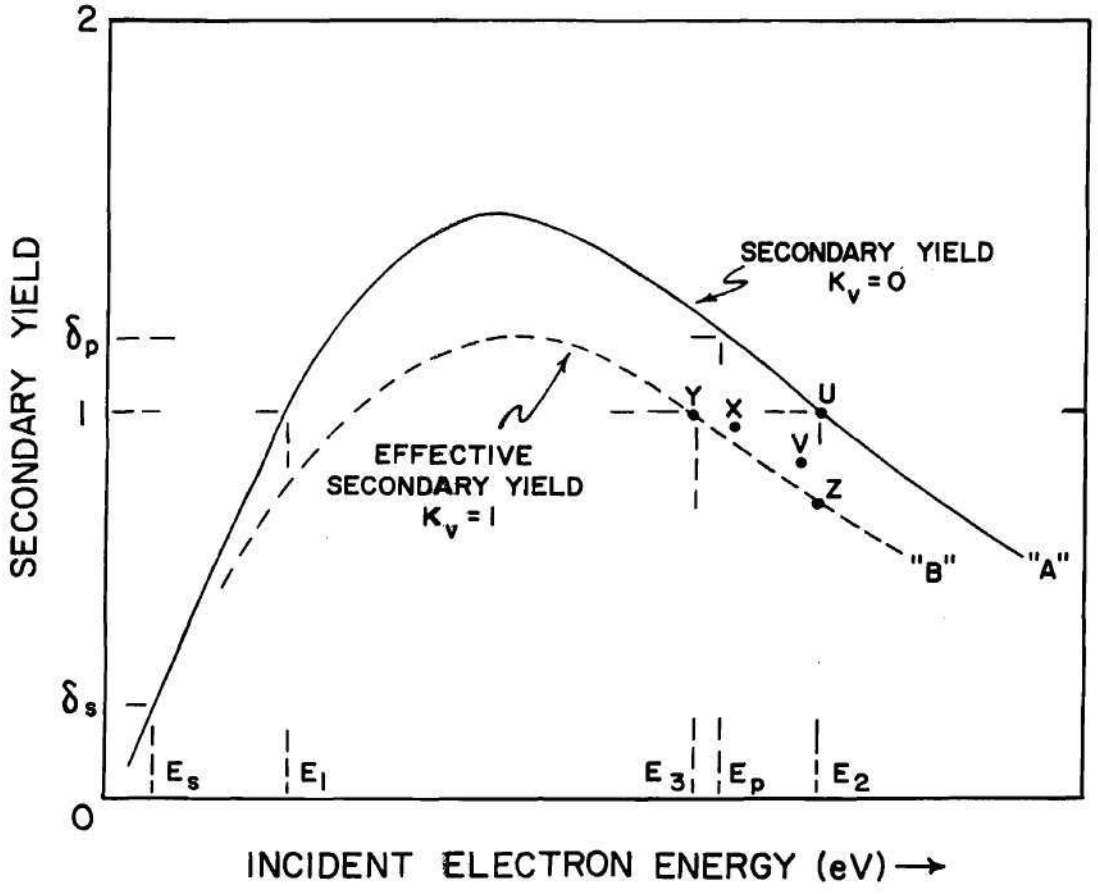

Figure 55. Secondary Yield Curves and Operating Points in a System with a Retarding Potential Analyzer.

where k_v expresses the fraction of the secondaries repelled by the retarding grid, and k_f expresses the fraction of those repelled electrons which actually return to bombarded area of the specimen. If there are no stray fields in the spectrometer and the grids are perfectly spherical, etc., k_f is one. When the retarding potential is zero, k_v is zero; k_v is almost one if the retarding potential is greater than, say, 100 volts. The $K\delta_p$ electrons characterized by energy E_s have a secondary yield δ_s, so $K\delta_p\delta_s$ leave the surface. The process continues, but the remaining terms are small enough to neglect. The above terms may be summed to give the net electron current I_e into the specimen surface, per incident primary.

$$I_e = 1 - \delta_p + K\delta_p - K\delta_p\delta_s = 1 - \delta_p[1 - K(1 - \delta_s)] \qquad (71)$$

The effective secondary yield δ_E for primaries of energy E_p is defined by the expression

$$\delta_E = \delta_p[1 - K(1 - \delta_s)]. \qquad (72)$$

The effective secondary yield is always positive and less than δ_p, since K is less than one and δ_s is a small positive number less than one. The factor multiplying δ_p in the effective secondary yield expression is approximately constant for retarding potentials greater than 100 volts. It is independent of E_p, if E_p is greater than 100 eV, because the normalized energy distribution function for secondaries is unchanged at higher primary energies. Thus, we can define the effective secondary yield as a constant fraction of the original secondary yield over the above domain. This curve, B, is shown in the figure for a typical value of k_f and δ_s. The effective

secondary yield for smaller values of retarding potential lies between the two curves shown. For example, when the retarding potential is zero, the effective secondary yield is the original secondary yield, curve A of the figure, since no electrons are repelled back to the specimen by the retarding grid.

Insulator specimens have an effective secondary yield defined in the same manner. In addition, the insulator specimen must have a stable charge state. When the specimen is isolated, we know there are two stable states: (1) the specimen charges negatively to cathode potential, or (2) the surface potential adjusts itself so that the effective secondary yield is one, and the derivative of the secondary yield with respect to incident electron energy is negative. Obviously, if the initial stable state is E_2, point U in Figure 55, when the retarding potential is zero, the stable state will change to E_3, point Y, as the retarding grid is made negative and electrons repelled back to the specimen. When an insulator specimen has some charge flow between the surface and electrical contact, the stable state will start at E_2 and move towards E_3 as the retarding potential is increased. If the insulator is a very thin film, then one observes a small shift in surface potential to point V; if the film is thick, then the shift in surface potential will be greater to point X. Finally, if the specimen is a conductor, the surface potential will remain constant, and only the secondary yield will change so that the operating point moves from U to Z.

Let us next consider the influence of the stray field factor k_f and the behavior of specimen current, current to the specimen contact, as the retarding potential is swept. The discussion associated with Figure 55 showed that there

will be a significant shift in surface potential with a thick insulator as the retarding potential is swept. Such a change in potential would make Auger spectroscopy impossible with a retarding grid analyzer. Equation 72 for the effective secondary yield reduces to $\delta_E = \delta_p$ if K is zero. This can be accomplished by having k_f, the fraction of the electrons repelled by the retarding grid which actually return to the specimen surface from which they originated, be zero. The convenient method is to apply a bias potential to the specimen. The first grid of the analyzer and the vacuum chamber walls are at ground potential. A bias potential of a few tens of volts is sufficient to cause a significant deflection in the paths of the slow secondaries, which constitute the bulk of the emitted current. Slow electrons repelled by the analyzer are deflected enough by non-radial field components from the bias that miss the specimen as they return.

Idealized specimen current curves as a function of retarding potential for a conductor specimen are shown in Figure 56. Bias potential is a parameter. Let us assume the primary beam current is one microampere and consider the case when the bias potential is zero. Then k_f is one. Given a secondary yield of two, the specimen current is +1 microampere when $k_v = 0$ and -1 microampere when $k_v = 1$. The principal effect of a positive bias potential is to change the net retarding potential so that the slow secondaries never escape the specimen region because of the potential barrier. Application of a negative bias results in a strong scattering of the repelled slow secondaries. Effectively k_f is zero until energetic secondaries are returned at high retarding potentials.

An understanding of specimen current, as a function of retarding potential,

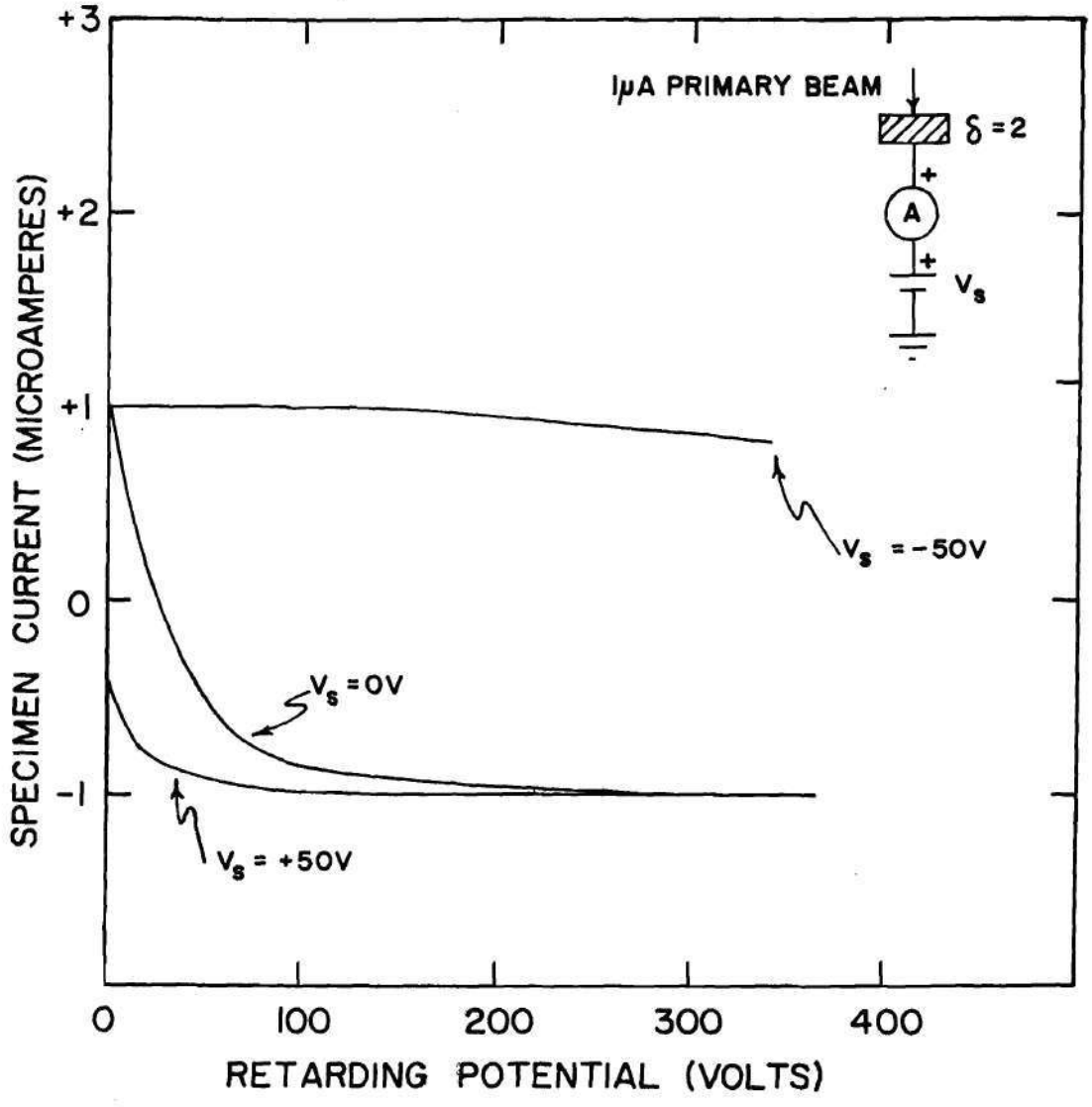

Figure 56. Specimen Current as a Function of Retarding Potential for Different Specimen Bias Potentials.

for insulator specimens requires a more exact model for the action of the retarding grid system. The ideal retarding grid is a 180^{o} elastic scatterer for electrons on a radial path. The real retarding grid system is constructed with grids which are made of wire with a finite diameter and finite spacing. The result is a retarding potential with local variations. Rather than having a scattering angle of $180^{o} \pm 0^{o}$, the real grid system scatters the incident electrons into a sector about 180^{o}. The size of this sector is proportional to the numerical difference between the incident electron energy, expressed in electron volts, and the retarding grid potential, expressed in volts. While the repelled electrons may return to the specimen, they will not return to their point of origin. This effect is important with insulator specimens, since the local surface potential is determined by the number and energy of the electrons incident upon the region.

Figure 57 shows the Auger spectrum for a wafer with a thick oxide. The wafer contained a large number of transistors. The electron beam covered one of these transistors for this spectrum. Superimposed on the Auger spectrum is a recording of specimen (wafer) current as a function of retarding potential, with retarding potential and electron energy being numerically equal. The wafer was biased at -75 volts. The clean slow secondary peak in the Auger spectrum shows that the Auger escape region is characterized by one potential, -73 volts, or +2 volts with respect to the specimen contact. The carbon peak occurs at 345 eV on the uncorrected energy axis.

$$345 - 73 = 272 \text{ eV} \qquad (73)$$

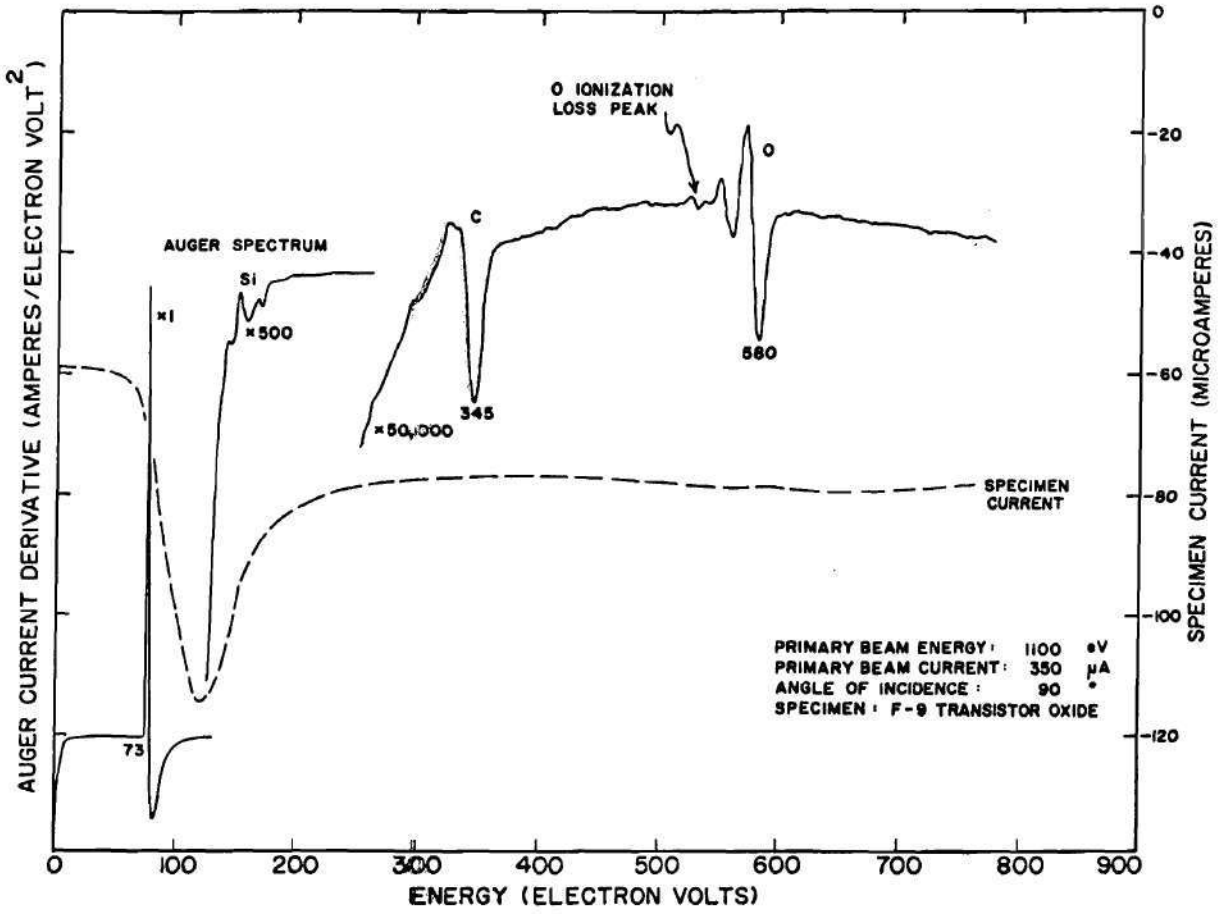

Figure 57. Specimen Current and Auger Spectrum for a Commercial Oxide Specimen.

This is the correct energy, indicating that the surface potential was stable as the retarding grid potential was swept.

Specimen current is constant at approximately - 60 microamperes in the low energy region, below 73 eV where no secondaries are returned to the specimen. The effective secondary yield in this energy region is 0.83. The specimen current becomes increasingly negative as the retarding potential returns secondaries to the region bombarded by the primary beam. The effective secondary yield decreases to 0.67 at 120 volts retarding potential. As the retarding potential is increased further, the retarding grid system scatters them towards other portions of the specimen. Figure 58 is a photograph of a wafer specimen. A typical region bombarded by the primary beam is shown as the small circle added to the photograph. Since the diameter of the wafer and holder is about 3.75 centimeters, the repelled electrons will still be returned on a path striking the specimen even though they will not hit the region bombarded by the primary beam. The oxide outside the primary beam impact area however will see only these low energy electrons. The energy of these repelled secondaries is less than E_1 in Figure 48. Therefore, the oxide will charge negatively. The less charge flow there is between the surface and the electrical contact, the more negative will the potential be. As the scattering of the grid system becomes greater at higher retarding potentials, the charging of the oxide becomes greater and the result is that the slow secondaries are deflected away from the specimen altogether. The constant specimen current, -80 microamperes in this example, at high retarding potentials is the sum of -60 microamperes into the primary beam bombardment area and -20 microamperes into the

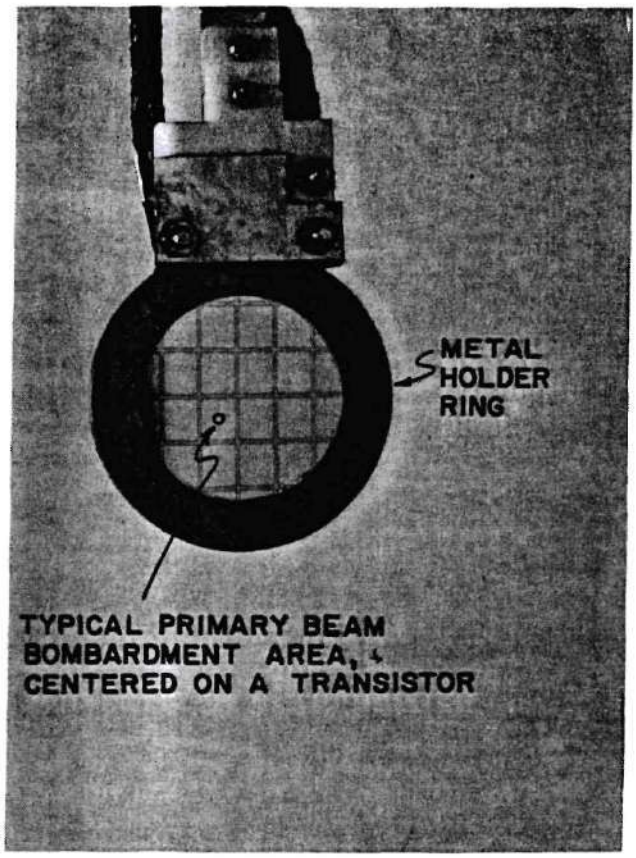

Figure 58. Photograph of Typical Commercial Wafer in Specimen Holder.

metal specimen holder. This behavior of the specimen current with retarding potential was noted consistently on oxide covered wafers. The observed behavior of specimen current for conductor specimens was essentially that portrayed in Figure 56, with the primary variance being the degree of deflection away from the specimen provided by negative bias.

One criterion for successful Auger spectroscopy is, again, that the potential be constant throughout the recording of the spectrum. The effect of specimen bias is to hold specimen current constant as the retarding potential is varied. The potential barrier caused by a positive bias limits the emission of slow secondaries, as indicated in Figure 56. A negative bias, on the other hand, deflects away the secondaries returned by the retarding grid because of non-radial field components. Experimentally it is found that negative bias leads to a more stable charge state. Specimens with only a thin oxide are stable with a few tens of volts negative bias, whereas some thick oxide samples required -150 volts. It is occasionally possible to obtain a stable charge state with zero bias, but the variation of specimen current with retarding potential is much larger than that of the example in Figure 57.

5. (Prevention) Use a negative bias of a few tens of volts when studying oxide covered specimens so as to deflect slow secondaries repelled by the analyzer.

6. (Detection) Monitor specimen current as the retarding potential is swept. Be suspicious of charge states which are accompanied by larger than usual variations in specimen current.

Summarizing, it is possible for the electron current into the Auger escape

region to either increase or decrease with retarding potential. The slow secondaries are scattered more at high retarding potentials, reducing the electron flux to the specimen. On the other hand, an increasing electron flux results from the more energetic secondaries repelled at high retarding potentials. Finally, the surrounding portions of the oxide may charge negatively and cause an additional scattering of repelled electrons.

Several types of artifices caused by time varying charge states will now be illustrated. The most obvious possibility, that the potential changes in the Auger escape region during a run is illustrated in Figure 59. The slow secondary peak is well shaped and the individual Auger peaks show normal resolution, indicating uniformity of potential across the region. However, the Auger peaks do not occur at the proper energy, measured from the beginning of the slow secondary peak. The carbon peak if located 260 eV above the start of the slow secondary peak. The surface potential shifted 12 volts as the retarding potential was swept from 122 volts out to higher values. The potential stabilized by the time the carbon peak was reached because the oxygen peak occurs 238 eV higher than carbon, which is approximately correct.

A second type of artifice occurs asynchronously with respect to the sweep when portions of the oxide on the periphery of the primary beam bombardment area charge negatively to some high potential. This is equivalent to having a second charge domain, except that the total primary current into the negatively charged domain is small, so that the secondary peak is comparable to Auger peaks in magnitude. Two such peaks appear at 520 eV and 720 eV in Figure 59. One characteristic

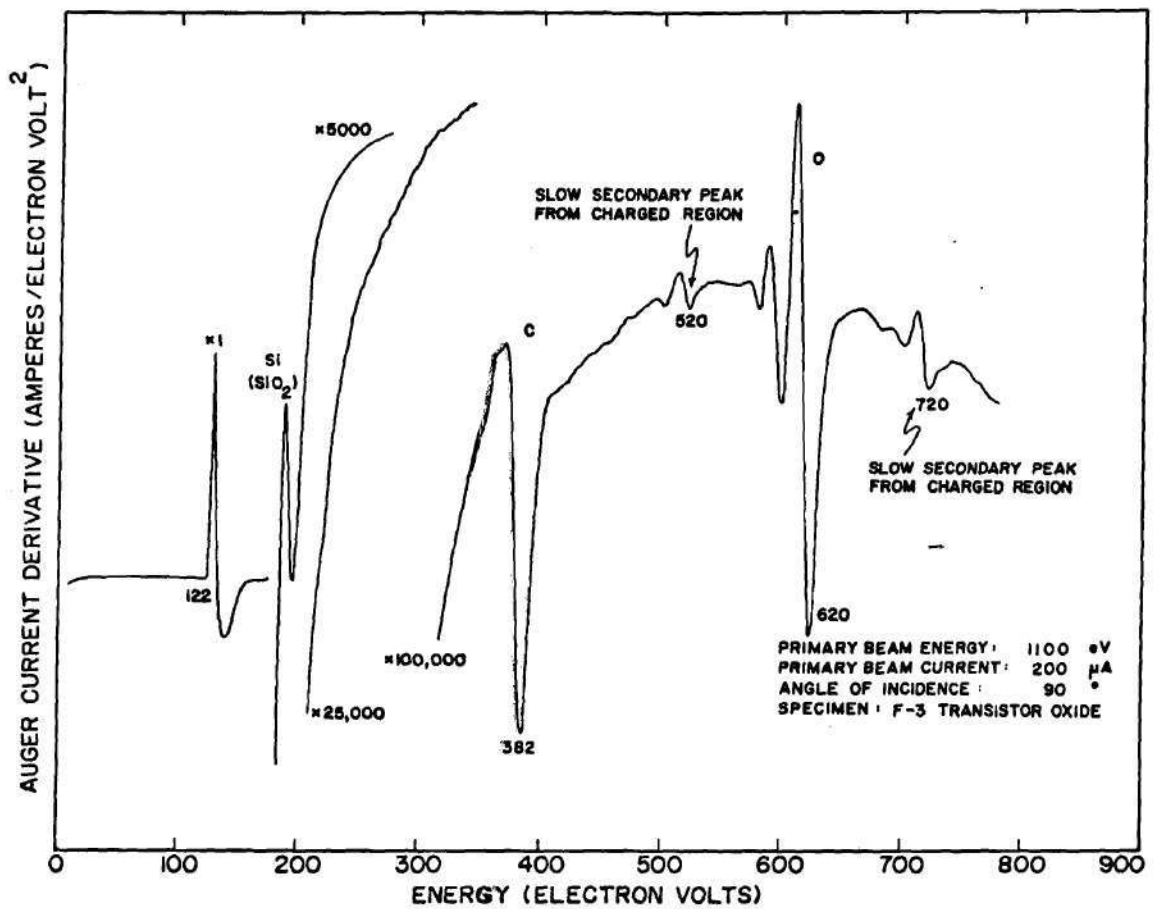

Figure 59. Example of Peaks in Auger Spectrum from Charged Region.

of these peaks is that they tend to move slowly to higher energy levels. The relaxation time for fixed charge in an oxide is very long, often hours or even days. These domains appear to accumulate fixed negative charge, with the rate of increase becoming less in time. For example, the potential might change at a rate of -0.01 volts per second after a few minutes exposure to the beam, and at a considerably slower rate after longer exposure times.

Figure 60 shows a sequence of Auger spectra for an oxidized transistor wafer. The movement of the charge peak to higher energy levels is easily seen. The charge peaks shown in these two examples are similar in size to the Auger peaks. Occasionally the charge peaks will be much larger than the Auger peaks. In these cases their detection is easy. Besides noting any movement in the location of a peak in the spectrum with time, the best method for detecting these artifices is move the beam to a slightly different position on the specimen. If the Auger spectrum is run immediately on the new position, the charge peak will either not appear or there will be a detectable difference in its energy level.

A third type of artifice occurs synchronously with the retarding potential sweep. It was noted above that specimen current could either increase or decrease as the retarding potential increases. Figure 61 shows that it is possible for the charge state to change very quickly. The process causing the abrupt change in specimen current is apparently regenerative because the electrometer was slew rate limited during the transition. Furthermore, the potential in the Auger escape region changed because the abrupt changes in specimen current are correlated with "peaks" in the Auger spectrum. The peak at 420 eV corresponds to a decrease in electron

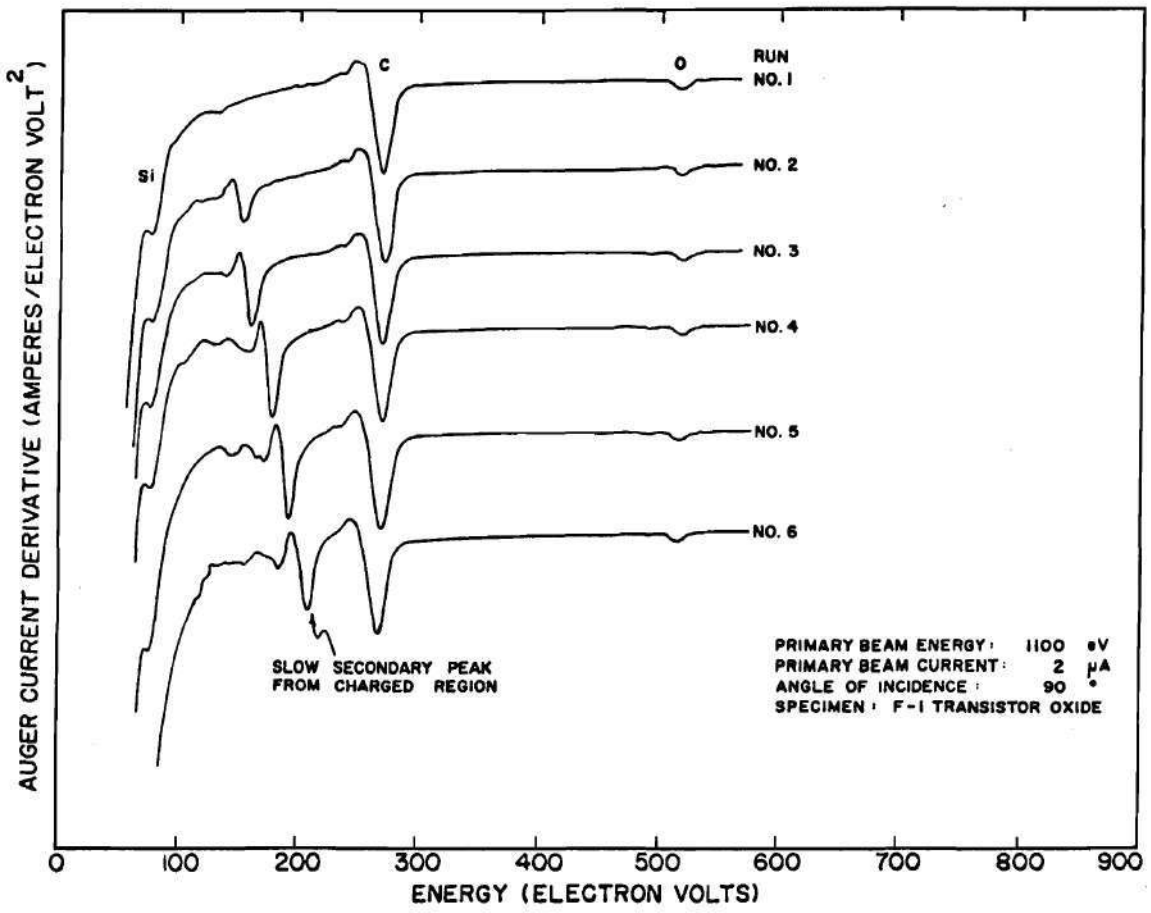

Figure 60. Auger Spectra Showing Movement of Charge Peak in Spectrum.

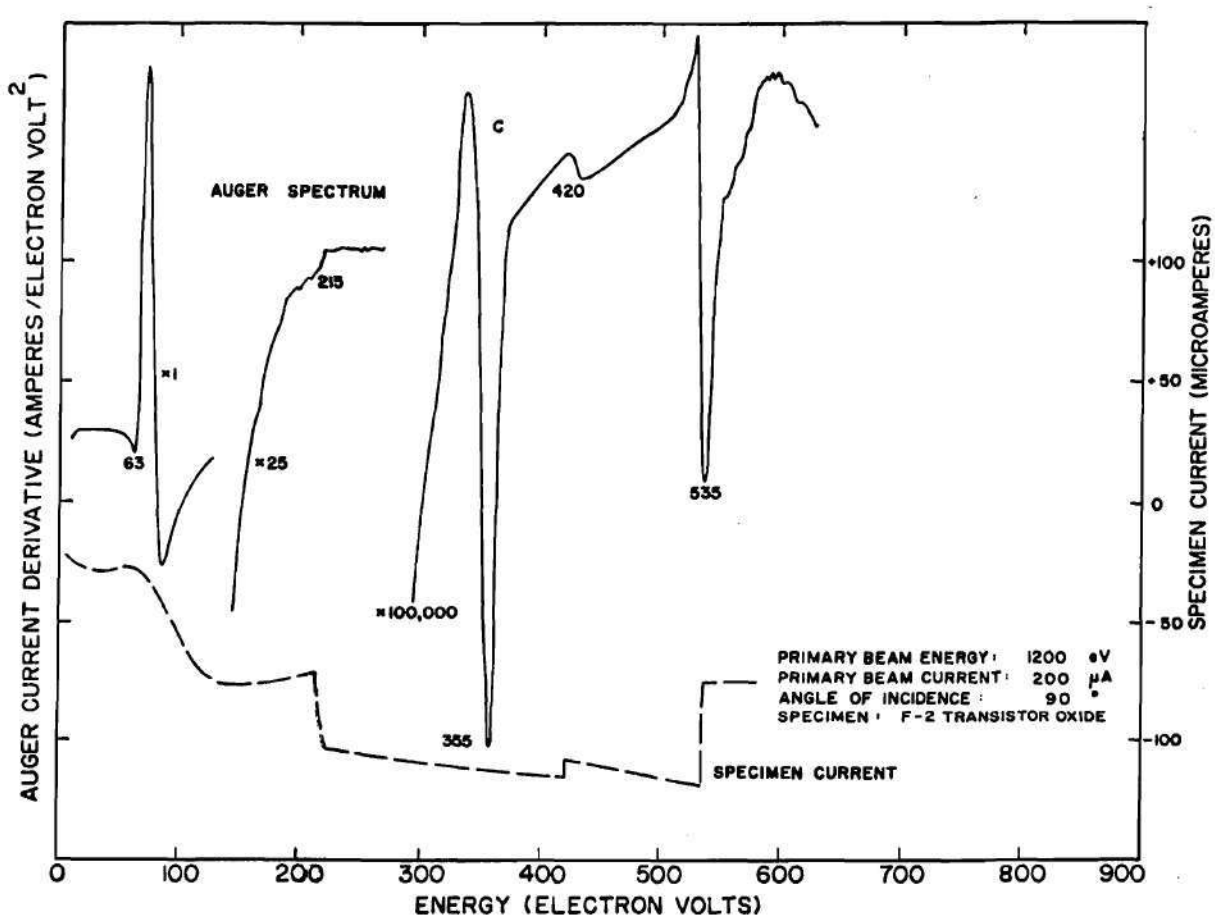

Figure 61. Auger Spectrum and Specimen Current Plot Showing Effect of Abrupt Change in Specimen Current on Auger Spectrum.

current to the electrometer and an increase in electron current to the analyzer. This abrupt change in background current was detected and appears in the spectrum with a characteristic non-symmetrical shape. The peak at 535 eV is of the same nature. Whereas both of these peaks appear as negative excursions in the Auger spectrum associated with decreases in specimen electron current, the positive jump in the spectrum at 215 eV is associated with an increase in specimen electron current.

Detection of artifices caused by time varying charge states may be summarized in the following additional rules.

7. (Detection) Look for any abrupt change in specimen current as a sign of an unstable charge state. In general, the specimen current function should be smooth with continuous derivatives.

8. (Detection) Repeat the retarding potential sweep several times so that any movement in the peaks may be detected.

9. (Detection) Record the Auger spectrum for two adjacent regions on the specimen. Any significant change in the spectrum is likely to be caused by a charged region.

10. (Detection) Record the slow secondary peak. In addition to having the correct shape and reasonable width, the energy axis should be correct when measured from the initial rise of the slow secondary peak. The carbon peak is a convenient measuring point.

Loss Peaks

Loss peaks were mentioned in Chapter I as one of the common non-Auger constituents of electron energy distributions and Auger spectra. This section will illustrate the presence of loss peaks in spectra and also show that certain charging artifices can cause similar peaks in an Auger spectrum. These artifices may be called "pseudo-loss" peaks because of their similar behavior as the primary beam energy is changed. Recognition of pseudo-loss peaks as such, and not as true loss peaks, is important as pseudo-loss peaks are symptomatic of spatial irregularities in surface charging, whereas true loss peaks are normal contributors to Auger spectra.

A true loss peak is formed when electrons having a characteristic energy undergo a characteristic energy loss before escape from the solid and collection by the energy analyzer. For example, consider again the situation shown in Figure 1. Let the excitation source be a primary beam electron. This primary electron creates a vacancy by exciting an electron, No. 1 in the figure, to some higher energy state. The energy loss by the primary electron depends on the state to which electron No. 1 is excited. In a solid there is a high density of available states in the conduction band and, in addition, the typical conduction band is only a few electron volts wide. Thus the primary which excites an electron from a low level to the conduction band loses a characteristic amount of energy; that is, the mean energy loss is precisely defined and the variance of the process is small. Primary electrons which undergo this loss process and then are elastically scattered out of the solid constitute an ionization loss peak in the spectrum. Ionization loss peaks

are not a major feature of electron energy distributions because of the great number of even higher energy states available to the excited electron. Electrons excited into the energy continuum of the solid do not contribute to discrete peaks in the energy spectrum.

The ionization loss peak for oxygen, in the form of SiO_2, was occasionally observed in this work. Two conditions are necessary for observation: the surface has to be relatively free of contamination and the primary beam energy has to be adjusted so that the ionization loss peak is not obscured by an Auger peak. The small number of primaries losing a characteristic energy in the ionization process, and suffering no other inelastic collision, necessitates both conditions. The signal to noise ratio for the oxygen loss peak was typically only five to one. A monolayer, or so, of carbon proves to be an efficient scatterer of the loss peak electrons. Any substantial Auger peak will overshadow the loss peak. Figure 62 shows an Auger spectrum from a SiO_2 surface with only light carbon contamination. The above features of the oxygen loss peak are exemplified in this spectrum. The binding energy for atomic oxygen is 532 eV. One would not expect such a deep level to be affected by chemical bonding. Thus the upper edge of the loss peak in the energy distribution should appear approximately 532 eV below the primary beam energy. The conduction band edge is approximately 4 eV above the Fermi level in SiO_2. Thus an improved estimate is 532 eV + 4 eV below the primary beam energy. When the oxygen loss peak was observed above the noise level in Auger spectra, the upper edge was observed 536 ± 5 eV below the primary beam energy. The uncertainty is the result of random noise in the spectrum and of measuring the primary beam energy with an

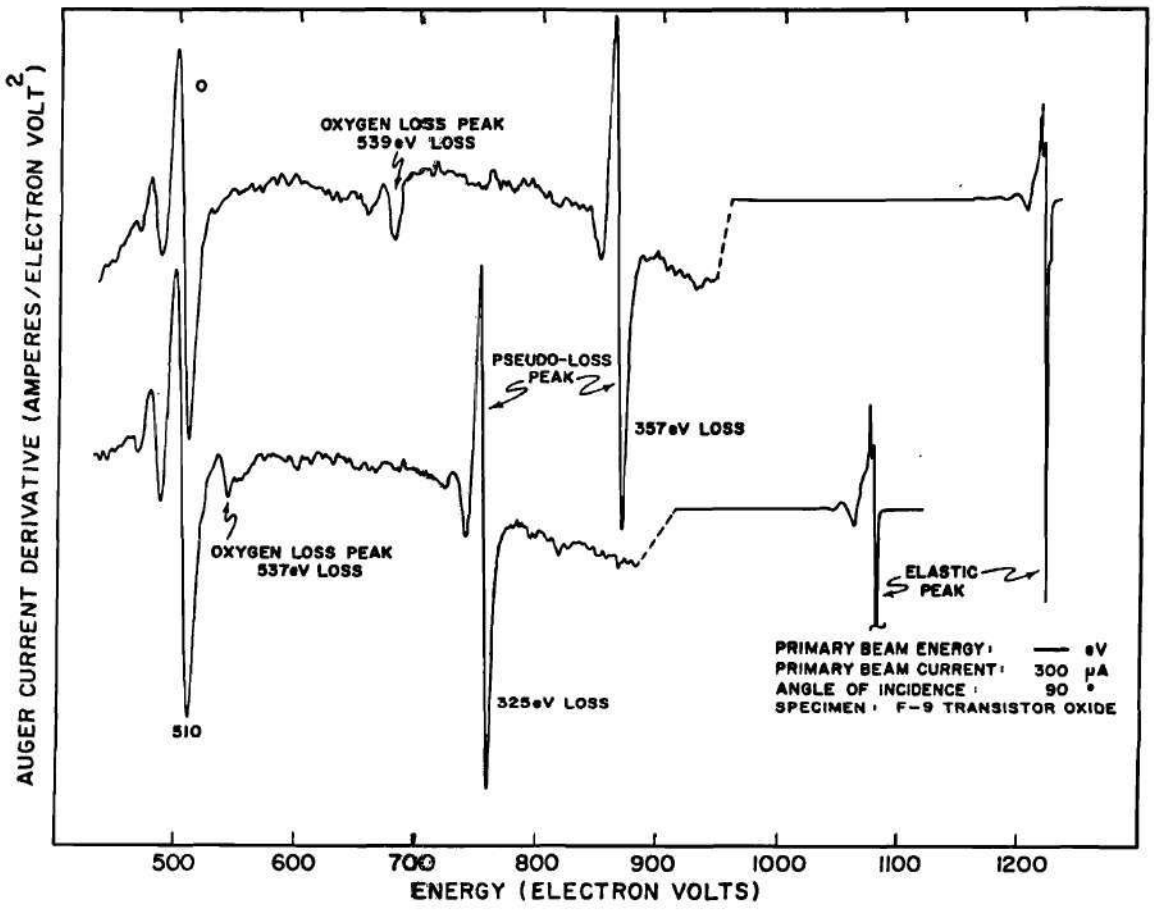

Figure 62. Auger Spectra Showing Pseudo-loss Peaks.

analog meter.

Figure 63 shows the carbon ionization loss peak. The specimen was graphite so there was no contamination problem. Notice that the loss peak has the same general shape as the Auger peak, a statement which is also true of the oxygen loss peak. Apparently, the distribution of states which determines the shape of the ionization loss peak is similar to that which determines the Auger peak shape. The calculation of the expected value of the upper energy edge of the carbon ionization loss peak is similar to that made for oxygen. Here the binding energy of the K shell electron is 283.8 eV and the observed edge is at 289 eV.

The obvious test for a loss peak is to observe whether or not the energy of the peak exactly follows changes in primary beam energy. The oxygen loss peak was observed with beam energies from 1000 eV to 1300 eV, the range over which stable charge states were obtained with thick oxides. The energy of the loss peak was always approximately 536 eV below the primary beam energy.

The previous section described the process by which regions on the periphery of the primary beam bombardment area will charge to a high negative potential because of bombardment by slow secondaries repelled by the analyzer. The slow secondaries emitted from these charged regions appear as peaks in the energy distribution, with energy corresponding to the potential of the charged region. This potential is often an appreciable fraction of cathode potential. The exact potential assumed by the region in question depends on the energy distribution of the repelled secondaries and the relative number of primaries incident on the region. What is observed in practice is that a region can charge to one half or three quarters of

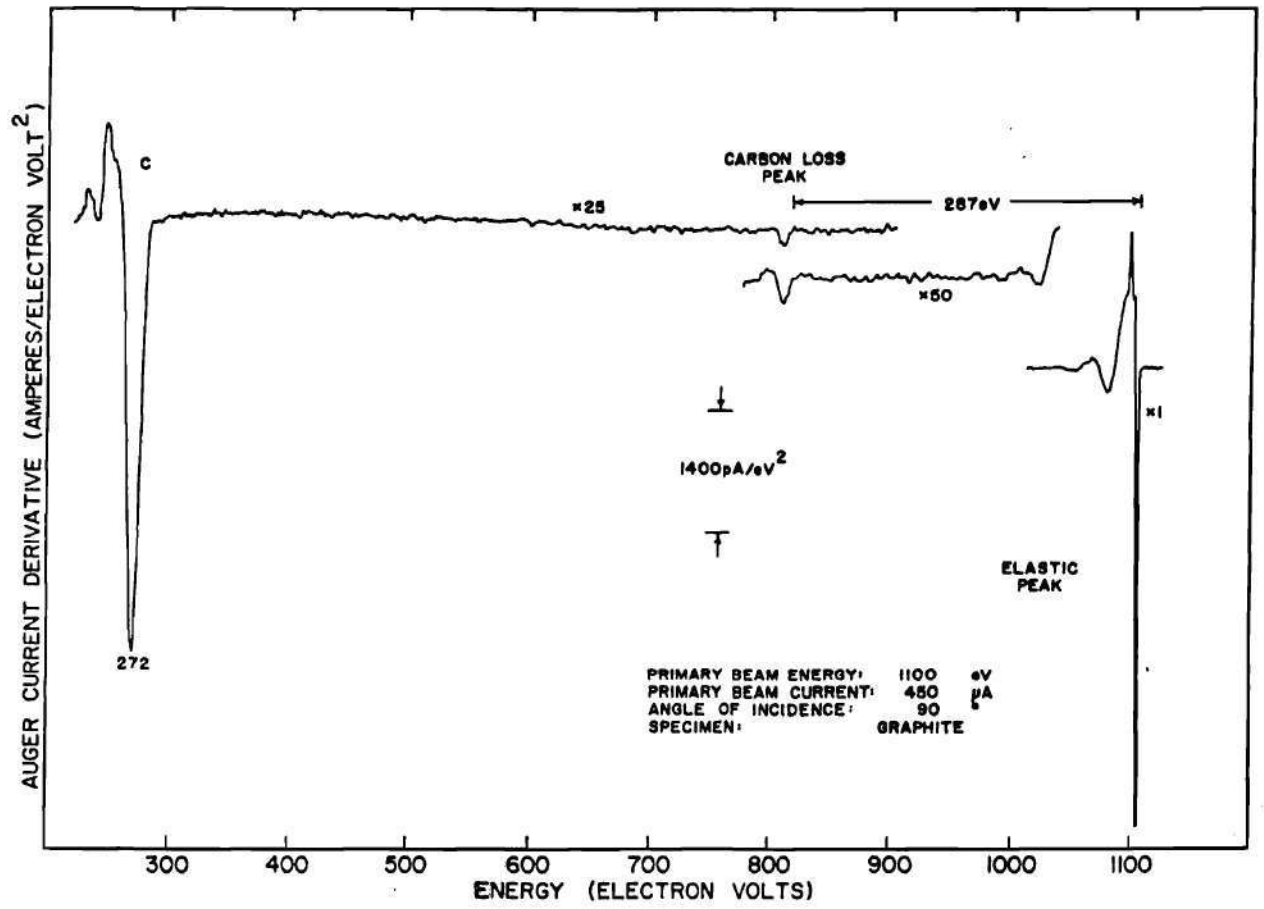

Figure 63. Auger Spectrum Showing True Loss Peak for Carbon.

cathode potential and remain stable in time. Changes in beam potential cause a similar, but not identical, change in the potential of the charged region. For example, with a true loss peak an increase of 100 eV in beam energy will cause the loss peak to move 100 eV higher in the spectrum. With a charging artifice, a pseudo-loss peak, the resulting increase may be only 75 eV. Therefore, the identification of true loss peaks requires an exact measurement of the change in beam potential and the resulting change in peak location.

Figure 62 shows pseudo-loss peaks occurring in the two spectra, taken on the same specimen but with different beam energies. Specimen current was stable and the slow secondary peak was satisfactory on both runs. It is seen that a pseudo-loss peak may have substantial height and appear similar to true Auger peaks. The two spectra shown in this figure were taken from a sequence of curves run over a three day span. The principal pseudo-loss peak varied from 325 eV to 362 eV below the primary beam energy over the sequence of runs. The lower curve was taken with a net accelerating potential of 1100 volts for the primaries; the upper curve was taken with 1250 volts. The principal pseudo-loss peak appears at 0.705 of primary energy in the lower curve and 0.715 in the upper. Thus the tendency is to hold constant the percentage of beam energy by the pseudo-loss peak.

Two techniques are therefore available for identifying true loss peaks and preventing pseudo-loss peaks. Continuing the list,

11. (Detection) Change the primary beam energy by 100 eV and observe changes in the Auger spectrum. Peaks which follow exactly the beam energy are probably true loss peaks. The amplitude of these peaks is

normally small compared to the dominant Auger peaks. Peaks which do not follow exactly are pseudo-loss peaks; they may have amplitudes comparable to the dominant Auger peaks.

12. (Detection, Prevention) Change primary beam focus and location on the specimen slightly. Pseudo-loss peaks will change energy significantly or disappear altogether.

The rationale behind the second test is the following. Formation of a pseudo-loss peak required a delicate balance between the slow secondaries and the primaries bombarding the region. Changes in beam focus, particularly achievement of a sharp cut-off on the current density profile of the beam, will reduce or eliminate a pseudo-loss peak. Other transistors on the same wafer as the one examined in the sequence of runs for Figure 62 were also studied. As an example, on the adjacent transistor to the unit studied in Figure 62, the principal pseudo-loss peak was present 392 eV below primary beam energy. Since the primary beam was the same in both cases, the difference in energy is attributable to the difference in electron paths and differences in oxide thickness.

Noise

Noise is the final charging artifice described in this chapter. Noise refers to random fluctuations in the Auger spectrum which are caused by electrical breakdown of the oxide. Noise is a difficult problem to handle because of its transient nature; it typically occurs in short bursts separated by long periods of stability. While it is easily recognized by its nonperiodic behavior, there is no easy prevention

and obtaining a complete "clean" spectrum of an oxide surface can become a test of patience.

Electrical breakdown of an oxide covered wafer is a possibility whenever the surface charges to an appreciable fraction of cathode potential. A simple estimate of the electric field in the oxide shows that breakdown is likely. Assume, for example, that the surface has charged to -600 volts with respect to the contact, and that the oxide is 6000 angstroms thick. The electric field strength is then 10^9 volts/meter if the potential gradient is uniform. This field strength is equal to the dielectric strength of a wet thermal oxide on silicon.[55]

The breakdown process causes a time varying surface potential. The number of slow secondaries emitted from the breakdown region varies rapidly and results in a perturbation of the collector current in the analyzer. The perturbation amplitude is often so significant that the noise level in the Auger spectrum is substantially increased. If the duration of the breakdown is brief, a spurious peak is created. A longer duration breakdown results in a noisy spectrum. Figure 64 shows two spectra taken from the same transistor on a commercial wafer. The lower trace is marred by noise from oxide breakdown. The beam position was changed slightly to take the upper spectrum. The upper trace appears satisfactory.

Detection of electrical breakdown is simple if analyzer collector current is monitored in real time by an oscilloscope. Figure 65 shows typical waveforms during normal operation and also during an oxide breakdown. These waveforms were monitored after a tuned amplifier in the preamplifier and before the synchronous detector. Therefore, the breakdown appears as a ringing waveform rather than a

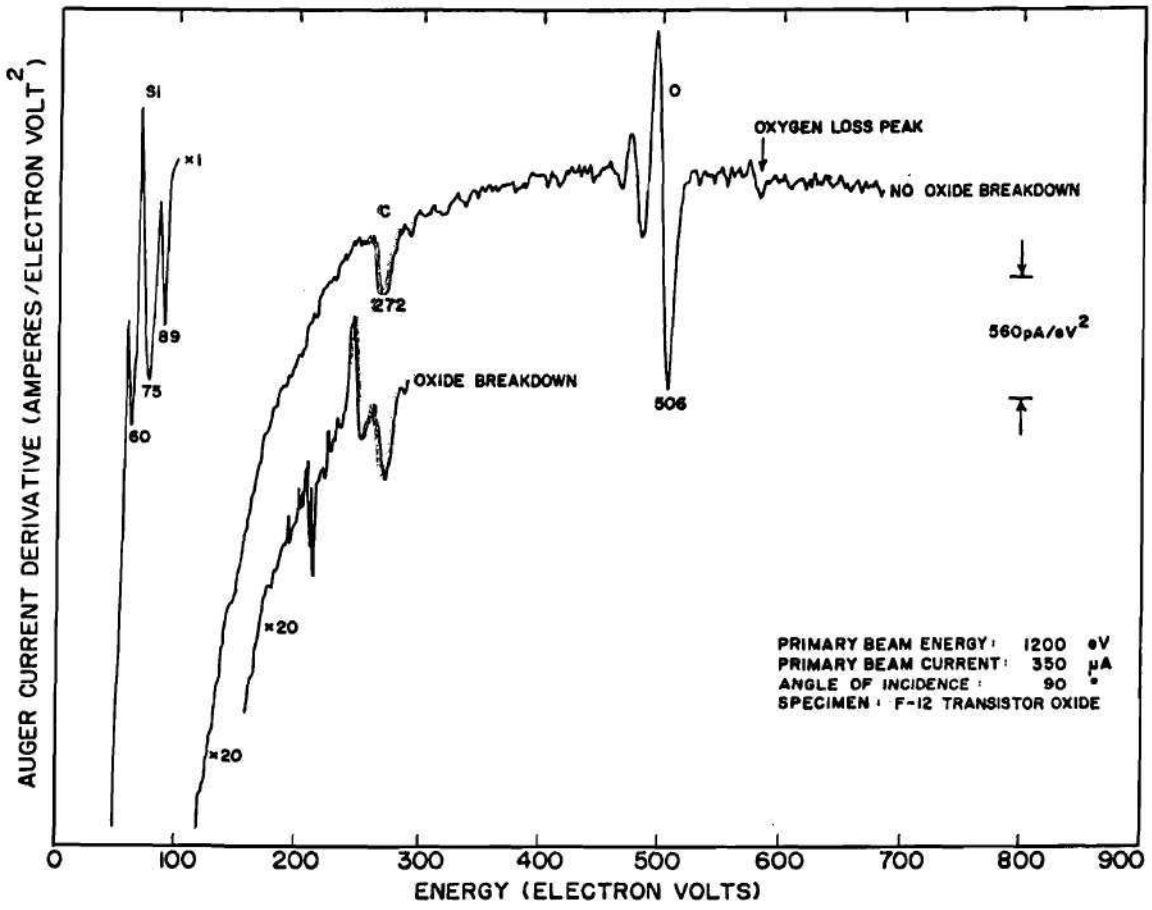

Figure 64. Auger Spectra Showing Increased Noise from Oxide Breakdown.

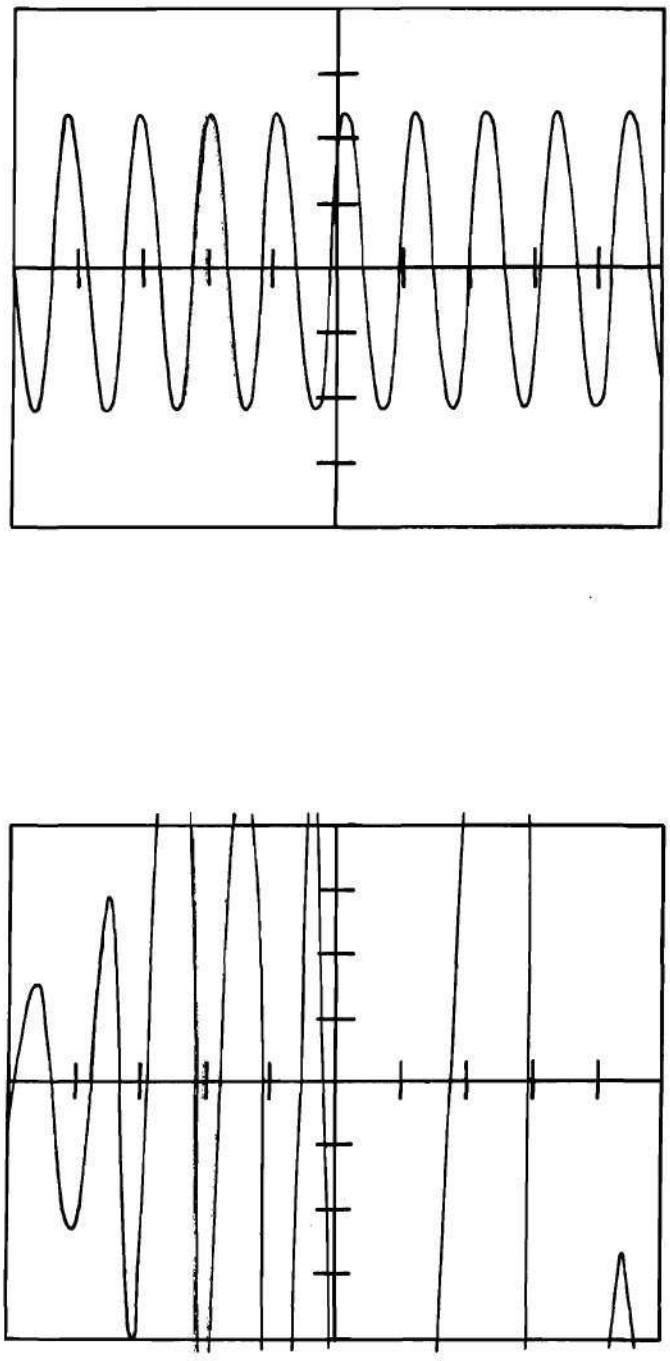

Figure 65. Preamplifier Output Waveforms with no Oxide Breakdown (top) and with Oxide Breakdown (bottom).

sequence of impulses. Notice that the breakdown waveform was driven completely off scale.

Prevention of oxide breakdown is difficult since the spectroscopist can not really ascertain the charge state of the surrounding oxide about the primary beam bombardment area. Damage to the oxide is apparently permanent; that is, the oxide will not support an electric field after breakdown, because the noise level will decrease and often disappear in time if the beam position is not disturbed. This discussion is the basis for the final rule for studying oxide surfaces.

13. (Detection) Monitor the analyzer collector current waveform so that oxide breakdowns are detected. Wait for the oxide to become "quiet" or move to a new position if noise persists.

Summary of Techniques for Prevention and Detection of Charging Artifices

The techniques described in this chapter are gathered together in this section for convenient reference.

1. (Prevention) Minimize oxide thickness, if allowable by other requirements of the experiment. A smaller driving field will be required to establish an equilibrium condition.

2. (Prevention) Chose a primary beam energy close to E_2, as defined in Figure 48. Having the secondary yield approximately one minimizes the net current to be transported through the oxide.

3. (Prevention) Use a primary electron beam with as small a diameter as possible, so as to minimize the effects of oxide variations.

4. (Prevention) Use a primary beam with a constant current density.

This insures that all portions of the oxide under the irradiated region have the same current flow through them.

5. (Prevention) Use a negative bias of a few tens of volts when studying oxide covered specimens so as to deflect slow secondaries repelled by the analyzer.

6. (Detection) Monitor specimen current as the retarding potential is swept. Be suspicious of charge states which are accompanied by larger than usual variations in specimen current.

7. (Detection) Look for an abrupt change in specimen current as a sign of an unstable charge state. In general, the specimen current function should be smooth with continuous derivatives.

8. (Detection) Repeat the retarding potential sweep several times so that any movement in the peaks may be detected.

9. (Detection) Record the Auger spectrum for two adjacent regions on the specimen. Any significant change in the spectrum is likely to be caused by a charged region.

10. (Detection) Record the slow secondary peak. In addition to having the correct shape and reasonable width, the energy axis should be correct when measured from the initial rise of the slow secondary peak. The carbon peak is a convenient measuring point.

11. (Detection) Change the primary beam energy by 100 eV and observe changes in the Auger spectrum. Peaks which follow exactly the beam

energy are probably true loss peaks. The amplitude of these peaks is normally small compared to the dominant Auger peaks. Peaks which do not follow exactly are pseudo-loss peaks; they may have amplitudes comparable to the dominant Auger peaks.

12. (Detection, Prevention) Change primary beam focus and location on the specimen slightly. Pseudo-loss peaks will change energy significantly or disappear altogether.

13. (Detection) Monitor the analyzer collector current waveform so that oxide breakdowns are detected. Wait for the oxide to become "quiet" or move to a new position if noise persists.

CHAPTER VII

THE NATURE OF CARBON ON SILICON DIOXIDE

The various sources and forms of carbon on silicon dioxide surfaces are discussed in this chapter with emphasis on the results of studying commercial semiconductor wafers. Carbon exists both as graphite,[50] a porous, layered material, and as silicon carbide,[50] a hard material distributed on the surface as discrete particles. The first section will describe the sources of graphite on surfaces and the second section describes the sources of silicon carbide. The third section discusses removal techniques for carbon, and the fourth section gives three examples of commercial wafer surface characteristics, with electron micrographs of the same regions studied by the Auger spectroscopy.

Sources of Graphite on Silicon Dioxide Surfaces

There are three sources for the graphite detected by Auger spectroscopy on most specimens. The vacuum system contributes graphite by the decomposition of residual carbon bearing gases. Exposure to the atmosphere results in the adsorption of carbon dioxide and carbon monoxide on many specimens. Finally, chemical treatments and handling will leave carbon residues. These sources will be discussed with particular reference to silicon and silicon dioxide specimens.

The residual gas of the vacuum system must always be considered as a source of carbon. Molecules containing carbon will adsorb on the specimen surface to some degree. Either the action of the electron beam or heat can decompose the molecule;[58]

the carbon atoms form graphite and, typically, the remainder of the molecule is volatile and returns to the residual gas. Carbon monoxide and carbon dioxide are principal residual gases in an ion pumped vacuum system (Figure 9 showed a typical residual gas spectrum in the baked vacuum system). Therefore, one should establish the influence of the primary electron beam and heat treatment on graphite coverage before attributing the carbon to any other source.

Coad, et al.[59] and Joyce and Neave[60] have studied electron beam assisted adsorption on silicon surfaces. Their general result is that graphite growth is proportional to carbon bearing gas partial pressure and to electron beam exposure. On the other hand, graphite deposition was not a problem in this work. The standard procedure in this work was to compare the last data with the first data taken on any particular spot. In no case did a graphite peak increase in height during data collection, although conversion of graphite to carbide was noted in experiments deliberately run for extended periods of time.

This lack of electron beam assisted adsorption is attributed to the low carbon monoxide and dioxide partial pressures achieved. A specimen would be introduced into the vacuum chamber, the chamber pumped down, and then baked. An initial data run was quickly made to establish the general characteristics of the sample. During this time the electron gun would complete its outgassing and the total system pressure dropped to the low 10^{-9} torr range. Thus the partial pressure of carbon monoxide and dioxide was on the 10^{-10} torr range when data for publication was collected. Often the electron beam was shifted to an adjoining spot for final data collection to insure that the beam had not affected the specimen in any way.

The effect of heat on the formation of graphite is more difficult to describe. Chang[21] performed an experiment in which a cleaned silicon surface was subjected to a six hour, 200°C vacuum system bake. His heaters were programmed to turn off if the gas pressure rose above 2×10^{-6} torr; presumably the pressure did rise to this pressure during the bake. This treatment resulted in a one half monolayer of graphite on the silicon surface. This rate of deposition is dependent on the residual gas composition, which was not stated. Thus it is not possible to use his results directly to determine the amount of graphite from the system bake. Another complicating factor is that the rate of deposition is very dependent on the temperature achieved by the specimen; temperatures quoted in the literature normally refer to the set point on the heater control and do not necessarily reflect actual specimen temperature.* These factors perhaps explain why graphite deposition of the magnitude noted by Chang was not a problem in this work.

Several experiments indicated that vacuum system baking, of the temperature and time employed in this work, does not contribute to significant (> $\frac{1}{2}$ monolayer) graphite deposition. Several wafers were studied in two vacuum chambers: the system utilized for the majority of this work and a second system equipped with a turbomolecular pump so that no baking was required. The spectra were qualitatively the same from both systems. Exact comparison was not possible because of experimental details.

---

*The oven used on the vacuum system for this work was somewhat inefficient; even though the set point was 200°C, it is not certain that the actual specimen temperature was this high since the set point was measured by a thermostat mounted near the heater elements, and was reached only near the end of the bake.

Two samples were chemically cleaned in this work in such a manner as to remove surface graphite, although both contained silicon carbide on the surface. One was a silicon dioxide surface and the other was bulk silicon carbide. Both were subjected to the standard bake and their spectra showed no graphite. The detectable limit, however, was only about one tenth of a monolayer because of the presence of the carbide peak.

In another experiment a silicon monoxide surface and an aluminum oxide surface were studied before and after system baking. For the aluminum oxide surface baking increased the sulfur peak, a contaminant, by 30% and the chlorine peak, another contaminant, by 25%. By comparison, the graphite peak increased 12% and the oxygen peak decreased by 30%. The decrease in oxygen is attributed to desorption of water vapor and, perhaps, carbon dioxide. Since adsorbed gases mask the other surface contaminants, baking should increase contaminant peak heights. The behavior of the silicon monoxide specimen was similar. Baking increased the graphite peak 13% but decreased the oxygen peak by 25%. Thus adsorbed gases containing oxygen, primarily water vapor, mask the surface before baking. Mild baking does not increase the graphite contamination per se, but rather removes adsorbed gases which mask graphite and the remainder of the surface constituents. In summary, with the experimental procedures followed in this work, baking the vacuum system does not contribute more than about a tenth of a monolayer of graphite to the surface. This amount is only a small fraction of that found on most specimens.

The effect of atmospheric exposure was studied on two specimens. A copper

specimen, prepared by Dr. John Carden, was cleaned by heating to 800°C for three minutes in a high vacuum. A residual carbon peak equivalent to about 1/10 monolayer surface coverage remained. There were also small sulfur, chlorine, nitrogen, and antimony peaks and a substantial oxygen peak. Exposure to the atmosphere and pumping down, without a bake, tripled the carbon peak, doubled the oxygen peak, and increased the sulfur and nitrogen peaks. The antimony peak was slightly decreased, as was the copper peak. Mild heating, of the order of 400°C for a few minutes, removed the sulfur, chlorine, nitrogen, and carbon peaks, while returning the oxygen peak to its original height. This experiment indicates that exposure to the atmosphere causes the adsorption of a number of gases on the surface but that these can be removed by heating the surface. The quantitative effects of atmospheric exposure depend on the specimen surface, as does the effectiveness of mild heating at removing these gases.

The second specimen studied was a silicon dioxide surface grown within the vacuum system. This surface was free of observable carbon (<0.05 monolayer of graphite). The system was backfilled to atmospheric pressure with dry oxygen and pumped down using the full complement of pumps but no bake. There was no observable carbon on the surface afterwards. The experiment was repeated with dry nitrogen and the result was the same. On the other hand, when the specimen was exposed to the atmosphere, about one-half monolayer of graphite remained on the surface after pumping. This result is similar to the one-fourth monolayer of graphite Chang[21] found on silicon after atmospheric exposure. Thus one concludes that atmospheric exposure is more detrimental with respect to graphite deposition

than the mild baking utilized in this work.

The principal source of graphite is the residue from chemical treatment of the surface.[21] Dust and grease from handling are secondary sources. An example of the effect of chemical treatment is given by Figure 66. This specimen was a commercial wafer taken from the line after the base diffusion. The silicon dioxide was removed by an HF etch and then re-etched with ultrasonic agitation. The specimen was pumped to the low 10^{-9} torr range without a bake. Obviously, a significant graphite residue remained on the surface. Utilizing a 5% enhancement of the carbon peak by backscattering from the silicon substrate (i.e., the increased backscattering from silicon, as compared to graphite, increases the Auger yield of the surface carbon film by 5%), the graphite peak corresponds to 1.7 monolayers. Such a significant coverage is not the result of atmospheric exposure or effects of the vacuum system. Whether the graphite was a residue of the etching process, per se, or whether the graphite was present on the oxide (which it almost certain was) and was not removed by the etching, however, was not determined.

Consider now the oxygen and silicon peaks. The specimen was subjected to the atmosphere about one hour before pump down. Therefore, one would expect an oxide film on the silicon. Figure 66 indicates that this oxide is similar to silicon monoxide rather than silicon dioxide. The silicon peak is definitely shifted to a lower energy than the pure silicon peak. Furthermore, the peak height is too small for it to be pure silicon. That is, the peak is not sufficiently large for the specimen to consist of 1.7 monolayers of graphite on a pure silicon substrate. If one uses 10 picoamperes/eV^2 per microampere beam current at 1200 eV and normal incidence

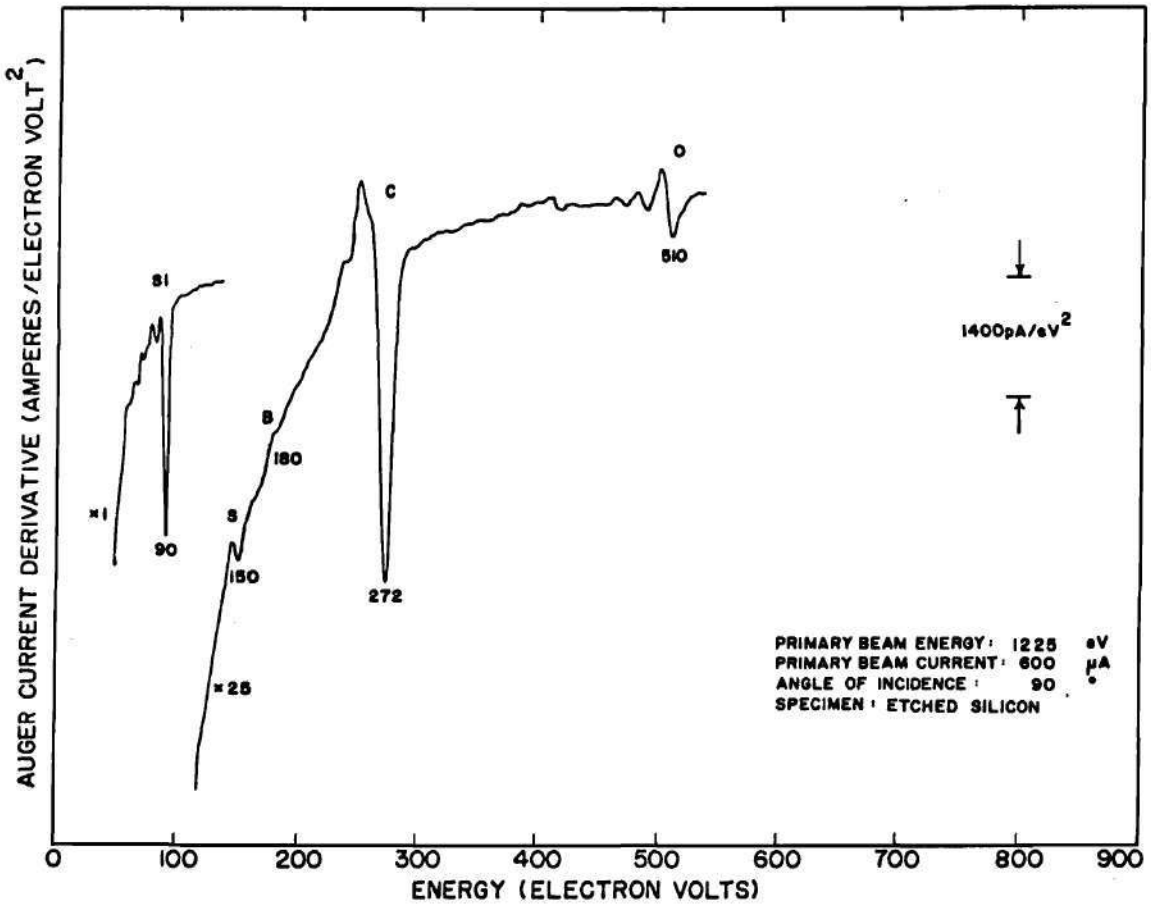

Figure 66. Auger Spectrum of HF Etched Silicon Wafer.

for silicon monoxide (an estimate from interpolating between the sensitivity of silicon in silicon dioxide and in elemental silicon), the peak height for silicon in Figure 66 agrees with the calculated value. Obviously, the oxide is not silicon dioxide because the 75 eV peak is insignificant. Also, the oxygen peak shows a sensitivity equivalent to about 0.08 picoamperes/eV^2 per microampere beam current for a bulk specimen. This is a factor of four below the sensitivity shown by oxygen in silicon dioxide (0.32 picoamperes/eV^2 per microampere beam current at 1175 eV, from Figure 21). Thus the oxide formed was not silicon dioxide, but rather was similar to silicon monoxide.

One final source of graphite on a semiconductor wafer deserves mention A silicon dioxide specimen with less than half a monolayer of graphite was subjected to an oil diffusion pumped system, with a pressure of about 10^{-5} torr, and was thereby coated with about three monolayers of graphite. This coverage was present even where the specimen had not been subjected to electron bombardment during the diffusion pumped time. Since the specimen had less than a half monolayer of graphite on the surface before exposure to the oil diffusion pumped system, the effect of the diffusion pumped system is clear.

Sources of Silicon Carbide on Semiconductor Surfaces

Silicon carbide is a technically important contaminant on semiconductor surfaces because it will affect subsequent processing steps. As shown by scanning electron microscope micrographs in this section, silicon carbide forms particles on the surfaces of silicon and silicon dioxide. Several methods of forming silicon carbide particles on semiconductor surfaces are described in this section.

The formation of silicon carbide particles on a pure silicon surface by heat treatment in ultra high vacuum was described by Henderson, Marcus, and Polite.[49] The carbide resulted from the chemical reaction of a carbon-containing adsorbate with a pure silicon substrate. Silicon carbide was formed over the temperature range of 800^{o}-1100^{o}C. Above 1100^{o}C the carbon was apparently absorbed by the silicon because silicon carbide was not formed on the surface. The particles were found to be approximately 400 angstroms in diameter with a surface density as high as 6×10^{9} per square centimeter. Elements of this experiment were repeated in this work and the experiment was extended to include silicon dioxide substrates and formation of silicon carbide at atmospheric pressure by heating a carbon (graphite) contaminated silicon surface.

The initial experiment described concerned the formation of silicon carbide by heating graphite contaminated silicon in high vacuum. Figure 67 shows the Auger spectrum of the initial surface, a graphite contaminated silicon wafer. Evaluation of the graphite coverage requires the use of Figure 27 to obtain the scattering characteristics of the substrate at the 14^{o} incidence angle. The response of the silicon reference specimen was 34 picoamperes/eV^{2} at 14^{o} compared with 18 picoamperes/eV^{2} at normal incidence. Therefore a thin graphite layer should have an Auger peak height enhanced by (34/18) = 1.89, relative to normal incidence. The increased backscattering of the silicon substrate, compared to a graphite substrate, results in a further increase of 5%. Since at 1200 eV bulk graphite, which is equivalent to 4.0 monolayers unattenuated emission strength, corresponds to 0.80 picoamperes/eV^{2}, each equivalent monolayer of graphite under these conditions should

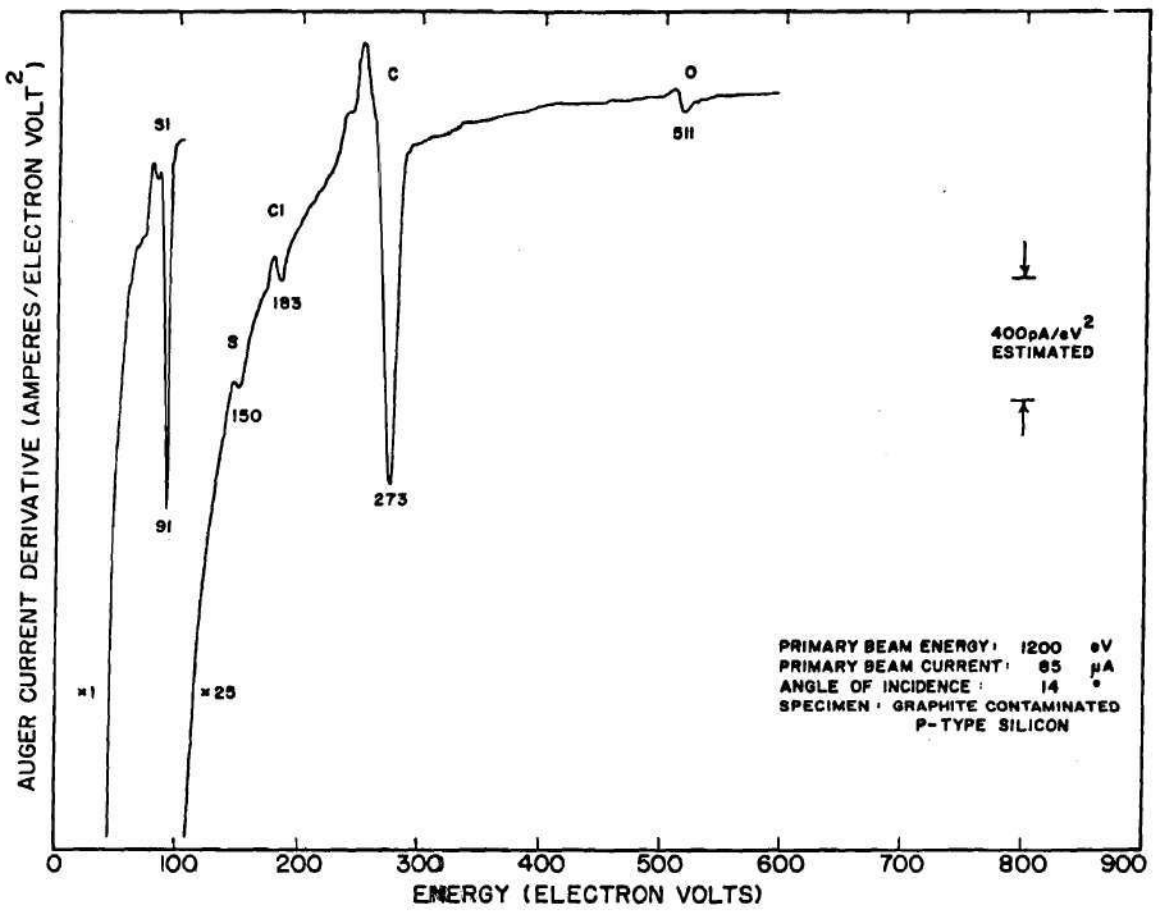

Figure 67. Auger Spectrum of Graphite Contaminated Wafer.

give rise to (0.80/4)(1.89)(1.05) = 0.40 picoamperes/eV^2 peak height in the Auger spectrum.

Unfortunately, a malfunction in the signal channel of the synchronous detector makes exact calibration of this, and several other, spectra impossible. This malfunction was not discovered until sometime after the sequence of experiments was finished and the specimens had been examined in the scanning electron microscope. However, since the only consequence of the malfunction is that the gain factor of the detector is not known exactly, the data is presented and an estimated scale factor is shown. This estimate is based on comparison of spectra from similar specimens taken with and without the malfunction present. This estimate does lead to a consistent interpretation; that is, the calculated silicon peak height, based on the calculated graphite coverage, agrees with the observed silicon peak.

Using the estimated scale factor, the graphite coverage on the specimen of Figure 67 was 2.2 monolayers. This carbon came from previous chemical treatment, handling, and atmospheric exposure, since the vacuum system was not baked for this study. The carbon peak shows the characteristic graphite shape and the silicon peak is characteristic of silicon. Notice that the oxygen peak is almost insignificant. Considering the shape of the silicon peak and the small size of the oxygen peak, it appears almost as if the graphite layer hindered oxidation of the surface by the atmosphere (the wafer was etched for 1000 seconds in 25% HF and then exposed to the atmosphere for about an hour before pump down). The specimen was heated to 950^{o}C for 2000 seconds in the high vacuum system by electron bombardment on the rear of the specimen holder. The background pressure rose

to a maximum of 2×10^{-8} torr during heating. Figure 68 shows the Auger spectrum of the resulting surface. The carbon peak is now characteristic of carbide, with no graphite present. Notice that the oxygen peak is absent, presumably because oxygen (or SiO) evaporation.[61] The silicon peak now displays a distinctive silicon carbide shape, but its energy, 90 eV, suggests that it is a combination of pure silicon and silicon carbide. The silicon peak height is 22.8 picoamperes/eV^2 per microampere of beam current, which is about two thirds the response of pure silicon under these conditions. Since silicon carbide is known to form particles on the silicon surface, electron microscopy must be employed to determine the topology of the surface before further interpretations can be made.

Figure 69 shows two scanning micrographs of the specimen after heating. The top, high magnification, micrograph was taken at the same angle of incidence, 14^{o}, as the Auger spectrum of Figure 68. Silicon carbide particles are clearly visible on the surface. The bottom, low magnification, micrograph shows a more or less uniform distribution of particles over the surface. The particles shown in the top micrograph have diameters of the order of 4000 angstroms, somewhat larger than the particles reported by Chang.

The problem of interpreting the carbide peak in Figure 68 will now be considered. The carbide peak height is 0.24 picoamperes/eV^2 per microampere beam current. These particles are larger than the primary beam penetration length at 1200 eV, so the bulk silicon carbide calibration spectrum is used. Figure 28 shows the response of silicon carbide's carbon peak is 0.50 picoamperes/eV^2 per microampere beam current. Thus, the peak in Figure 68 is essentially one half that of

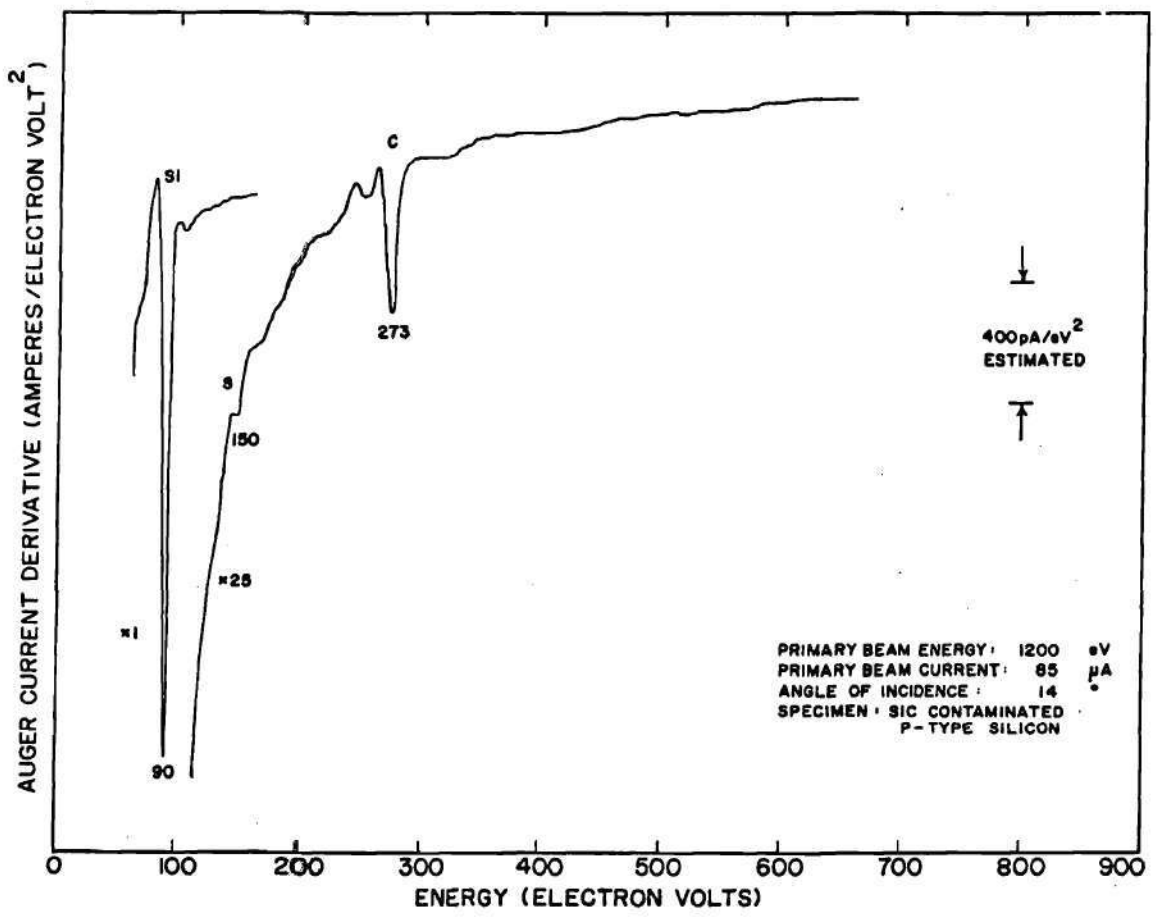

Figure 68. Auger Spectrum of Graphite Contaminated Wafer after Heating in High Vacuum.

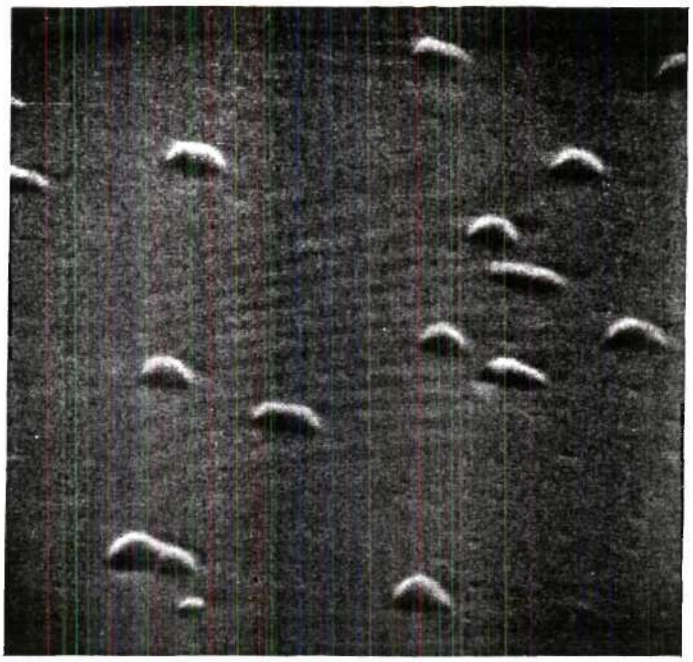

(a)

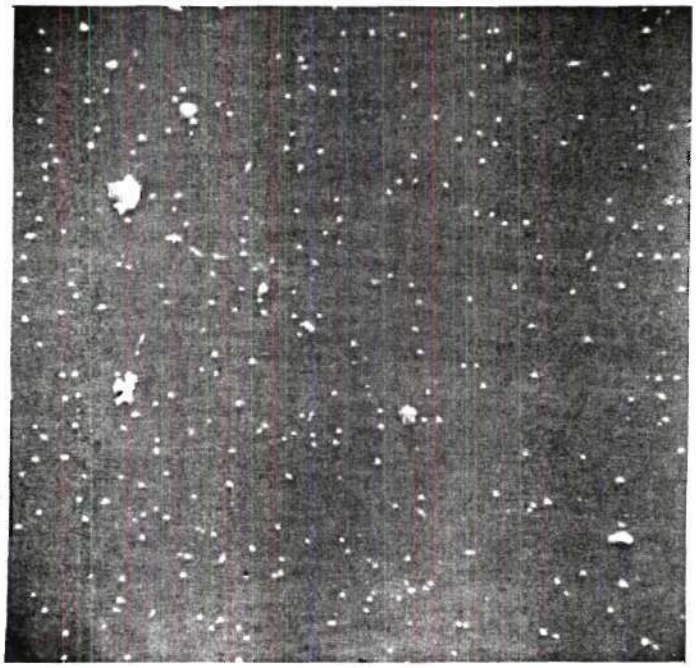

(b)

Figure 69. Scanning Micrographs of Graphite Contaminated Wafer after Heating in High Vacuum. Top Micrograph has Magnification of 19,200 and the Bottom Micrograph has Magnification of 2000.

a bulk specimen, yet the area occupied by silicon carbide particles in the micrograph taken at 14^{o} is only about 10%. The explanation of this discrepancy is given by Figure 70 which shows a transmission micrograph of a plastic replica of the surface. This technique offers substantially greater resolution than the scanning micrograph. A great number of smaller particles, with diameters of the order of 400 angstroms, are now visible. These smaller particles contribute to the large carbide peak height.

The same basic experiment was performed on a graphite contaminated silicon dioxide surface. The specimen was a NPN power transistor taken from the line after base diffusion. The initial Auger spectrum, not shown, displayed a graphite carbon peak equivalent to about two monolayers coverage, and a small 77 eV silicon peak characteristic of silicon dioxide and the corresponding oxygen peak at 510 eV. The specimen was heated to 1000^{o}C in the ultra high vacuum, again by electron bombardment of the back side of the specimen holder. The Auger spectrum of the resulting surface is shown in Figure 71. The silicon peak is now at 89 eV, indicating silicon carbide. Interestingly enough the carbon peak shape is still similar to graphite, rather than carbide. The interpretation of the graphite-like carbon peak is that only a portion of the graphite on the surface was converted to silicon carbide. This figure shows that it is possible to detect graphite covered silicon carbide by the 89 eV silicon peak, rather than by the carbon peak shape.

Figure 72 shows a transmission micrograph of a plastic replica of the heated surface. The significant difference between this oxide surface and the silicon surface is that silicon carbide is formed more slowly on silicon dioxide, since carbon must

Figure 70. Transmission Micrograph of Plastic Replica of Graphite Contaminated Wafer Surface after Heating. Magnification is 20,500.

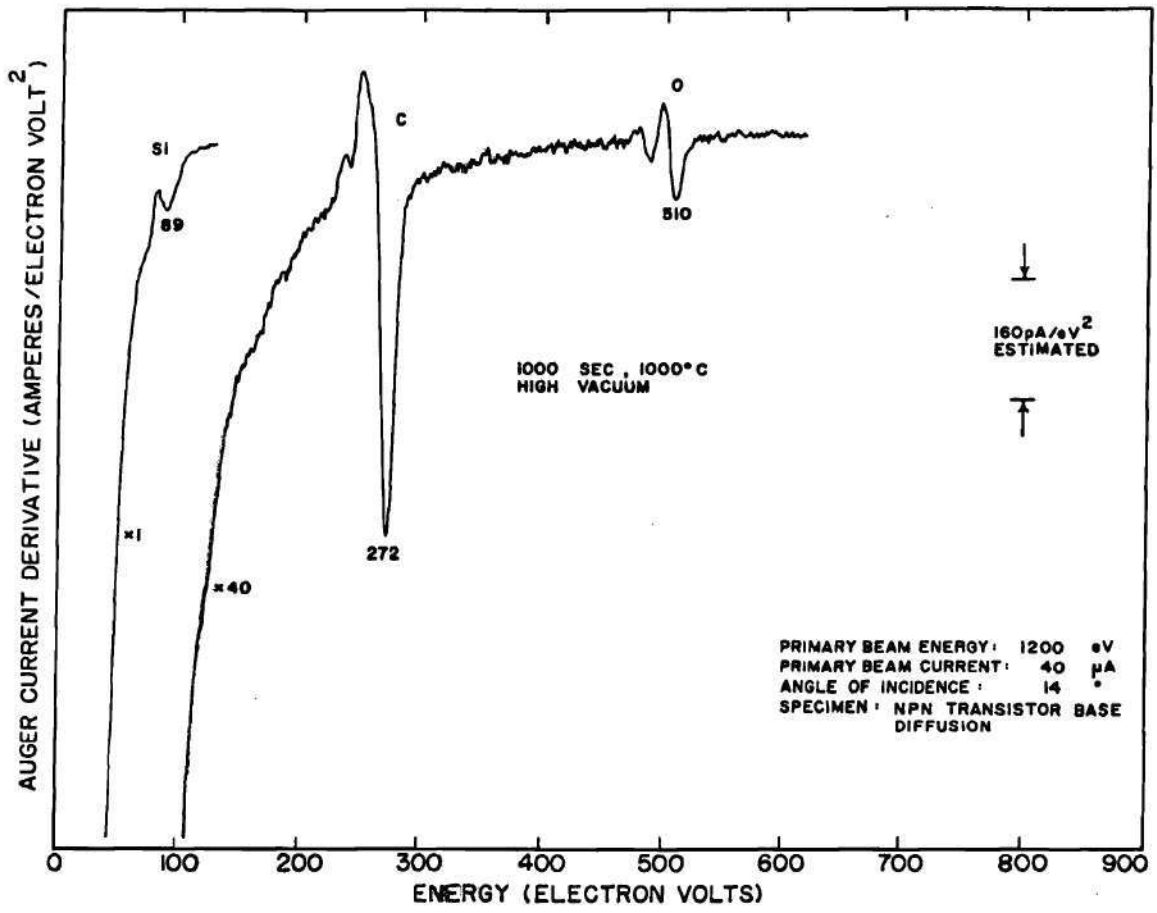

Figure 71. Auger Spectrum of Graphite Contaminated Commercial Oxide Surface after Heating in High Vacuum.

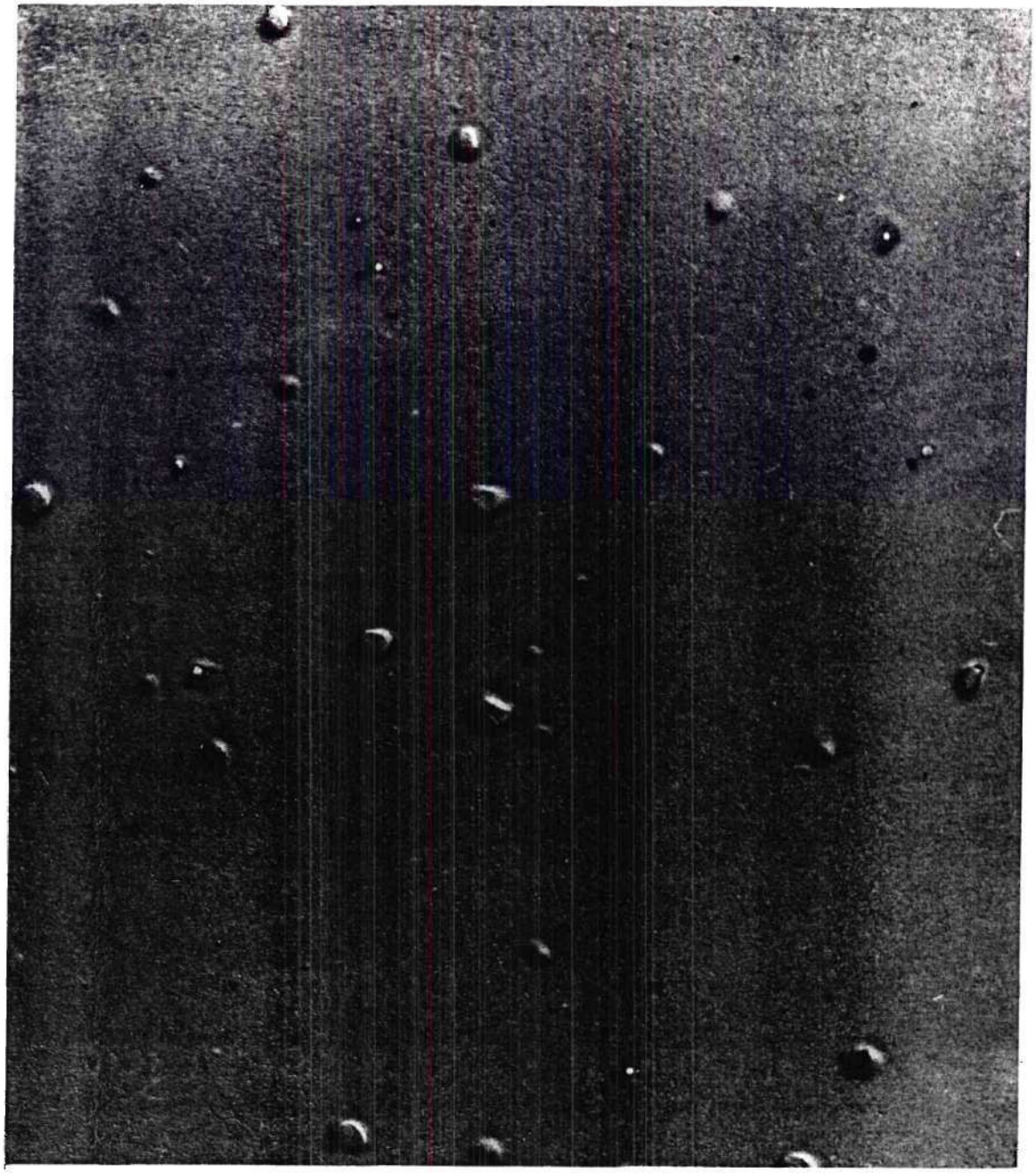

Figure 72. Transmission Micrograph of Plastic Replica of Graphite Contaminated Oxide Surface after Heating. Magnification is 20,500.

reduce the oxide before forming silicon carbide. This reduction requires a significant amount of energy and proceeds slowly. The basic reaction therefore is

$$SiO_2 + C \xrightarrow{\text{energy}} SiC + O_2 . \qquad (74)$$

The ultimate fate of the oxygen was not determined, but probably depends on the atmosphere surrounding the specimen. If the reaction were carried out with a high partial pressure of oxygen, one would expect the oxygen to remain adsorbed on the silicon, as in the case of oxidation. In a high vacuum, on the other hand, one would expect the oxygen to be volatile and escape to the vacuum.

Other sources of energy besides heating will promote the reaction described by Equation 74. One such source is the primary electron beam used in electron excited Auger spectroscopy. Harris and others[58] have noted that the primary beam would decompose adsorbed carbon bearing gases and thus form a graphite layer on the surface. Maintenance of a sufficiently low partial pressure of CO and CO_2 prevented this problem in the work, but other chemical reactions caused by the primary beam were ncted.

An example of the reduction of silicon dioxide and the formation of silicon carbide by the electron beam is shown in the Auger spectra, Figure 73, of the base region of a NPN power transistor. The beam current employed for these spectra is not known exactly because of a difficulty in the electrometer which was not discovered until the experiment was completed. Thus, the scale factor was estimated by comparison with similar samples. With the estimated scale factor the initial graphite coverage was 2.6 monolayers. Since the area of the incident beam was approximately

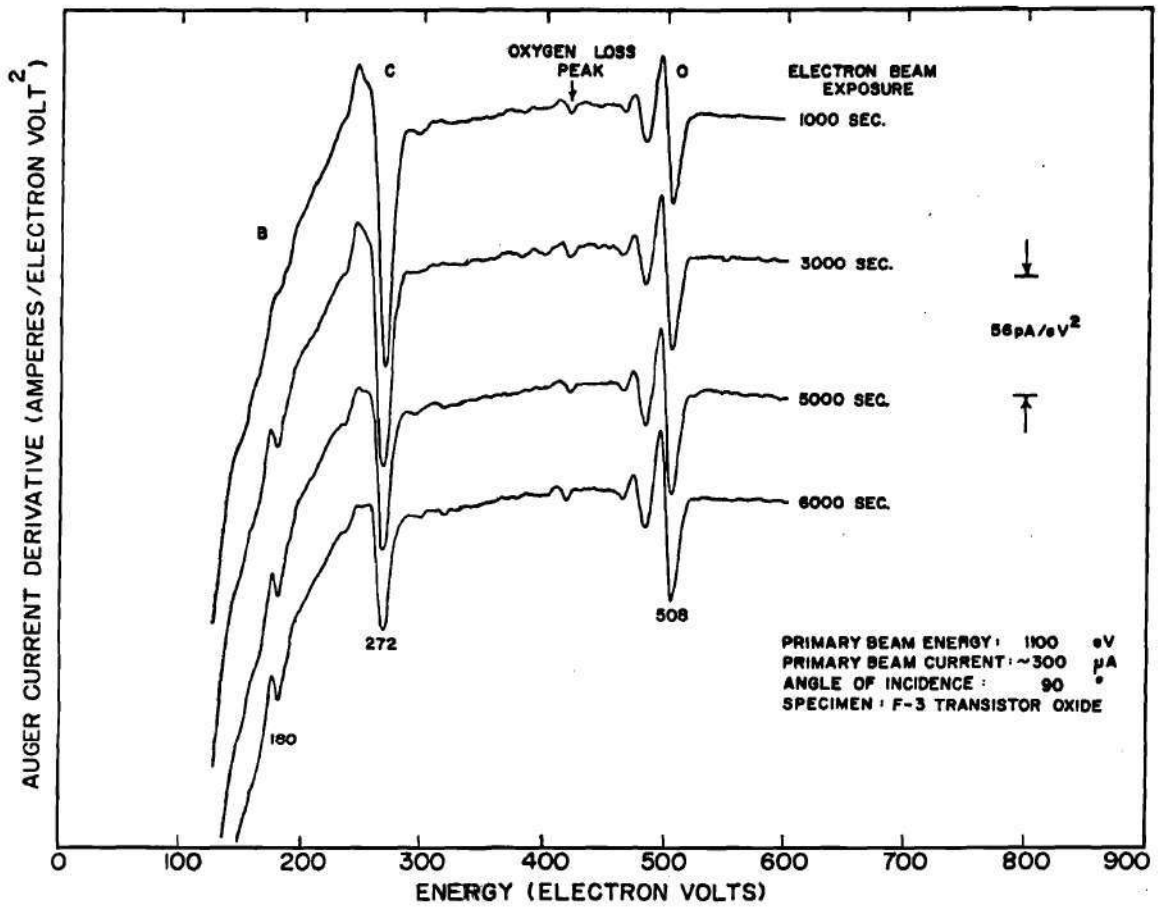

Figure 73. Auger Spectra Showing the Formation of SiC by Electron Bombardment of Graphite Contaminated Oxide.

10 square millimeters, the current density was about 30 microamperes per square millimeter. The 100 minute total exposure is seen to convert a substantial portion of the graphite to carbide. Notice that the boron peak, the dopant for the base, is enhanced by the bombardment. Whether this enhancement was the result of removing the graphite from a portion of the surface, or of electron induced segregation of the boron at the surface, was not determined. Notice also that the oxygen peak is only slightly enhanced, 17%, by the conversion of graphite to carbide. This could be either the result of a net removal of oxygen from the surface region, thus compensating for the reduced masking by graphite, or it could be the result of the long escape depth, five monolayers, for 510 eV electrons. Again, the exact cause was not determined. The obvious experiment, that of using a mass spectrometer to monitor the evolution of gas from the surface, is very difficult because of the desorption of gases from the electron gun. This problem was discussed in Chapter V in the section on electron stimulated desorption.

The reduction of oxidized silicon by the electron beam will take place even if no carbon is present. The clean silicon dioxide grown within the vacuum system, and described in Chapter IV in the section on calibration spectra, was subjected to electron bombardment for several hours with a current density of about 30 microamperes per square millimeter. The original surface, with Auger spectrum shown in Figure 21, was substantially altered by the electron bombardment, as is shown in Figures 74 and 75. Figure 74 shows the full spectrum, whereas Figure 75 is an expanded view of the silicon peak. The 90 eV peak, characteristic of silicon monoxide, is seen clearly. The remaining features of the silicon peak are

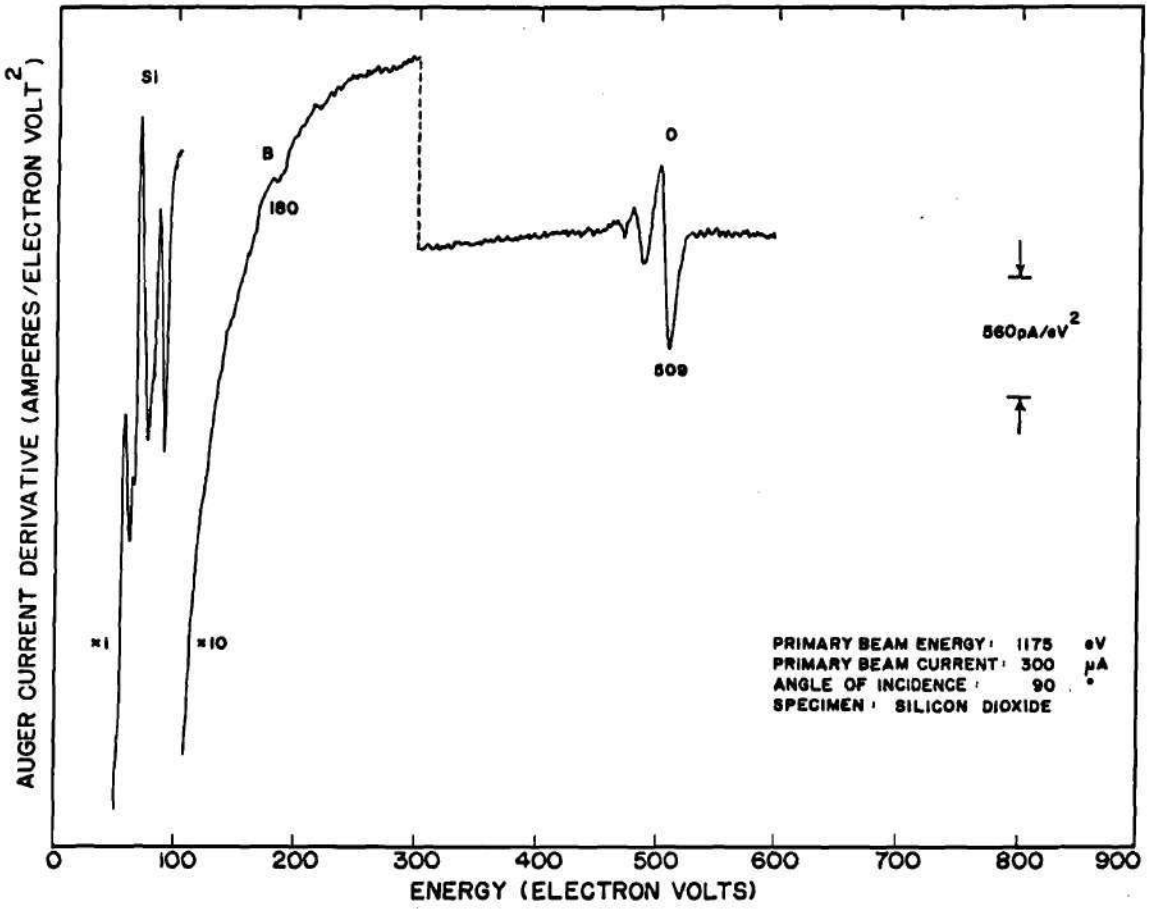

Figure 74. Auger Spectrum of Silicon Dioxide after Electron Bombardment.

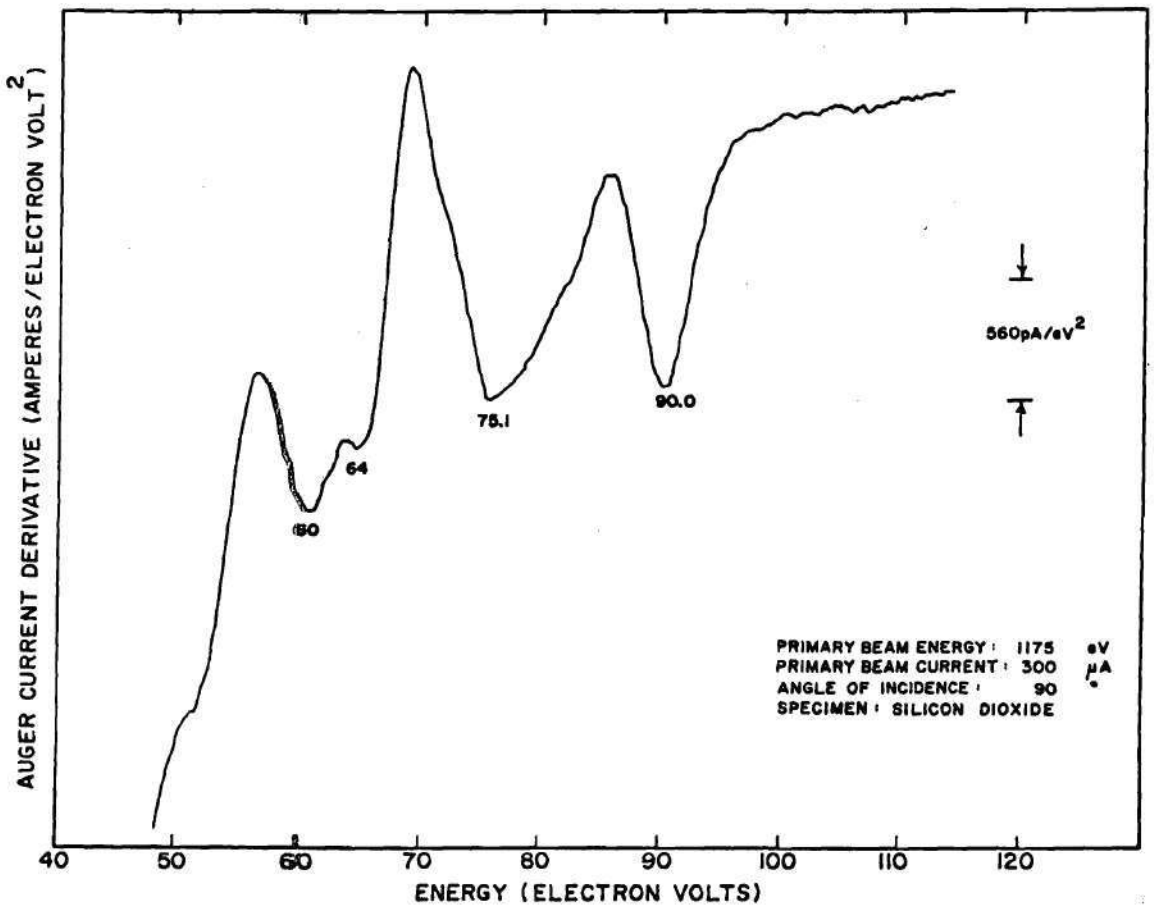

Figure 75. Expanded View of Silicon Peak of Silicon Dioxide after Electron Bombardment.

characteristic of silicon dioxide. This spectrum is interpreted as a film of silicon monoxide on a silicon dioxide substrate. The thickness of this film could be determined if the sensitivity of silicon monoxide were accurately known, which unfortunately it is not. As a final note, the reduction of the oxygen peak because of the electron bombardment was 13%. This should correspond to the reduced oxygen content in the silicon monoxide film, compared to silicon dioxide.

Another source of energy for the reduction of silicon dioxide and the formation of silicon carbide is ion bombardment. Argon ion bombardment was found to reduce silicon dioxide and also form silicon carbide on silicon dioxide, silicon monoxide, and silicon surfaces in this work. One experiment, on a silicon surface, will be described in greater detail. In this experiment a graphite contaminated P type specimen, similar to that described by the Auger spectrum of Figure 67, was argon ion bombarded as a cleaning operation. The surface was ion bombarded with 1700 volt ions for three hours with a current density of 20 microamperes per square centimeter. The argon pressure was 2×10^{-4} torr. An Auger spectrum taken at this point was essentially identical to Figure 76, except that the argon peak was a factor of four larger. The surface was then heated to 750^{o}C for 1000 seconds in the high vacuum to drive off most of the argon. The Auger spectrum of the surface after heating is shown in Figure 76. The carbide-like carbon peak was unchanged by this heating. Mild heating is thus seen to be effective at removing argon from the surface.

The silicon peak in Figure 76 has approximately one half the height of a bulk specimen peak. The carbide and oxygen peaks indicate that both silicon carbide and

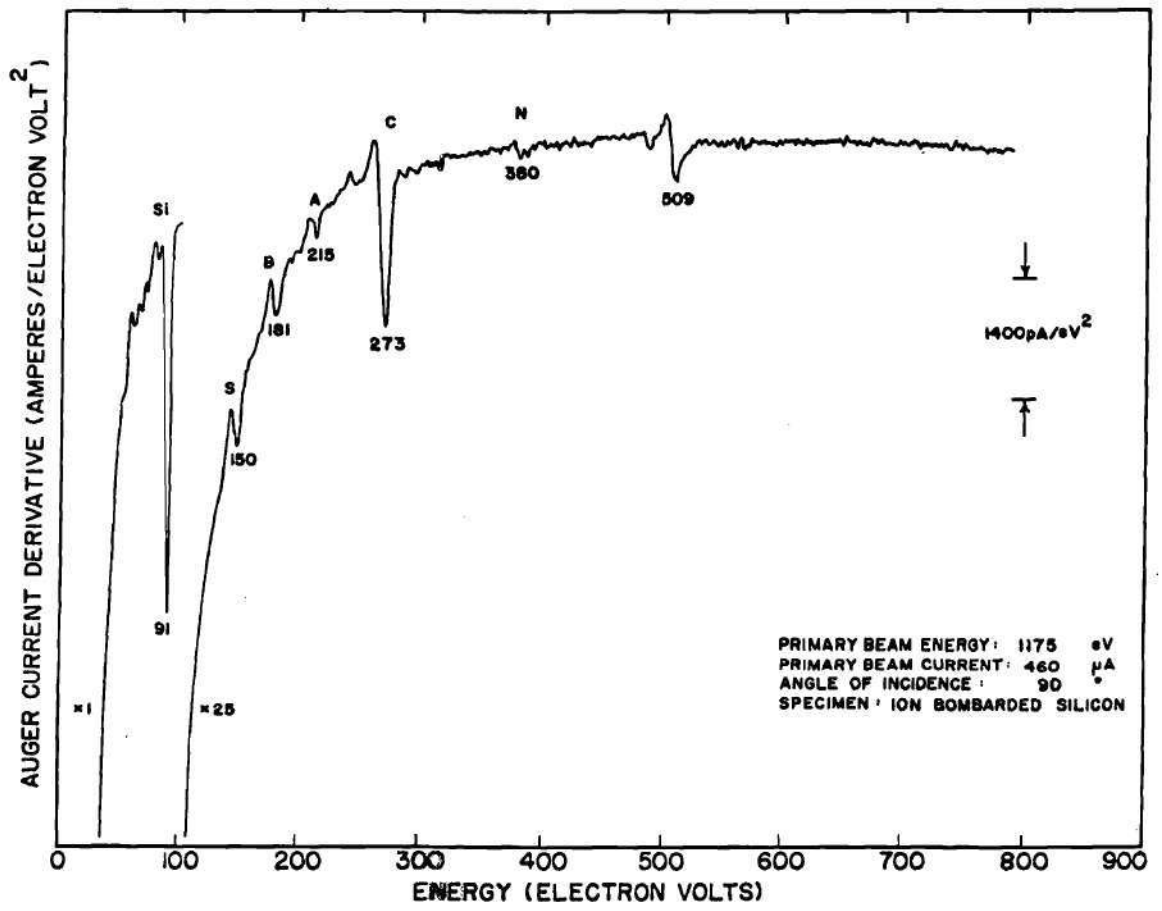

Figure 76. Auger Spectrum of Graphite Contaminated Silicon Surface after Argon Ion Bombardment.

silicon monoxide likely remain on the surface, and the response of silicon in these forms is much less than as pure silicon. Notice that the 75 eV silicon peak, characteristic of silicon dioxide, is again insignificant.

Since the Auger spectrum of the original, unbombarded surface, was free of any sign of silicon carbide, either at 89 eV or in the shape of the carbon peak, ion bombardment is seen to be another way in which silicon carbide may be formed from graphite and a surface containing silicon. It should be remarked that further ion bombardment removed the silicon carbide, so ion bombardment remains a viable surface cleaning technique.

The Removal of Carbon from Semiconductor Surfaces

The previous two sections of this chapter have described the sources of graphite and carbide on silicon semiconductor surfaces. This section will describe a sequence of experiments aimed at determining what treatments will successfully remove carbon from silicon surfaces.[21] The first portion of the section is devoted to graphite, the latter portion to silicon carbide.

A sequence of commercial wafers was studied in an attempt to ascertain surface treatments capable of removing graphite. The specimens were NPN power transistors removed from a commercial manufacturing line after the base diffusion. Each of the wafers studied before treatment displayed the characteristic one to two monolayers of graphite. This is, the wafers as removed from the manufacturing line were uniformly coated with a layer of graphite. These wafers, some after an initial Auger study, were subjected to a variety of chemical treatments and then studied with Auger spectroscopy. Of the chemical techniques studied, only strong oxidation was

successful at removing all of the graphite layer, although a methanol and distilled water treatment may also be adequate. The presence of silicon carbide prevented complete evaluation of the effectiveness of the methanol and distilled water treatment.

The first surface treatment considered in greater detail is chemical etching. A mild HF etch was prepared with approximately 0.25 cc of concentrated HF in 50 cc of distilled water. One half of an oxidized wafer was dipped in this etch for 60 seconds and then the entire wafer was rinsed in distilled water and blown dry. The graphite coverage was approximately two monolayers and there was some indication of SiC in the shape of the carbon peak. No difference in the graphite level could be detected between the two halves in the Auger spectra. Another similar wafer was treated with a stronger HF etch, in this case a 1.8 molar etch. The etching rate of this solution is 2.7 angstroms per second[55] and one half of the wafer was etched for 25 seconds. The entire wafer was then rinsed in distilled water and blown dry. The graphite coverage, as usual, was approximately two monolayers. Again no difference could be detected between the two halves in the Auger spectra. Finally, an oxidized wafer was completely stripped of oxide by HF and then further etched in a 1.8 molar solution for several minutes with ultrasonic agitation. The Auger spectrum of this wafer was shown in Figure 66. Even through this strong etching the graphite layer remained present.

The conclusion drawn from these experiments is that the graphite layer remains on the surface even while the underlying oxide is etched away. The graphite is present before treatment, as shown by the experiments in which only one half of the wafer was treated, and these treatments neither increase nor decrease the

coverage. The ability of the graphite layer to "ride along" on the surface while the underlying layer is removed was also noted in RF sputtering experiments in this work aimed at cleaning silicon surfaces prior to oxidation. Several silicon specimens with natural oxides were sputtered in an argon plasma. Different argon pressures and bias potentials on the specimen were tried. In all cases the oxide was removed but not the graphite layer. The graphite peak height would neither increase nor decrease as the oxide was removed. That the graphite was merely remaining in place, and not being deposited by the sputtering process, was shown by a separate experiment on aluminum. In this case RF sputtering did remove carbon completely and the surface remained free of graphite during subsequent sputtering. Since the same well controlled plasma was used in both cases, the implication is that the sputtering process is not a source of graphite. Graphite is simply very tenacious on silicon and the oxides of silicon.

A rinse in methanol and distilled water was tried on one oxidized wafer. This wafer was described in connection with Figure 40. The Auger spectra in this case showed no graphite explicitly but did show SiC, so the detection limit for graphite is an appreciable fraction of a monolayer. It is the opinion of some in the semiconductor community that this treatment, or a variation of it, may be effective at removing carbon in the form of graphite.[56] Limitations on time prevented a more complete evaluation of the technique in this work.

Oxidation was the third basic treatment studied. A mild oxidizing agent, concentrated H_2O_2, was evaluated first. One half of an oxidized wafer was dipped in the H_2O_2 solution for five minutes. The results of the Auger study were essentially

identical with the etching experiments. No difference in the two halves could be detected as both showed a monolayer or so of graphite.

Strong oxidation was tried next. This was accomplished by heating the wafer resistively in an oxygen atmosphere in the vacuum system. Figure 77 shows the Auger spectrum of the specimen before oxidation. The surface is seen to consist of SiO_2 and a heavy coverage of graphite (3.2 monolayers). The graphite layer is so thick that the low energy, 76 eV, silicon Auger electrons are almost completely attenuated. Figure 78 shows two spectra taken after oxidation treatments. The upper spectrum is after 120 seconds at 875°C in an atmosphere of pure oxygen. The indicated graphite coverage is 0.5 monolayers after this oxidation. Notice that there is little indication of SiC, either in the form of a peak at 89 eV or in the shape of the carbon peak. The specimen was then oxidized for an additional 300 seconds, this time at 950°C. The graphite coverage is reduced to less than a tenth of a monolayer but now there is a substantial indication of SiC. The presence of SiC is indicated both by the 89 eV peak and by the shape of the carbon peak. Silicon carbide is formed at a significant rate at 950°C but at a much lower rate at 875°C.[49] Notice also that the carbide is formed even when an oxidizing atmosphere is present. Whether or not it is formed is strictly a function of the presence of graphite and the proper temperature range. Therefore, we see that thermal oxidation can be an efficient means of removing graphite. The only precaution necessary is to limit the temperature range so that SiC is not formed. A final comment is that the carbon was not simply diffusing into the oxide in this experiment. The experiment was repeated on another portion of the same wafer, but with only 10^{-6} torr of oxygen present. In

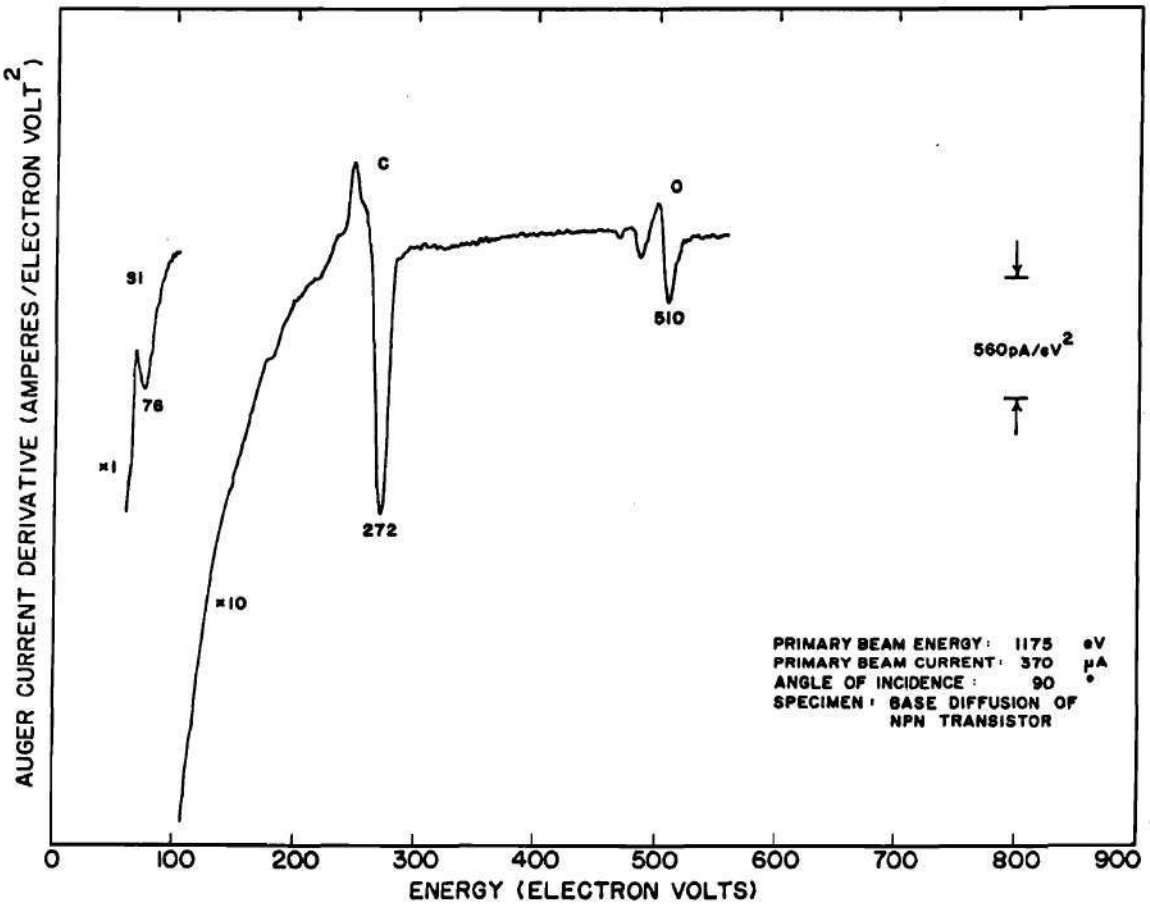

Figure 77. Auger Spectrum of Graphite Contaminated Oxide before Thermal Oxidation in the Vacuum System.

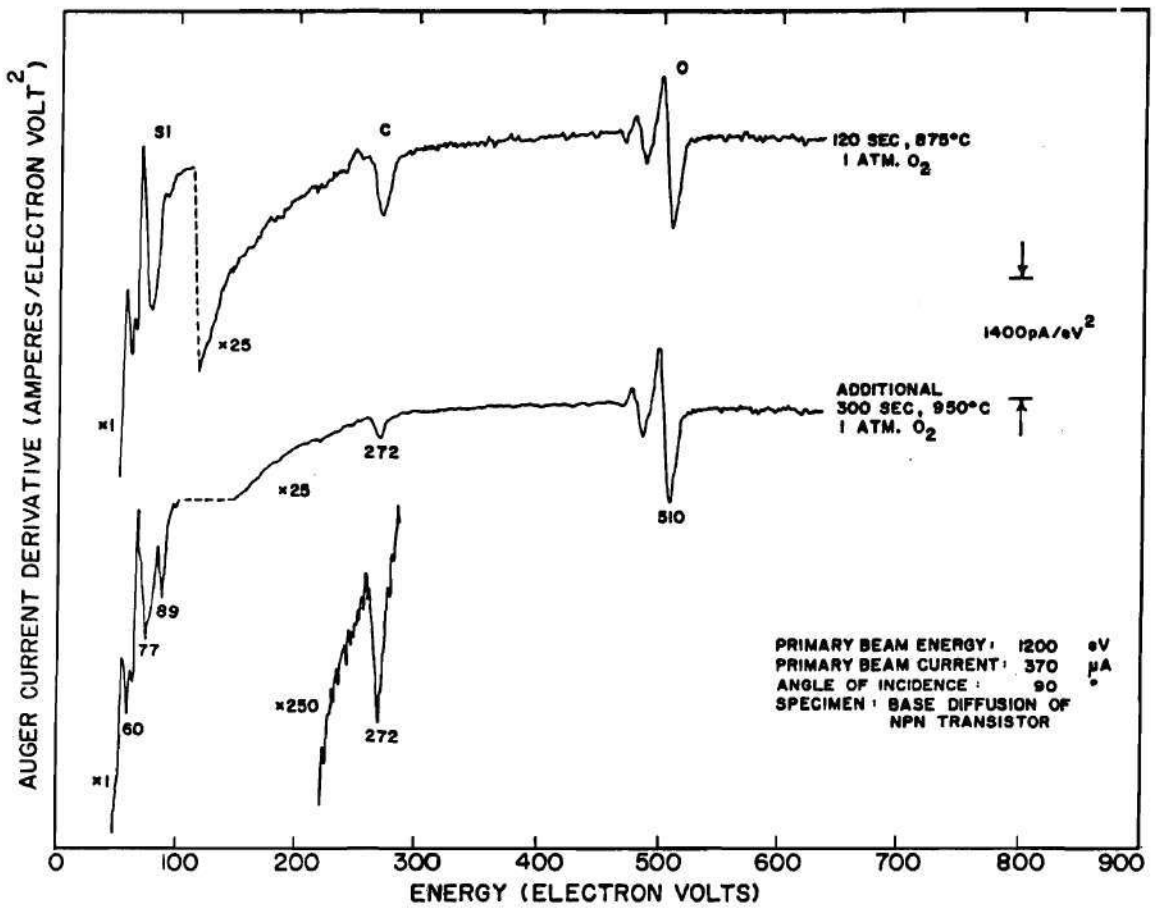

Figure 78. Auger Spectra of Graphite Contaminated Oxide Surfaces after Thermal Oxidation Treatments in Vacuum System.

this case there was no detectable reduction in the graphite coverage except to the extent that SiC was formed at the higher temperature range.

Argon ion bombardment was the final technique studied for the removal of graphite from silicon surfaces. While very slow, ion bombardment is an effective means of cleaning silicon. Unfortunately, the technique can not be used on heavily oxidized surfaces because of charging.* The natural oxide on silicon is thin enough so that charging is not a problem. The surface which served as the silicon standard in the calibration spectra section of Chapter IV was prepared in this way.

Silicon carbide was noted on a number of wafers and was formed by some of the heat treatments, as discussed above. None of the wet chemical treatments tried for graphite removal showed any effect on SiC. Only argon ion bombardment removed silicon carbide particles. This was discovered when ion bombardment of silicon surfaces was found to form SiC when substantial graphite is present. Only after the graphite has been removed is the carbide removed by bombardment. Finally, it has been reported in the literature that heat treatment at temperatures above 1100°C removes SiC by dissolving the carbide into the bulk silicon.[49] Technical difficulties prevented heat treatment at this high a temperature in this work. However, extensive heat treatment at 1000°C was carried out on SiC contaminated oxide surfaces in the high vacuum. In no case was the carbide peak reduced by the heat treatment.

---

*Unless, of course, some auxiliary technique such as electron bombardment is employed to maintain charge neutrality.

Combined Electron Microscopy and Auger Spectroscopy of Commercial Wafers

This section presents electron micrographs and Auger spectra from three commercial wafers which were studied in detail. In each case the micrographs and Auger spectra are from the same area of the wafer. Since the electron microscopy and Auger spectroscopy were performed on different instruments, the subject area was marked with silver paint dots around the periphery so that the same region was studied in each case. The spatial resolution of the combined study is only that of the Auger spectrometer, a millimeter or so in this case; for each region selected the Auger spectrum is the average over the region. Thus the spatial resolution of the material analysis (Auger spectroscopy) is a millimeter but the spatial resolution of the topographic analysis (electron microscopy) is that of the scanning electron microscope or the transmission electron microscope, whichever was used. However, in this case little information is lost because the material of interest, silicon carbide, is in the form of particles and is therefore obvious in the micrographs. The situation would be very different if both graphite and silicon carbide had the same morphology on silicon surfaces.

The geometry of the study is illustrated in Figures 79 and 80. Recall from Figure 58 in Chapter VI the mounting procedure for commercial wafers. The photographs of Figures 79 and 80 were taken with the specimen mounted in the vacuum system. Since the specimen surface can not be seen directly, it was necessary to use a small mirror mounted on the analyzer for viewing the surface. The small size and low intensity of the image account for the low resolution of the photographs.

Figure 79a is an overall view of the wafer. The circular mounting ring can

(a)

(b)

Figure 79. Fluorescence of Commercial Wafer under Electron Bombardment.

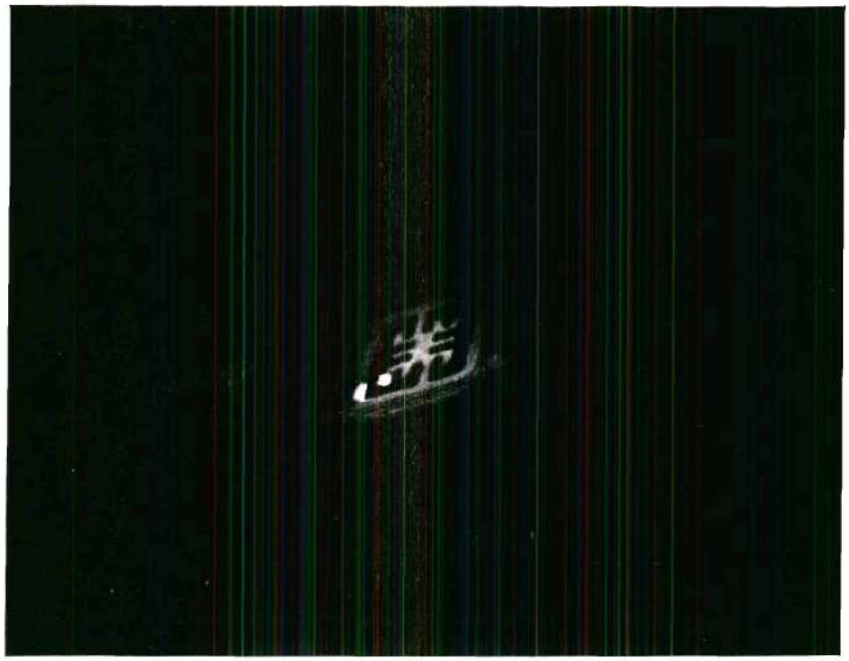

(a)

(b)

Figure 80. Fluorescence of Different Regions of a Transistor.

be seen around most of the periphery of the wafer. The diameter of the opening in the ring is approximately three centimeters. Each of the square patterns is one NPN power transistor. The thin white line between each square is the scribe line. The pair of "E" shaped patterns on each transistor is the emitter region; the emitter appears light against the dark base region in Figure 79a. One of the transistors has an elliptical bright spot on it. This is the fluorescence caused by the primary beam striking the specimen. The beam in this case is covering most of a transistor. The remainder of the photograph was taken by reflecting light from a flashlight off of the analyzer and onto the specimen. Since the brightness of the fluorescence is much less than that obtainable from a flashlight, a double exposure was used to create this image.

Figure 79b is an expanded view of one transistor. This image was formed completely by fluorescence from the primary beam. The beam was expanded to cover an area approximately equal to two transistors in this case. Notice that the gray scale of this image is inverted from that of Figure 79a. Silicon reflects light better than the thick oxides on these transistors. Since this wafer was removed after emitter masking, the emitter areas are silicon and by base and collector regions are oxide covered. Therefore, in the upper image the emitter appears white against a dark background. However, silicon dioxide fluoresces much more than silicon* or, for that matter, silicon monoxide or silicon carbide. Therefore,

*The relative fluorescence of silicon, silicon monoxide, silicon carbide, and silicon dioxide was determined, qualitatively, by observation with the eye of the fluorescence of bulk specimens when bombarded by a 300 microampere, 1200 eV, normal incidence beam.

in the lower image the emitter appears dark against a white background. Notice there is an eliptical shadow in the center of the transistor of Figure 79b. This is silicon monoxide, and perhaps silicon carbide, formed from previous electron bombardment. This darkening of the fluorescence of silicon dioxide is observed after a few minute electron bombardment and serves as a convenient indicator of damage to the surface by the primary beam. It is actually a more sensitive indicator than the appearance of the SiO or SiC peaks in the Auger spectra. The darkening seen in Figure 79b does result in an observable peak at 90 eV in the Auger spectra, but the eye can detect the darkening from far less damage.

Figure 80 shows photographs of a transistor discussed in detail later in this section. Figure 80a is a double exposure using fluorescence. The whole transistor was first illuminated with the primary beam and then the bright spot was formed by focusing the beam on the emitter. It is seen that the spot overlaps the base and collector regions somewhat. About one half of the spot is on the emitter region. One would like to be able to focus the beam separately on each portion of the transistor. This overlap will cloud interpretation of the spectra, but it could not be avoided with the equipment used in this work. Figure 80b shows the beam on the collector oxide between two transistors. Notice the extensive damage to the base region from prior bombardment.

The first wafer discussed in greater detail is that of Figure 39 in Chapter V. This wafer was removed from the line after the collector oxide was grown, but before base masking. This is an N type oxide. The Auger spectrum showed no SiC contamination. Thus, this specimen serves as a control to indicate surface morphology in

the absence of SiC. Figure 81 is a scanning electron micrograph of the surface. The surface appears very smooth to the scanning scene. The only features of the micrograph are 60 Hz hum bars and random noise. A plastic (negative) replica was also made of the surface. Figure 82 is a transmission micrograph of the replica. The surface of Figure 82 is from a similar, but not identical, region of the specimen as that of Figure 81. A minor amount of surface roughness is seen with the improved resolution of the transmission scope. The prominent features of the transmission micrograph correspond to indentations of the surface. The resolution of the transmission scope, compared to the scanning scope, is evident in the two figures since both are at approximately the same magnification. The indentations of the surface are 500 angstroms in diameter, or smaller. This is a measurement of the area of the indentation, not the depth.

Scanning and transmission micrographs were also made on a second surface free of SiC in the Auger spectrum. This surface was the silicon dioxide grown in the vacuum system and discussed in the calibration spectra section of Chapter IV. These micrographs, not presented here, were equivalent to Figures 81 and 82.

The second wafer to be discussed also was removed from a NPN transistor line, but a different one from the transistors shown in Figures 79 and 80. This wafer was removed after emitter masking. The Auger spectra showed varying indications of SiC across the wafer. Figure 83 is a transmission micrograph of a plastic replica. A number of particles are seen on the surface. Since this replica is a negative, representative particles and indentations are identified on the figure. Notice there is a cluster of particles in the lower right hand corner. The overall

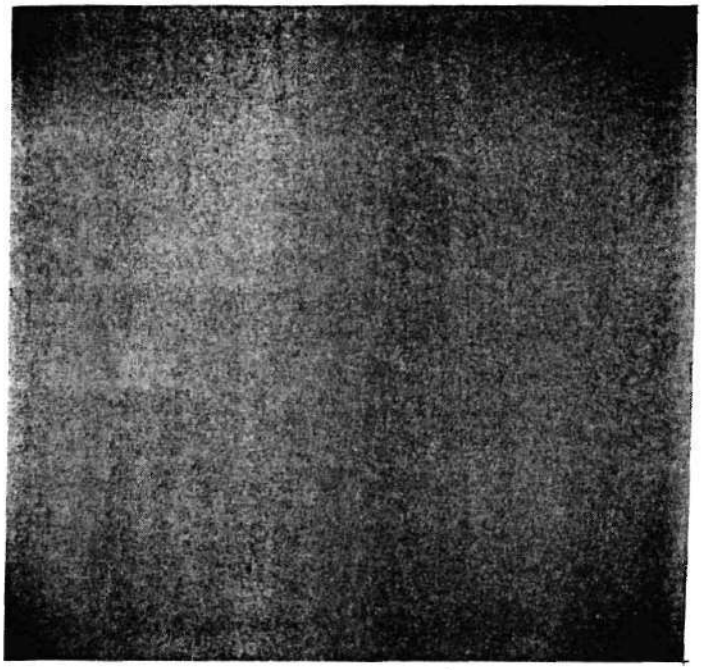

Figure 81. Scanning Micrograph of Commercial Oxide Surface Free of SiC Contamination. Magnification is 18,700.

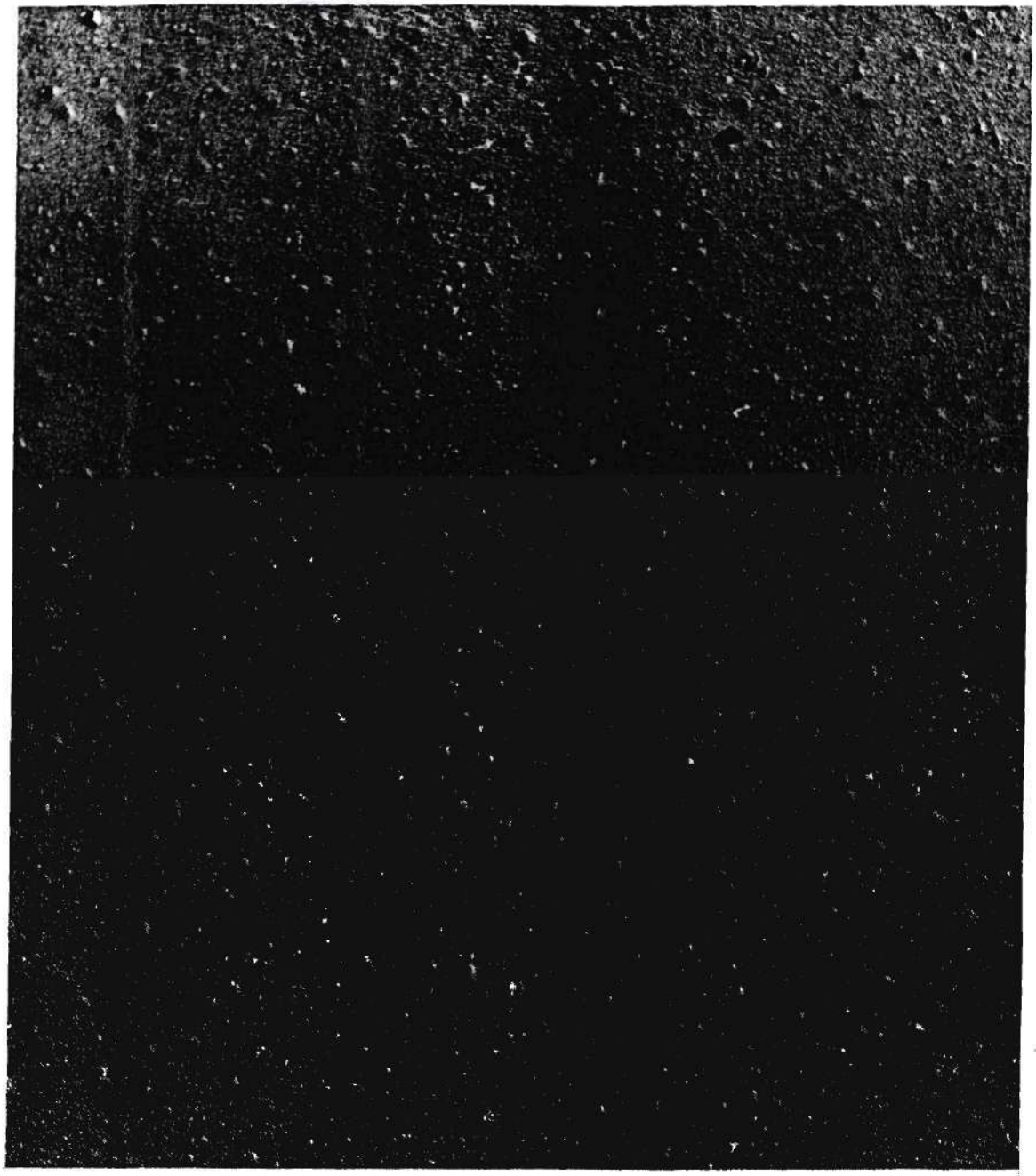

Figure 82. Transmission Micrograph of Plastic Replica of Commercial Oxide Surface Free of SiC Contamination. Magnification is 20,500.

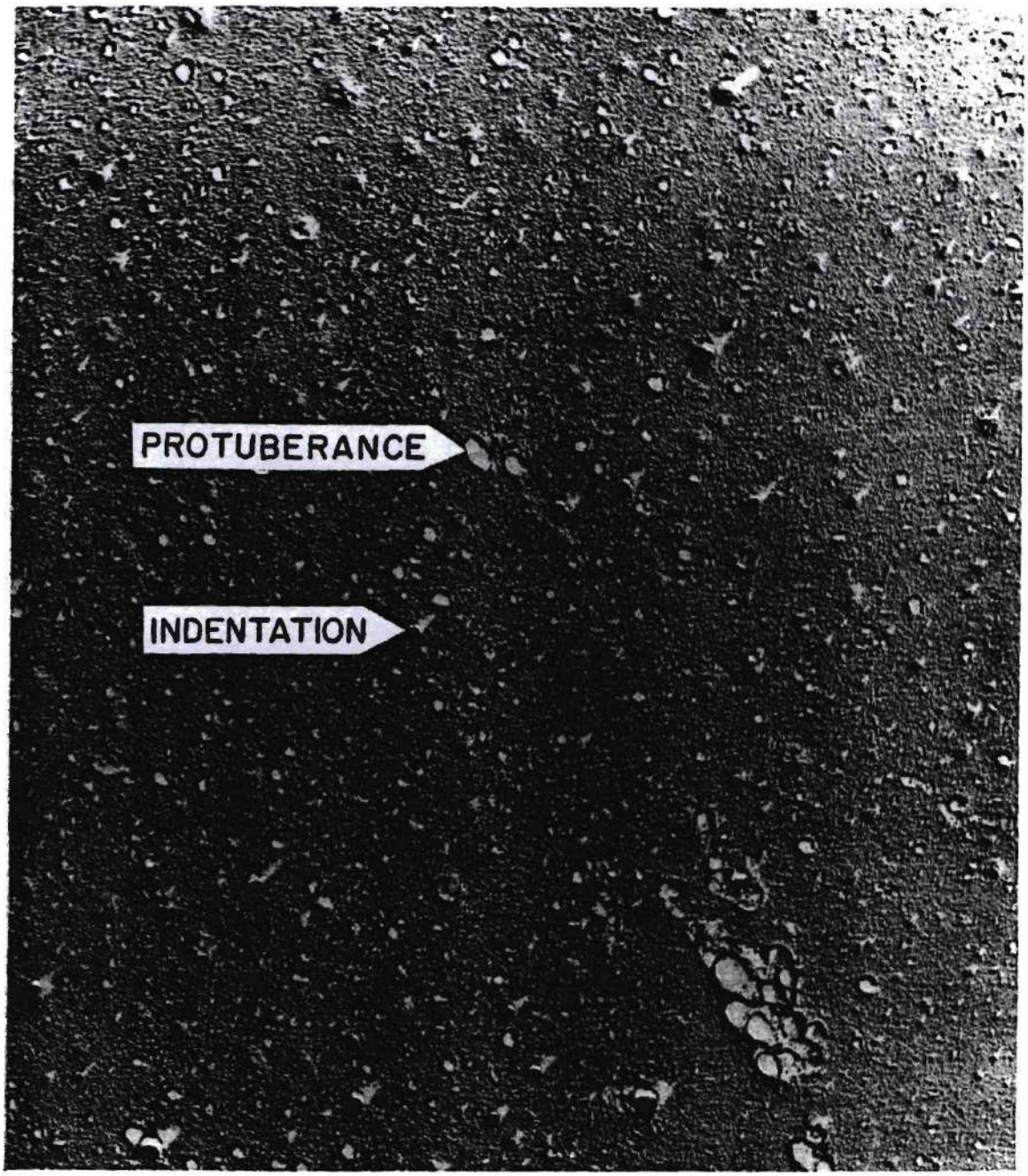

Figure 83. Transmission Micrograph of Plastic Replica of Commercial Oxide Surface Showing some SiC Contamination. Magnification is 20,500.

coverage by particles is fairly small though. Figure 84 is another transmission micrograph of the plastic replica. Even fewer particles are seen in this portion of the surface. The number and size of the indentations remains constant and similar to Figure 82, the uncontaminated oxide. Finally, Figure 85 is yet another transmission micrograph of the replica, this time showing a higher density of particles and made at higher magnification than Figures 83 and 84.

The variance in the number of particles seen in these micrographs is attributed both to a natural variation across the wafer as a whole and to variations across each transistor. The transistors on this wafer were much smaller than those in Figure 79. Thus, the beam covered most of a transistor. As the beam was moved about it was variously distributed between emitter region and base oxide. The next example shows there may be significant variations in SiC particle density between emitter and base regions. Thus, different positions would show different particle densities.

A representative Auger spectrum for the surface is shown in Figure 86. The spectrum is characteristic of silicon dioxide, with a small indication of SiC at 89 eV. Notice that the carbon peak is in the form of graphite, not SiC. Thus, the surface has some SiC and is covered overall by a graphite layer. This spectrum shows that a small number of SiC particles can be detected in the presence of graphite by looking for the 89 eV peak. That the 89 eV peak is truly at 89 eV is shown in the next figure, Figure 87, which has an expanded energy scale. The 75 eV silicon peak from the SiO_2 serves as a reference mark. The SiC peak is located 14 eV higher in energy. The stability of the charge state was assured by the techniques of Chapter VI and the

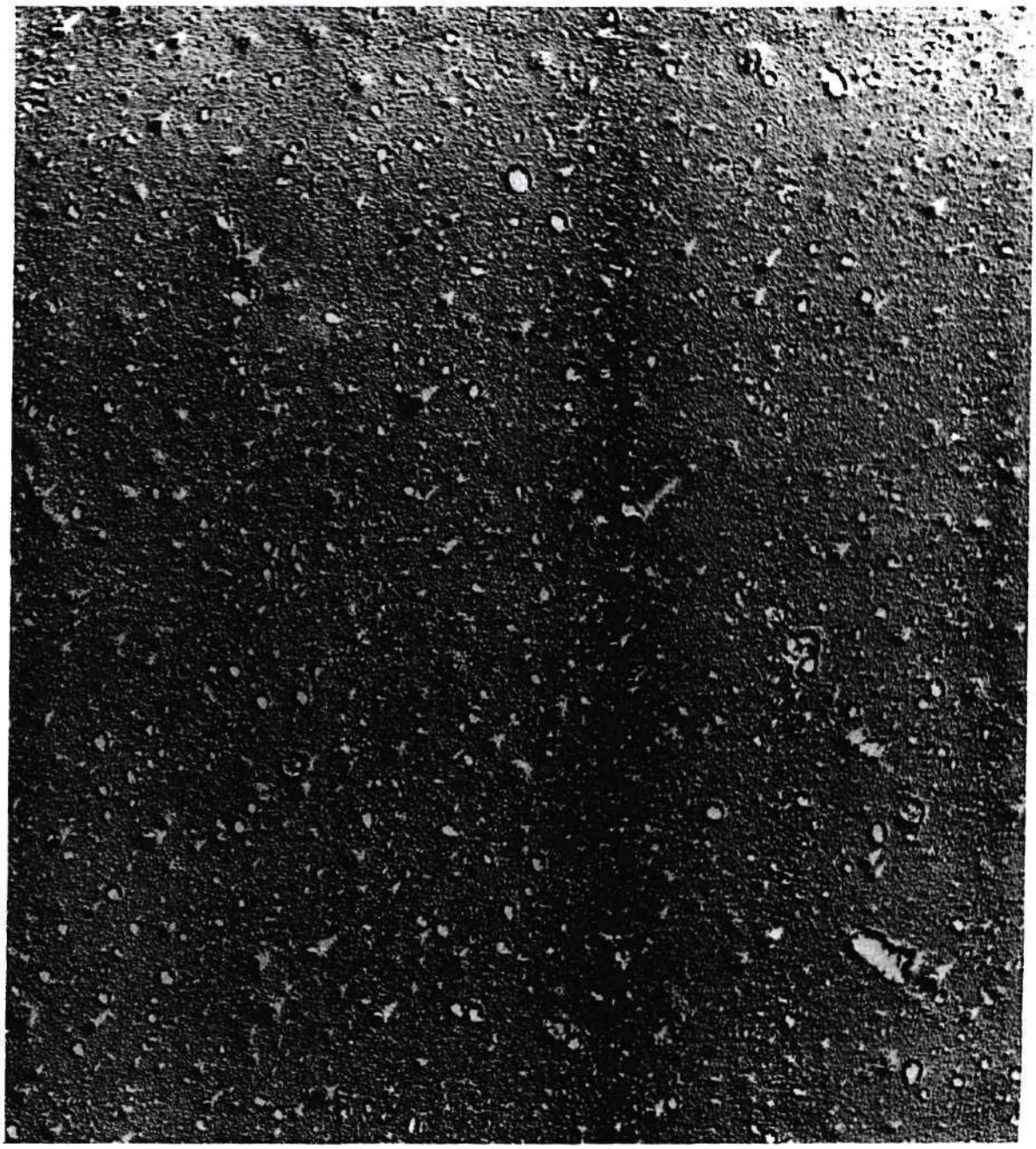

Figure 84. Transmission Micrograph of Plastic Replica of Commercial Oxide Surface Showing Less SiC Contamination Than in Figure 83. Magnification is 20,500.

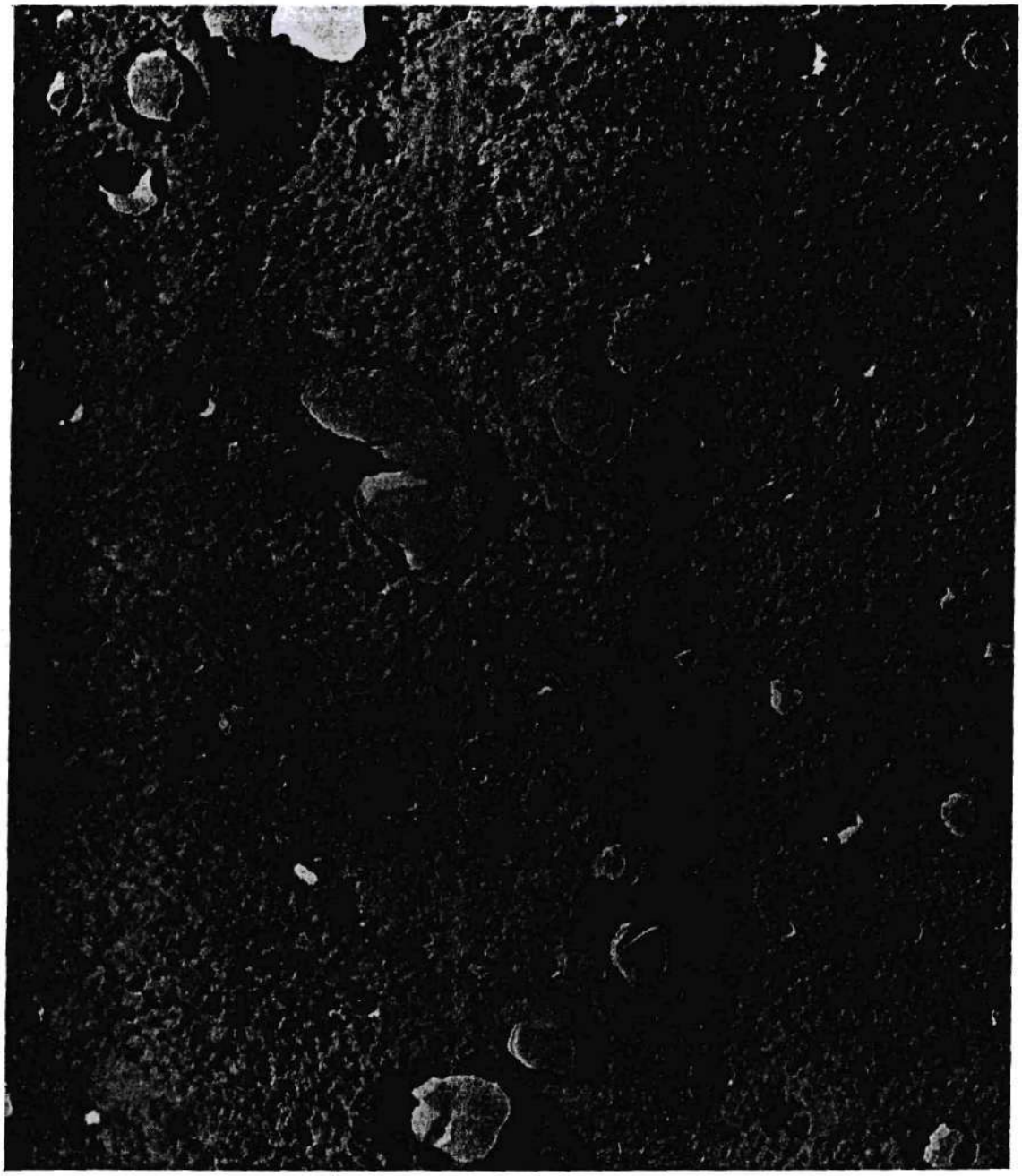

Figure 85. Transmission Micrograph of Plastic Replica of Commercial Oxide Surface Showing SiC Contamination. Magnification is 69,800.

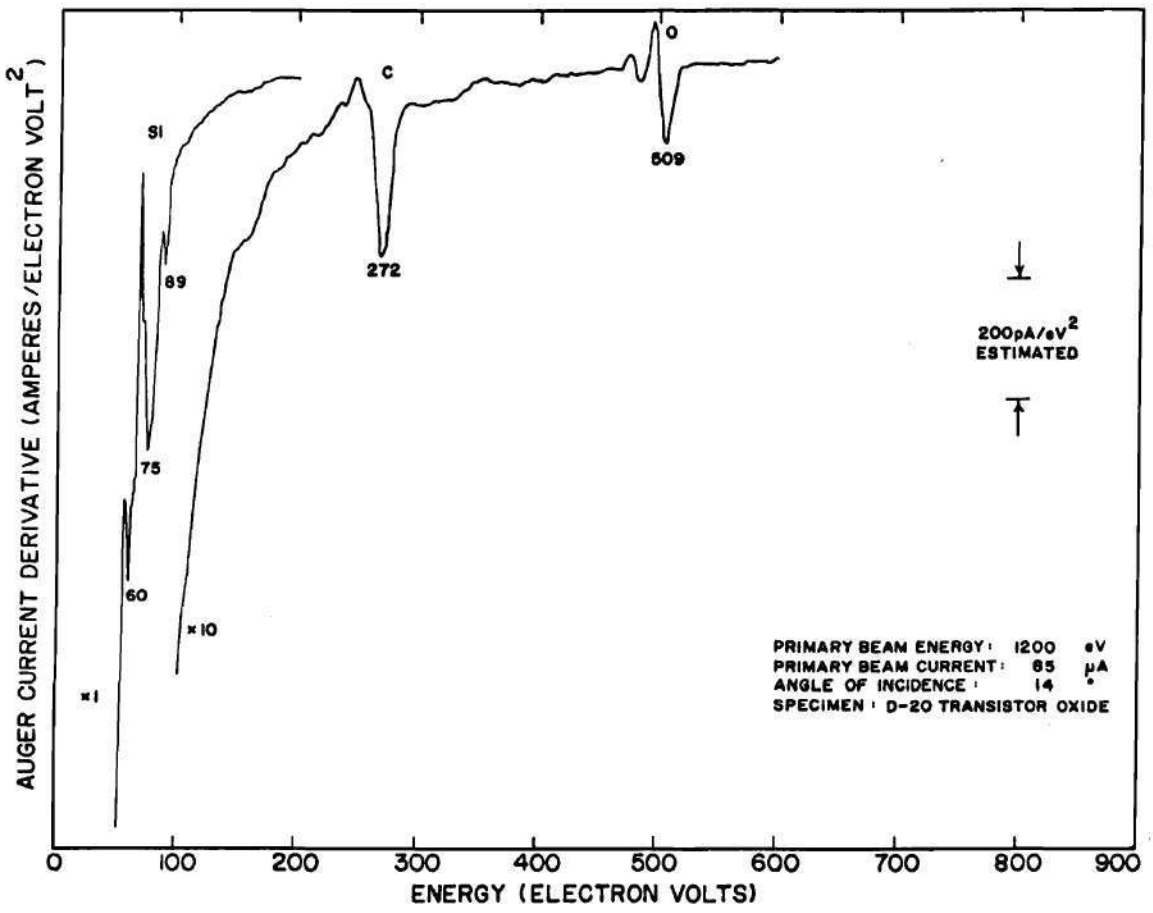

Figure 86. Auger Spectrum of Silicon Carbide Contaminated Commercial Oxide.

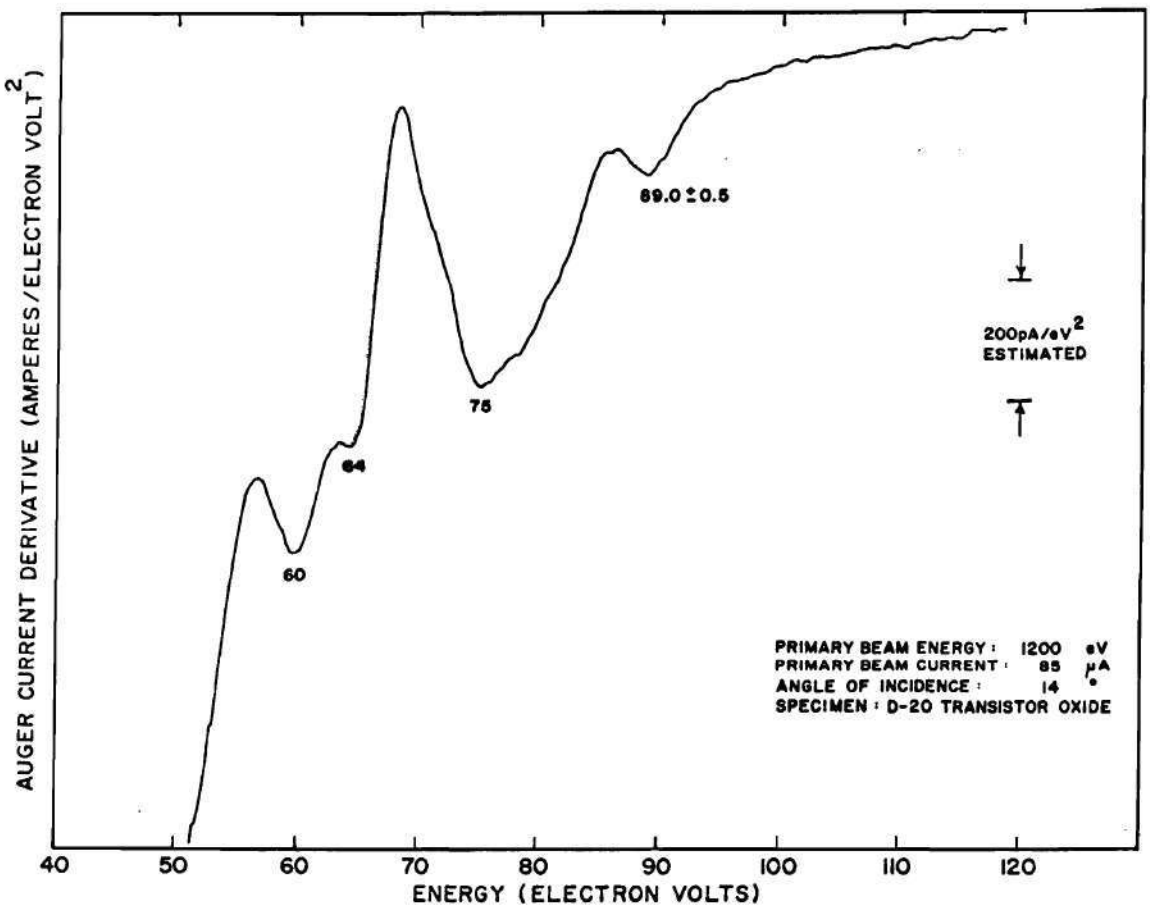

Figure 87. Expanded View of Silicon Peak in Auger Spectrum of SiC Contaminated Commercial Oxide.

remaining peaks of the SiO_2 complex occur at their correct energy. The good signal to noise ratio in this figure shows that a significantly smaller coverage of SiC could be detected with this technique.

The final example considered is a transistor from the wafer pictured in Figure 80. These were large NPN power transistors, removed from the line after emitter masking. An Auger spectrum for the entire transistor was shown in Figure 64 in Chapter VI. This spectrum showed an indication of SiC. Figure 88 is an expanded energy scale spectrum with the beam localized on the collector oxide. Although the signal to noise ratio is not as good as that of the previous example, the SiC indication is still clear. The same area bombarded by the primary beam in taking this Auger spectrum is shown in the scanning micrograph of Figure 89a. Only a few particles, the white dots in this low magnification micrograph, are seen. The collector-base step is the diagonal line in the upper right hand corner; the collector covers the majority of the micrograph. Some of the SiC indication in the Auger spectrum for the collector oxide is attributed to beam overlap into the base region, which contained a greater amount of SiC.

The lower micrograph, Figure 89b, shows basically emitter region, with the emitter-base step being the diagonal line across the upper right hand portion of the micrograph. The emitter region contains a great number of particles and the base regions contain some, but far less. Some of the larger particles are probably "dust and dirt" but the smaller, more numerous particles are SiC. This interpretation is verified by the Auger spectrum taken with the beam centered on the emitter. This spectrum is shown in Figure 90. There is now a substantial SiC indication. That

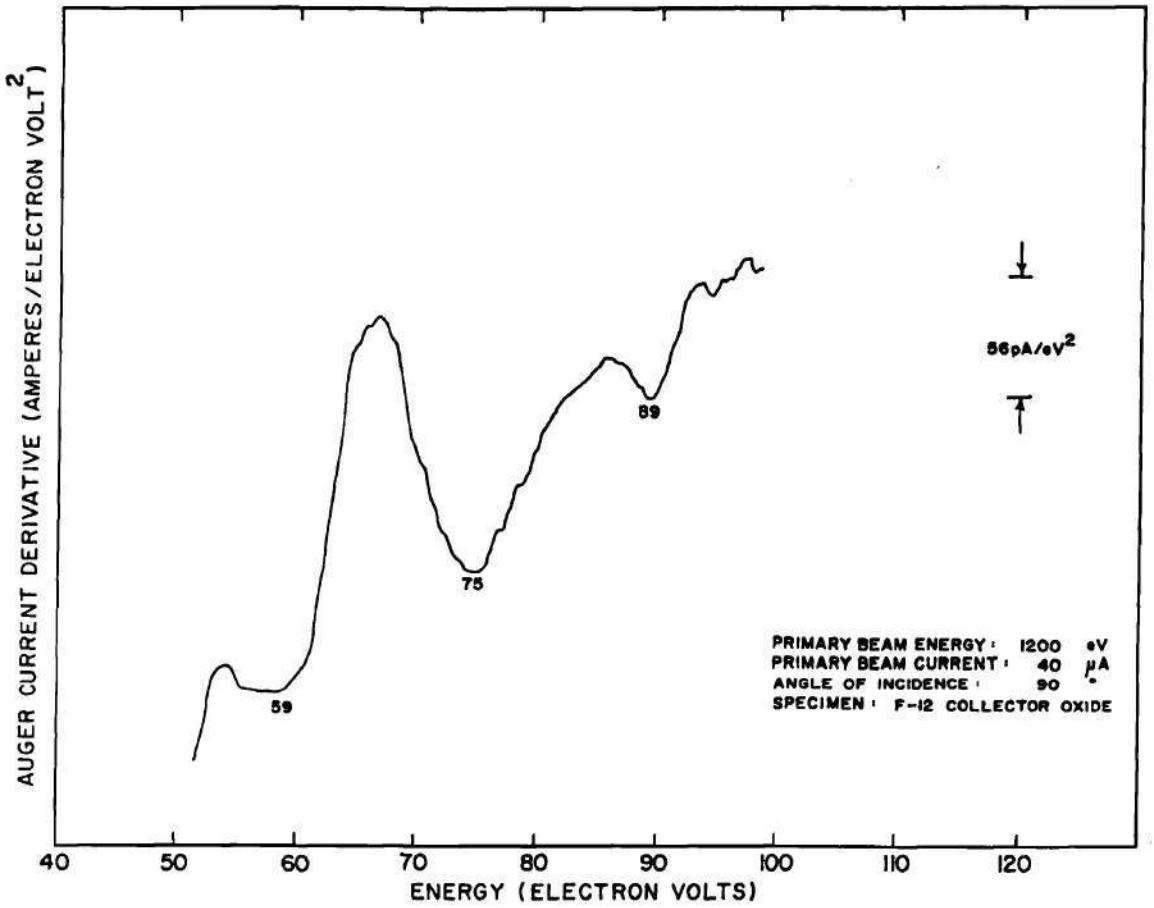

Figure 88. Expanded View of Silicon Peak of Auger Spectrum of Collector Oxide of Transistor.

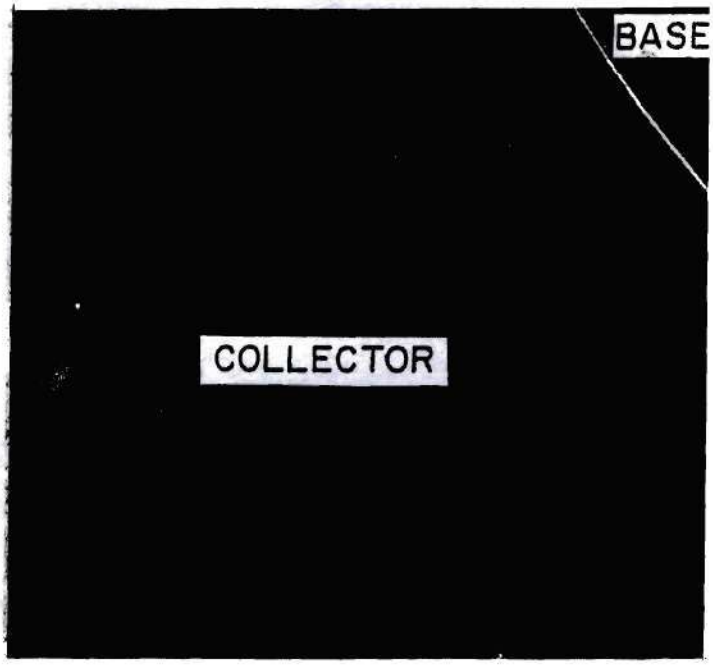

(a)

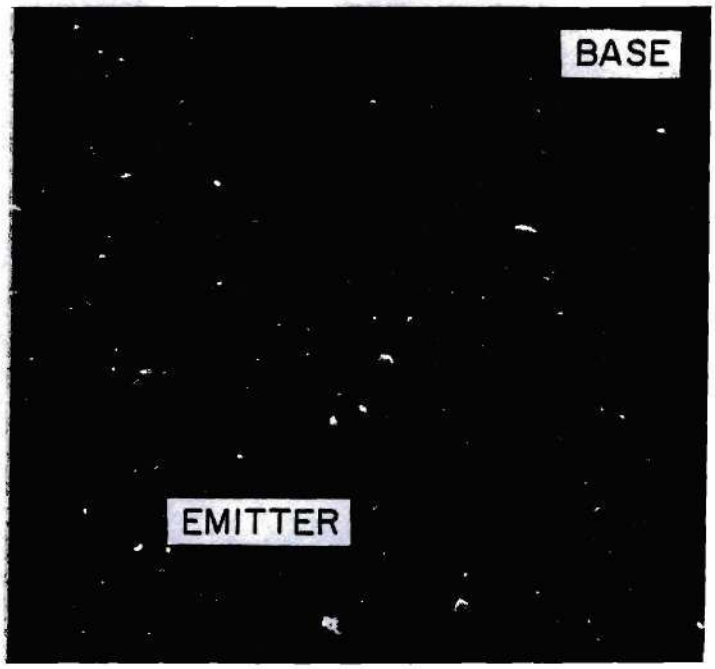

(b)

Figure 89. Scanning Micrographs of SiC Contaminated Transistor. Magnification is 450.

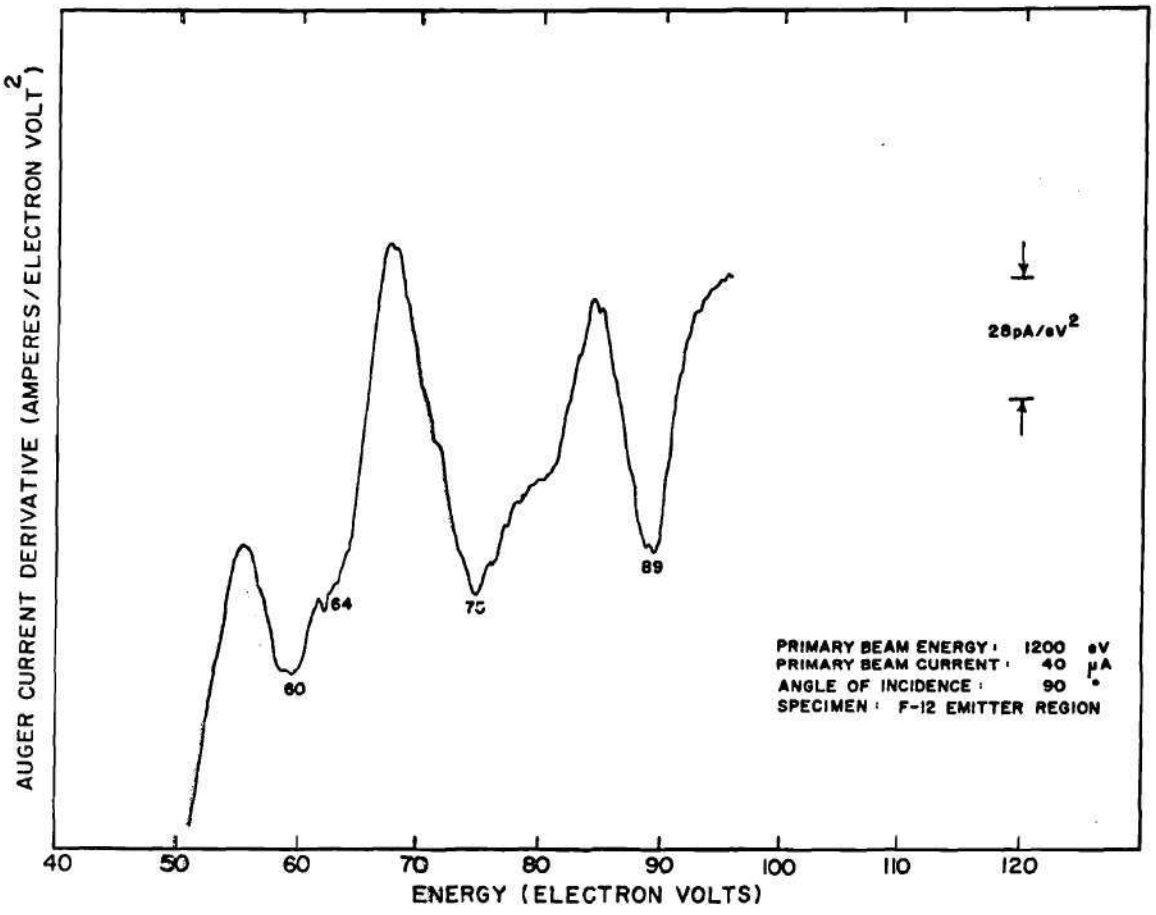

Figure 90. Expanded View of Silicon Peak of Auger Spectrum of Emitter Region of Transistor.

the indication is not even larger is due to the beam overlap onto the base region where the SiC particle density is less. The conclusion reached from this correlated Auger spectroscopy and electron microscopy is that the SiC coverage is proportional to the number of etchings and diffusions an area has received. Thus the emitter has more than the base, which in turn has more than the collector.

The final figure, Figure 91, shows scanning micrographs of particularly large particles which are believed to the SiC. The upper micrograph, Figure 91a, is from the emitter region of the transistor just discussed. Notice that the particles appear to grow out of the surface; this is one basis for interpreting them as SiC. The lower micrograph is from a graphite contaminated silicon specimen which was ion bombarded and heated to purposely form SiC. Although the particle in the lower micrograph is somewhat smaller (notice the difference in magnification) the morphology is the same. The indentations of the lower surface are the result of extensive ion bombardment.

In summary, these three examples illustrate a general result noted in the study of SiC on commercial wafers: that the SiC contamination increases with process steps and the availability of elemental silicon. Thus SiC is a particular problem after emitter masking because of the accumulation of graphite, to be converted to SiC, and the presence of exposed silicon to form the SiC.

For practical purposes SiC is formed from graphite and silicon over the temperature range 900^{o}C to 1100^{o}C. Thus, prevention of SiC contamination may be affected by limiting the temperature range of the processing steps, which may be feasible with ion implantation techniques, or by removal of the graphite layer. The

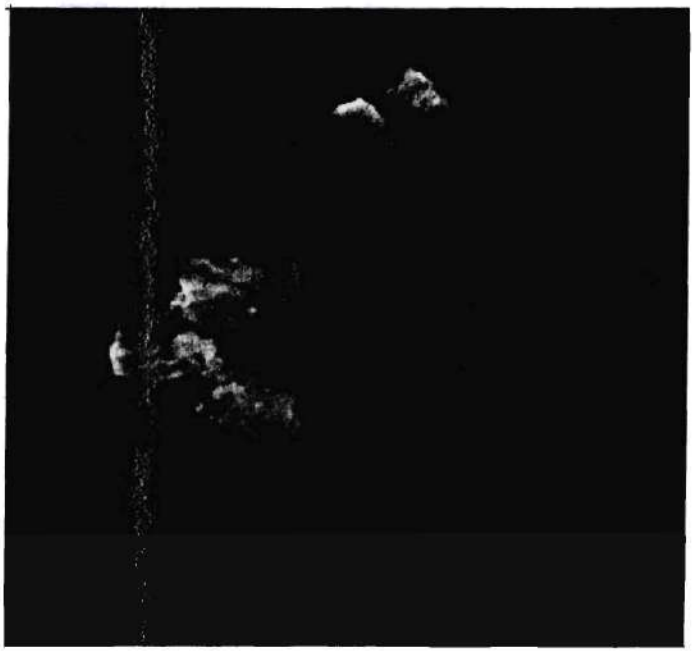

(a)

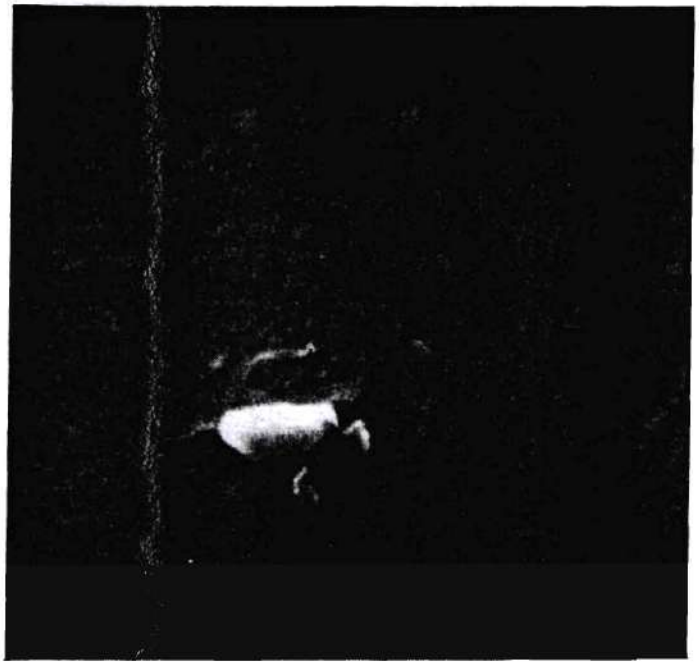

(b)

Figure 91. Scanning Micrographs of Particles Believed to be Silicon Carbide. Magnification is 9010 for the Top Micrograph and 31,000 for the Bottom Micrograph.

experiments of this chapter showed that the most effective way of removing graphite is by oxidation. Graphite is effectively removed by thermal oxidation in the 800°C temperature range, which is less than the temperature range for the formation of SiC. Therefore, a short exposure to an oxidizing atmosphere may prove useful in diffusion work where SiC particle formation proves to be a problem.

The electrical effects of graphite and SiC were not determined explicitly in this work, but some comments on their likely effect may be made. Graphite, per se, probably does not affect processing steps because it is normally present in one or two monolayer thicknesses and forms a uniform layer on the surface. Additionally it is very porous, and therefore would not be expected to affect diffusion or oxidation processes. On the other hand, the presence of graphite at an interface, e.g., Si-SiO_2, SiO_2-metal, etc., could very well introduce trapping centers[57] and therefore would affect the electrical performance of the device. Field effect devices would be particularly susceptible to charge in such trapping centers.

The primary effects of SiC are likely in affecting the manufacturing process because of the particle nature of SiC. Silicon carbide is not at all porous; it acts like a barrier to diffusion and oxidation. Thus SiC particles will cause irregularities in the diffusion profile. This effect will become more critical as geometries are made smaller and emitter diffusions become shallower. The size of the particles noted in this work was sufficient to also materially affect oxidation processes in thin oxide MOS devices.

CHAPTER VIII

SUMMARY AND RECOMMENDATIONS FOR FURTHER WORK

The objectives of the research were to affect an improvement in Auger spectroscopy as an analytical tool and to apply the spectroscopy to surface contamination on typical semiconductor devices. This chapter is a summary of the accomplishments of the research and recommendations for further work.

The first three chapters of this dissertation introduce the reader to the Auger effect and Auger spectroscopy. The emphasis in the remainder of the work is placed on Auger spectroscopy and, in particular, on the application of Auger spectroscopy to the study of contamination found on commercial semiconductor wafers. Previous efforts by others at applying Auger spectroscopy to semiconductor wafers are reviewed with a critique of interpretations of spectra taken on oxide surfaces.

The theory necessary for quantitative interpretation of Auger spectra is developed in the fourth chapter. The factors contributing to the fingerprint of each element are described first, for it is the fingerprint of the element which allows identification to be made and the nature of the chemical bonding to often be determined. Calibration spectra for Si, SiO, SiO_2, SiC, and C are presented. These spectra allow each substance to be identified and, in most cases, analyzed quantitatively. Basic quantitative considerations for Auger spectroscopy are then outlined and the two existing models for quantitative interpretation described. It is pointed out that a model containing both isotropic and oriented sources is necessary

to explain the response of Auger spectra as the primary beam angle of incidence is varied. Each of the four quantities contributing to Auger peak height--the source functions, Auger electron yield, Auger electron escape probability, and detector efficiency--are then discussed in detail and a new model for quantitative interpretation of Auger spectra is formulated. The final section of the fourth chapter outlines the calculations necessary both to predict Auger peak height a priori with the new model and to interpret peak heights with the model using calibration spectra.

Techniques necessary to successfully perform Auger spectroscopy on oxide surfaces are described in the sixth chapter. These techniques are for the detection and prevention of charging artifices. This compilation is a vital contribution to those interested in studying commercial semiconductor wafers with Auger spectroscopy for they allow the spectroscopist to take and interpret reliable data from oxide covered surfaces. Thus, the fourth and sixth chapters constitute a contribution to the improvement of Auger spectroscopy as analytical tool, both for general applications and for the specific application of studying oxide covered semiconductor wafers.

The achievements of the study of commercial semiconductor wafers are outlined in the fifth chapter. Representative spectra from oxide covered surfaces are presented and quantitatively interpreted. The effects of the primary electron beam are described and electron stimulated desorption is shown to be a complementary technique to Auger spectroscopy. One particular aspect of the commercial wafer results, the nature of carbon on semiconductor surfaces, is expanded in the seventh chapter. Sources for the two principal forms of carbon, graphite and

silicon carbide, are described, as are removal techniques for each. It is noted that electron and ion bombardment will reduce SiO_2 and form SiC when graphite is present. Electron bombardment was also found to reduce SiO_2 with no graphite present. The nature of SiC as a contaminant on commercial wafers was explored with the aid of electron microscopy. Generally speaking, the concentration of SiC increases with the number of processing steps completed and the availability of elemental silicon. Finally, some of the possible effects of graphite and SiC contamination are presented.

Two subjects explored in this dissertation definitely merit further study. These are the details of the interpretation calculation and the effects of graphite and silicon carbide on semiconductor surfaces.

In one sense Chapter IV is an outline of the calculations necessary for quantitative interpretation of Auger spectra. Though the outline is complete in that all significant factors are described, many details need to be added and estimates improved. The whole subject of moderate energy ($\sim$1000 eV) electron-solid interactions deserves further work. The electron transmission experiments of Mahkov offer a valuable guide in designing experiments in this energy range. These can be coupled with experimental determination of Auger response as a function of primary beam angle to yield a more complete understanding of these interactions. Auger electron escape depth also needs to be determined for a greater number of materials and energies so that a comprehensive theory may be developed. In summary, the Auger process actually offers an ideal tool for studying electron-solid interactions. Until these studies are complete, though, improved interpretations of

Auger spectra from general specimens will be difficult.

The effects of graphite and silicon carbide on semiconductor surfaces also merit further work. These effects can be both electrical, e.g., introducing states in the energy gap, or physical, as in the case of altering diffusion profiles. The electrical effects of these contaminants could be determined by fabricating MOS interfaces with and without contamination and then using capacitance-voltage analysis techniques. The effects of silicon carbide on diffusion could be determined by correlating electron microscopy of a contaminated area and standard wet chemistry profile analysis of the same area.

Finally, a number of interesting surface science observations were made during the course of the work. These observations were not pursued in the research reported in this dissertation for they were tangential to the objectives of the work. However, they do offer worthwhile starting points for future work.

The subject of oxidation of silicon should be studied in detail using Auger spectroscopy because of the capability of separating the various oxidized states. On a number of occasions an indication of SiO was obtained when SiO_2 was expected. The role of SiO in the formation of SiO_2 is one interesting topic in this subject. Another is the role of graphite as a possible inhibitor of oxidation.

Quantitative calibration of electron stimulated desorption is another worthwhile subject. An alternative technique for surface analysis would allow the Auger yield from adsorbed gases to be determined with greater precision. This would be an interesting study because it would show the influence of binding, the forces holding the atom or molecule to the surface, on Auger neutralization probability.

Two analytical instruments have also been suggested by the work. The first of these is a cathodoluminescence attachment for the scanning electron microscope for detection of SiC particles. This device would utilize the great difference in fluorescence between SiO_2 and SiC to detect the presence of SiC. The second instrument is also an attachment to the scanning microscope. This is an improved voltage contrast display based on the theory developed in Chapter VI for determination of surface potential. Both of these instruments are still in preliminary stages of development.

BIBLIOGRAPHY

1. R. M. Warner, Jr., Editor, Integrated Circuits, Design Principles and Fabrication, McGraw-Hill, New York, 1965, p. 79.

2. M. M. Atalla, E. Tannenbaum, and E. J. Scheibner, Bell System Technical Journal 38, 749 (1959).

3. See E. S. Schlegel, IEEE Transactions on Electron Devices ED-14, 728 (1967) for an extensive bibliography on the relationship between transistor performance and surface states. IEEE Transactions on Electron Devices ED-15, 951 (1968) contains an additional bibliography by the same author.

4. P. Auger, C. R. Acad. Sci. Paris 180, 65 (1925).

5. H. E. Bishop and J. C. Riviere, J. Appl. Phys. 40, 1740 (1969).

6. J. D. Phillips, Ph.D. Thesis, Georgia Institute of Technology (1972).

7. E. Burhop, The Auger Effect and Other Radiationless Transitions, Cambridge University Press, New York, 1952.

8. T. W. Hass, J. T. Grant, and G. V. Dooley, Phys. Rev. B 1, 1449 (1970).

9. C. C. Chang, Surf. Sci. 25, 53 (1971).

10. G. W. Simmons, Journal of Colloid and Interface Science 34, 343 (1970).

11. G. F. Amelio, Ph.D. Thesis, Georgia Institute of Technology (1969).

12. Varian Chart of Auger Electron Energies, Vacuum Division, Varian Associates, Palo Alto, California, 1970.

13. P. W. Palmberg, G. E. Riach, R. E. Weber, and N. C. MacDonald, Handbook of Auger Electron Spectroscopy, Physical Electronics Industries, Edina, Minnesota, 1972.

14. J. J. Lander, Phys. Rev. 91, 1382 (1953).

15. L. N. Tharp and E. J. Scheibner, J. Appl. Phys. 38, 3320 (1967).

16. L. A. Harris, J. Appl. Phys. 39, 1419 (1968).

17. K. Siegbahn, Uppsala University Institute of Physics UUIP-670 (1969).

18. P. W. Palmberg, G. K. Bohn, J. C. Tracy, Appl. Phys. Letters 15, 254 (1969).

19. D. K. Hartman, L. A. Harris, and J. H. Affleck, Interim Engineering Progress Reports IR-531-8B-(1-6), In-Process Control Techniques for Complex Semiconductor Structures, Contract F33615-68-C-1481 between General Electric Company, Semiconductor Products Department, Syracuse, New York and the Air Force Materials Laboratory, Wright Patterson AFB, Ohio, 1969.

20. L. N. Tharp, Final Report Project No. A-1240, Contract No. NAS 8-25667 between the Engineering Experiment Station, Georgia Institute of Technology, and the NASA Marshall Space Flight Center, Huntsville, Alabama, 1971.

21. C. C. Chang, Surf. Sci. 23, 283 (1970).

22. T. W. Haas, J. T. Grant, and G. J. Dooley, J. Appl. Phys. 43, 1853 (1972).

23. P. W. Palmberg, Appl. Phys. Letters 13, 183 (1968).

24. P. W. Palmberg, G. K. Born, and J. C. Tracy, Appl. Phys. Letters 15, 254 (1969).

25. Auger Electron Spectroscopy--Selected Bibliography, Vacuum Division, Varian Associates, Palo Alto, California, July 1971.

26. N. J. Taylor, Rev. Sci. Instr. 40, 792 (1969).

27. J. R. Pierce, Theory and Design of Electron Beams, Van Nostrand Co., New York, 1949.

28. J. L. Vossen and J. J. O'Neill, Jr., RCA Review 29, 149 (1968).

29. J. A. Bearden and A. F. Burr, Rev. Mod. Phys. 39, 125 (1967).

30. T. W. Haas and J. T. Grant, Appl. Phys. Lett. 16, 172 (1970).

31. N. J. Taylor, Surf. Sci. 15, 169 (1969).

32. H. E. Bishop and J. C. Riviere, Surf. Sci. 17, 462 (1969).

33. R. M. Burger and R. P. Donovan, Fundamentals of Silicon Integrated Device Technology, Volume I, Prentice Hall, Englewood Cliffs, 1967, p. 49.

34. J. T. Grant and T. W. Haas, Surf. Sci. 23, 347 (1970).

35. J. E. Houston and R. L. Park, Appl. Phys. Lett. 14, 358 (1969).

36. M. P. Seah, Surf. Sci. 32, 703 (1972).

37. T. E. Gallon, J. Phys. D: Appl. Phys. 5, 822 (1972).

38. A. F. Makhov, Soviet Physics-Solid State 2, 1934, 1942, 1945 (1960).

39. F. Meyer and J. J. Vrakking, Surf. Sci. 33, 271 (1972).

40. T. E. Everhart and P. H. Hoff, J. Appl. Phys. 42, 5837 (1971).

41. A. Messiah, Quantum Mechanics, Volume I, John Wiley & Sons, New York, 1961, pp. 388, 423, 424.

42. J. L. H. Jonker, Philips Research Repts. 6, 372 (1951). See also V. O. Hachenberg and W. Braver, Advances in Electronics and Electron Physics, Vol. XI, Academic Press, New York, 1959.

43. P. A. Wolff, Phys. Rev. 95, 56 (1954).

44. H. W. Streitwolf, Ann. Physik 3, 183 (1959).

45. H. E. Bishop, Brit. J. Appl. Phys. 18, 703 (1967).

46. L. N. Tharp, Ph.D. Thesis, Georgia Institute of Technology (1968).

47. J. J. Lander, Progress in Solid State Chemistry, Volume 2, Pergamon Press, New York, 1965, p. 26.

48. P. Beckmann and A. Spizzichino, The Scattering of Electromagnetic Waves from Rough Surfaces, The MacMillan Co., New York, 1963, p. 9.

49. R. C. Henderson, R. B. Marcus, and W. J. Polito, J. Appl. Phys. 42, 1208 (1971).

50. F. A. Cotton and G. Wilkinson, Advanced Inorganic Chemistry, John Wiley & Sons, New York, 1962, pp. 215-222.

51. P. R. Thornton, Scanning Electron Microscopy, Chapman and Hall, London, 1968, p. 100.

52. T. W. Madey and J. T. Yates, Jr., J. Vac. Sci. Tech. 8, 525 (1971).

53. M. Simons, Jr., L. K. Monteith, and J. R. Hauser, IEEE Trans. Electron. Devices ED-15, 966 (1968).

54. F. J. Blatt, Physics of Electronic Conduction in Solids, McGraw-Hill, New York, 1968.

55. Reference 33, p. 109.

56. Private communication, J. M. Blasingame, Jr.

57. Private communication, E. J. Scheibner.

58. Reference 51, pp. 168-178.

59. J. P. Coad, H. E. Bishop, and J. C. Riviere, Surf. Sci. 21, 253 (1970)

60. B. A. Joyce and J. H. Neave, Surf. Sci. 27, 499 (1971).

61. Reference 33, pp. 69-70.

VITA

Roger Paul Woodward was born May 11, 1943 in Norfolk, Virginia, the son of Paul D. and Evelyn E. Woodward. He married the former Patricia Jane Bucher of Lancaster, Pennsylvania, in November, 1962. They have two children.

Mr. Woodward attended public school in Norfolk, Virginia, where he graduated from Granby High School in 1961. He received his B.E.E. Degree in 1965 and his M.S.E.E. Degree in 1968, both from the Georgia Institute of Technology. He received the Eta Kappa Nu award as the outstanding student in electrical engineering at Georgia Tech in 1965.

Mr. Woodward has served on the staff of the Engineering Experiment Station of Georgia Tech since 1965. He currently serves as a Research Engineer and is a Lecturer in the School of Electrical Engineering.

He is a member of Tau Beta Pi, Sigma Xi, Eta Kappa Nu, and Phi Kappa Phi.